UNIVERSIDADE ESTADUAL DE CAMPINAS
FACULDADE DE ENGENHARIA ELÉTRICA E DE COMPUTAÇÃO

Jonathan Aguiar Soares

Machine Learning Techniques for Massive-MIMO Communications Systems

Técnicas de Aprendizado de Máquina para Sistemas de Comunicação MIMO Massivo

Campinas

2024

Jonathan Aguiar Soares

Machine Learning Techniques for Massive-MIMO Communications Systems

Técnicas de Aprendizado de Máquina para Sistemas de Comunicação MIMO Massivo

Thesis presented to the School of Electrical and Computer Engineering at the University of Campinas in partial fulfillment of the requirements for the Doctoral degree in Electrical Engineering, in the area of Telecommunications and Telematics.

Tese apresentada à Faculdade de Engenharia Elétrica e de Computação da Universidade Estadual de Campinas como parte dos requisitos exigidos para a obtenção do título de Doutor em Engenharia Elétrica, na área de Telecomunicações e Telemática.

Advisor: Prof. Dalton Soares Arantes
Co-advisor: Dr. Kayol Soares Mayer

Este exemplar corresponde à versão final da tese defendida pelo aluno Jonathan Aguiar Soares, e orientada pelo Prof. Dalton Soares Arantes.

Campinas

2024

Ficha catalográfica
Universidade Estadual de Campinas (UNICAMP)
Biblioteca da Área de Engenharia e Arquitetura
Rose Meire da Silva - CRB 8/5974

So11m Soares, Jonathan Aguiar, 1991-
Machine learning techniques for massive-MIMO communications systems / Jonathan Aguiar Soares. – Campinas, SP : [s.n.], 2024.

Orientador: Dalton Soares Arantes.
Coorientador: Kayol Soares Mayer.
Tese (doutorado) – Universidade Estadual de Campinas (UNICAMP), Faculdade de Engenharia Elétrica e de Computação.

1. Telecomunicações. 2. Sistemas MIMO. 3. Redes neurais (Computação). 4. Aprendizado de máquina. I. Arantes, Dalton Soares, 1946-. II. Mayer, Kayol Soares, 1993-. III. Universidade Estadual de Campinas (UNICAMP). Faculdade de Engenharia Elétrica e de Computação. IV. Título.

Informações complementares

Título em outro idioma: Técnicas de aprendizado de máquina para sistemas de comunicação MIMO massivo
Palavras-chave em inglês:
Telecommunications
MIMO systems
Neural networks (Computing)
Machine learning
Área de concentração: Telecomunicações e Telemática
Titulação: Doutor em Engenharia Elétrica
Banca examinadora:
Dalton Soares Arantes [Orientador]
José Cândido Silveira Santos Filho
Rafael Ferrari
Candice Müller
Marcelo Augusto Costa Fernandes
Data de defesa: 05-12-2024
Programa de Pós-Graduação: Engenharia Elétrica

Objetivos de Desenvolvimento Sustentável (ODS)
ODS: 9. Inovação e infraestrutura

Identificação e informações acadêmicas do(a) aluno(a)
- ORCID do autor: https://orcid.org/0000-0002-1659-7599
- Currículo Lattes do autor: http://lattes.cnpq.br/2866994149869821

COMISSÃO JULGADORA - TESE DE DOUTORADO

Candidato: Jonathan Aguiar Soares **RA**: 229966

Data da Defesa: 05 de dez de 2024

Título da Dissertação: “Machine Learning Techniques for Massive-MIMO Communications Systems”.

Título da Dissertação em Português: “Técnicas de Aprendizado de Máquina para Sistemas de Comunicação MIMO Massivo”.

Prof. Dr. Dalton Soares Arantes — Presidente — DECOM/UNICAMP.
Prof. Dr. José Cândido Silveira Santos Filho — DECOM/UNICAMP.
Prof. Dr. Rafael Ferrari — DCA/UNICAMP.
Profa. Dra. Candice Müller — Universidade Federal de Santa Maria.
Prof. Dr. Marcelo Augusto Costa Fernandes — Universidade Federal do Rio Grande do Norte.

A Ata de Defesa, com as respectivas assinaturas dos membros da Comissão Julgadora, encontra-se no SIGA (Sistema de Fluxo de Dissertação/Tese) e na Secretaria de Pós-Graduação da Faculdade de Engenharia Elétrica e de Computação.

I dedicate this thesis to my family, who have supported me and waited patiently for me to finish it. I would also like to extend this dedication to anyone who has made any contribution, as even the simplest, most controversial, and improbable contributions play a part in our paths.

ACKNOWLEDGEMENTS

This work would not have been possible without the unwavering support from my family. I owe my deepest gratitude to my devoted and loving wife, Juliana, who has gracefully shared with me the burden and joy of raising our children, Ravi and Luna, and who is now pregnant with our third child, Bento, who should be born very soon. I could not be more grateful to have such a healthy and happy family, whose love and warmth have given me tremendous strength. Your enduring love, patience, and tenderness have supported me at every step of this journey.

I would like to express my heartfelt thanks to my advisor, Prof. Dalton S. Arantes, for his continuous support and guidance in the development of this work. Your wisdom and encouragement have been instrumental in shaping this dissertation. A very special thanks goes to my gifted friend and now co-advisor, Kayol S. Mayer, for the invaluable help, guidance, and collaboration throughout all phases of this dissertation. Your insights and mentorship have been a great honor and privilege.

I also extend my gratitude to all my colleagues at ComLab - Digital Communications Laboratory, for their friendship and support. Your camaraderie has made the challenging moments more bearable and the successes more enjoyable. Additionally, I would like to acknowledge the dedicated and talented professors and staff at FEEC-UNICAMP, for their invaluable lessons, support, and inspiration. Your contributions have profoundly enriched my academic and professional journey.

Thank you all for being a part of this incredible journey.

“Knowledge is a paradox. The more one understands, the more one realizes the vastness of their ignorance.”

(Christian Linke)

RESUMO

Esta tese explora metodologias avançadas e aplicações de redes neurais complexas (CVNNs) e técnicas de aprendizado de máquina para aprimorar a estimativa de canal, decodificação e processamento de sinal em sistemas de comunicação MIMO (múltiplas entradas e múltiplas saídas). Abordando os desafios impostos pela crescente demanda por maiores taxas de dados e comunicação sem fio confiável, introduzimos arquiteturas CVNN inovadoras e abordagens de aprendizado semissupervisionado projetadas para melhorar o desempenho e a eficiência. As principais contribuições incluem avanços no desenvolvimento de redes neurais de função de base radial de transmitância de fase (PT-RBF), que demonstram desempenho superior em sistemas MIMO-OFDM massivos com menor complexidade computacional em comparação com os métodos convencionais. Além disso, técnicas inovadoras de inicialização de parâmetros garantem a convergência bem-sucedida de CVNNs multicamadas, aumentando a robustez e a adaptabilidade. Também introduzimos técnicas de aprendizado semissupervisionado, como aprendizado de inferência rígida (HIL) e aprendizado de inferência gaussiana (GIL), permitindo que CVNNs aprendam com dados não auxiliados por piloto e aumentem sua capacidade de rastreamento em canais dinâmicos. Além disso, foi desenvolvido um método de decodificação paralela usando redes neurais PT-RBF distintas para cada subportadora, reduzindo significativamente o tempo de decodificação e melhorando a adaptabilidade do sistema. Simulações extensivas validam os métodos propostos, mostrando melhorias substanciais na taxa de erro de bit (BER) e eficiência computacional em vários cenários desafiadores. Esses achados abrem caminho para soluções de redes neurais escaláveis e adaptáveis adequadas para sistemas de telecomunicações de próxima geração, incluindo 5G, 6G e além. Em resumo, esta tese avança na aplicação de CVNNs e aprendizado de máquina para telecomunicações, contribuindo para sistemas de comunicação mais eficientes, robustos e adaptáveis.

Palavras-chaves: Telecomunicações; MIMO massivo; Aprendizado de Máquina; Redes neurais; Redes neurais de Valor Complexo.

ABSTRACT

This thesis explores advanced methodologies and applications of complex-valued neural networks (CVNNs) and machine learning techniques to enhance channel estimation, decoding, and signal processing in multiple-input multiple-output (MIMO) communication systems. Addressing the challenges posed by the increasing demand for higher data rates and reliable wireless communication, we introduce novel CVNN architectures and semi-supervised learning approaches designed to improve performance and efficiency. Key contributions include further developments of phase-transmittance radial basis function (PT-RBF) neural networks, which demonstrate superior performance in massive MIMO-OFDM systems, with lower computational complexity compared to conventional methods. Additionally, novel parameter initialization techniques ensure successful convergence of multi-layered CVNNs, enhancing robustness and adaptability. We also introduce semi-supervised learning techniques, such as hard inference learning (HIL) and Gaussian inference learning (GIL), enabling CVNNs to learn from non-pilot-aided data and increasing their tracking ability in dynamic channels. Furthermore, a parallel decoding method using distinct PT-RBF neural networks for each subcarrier is developed, significantly reducing decoding time and improving system adaptability. Extensive simulations validate the proposed methods, showing substantial improvements in bit error rate (BER) and computational efficiency across various challenging scenarios. These findings pave the way for scalable and adaptable neural network solutions suitable for next-generation telecommunication systems, including 5G, 6G, and beyond. In summary, this thesis advances the application of CVNNs and machine learning for telecommunications, contributing to more efficient, robust, and adaptive communication systems.

Keywords: Telecommunications; Massive MIMO; Machine Learning; Neural Networks; Complex-Valued Neural Networks.

LIST OF FIGURES

LIST OF TABLES

LIST OF ABBREVIATIONS AND ACRONYMS

E_b/N_0 energy per bit to noise power spectral density ratio

3GPP 3rd Generation Partnership Project

5G fifth-generation wireless technology

6G sixth-generation wireless technology

ANNs artificial neural networks

AWGN additive white Gaussian noise

BER bit error rate

BLER block error rate

C-RBF complex-valued radial basis function

CNN convolutional neural network

CNNs convolutional neural networks

CP cyclic prefix

CSI channel state information

CSIRS channel state information reference signal

CVFNN complex-valued feedforward neural network

CVNNs complex-valued neural networks

DL deep learning

DNN deep neural network

DSP digital signal processing

E2E end-to-end

FFT fast Fourier transform

GANs generative adversarial networks

GIL Gaussian inference learning

GNNs graph neural networks

HIL hard inference learning

HIs hardware impairments

I/Q in-phase/quadrature-phase

IFFT inverse fast Fourier transform

IoT Internet of Things

ISI intersymbol interference

LS least squares

LSPCA least squares principal component analysis

m-MIMO massive multiple-input multiple-output

M-QAM M-ary quadrature amplitude modulation

MI mutual information

MIMO Multiple-Input Multiple-Output

MIMO-OFDM Multiple-Input Multiple-Output Orthogonal Frequency Division Multiplexing

ML maximum likelihood

mMIMO massive MIMO

MMSE minimum mean square error

mmWave millimeter-wave

MSE mean square error

MU-MIMO multi-user MIMO

NextG next-generation

NNs neural networks

OFDM orthogonal frequency division multiplexing

OSTBC orthogonal space time coding

OTFS orthogonal time frequency space

P/S parallel to serial

PAPR peak-to-average power ratio

PCA principal component analysis

PSK phase-shift keying

PT-RBF phase-transmittance radial basis function

PTRBF phase transmittance radial basis function

QAM quadrature amplitude modulation

QOSTBC quasi-orthogonal space-time block codes

RBF radial basis function

RF radiofrequency

RISs reconfigurable intelligent surfaces

RVNNs real-valued neural networks

Rx receiver

S/P serial-to-parallel

SCFNN split complex feedforward neural network

SDRs software-defined radios

SISO single-input single-output

SNR signal-to-noise ratio

STBC space-time block coding

SVD single-value decomposition

TDL Tapped Delay Line

Tx transmitter

UEs user equipment

VLC visible light communications

ZC Zadoff-Chu

ZF zero-forcing

ZIC z-interference channel

LIST OF PUBLICATIONS

Journal Papers

- Soares, J.A., Mayer, K.S., & Arantes, D.S. (2024). End-to-End Learning for Massive MIMO Systems Using Complex-Valued Neural Networks. Submitted to *IEEE Transactions on Wireless Communications*.

- Mayer, K.S., Soares, J.A., Cruz, A.A., & Arantes, D.S. (2024). Adaptive Learning Rate Methods for Complex-valued Neural Networks. Submitted to *IEEE Transactions on Neural Networks and Learning Systems*.

- Kayol S. Mayer, Jonathan A. Soares, Dalton S. Arantes, Christian E. Rothenberg, and Darli A. A. Mello (2024). Network-wide QoT Estimation with Optimized Gradient Transfer Between Wavelengths. *IEEE Journal of Lightwave Technology*. `https://doi.org/10.1109/JLT.2025.3538951`

- Soares, J.A., Mayer, K.S., & Arantes, D.S. (2023). Semi-Supervised ML-Based Joint Channel Estimation and Decoding for m-MIMO With Gaussian Inference Learning. *IEEE Wireless Communications Letters, 12*(12), 2123–2127. `http://dx.doi.org/10.1109/LWC.2023.3309479`

- Mayer, K.S., Müller, C., Soares, J.A., de Castro, F.C.C., & Arantes, D.S. (2022). Deep Phase-Transmittance RBF Neural Network for Beamforming With Multiple Users. *IEEE Wireless Communications Letters, 11*(7), 1498–1502. `http://dx.doi.org/10.1109/LWC.2022.3177162`

- Mayer, K.S., Pinto, R.P., Soares, J.A., Arantes, D.S., Rothenberg, C.E., Cavalcante, V., Santos, L.L., Moraes, F.D., & Mello, D.A.A. (2022). Demonstration of ML-Assisted Soft-Failure Localization Based on Network Digital Twins. *Journal of Lightwave Technology, 40*(14), 4514–4520. `http://dx.doi.org/10.1109/JLT.2022.3170278`

- Soares, J.A., Mayer, K.S., de Castro, F.C.C., & Arantes, D.S. (2021). Complex-Valued Phase Transmittance RBF Neural Networks for Massive MIMO-OFDM Receivers. *Sensors, 21*(24), 8200. `http://dx.doi.org/10.3390/s21248200`

- Mayer, K.S., Soares, J.A., & Arantes, D.S. (2021). A Nonlinear Concurrent Butterfly Equalizer. *Radioengineering, 30*(2), 261–270. `http://dx.doi.org/10.13164/re.2021.0261`

- Mayer, K.S., Soares, J.A., Pinto, R.P., Rothenberg, C.E., Arantes, D.S., & Mello, D.A.A. (2021). Machine-learning-based Soft-Failure Localization With Partial Software-Defined Networking Telemetry. *Journal of Optical Communications and Networking, 13*(10), E122–E131. `http://dx.doi.org/10.1364/JOCN.424654`

Conference Papers

- Soares, J.A., Mayer, K.S., & Arantes, D.S. (2024). Neural Network-based Subcarrier-level Joint Channel Estimation and Decoding for MIMO-OFDM Receivers. In *2024 IEEE Latin-American Conference on Communications (LATINCOM)* `https://doi.org/10.1109/LATINCOM62985.2024.10770650`
- Teixeira, L.F.M., Luiz, V.H., Soares, J.A., Mayer, K.S., & Arantes, D.S. (2024). Online ML-based Joint Channel Estimation and MIMO Decoding for Dynamic Channels. In *XL Simpósio Brasileiro de Telecomunicações e Processamento de Sinais (SBrT2024)*. `http://dx.doi.org/10.14209/sbrt.2024.1571036775`
- Soares, J.A., Luiz, V.H., Arantes, D.S., & Mayer, K.S. (2024). Deep Complex-valued Radial Basis Function Neural Networks and Parameter Selection. In *2024 19th International Symposium on Wireless Communication Systems (ISWCS)*, 1–6. `http://dx.doi.org/10.1109/ISWCS61526.2024.10639101`
- Soares, J.A., Mayer, K.S., & Arantes, D.S. (2024). On the Parameter Selection of Phase-transmittance Radial Basis Function Neural Networks for Communication Systems. In *2024 IEEE International Conference on Machine Learning for Communication and Networking (ICMLCN)*, 530–536. `http://dx.doi.org/10.1109/ICMLCN59089.2024.10624891`
- Mayer, K.S., Soares, J.A., Dal Maso, M.P.A., Rothenberg, C.E., Arantes, D.S., & Mello, D.A.A. (2024). Network-wide QoT Estimation Using SGD with Gradient Transfer Between Wavelengths. In *Optical Fiber Communication Conference (OFC) 2024*. `http://dx.doi.org/10.1364/ofc.2024.m1h.7`
- Mayer, K.S., Soares, J.A., Cruz, A.A., & Arantes, D.S. (2023). On the Computational Complexities of Complex-Valued Neural Networks. In *2023 IEEE Latin-American Conference on Communications (LATINCOM)*. `http://dx.doi.org/10.1109/latincom59467.2023.10361866`
- Sousa, H.S., Soares, J.A., Mayer, K.S., & Arantes, D. (2023). CVNN-based Channel Estimation and Equalization in OFDM Systems Without Cyclic Prefix. In *Anais do XLI Simpósio Brasileiro de Telecomunicações e Processamento de Sinais (SBrT2023)*. `http://dx.doi.org/10.14209/sbrt.2023.1570923809`

- Soares, J.A., Mayer, K., Valadares, P., & Arantes, D. (2022). PCA-based Channel Estimation for MIMO Communications. In *Anais do XL Simpósio Brasileiro de Telecomunicações e Processamento de Sinais (SBrT2022)*. `http://dx.doi.org/10.14209/sbrt.2022.1570825011`

- Pinto, R.P., Mayer, K.S., Soares, J.A., Arantes, D.S., Mello, D.A.A., Cavalcante, V., Santos, L.L., & Rothenberg, C.E. (2021). Demonstration of Machine-Intelligent Soft-Failure Localization Using SDN Telemetry. In *Optical Fiber Communication Conference (OFC) 2021*. `http://dx.doi.org/10.1364/OFC.2021.M2B.5`

- Mayer, K.S., Soares, J.A., Pinto, R.P., Rothenberg, C.E., Arantes, D.S., & Mello, D.A.A. (2020). Soft Failure Localization Using Machine Learning with SDN-based Network-wide Telemetry. In *2020 European Conference on Optical Communications (ECOC)*. `http://dx.doi.org/10.1109/ECOC48923.2020.9333313`

Patents

- Soares, J.A., Mayer, K., de Castro, F.C.C., & Arantes, D.S. (2021). *Método de estimação de canal e decodificação baseado em rede neural de arquitetura diferenciada*. Patent: BR 10 2021 025709 1. Digital Communications Laboratory - ComLab.

- Mayer, K., Soares, J.A., Pinto, R.P., Mello, D.A.A., Rothenberg, C.E., & Arantes, D.S. (2021). *Método de Localização de Falhas em Redes Ópticas com o Uso de Algoritmos de Aprendizado de Máquina Treinados com Espelho Virtual da Rede sem Falha*. Patent: BR 10 2021 022406 1. INTRIG and Digital Communications Laboratory - ComLab.

CONTENTS

Chapter 1

Introduction

The rapid evolution of telecommunications has been driven by the need for faster, more reliable, and more efficient communication systems. In recent years, the integration of neural networks and machine learning techniques has opened new frontiers in the field, enabling the development of advanced communication systems that can adapt to changing environments and optimize performance in real time. Among these techniques, complex-valued neural networks (CVNNs) have emerged as a powerful tool for addressing the unique challenges posed by modern communication systems.

A central pillar of contemporary wireless networks is Multiple-Input Multiple-Output (MIMO) technology, which leverages multiple antennas at the transmitter and receiver to improve both throughput and link reliability (BJÖRNSON et al., 2023). By exploiting spatial diversity, MIMO provides significant enhancements in spectral efficiency—capabilities that become particularly indispensable for next-generation standards such as 5G and beyond (WANG et al., 2023). The growing emphasis on massive MIMO (mMIMO), wherein large numbers of antennas are deployed to further increase capacity and reduce interference, has likewise introduced new technical challenges. This thesis aims to address these complexities by exploring how ML-based approaches, particularly those using CVNNs, can deliver effective solutions for modern and evolving MIMO-centric communication infrastructures.

This thesis explores the application of CVNNs and other machine learning algorithms in telecommunications, with a focus on enhancing signal processing, data transmission, and system reliability within massive MIMO contexts. Each chapter presents a distinct study that contributes to the overall goal of improving telecommunications through innovative neural network architectures and methodologies.

1.1 MOTIVATION

The integration of neural networks into telecommunications is not a novel concept. As early as the 1990s, researchers proposed neural network-based methods to handle tasks such as channel equalization and noise reduction, demonstrating that data-driven approaches could provide tangible performance benefits over purely analytical solutions. However, these foundational efforts also exposed significant challenges, in particular, on how to design robust training algorithms and ensure that the network can generalize across diverse operating conditions.

With the recent surge of advanced machine learning techniques, CVNNs have gained considerable attention in the telecommunications community. Unlike real-valued networks, which must separate signals into in-phase and quadrature components, CVNNs handle amplitudes and phases jointly in their native complex form. This property proves advantageous for many communication problems, such as modulation classification and adaptive filtering, where channel effects often manifest as complex-valued distortions. Empirical studies have shown that CVNNs often outperform traditional methods in challenging scenarios characterized by high noise or interference.

1.1.1 Expanding Community and Theoretical Guarantees

The growing importance of CVNNs is also reflected in broader machine learning forums. During the past decade, the IEEE World Congress on Computational Intelligence (WCCI) has hosted a recurring special session solely dedicated to neural networks with complex and hypercomplex value. Organized regularly since 2006, these sessions have attracted numerous submissions and vibrant discussions, underscoring the field's rapid development and the community's recognition that complex-domain methods can tackle specialized tasks that real-valued solutions sometimes struggle with. One of the co-organizers, Hirose Akira, remains a leading researcher in applying CVNNs to physics and engineering problems, further illustrating the breadth of CVNN applications beyond standard telecommunications contexts.

From a theoretical point of view, recent results have reinforced the mathematical foundation of CVNNs, extending classical theorems about real-valued networks to the complex domain. Notably, Voigtlaender's universal approximation theorem (VOIGTLAENDER, 2023) shows that feedforward CVNNs with sufficiently flexible activation functions can uniformly approximate any continuous function on any compact subset of $\mathbb{C}^N$. This parallels well-known results for real-valued neural networks while accounting for holomorphic or polyharmonic constraints unique to complex signals. Such developments further strengthen the case for adopting CVNNs in high-stakes telecommunication tasks, where the ability to approximate sophisticated nonlinear channel relationships can translate into substantial performance gains.

1.1.2 RBF-Based CVNNs and Their Connection to the MAP Equalizer

Within the broader spectrum of CVNN architectures, one significant milestone came in 1993, when Chen *et al.* first introduced a dedicated complex-valued radial basis function (C-RBF) network (CHEN et al., 1993). Although existing real-valued RBF frameworks had been adapted to certain communication tasks, this complex RBF network formally incorporated complex-valued centers and weights, permitting more natural handling of phase and amplitude relationships. Subsequently, Chen and coauthors demonstrated that, under idealized conditions involving additive white Gaussian noise (AWGN) and intersymbol interference, the structure of the Bayesian or maximum a posteriori (MAP) equalizer could be assigned to an RBF network (CHEN; MULGREW; GRANT, 1993), a perspective further reinforced by Patra and Mulgrew (PATRA; MULGREW, 1998). Although these initial proofs were limited to simpler channels and lower-order constellations (e.g., BPSK), additional work (FERRARI, 2005; FERRARI et al., 2003) broadened the argument to fuzzy-based filters, revealing that many fuzzy equalizers share core mathematical elements with RBF networks.

More recently, our own empirical investigations (MAYER et al., 2022; SOARES; MAYER; ARANTES, 2023) compared multiple CVNN architectures—multilayer perceptrons, convolutional designs, and complex-valued RBF networks—across different communication tasks. In these studies, RBF-based CVNNs consistently yielded the best performance, demonstrating superior resilience to noise, interference, and moderate nonlinearities. Although a fully comprehensive proof of the equivalence of MAP—-RBF for higher-order constellations and strongly nonlinear channels remains elusive, these practical outcomes reinforce the intuition that RBF's localized activation functions provide reliable decision boundaries in environments with Gaussian-like noise clusters.

1.1.3 Research Group Background

In parallel with these theoretical and empirical advances, our research group has maintained a decades-long commitment to applying machine learning in wireless communications. Starting in the 1990s, the group investigated neural networks, fuzzy logic, radial basis function (RBF) architectures, and genetic algorithms to address a wide array of telecommunication problems, such as video encoding and channel equalization (DE CASTRO; DE CASTRO; ARANTES, 1998; DE CASTRO; DE CASTRO; ARANTES, 1999; CARDOSO; ARANTES, 1999; CARDOSO et al., 2000; CASTRO et al., 2000; LOSS et al., 2007b). This tradition forms a direct mentor–student lineage: my own undergraduate research in MIMO detection took place under Professor Fernando César Comparsi de Castro, while my subsequent master's and doctoral studies have been supervised by Professor Dalton Soares Arantes—who, in the early 2000s, guided Professor Fernando in his doctoral work. Such deep-rooted collaborations underscore the pioneering nature of our group's work, culminating in the advanced CVNN-based strategies examined in this thesis.

1.1.4 Open Challenges and thesis Scope

Despite encouraging results and strong theoretical underpinnings for RBF-based CVNNs, several open questions persist. For example, scaling these techniques to mMIMO systems with potentially hundreds of antennas is far from trivial, and designing robust training algorithms for severely nonlinear or time-varying channels requires further innovation. Additionally, while RBF-based networks are known to approximate MAP solutions under certain assumptions, the exact conditions under which they remain optimal or near-optimal for large-scale higher-order constellations remain an active research topic.

Accordingly, this thesis targets these gaps by developing, analyzing, and validating novel CVNN architectures and machine learning tools to enhance signal processing, data transmission, and reliability in modern communication systems. Through a series of replicated manuscripts, we demonstrate the transformative potential of RBF-based CVNN solutions across various scenarios, thereby expanding the applicability of machine learning in the context of massive MIMO and beyond.

1.2 CONTRIBUTIONS AND OUTLINE

In light of the above discussion, the main scope of this thesis is to conceive and test a myriad of CVNNs and machine learning applications for telecommunications. The following chapters are replicas of manuscripts that we have published in or submitted to journals and conferences along our research activities. Below we present an annotated outline of each chapter.

To supplement this textual overview, Figure 1.1 visually depicts the relationships among the core chapters and concepts. It highlights how themes like MIMO, space-time block coding (STBC), CVNNs, and channel estimation naturally intertwine, culminating in novel end-to-end solutions and parameter-optimization strategies.

1.2.1 Reliability in MIMO communications

My investigation into MIMO reliability, STBC, and machine learning techniques—particularly those involving CVNNs—did not begin strictly with this doctoral research. It actually dates back to my undergraduate research program, where I worked on a project entitled Development of a Sphere Detector Simulator for High-Order MIMO Systems. Building on that foundation, I pursued a master's thesis, Complex Phase-Transmittance RBF Neural Network for Massive MIMO-OFDM Decoding, further refining novel decoding strategies for massive MIMO setups (see also (MAYER; SOARES; ARANTES, 2020)). Over the course of these earlier studies, the synergy between robust STBC schemes and machine learning became increasingly evident, eventually culminating

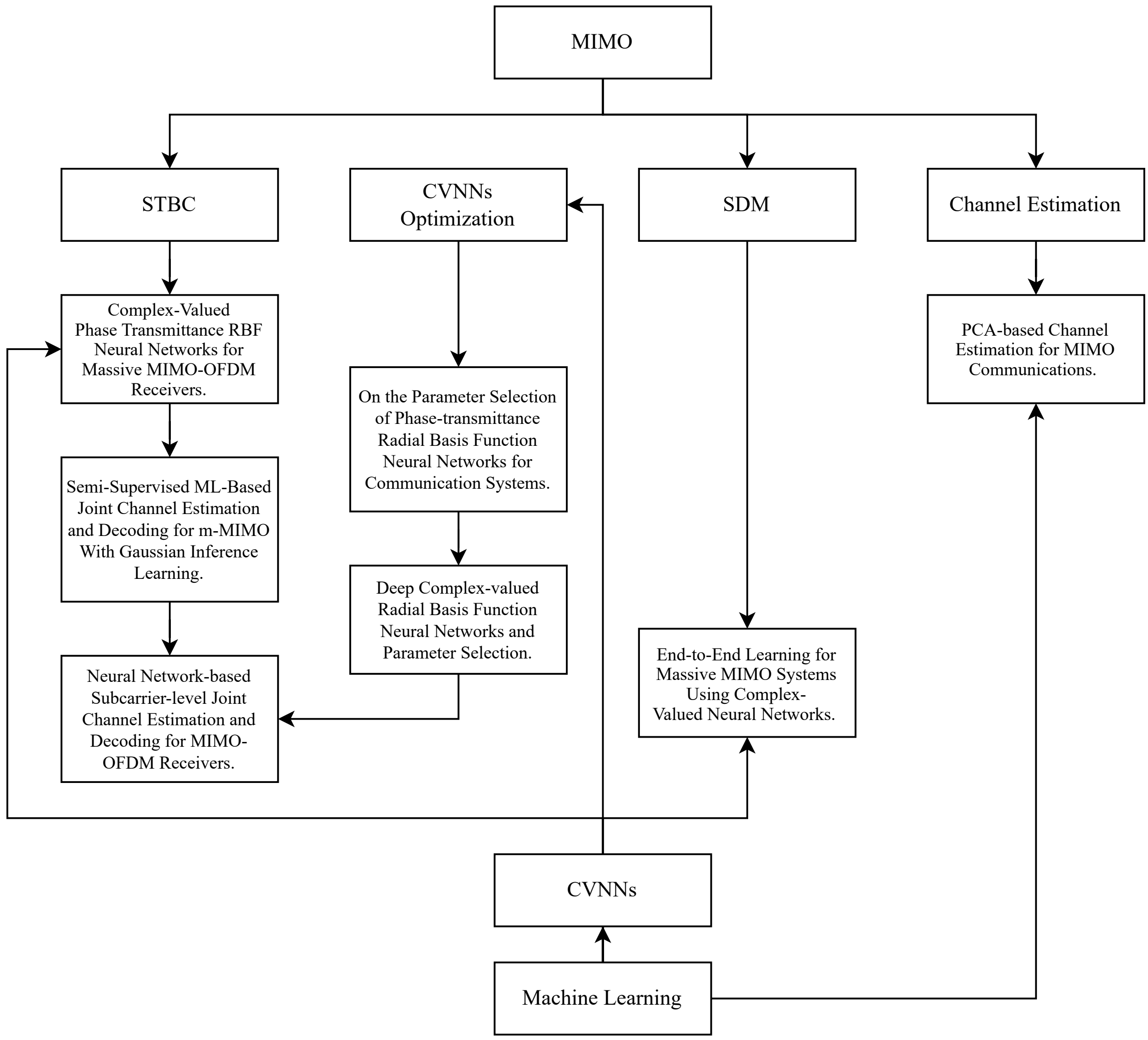

Figure 1.1 – High-level flow chart illustrating how the main chapters/articles of this thesis interrelate. Each box represents a chapter's central topic, and the arrows indicate conceptual or methodological links among them.

in the more advanced topics I address in this doctoral work. The following chapters present the resulting contributions, showcasing how the integration of STBC designs, CVNN-based architectures, and other neural-network-driven approaches can significantly enhance reliability in MIMO communications.

Chapter 2 Complex-Valued Phase Transmittance RBF Neural Networks for Massive MIMO-OFDM Receivers: This chapter introduces a novel MIMO scheme employing a phase transmittance radial basis function (PTRBF) neural network for massive Multiple-Input Multiple-Output Orthogonal Frequency Division Multiplexing (MIMO-OFDM) systems. The proposed scheme addresses the challenge of designing cost-effective receivers for MIMO channels by offering a decoding algorithm that achieves improved performance with lower computational complexity compared to traditional maximum likelihood decoding. The study highlights the increasing demand for technologies to enhance spectral efficiency in bandwidth-congested areas, driven by the real-time processing of big data, Internet of Things (IoT), and 4K video streaming. The proposed MIMO-PTRBF neural network leverages its architecture to provide superior performance in 5G wireless Rayleigh channels, effectively managing nonlinear impairments and intersymbol interference (ISI). Simulation results demonstrate significant improvements in bit error rate (BER) and computational complexity, showcasing the feasibility and scalability of the approach for future mobile communication systems, including fifth-generation wireless technology (5G), sixth-generation wireless technology (6G), and beyond.

Chapter 4 Semi-supervised ML-based Joint Channel Estimation and Decoding for m-MIMO with Gaussian Inference Learning: This chapter proposes an innovative approach to enhance link quality and reliability in mMIMO systems using quasi-orthogonal space-time block codes (QOSTBC). The study addresses the high computational complexity of classical decoding algorithms by utilizing CVNNs for joint channel estimation and decoding. The work extends previous research by incorporating two semi-supervised learning techniques: hard inference learning (HIL) and Gaussian inference learning (GIL). These techniques enable the CVNNs to self-learn from non-pilot-aided data, increasing their tracking ability and robustness in dynamic channels. Simulation results demonstrate significant improvements in performance and robustness, particularly in handling high Doppler frequencies, making this approach suitable for dynamic 5G channels and beyond.

Chapter 7 Neural Network-based Subcarrier-level Joint Channel Estimation and Decoding for MIMO-OFDM Receivers: This chapter presents a novel decoding method for MIMO-OFDM systems that employs parallel neural networks to significantly enhance decoding speed and accuracy. Unlike traditional serial decoding methods, which do not address the unique characteristics of individual subcarriers, this approach utilizes distinct PTRBF neural networks for each subcarrier. This parallel processing method reduces decoding time and improves system adaptability by effectively managing nonlinear impairments and intersymbol interference. Simulation results demonstrate that this method outperforms conventional decoding techniques, achieving lower bit error rates (BER) in both linear and nonlinear scenarios, and showing great potential for scalability in ultra-massive MIMO setups.

1.2.2 Channel estimation in MIMO communications

This chapter is an isolated contribution, since it is somewhat separate from the other main threads. However, it is a natural product of the research on channel estimation in MIMO systems, which is mandatory in many of the linear approaches used as baselines in the works presented in this thesis.

Chapter 3 PCA-based Channel Estimation for MIMO Communications: This chapter presents a novel principal component analysis (PCA)-based channel estimation approach for MIMO-OFDM systems. The method first estimates the channel frequency response using the least squares (LS) method and then applies PCA to filter out noise components, retaining only the significant channel components. This approach improves the accuracy of channel estimation while maintaining lower computational complexity compared to the minimum mean square error (MMSE) method. The effectiveness of the proposed PCA-based technique is demonstrated through comparisons with MMSE in terms of bit error rate (BER) versus energy per bit to noise power spectral density ratio ($\mathrm{E_b/N_0}$), especially under dynamic channel conditions with Doppler frequencies. The results indicate that the proposed approach offers significant performance improvements and is particularly suitable for massive MIMO architectures due to its scalability and reduced computational complexity.

1.2.3 Optimization in Neural Networks

We observed that our machine learning models could be further improved via specific theoretical optimizations. When working with the PTRBF architecture, we noted a significant sensitivity to initialization parameters, prompting us to develop a systematic initialization method. Encouraged by these results, we extended the approach to the C-RBF framework, and we believe similar principles can be generalized to other RBF-based models. Some architectures and results were only feasible through our proposed initialization strategy, as demonstrated in the works below.

Chapter 5 On the Parameter Selection of Phase-transmittance Radial Basis Function Neural Networks for Communication Systems: This chapter delves into the parameter selection for PTRBF neural networks, which are crucial for various tasks in digital communication systems such as equalization, channel estimation, beamforming, and decoding. The study presents a novel parameter initialization technique specifically designed for multi-layered, multi-input, and multi-output PTRBF architectures. Through rigorous simulations conforming to 3rd Generation Partnership Project (3GPP) TS 38 standards, the proposed initialization method outperforms conventional strategies like random, K-means, and constellation-based methods. This work highlights the method's effectiveness in ensuring successful convergence in deep PTRBF architectures, paving the way for more robust and efficient neural network deployments in complex digital communication environments.

The findings emphasize the importance of proper initialization in achieving optimal performance and scalability in real-world applications.

Chapter 6 Deep Complex-valued Radial Basis Function Neural Networks and Parameter Selection: This chapter investigates the extension of classical shallow C-RBF neural networks to deep architectures, enhancing their applicability and performance in digital communication systems. The study introduces a novel parameter initialization scheme for deep C-RBF neural networks, focusing on initializing synaptic weights, biases, center vectors, and center variances in the complex domain. Rigorous simulations conforming to 3GPP TS 38 standards demonstrate the proposed method's superior performance compared to conventional initialization strategies like random, K-means, and constellation-based methods. The findings highlight the method's unique efficacy and adaptability in achieving successful convergence for deep C-RBF architectures, paving the way for more robust and efficient neural network deployments in complex-valued digital communication environments.

1.2.4 Spatial Division Multiplexing and Multi-user

Finally, in the last year of this doctoral work, we noticed several studies addressing end-to-end (E2E) learning in MIMO communications. This trend motivated us to investigate similar approaches that exploit CVNNs in multi-user scenarios. Our findings were particularly promising, and combined with some innovative solutions for user multiplexing, they led us to publish the work below.

Chapter 8 Complex-valued NN-based End-to-end Learning in Massive-MIMO Communications: This chapter presents a novel end-to-end (E2E) learning architecture for massive MIMO communication systems using CVNNs. The proposed architecture integrates both encoding and decoding stages, optimized for flat-fading Rayleigh channel conditions, focusing on maximizing system capacity and transmission efficiency. A key contribution is the extension of the approach to multi-user MIMO (MU-MIMO) scenarios, where data streams are orthogonalized for several user equipment (UEs), improving spectral efficiency with federated learning. Additionally, a power control mechanism based on regularization is introduced to ensure stable transmission power and prevent hardware overflow. Simulation results demonstrate significant improvements in system capacity and mutual information, with performance compared against classical approaches like zero-forcing (ZF) and minimum mean square error (MMSE) precoding. The findings emphasize the potential of CVNN-based architectures for future wireless communication systems.

In addition to these replicated chapters, chapter 9 concludes the thesis by synthesizing the main results, discussing their implications, and identifying potential avenues for further research, such as ultra-massive MIMO implementations, advanced hardware acceleration for neural networks, and exploration of nonlinear PCA-based denoising methods. Overall, the contributions throughout the thesis demonstrate the transformative role that CVNN-based solutions can play in modern wireless networks.

REFERENCES

BJÖRNSON, E. et al. Twenty-Five Years of Signal Processing Advances for Multiantenna Communications: From theory to mainstream technology. **IEEE Signal Processing Magazine**, v. 40, n. 4, p. 107–117, June 2023. ISSN 1558-0792. DOI: 10.1109/MSP.2023.3261505. Cited on pages 28, 155.

CARDOSO, F. A. C. M. et al. Uma Versão Evolutiva do Algoritmo de Godard. *In*: XVIII Simpósio Brasileiro de Telecomunicações (SBrT2000). [S.l.: s.n.], 2000. DOI: 10.14209/sbrt.2000.5300275. Cited on page 30.

CARDOSO, F.; ARANTES, D. Genetic decoding of linear block codes. *In*: PROCEEDINGS of the 1999 Congress on Evolutionary Computation-CEC99 (Cat. No. 99TH8406). [S.l.: s.n.], July 1999. v. 3, 2302–2309 vol. 3. DOI: 10.1109/CEC.1999.785561. Cited on page 30.

CASTRO, M. C. F. d. et al. A Fuzzy Neural CBR Channel Rate Controller for MPEG2 Encoders. *In*: XVIII Simpósio Brasileiro de Telecomunicações (SBrT2000). [S.l.: s.n.], 2000. DOI: 10.14209/sbrt.2000.4120017. Cited on page 30.

CHEN, S.; MULGREW, B.; GRANT, P. A clustering technique for digital communications channel equalization using radial basis function networks. **IEEE Transactions on Neural Networks**, v. 4, n. 4, p. 570–590, July 1993. ISSN 1941-0093. DOI: 10.1109/72.238312. Cited on page 30.

CHEN, S. et al. Complex-valued radial basis function networks. *In*: 1993 Third International Conference on Artificial Neural Networks. [S.l.: s.n.], May 1993. P. 148–152. Cited on page 29.

DE CASTRO, F.; DE CASTRO, M.; ARANTES, D. A supervised neural constant bit rate video controller for MPEG2 encoders. *In*: ITS'98 Proceedings. SBT/IEEE International Telecommunications Symposium (Cat. No.98EX202). [S.l.: s.n.], Aug. 1998. v. 2, 504–509 vol.2. DOI: 10.1109/ITS.1998.718445. Cited on page 30.

DE CASTRO, M.; DE CASTRO, C.; ARANTES, D. RBF neural networks with centers assignment via Karhunen-Loeve transform. *In*: IJCNN'99. International Joint Conference on Neural Networks. Proceedings (Cat. No.99CH36339). [S.l.: s.n.], July 1999. v. 2, 1265–1270 vol.2. DOI: 10.1109/IJCNN.1999.831143. Cited on page 30.

FERRARI, R. et al. Unsupervised channel equalization using fuzzy prediction-error filters. *In*: 2003 IEEE XIII Workshop on Neural Networks for Signal Processing (IEEE Cat. No.03TH8718). [S.l.: s.n.], Sept. 2003. P. 869–878. DOI: 10.1109/NNSP.2003.1318086. Cited on page 30.

FERRARI, R. **Fuzzy filters based communication channels equalization**. 2005. Dissertação de Mestrado – Universidade Estadual de Campinas, Faculdade de Engenharia Elétrica e de Computação, Campinas, SP, Brazil. Orientador: João Marcos Travassos Romano. DOI: `10.47749/T/UNICAMP.2005.359287`. Available from: <`https://doi.org/10.47749/T/UNICAMP.2005.359287`>. Cited on page 30.

LOSS, D. V. et al. Concurrent Blind Channel Equalization with Phase Transmittance RBF Neural Networks. **Journal of the Brazilian Computer Society**, v. 13, n. 1, p. 18–25, 2007b. ISSN 1678-4804. DOI: `10.1007/BF03192398`. Available from: <`https://doi.org/10.1007/BF03192398`>. Cited on page 30.

MAYER, K. S.; SOARES, J. A.; ARANTES, D. S. Complex MIMO RBF Neural Networks for Transmitter Beamforming over Nonlinear Channels. **Sensors**, v. 20, n. 2, p. 1–15, Jan. 2020. DOI: `10.3390/s20020378`. Cited on pages 31, 40, 41, 51, 54, 79, 83, 95, 96, 109, 127.

MAYER, K. S. et al. Deep Phase-Transmittance RBF Neural Network for Beamforming With Multiple Users. **IEEE Wireless Communications Letters**, v. 11, n. 7, p. 1498–1502, 2022. DOI: `10.1109/LWC.2022.3177162`. Cited on pages 30, 83, 95–97, 109, 127, 142, 145, 155, 156, 161–163.

PATRA, S.; MULGREW, B. Efficient architecture for Bayesian equalization using fuzzy filters. **IEEE Transactions on Circuits and Systems II: Analog and Digital Signal Processing**, v. 45, n. 7, p. 812–820, July 1998. ISSN 1558-125X. DOI: `10.1109/82.700928`. Cited on page 30.

SOARES, J. A.; MAYER, K. S.; ARANTES, D. S. Semi-Supervised ML-Based Joint Channel Estimation and Decoding for m-MIMO With Gaussian Inference Learning. **IEEE Wireless Communications Letters**, v. 12, n. 12, p. 2123–2127, 2023. DOI: `10.1109/LWC.2023.3309479`. Cited on pages 30, 114, 133, 146, 155, 161, 162.

VOIGTLAENDER, F. The universal approximation theorem for complex-valued neural networks. **Applied and Computational Harmonic Analysis**, v. 64, p. 33–61, 2023. ISSN 1063-5203. DOI: `https://doi.org/10.1016/j.acha.2022.12.002`. Available from: <`https://www.sciencedirect.com/science/article/pii/S1063520322001014`>. Cited on pages 29, 95.

WANG, C.-X. et al. On the Road to 6G: Visions, Requirements, Key Technologies, and Testbeds. **IEEE Communications Surveys & Tutorials**, v. 25, n. 2, p. 905–974, Apr. 2023. ISSN 1553-877X. DOI: `10.1109/COMST.2023.3249835`. Cited on pages 28, 155.

Chapter 2

Complex-Valued Phase Transmittance RBF Neural Networks for Massive MIMO-OFDM Receivers

Authors: Jonathan Aguiar Soares, Kayol Soares Mayer, Fernando César Comparsi de Castro, and Dalton Soares Arantes

Abstract

Multi-input multi-output (MIMO) transmission schemes have become the techniques of choice for increasing spectral efficiency in bandwidth-congested areas. However, the design of cost-effective receivers for MIMO channels remains a challenging task. The maximum likelihood detector can achieve excellent performance—usually, the best performance—but its computational complexity is a limiting factor in practical implementation. In the present work, a novel MIMO scheme using a practically feasible decoding algorithm based on the phase transmittance radial basis function (PTRBF) neural network is proposed. For some practical scenarios, the proposed scheme achieves improved receiver performance with lower computational complexity relative to the maximum likelihood decoding, thus substantially increasing the applicability of the algorithm. Simulation results are presented for MIMO-OFDM under 5G wireless Rayleigh channels so that a fair performance comparison with other reference techniques can be established.

Keywords: artificial neural networks; phase transmittance radial basis function; massive MIMO; MIMO decoding; 5G.

This Chapter is a replica of the following manuscript: Jonathan Aguiar Soares, Kayol Soares Mayer, Fernando César Comparsi de Castro, and Dalton Soares Arantes, "Complex-Valued Phase Transmittance RBF Neural Networks for Massive MIMO-OFDM Receivers" in Sensors 2021, 21, 8200, doi: 10.3390/s21248200.

2.1 INTRODUCTION

In recent years, with the increasing demand for the real-time processing of big data, the Internet of Things (IoT), and 4K video streaming, technologies to increase area throughput (ASIF et al., 2020) in base station (BS) coverage and hotspot tiers (SHANG et al., 2020) have become increasingly important. In general, the system throughput can be improved by three independent factors: the number of BSs, bandwidth, and spectral efficiency. While the number of base stations is a complicated variable to handle, there are substantial bandwidths in the millimeter wavelength (mmWave) bands that could be employed for BS hotspot tiers. On the other hand, as objects and human bodies easily block mmWaves, increasing the spectral efficiency (SE) of BS coverage tiers arises as a potential solution for wide-area coverage. In order to increase SE, advanced techniques are necessary to use the available BSs and bandwidth more efficiently. In view of this, both BSs and user equipment (UE) currently operate with multiple antennas and orthogonal frequency-division multiplexing (OFDM) (TEMIZ; ALSUSA; BAIDAS, 2020; MIRFARSHBAFAN et al., 2020; GHZAOUI et al., 2020) to increase spectral efficiency.

Multicarrier modulation schemes, such as OFDM, have been widely employed in digital communications systems due to their low susceptibility to intersymbol interference (ISI) (YOON et al., 2021; MAREY; MOSTAFA, 2021; HWANG et al., 2021; CONDOLUCI et al., 2021). OFDM divides the channel bandwidth into K orthogonal subcarriers (HASSAN, 2021). The serial stream at a high data rate applied to the OFDM input is first converted to multiple parallel low transmission rate sub-streams. Each of the K parallel sub-streams modulates one of the K subcarriers. In this way, the OFDM symbol duration is K times longer than the symbol duration of the equivalent single carrier system, thus avoiding ISI (SOARES, 2021). Another important characteristic of OFDM systems is that multiple users can be multiplexed in frequency, using K subcarriers.

Multiple-input and multiple-output (MIMO) technologies use multiple antennas on the transmitter and receiver sides, increasing the wireless channel capacity without extra bandwidth, extra power transmission, or both (SOARES, 2021). Usually, as BSs have more computational power than UEs, a larger number of antennas is applied at the transmitter. In this context, when the number of antennas exceeds the number of users, the term massive MIMO (mMIMO) is frequently used. Generally, mMIMO systems operate with 16 or more antennas in BSs. In addition, the uplink can be composed of one or more UEs, where the former characterizes a single-user mMIMO (SU-mMIMO) (KO et al., 2021) and the latter a multi-user mMIMO (MU-mMIMO) (DILLI, 2021). For 6G technologies, ultra-massive MIMO (UM-MIMO) schemes have been explored to support data throughputs of Terabits (JAMALI et al., 2021). MIMO and mMIMO communications are broadly implemented either by beamforming, space-time block coding (STBC), or both (HE; SU; HUANG, 2021; LI et al., 2021). While beamforming techniques (either analog, digital, or hybrid (HAN et al., 2021)) may be more attractive to BSs, because of the necessity of many transmitting antennas, STBC, on the other hand, is feasible for use in both downlink and uplink connections.

The combination of OFDM and MIMO is a major trend in mobile communication systems (SOKAL et al., 2021; ELNAKEEB; MITRA, 2021; MAJUMDER et al., 2021; YERRAPRAGADA; KELLEY, 2020; GUERREIRO; DINIS; CAMPOS, 2020), such as 5G and next-generations, which are based on the so-called MIMO-OFDM and mMIMO-OFDM approaches (SAAD; BENNIS; CHEN, 2020). Nonetheless, digital communication systems over wireless channels may suffer severe signal degradations due to multipath propagation, additive white Gaussian noise (AWGN) (MAYER et al., 2020a, 2019a), and Doppler effects (OSMAN et al., 2021). Moreover, another frequent impairment in OFDM systems is signal distortion, characterized by the PAPR (peak-to-average power ratio), due to nonlinearities at the high-power transmitter amplifier (MAYER et al., 2019c; ZOU et al., 2021). Since nonlinear impairments usually degrade the performance of linear filters, the search for robust nonlinear filters at the receiver is essential to circumvent this issue (SOARES, 2021; MAYER et al., 2019c; MAYER et al., 2019b).

Along with the application of nonlinear filters designed for specific problems in telecommunications, artificial neural networks (ANNs) have been extensively studied in various challenging areas of digital communications, including soft and hard fault detection, channel estimation, equalization, and beamforming (DE SOUSA; FERNANDES, 2018; DE SOUSA; ARANTES; FERNANDES, 2018; DE SOUSA; FERNANDES, 2019; DONG; HUANG, 2021; ENRICONI et al., 2020; MAYER; SOARES; ARANTES, 2020; MAYER et al., 2020b; MAYER et al., 2021; SHIMIZU et al., 2020; SWAIN; KHILAR; DASH, 2020; PINTO et al., 2021). Neural networks can operate like nonlinear filters, in a structure that can be modeled by nonlinear activation functions, as in multilayer perceptrons (MLPs), or by Gaussian neurons in radial basis function neural networks (RBFNN) (MAYER; SOARES; ARANTES, 2020). RBFNN Gaussian neurons have two free parameters, namely the Gaussian centers and the variances. Moreover, there is a linear free parameter vector of weights, which linearly weighs the neuron outputs to yield the network output (LOSS et al., 2007a; MAYER; SOARES; ARANTES, 2020). With these three independent sets of parameters, RBFNNs are able to represent high-order nonlinear surfaces without increasing the number of layers, thereby reducing complexity compared with deep neural networks (SOARES, 2021; MAYER; SOARES; ARANTES, 2020).

In this context, this work proposes a novel complex-valued RBF neural network architecture: a multiple-input multiple-output phase transmittance RBF (MIMO-PTRBF) neural network for channel estimation and symbol detection in massive MIMO-OFDM communication systems. The PTRBF neural network model was chosen due to its lower computational complexity when compared with deep neural networks and due to its crucial role in avoiding the phase invariance which occurs in a standard complex-valued RBFNN (SOARES, 2021; MAYER; SOARES; ARANTES, 2020; LOSS et al., 2007a). The proposed MIMO-PTRBF is an extension to multiple outputs of the single-output PTRBF neural network presented in (LOSS et al., 2007a). This work is based on (MAYER; SOARES; ARANTES, 2020), in which the authors redesigned the PTRBF neural network of (LOSS et al., 2007a) to obtain a low-complexity MIMO beamforming transmitter with the complex-MIMO RBF (CMM-RBF). In the present paper, using the Gaussian neuron output bounds presented in (MAYER; SOARES; ARANTES, 2020), we prove convergence in the mean of the PTRBF neural network, relaxing the condition of the trans-dimensional transformation of the complex-valued Gaussian neuron layer. Preliminary results indicate that the proposed architecture competes quite favorably with the conventional MIMO quasi-orthogonal space–time block coding (QOSTBC) with maximum likelihood (ML) decoding based on linear processing (SOARES, 2021). In addition, an STBC coding algorithm with full-rate and half-diversity was developed for massive MIMO coding with square matrices. However, because of its high computational complexity, the ML decoding may be unfeasible for mMIMO with a large number of antennas, as opposed to the MIMO-PTRBF neural network proposed here. Although other decoding techniques with lower computational complexities could be taken into account, for performance comparison, we chose ML decoding because of its optimal performance in linear channels. For example, the sphere decoding has lower computational complexity compared to the ML decoding, but its performance is only lower-bounded by the ML decoding (DURGA; MCLAUCHLIN, 2021). Furthermore, the MIMO-PTRBF is able to both estimate the channel and decode the received signal, relying on a training sequence. Simulation results show that the proposed architecture achieves significantly improved BER figures when compared with MIMO QOSTBC in an equal scenario, either with linear or with nonlinear impairments under 5G channels.

This paper is an extension of J. A. Soares' MSc. dissertation developed at the School of Electrical and Computer Engineering, University of Campinas, in the area of Telecommunications and Telematics (SOARES, 2021). In addition to the complex-valued RBF-based MIMO system proposed in the dissertation (SOARES, 2021), in this paper, the MIMO-PTRBF receiver is further elaborated with additional results and with the use of 5G channel models.

The remainder of this work is organized as follows. In Section 2.2, a brief review of multi-antenna systems is presented. The proposed STBC coding scheme and the MIMO-PTRBF for channel estimation and symbol detection in massive MIMO-OFDM systems are presented in Section 2.3. In Section 2.4, simulation results of the MIMO-PTRBF are compared with the results obtained with the OSTBC under maximum likelihood decoding in 5G channel models. Computational complexities are presented in Section 2.5

and conclusions are discussed in Section 2.6.

2.2 BACKGROUND

The main goal in multi-antenna systems is to increase the channel capacity with M_T transmit and M_R receive antennas by a factor of $\min(M_T, M_R)$ without using additional transmit power or spectral bandwidth (YAO; CHEN; HU, 2021). Considering the MIMO digital communication system $\mathbf{r}(k) = \mathbf{H}^T\mathbf{x}(k) + \boldsymbol{\eta}(k)$, with transmitted signal $\mathbf{x}(k) \in \mathbb{C}^{M_T}$, received signal $\mathbf{r}(k) \in \mathbb{C}^{M_R}$, and additive white Gaussian noise (AWGN) vector $\boldsymbol{\eta}(k) \in \mathbb{C}^{M_R}$, the channel capacity of $\mathbf{H} \in \mathbb{C}^{M_T \times M_R}$ is expressed as (JANKIRAMAN, 2004)

$$C = \log_2 \left[\det\left(\mathbf{I}_{M_R} + \frac{E_s}{M_T E_0}\mathbf{H}^H\mathbf{R}_{xx}\mathbf{H}\right)\right], \tag{2.1}$$

in which $\mathbf{I}_{M_R}$ is an $M_R \times M_R$ identity matrix, $[\cdot]^T$ is the transpose operator, $[\cdot]^H$ is the conjugate transpose operator, E_s is the total transmitted signal power, E_0 is the AWGN power, $\mathbf{R}_{xx} = \mathrm{E}\{\mathbf{x}(k)\mathbf{x}^H(k)\}$ is the correlation matrix of $\mathbf{x}(k)$, and $\mathrm{E}\{\cdot\}$ is the expectation operator.

However, if no channel state information (CSI) is available at the transmitter, we can assume that the channel components are equally probable. In this case, we consider that power is equally divided among the transmitting antennas, which implies $\mathbf{R}_{xx} = \mathbf{I}_{M_T}$. The capacity in such a case is then given by (SOARES, 2021; ZHAO et al., 2019)

$$C = \log_2 \left[\det\left(\mathbf{I}_{M_R} + \frac{E_S}{M_T N_0}\mathbf{H}^H\mathbf{H}\right)\right]. \tag{2.2}$$

Note that Equation (2.2) can be outperformed if the channel information is available at the transmitter (leading to a coding gain). However, Equation (2.2) is the maximum diversity capacity without channel knowledge at the transmitter. Furthermore, if $M_T = M_R = 1$, Equation (2.2) represents the Shannon capacity for single-input single-output (SISO) systems (SOARES, 2021).

In order to increase capacity, the concepts of diversity (ZHANG et al., 2021a), coding (CHOPRA; GUPTA, 2021), and array (TOKA; KUCUR, 2021) gains play key roles in MIMO systems. The array gain is the average increase in the signal-to-noise ratio (SNR) at the receiver that arises from the coherent combining effect of multiple antennas at the transmitter, receiver, or both. Multiple antenna systems require perfect channel knowledge at the transmitter, receiver, or both to achieve this array gain (TOKA; KUCUR, 2021). On the other hand, diversity gain is obtained by the provision of replicas of the transmitted signal at the receiver (ZHANG et al., 2021a). Diversity gain techniques are used to mitigate degradations in the error performance due to wireless fading channels (e.g., due to multipath). Since the probability that statistically independent fading channels simultaneously experience deep fading is insignificant, there are various ways of performing diversity gain and space diversity. To accomplish this, it is necessary to use sufficiently separated antennas in the array (by more than 10λ on base stations and 2λ to 5λ on mobile devices (JANKIRAMAN, 2004)) to guarantee independent wireless channels. In contrast, coding gain is usually provided by temporal channel coding, e.g., convolutional and block codes (SOARES, 2021).

Space–time code is a digital communication technique used to transmit multiple copies of a data stream via multiple antennas to compensate for fading and AWGN. At the receiver side, these multiple copies of the signal are received by one or more antennas, improving the communication reliability. Depending on the encoder algorithm at the transmitter, we can have different space–time codes. Space–time trellis codes (STTCs) combine modulation and trellis coding to transmit signals over a MIMO channel. Although STTCs provide both coding gain and diversity gain, the computational complexity is higher than other space–time codes, mainly in the receiver, where a Viterbi decoder is necessary (SHR; CHEN; HUANG, 2010). Space–time block codes (STBCs) combine multiple symbols from a digital modulation, creating a block of symbols. The components of this block (i.e., matrix of symbols) are indexed by the transmitting antenna and the transmitting time. At the transmitter, STBC decoding is performed in linear processing. Another technique is the space–time labeling diversity (STLD), a variation of STBC that takes two bit-streams and outputs two pairs of symbols. Two symbols in each pair are transmitted by two transmit antennas in two time slots, which results in full-diversity and half-rate (XU; PILLAY, 2021). In addition, STLD only works with a limited number of transmit antennas.

2.2.1 Space–Time Block Coding and OFDM

MIMO systems are mainly designed for narrowband or flat channels. Applying MIMO systems in the wideband frequency selective channel implies a constant penalty factor in the coding gain compared with that in flat-frequency channels. Furthermore, at high SNRs, an irreducible error rate floor is inevitable (GONG; LETAIEF, 2000). This irreducible error rate *floor* is due to the existence of multipath delay spread, and it persists even if we increase the number of antennas. Since the ISI is the root cause of the error *floor*, in principle, it can be mitigated by resorting to adaptive equalization, but this can be too complex to implement in such an environment. Another option that is widely used is to resort to OFDM, which naturally converts a frequency-selective fading channel into a frequency-nonselective fading channel. The subcarriers (i.e., tones) in an OFDM symbol are essentially narrowband signals. Since these tones fit perfectly as vehicles for space–time codes, OFDM is an enabler for this efficient coding technique (SOARES, 2021).

Figure 2.1 shows the coding scheme for a generic coding matrix $\mathbf{X}[k] \in \mathbb{C}^{M_T \times P}$, where P is the number of time samples for the transmission of one block of coded symbols and $k = 1,\ 2, \cdots,\ K$ is the carrier index of the kth MIMO-STBC encoded symbol matrix $\mathbf{X}[k]$ along the OFDM symbol. $\mathbf{R}[k] \in \mathbb{C}^{M_R \times P}$ is the matrix of received symbols, $\hat{\mathbf{s}} \in \mathbb{C}^{M_S}$ is the decoded vector, and M_S is the number of modulated symbols in a MIMO-STBC matrix.

The transmitting space–time block coder (STBC) encodes the data symbol vector $\mathbf{s}[k] \in \mathbb{C}^{M_S}$ using the code matrix to construct the transmitting matrix $\mathbf{X}[k]$ of length K. The streams $\mathbf{X}_{m_T,p}[k]$ are fed to the inverse fast Fourier transform (IFFT) modulator of each m_T transmitting antenna, at each p period of time relative to the OFDM symbol sequence. In this manner, the information is transmitted in $\mathbf{X}[k]$ blocks of M_T antennas and P OFDM symbols in each k-th carrier. To illustrate this scheme, Figure 2.2 shows an example for a two-transmitting antenna system using Alamouti coding. Consequently, the channel is given by $\mathbf{H} \in \mathbb{C}^{M_T \times M_R \times P \times K}$. It should be emphasized that in the simulation in Section 2.4 of this work, the channel is not assumed to be static over the entire MIMO-STBC block since it spreads over time in P-consecutive OFDM symbols. This is particularly necessary for the proposed work, as the receiver will fit and adapt to the characteristics and variations of the channel over time. This is also necessary for a massive number of broadcast antennas due to the length of the long block coding P that transmits over time in consecutive OFDM symbols (SOARES, 2021).

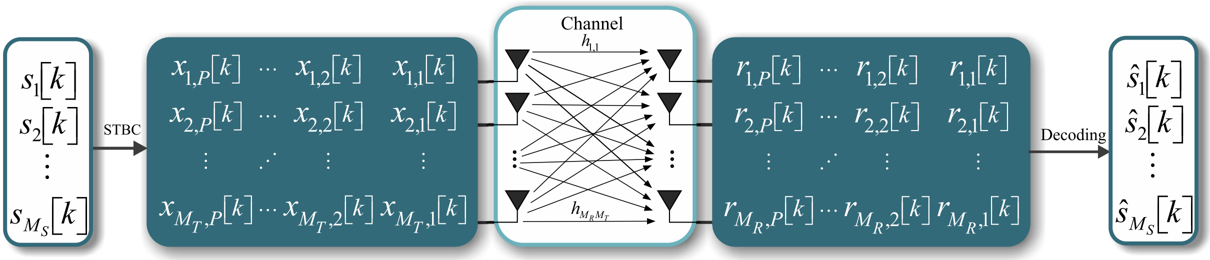

Figure 2.1 – Coding scheme for a MIMO-OFDM system in which k is the index of the kth MIMO-STBC-encoded symbol matrix $\mathbf{X}[k]$ along the OFDM symbol (SOARES, 2021).

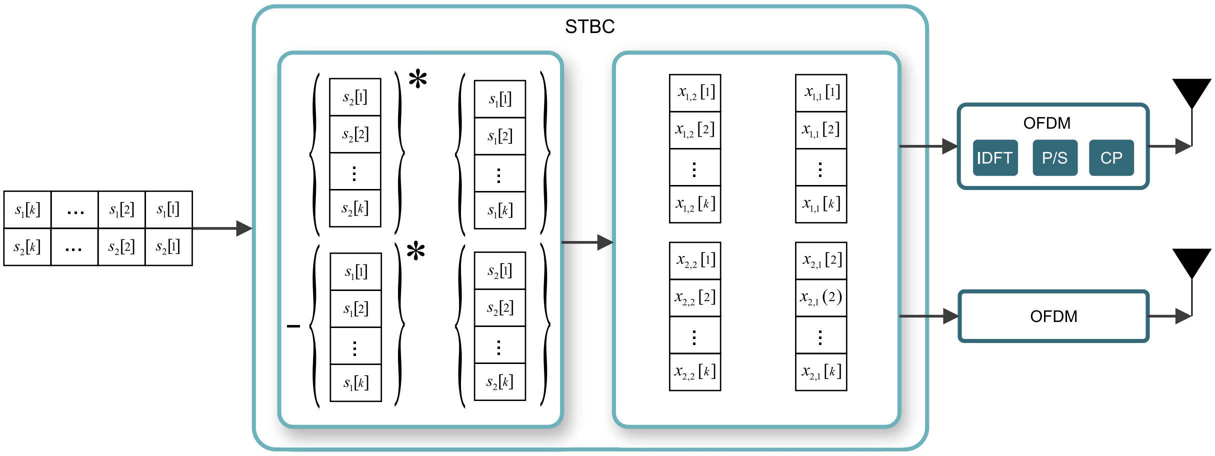

Figure 2.2 – Detailed MIMO-OFDM coding system. $\{\cdot\}^*$ denotes the conjugate operator.

As in OFDM systems, MIMO-OFDM also requires the channel state information to decode the received symbols. One of the most popular and widely used approaches to MIMO channel estimation is to employ pilot signals (also referred to as training sequences) and then estimate the channel based on the received data and the knowledge of the training sequence, as detailed in Figure 2.3. Based on pilot signals, in (LI, 2000; BIGUESH; GERSHMAN, 2006), the least-squares (LS) channel estimation technique is applied for orthogonal frequency-division multiplexing systems with multiple transmit antennas (SOARES, 2021).

A generalized coding scheme referred to as space–time block codes (STBCs) (JANKIRAMAN, 2004; TAROKH; JAFARKHANI; CALDERBANK, 1999; LI et al., 2021), based on the theory of orthogonal matrix designs, can achieve the full-transmit diversity of $M_T M_R$ employing the maximum likelihood decoding algorithm at the receiver (JANKIRAMAN, 2004). The idea is to transmit M_T orthogonal streams, which implies that the receiver antennas receive M_T orthogonal streams. This special class of space–time block codes is the so-called orthogonal STBC (OSTBC) (SOARES, 2021; TAROKH; JAFARKHANI; CALDERBANK, 1999; HU; ZHAO; XUE, 2020).

An OSTBC example of coding matrix for $M_T = 4$ (JANKIRAMAN, 2004) is given by

$$\mathbf{OSTBC_{4,8}} = \begin{bmatrix} s[1] & -s[2] & -s[3] & -s[4] & s[1]^* & -s[2]^* & -s[3]^* & -s[4]^* \\ s[2] & s[1] & s[4] & -s[3] & s[2]^* & s[1]^* & s[4]^* & -s[3]^* \\ s[3] & -s[4] & s[1] & s[2] & s[3]^* & -s[4]^* & s[1]^* & s[2]^* \\ s[4] & s[3] & -s[2] & s[1] & s[4]^* & s[3]^* & -s[2]^* & s[1]^* \end{bmatrix}, \tag{2.3}$$

in which $s[m_s]$ is the transmitted signal in the discrete symbol index m_s. Notice that, as proved by Tarokh et al. (TAROKH; JAFARKHANI; CALDERBANK, 1999), the inner product of any two distinct rows of this matrix is equal to zero (i.e., the matrix is orthogonal) and of full-rank, yielding full-diversity (SOARES, 2021).

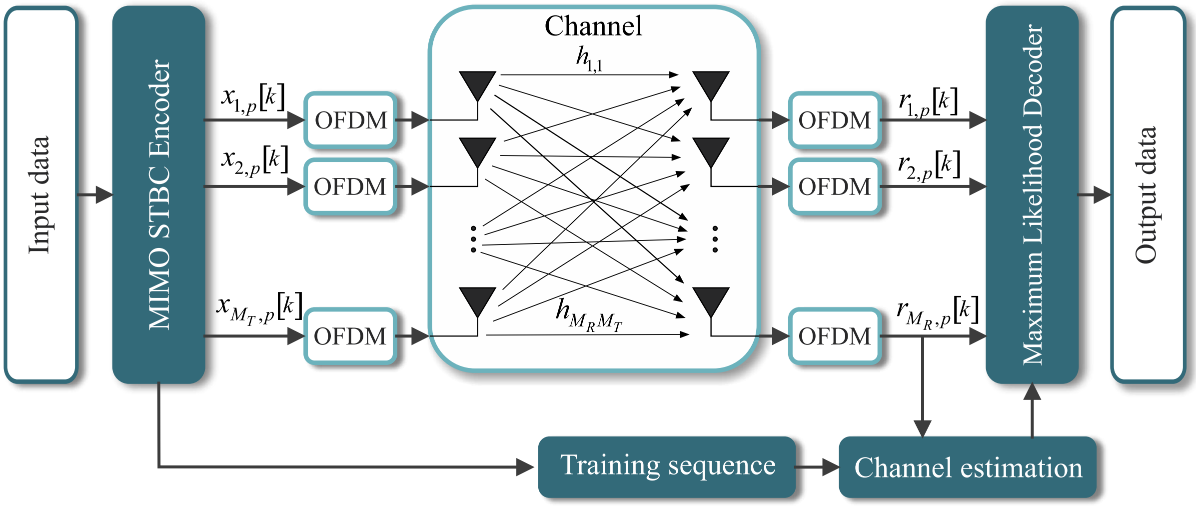

Figure 2.3 – MIMO-OFDM model system with channel estimation.

One of the disadvantages of OSTBC is the code rate. Let P represent the number of time samples to convey one block of coded symbols and M_s represent the number of symbols transmitted per block. The space–time block code rate is defined as the ratio between the number of symbols that the encoder receives at its input and the number of space–time coded symbols transmitted from each antenna, given by $R = M_s/P$. This implies that Equation (2.3) has a code rate $R = 1/2$, which consequently reduces the spectral efficiency. Supplementary to the diversity gain, the OSTBC leads to a secondary linear coding gain $G_c = 10 \log (R)$ at the receiver due to the coherent detection of multiple copies of the signal over time. Furthermore, the multi-antenna system, as presented in Figure 2.1, will lead to an array gain $G_a = 10 \log (M_R)$ due to the coherent combination of multiple received signals over the receiving antennas (SOARES, 2021).

2.2.2 Quasi-Orthogonal Special Case

In order to increase the spectral efficiency in orthogonal codes, Jafarkhani (JAFARKHANI, 2001) proposed quasi-orthogonal STBC (QOSTBC) of rate one, relaxing the requirement of orthogonality. However, when compared with orthogonal codes, the diversity gain is reduced by a factor of two. Besides, in contrast to orthogonally designed codes that process one symbol at a time at the decoder, quasi-orthogonal codes process pairs of transmitted symbols, which exponentially increases the computational complexity of decoding (SOARES, 2021).

Jafarkhani (JAFARKHANI, 2001) proposed a coding matrix of rate one for $M_T = 4$, given by

$$\mathbf{QOSTBC_{4,4}} = \begin{bmatrix} s[1] & s[2] & s[3] & s[4] \\ -s[2]^* & s[1]^* & -s[4]^* & s[3]^* \\ -s[3]^* & -s[4]^* & s[1]^* & s[2]^* \\ s[4] & -s[3] & -s[2] & s[1] \end{bmatrix}. \tag{2.4}$$

In the literature, related approaches with a maximum of $M_T = 6$ antennas were proposed for quasi-orthogonal codes (TIRKKONEN; BOARIU; HOTTINEN, 2000; WEIFENG SU; XIANG-GEN XIA, 2002; SINDHU; HAMEED, 2015). In (WEIFENG SU; XIANG-GEN XIA, 2002), the authors developed an architecture similar to (JAFARKHANI, 2001); however, this presents full-diversity at the cost of more processing and is limited to $M_T = 4$ antennas. In the same way, by increasing the decoding processing, Sindhu and Hameed (SINDHU; HAMEED, 2015) proposed two quasi-orthogonal schemes with $M_T = 5$ and 6 antennas (SOARES, 2021).

2.2.3 Decoding for Space–Time Block Codes

Maximum likelihood (ML) detection calculates the Euclidean distance among the received signal matrix $\mathbf{R}$ and the product of all possible transmitted signal vectors by the channel matrix $\mathbf{H}$. Considering $\mathbb{A}$, the set of constellation symbols of the transmitted signal, and M_S, the number of transmitted symbols per MIMO block, ML detection determines the estimation of the conveyed signal vector $\mathbf{s}$ as (SOARES, 2021)

$$\widehat{\mathbf{s}} = \underset{\mathbf{s} \in \mathbb{A}^{M_S}}{\operatorname{argmin}} \left\| \mathbf{R} - \mathbf{H}^T \mathbf{X} \right\|^2. \tag{2.5}$$

As in maximum a posteriori (MAP) detection, ML detection achieves the optimal performance when all transmitted vectors are equally probable. However, the number of ML computation metrics is A^{M_S}, where A is the modulation order. Thus, the ML complexity increases exponentially with the modulation order or the number of transmit symbols, or both (CHO et al., 2010; JANKIRAMAN, 2004; TAROKH; JAFARKHANI; CALDERBANK, 1999). Although this method has a high computational complexity, the ML decoding is used as a benchmark due to its optimal performance (SOARES, 2021).

For orthogonal coding schemes, the ML metric can be simplified, decoding symbol by symbol (TAROKH; JAFARKHANI; CALDERBANK, 1999). Via this simplification, it is possible to circumvent the issue of exponential computational complexity. However, even with this simplification, the computational complexity can be considerably high. In QOSTBC, the ML metric can be also simplified, but the computational complexity remains higher than the orthogonal case, because QOSTBC is decoded in pairs of symbols (SOARES, 2021).

2.3 PROPOSED APPROACH

2.3.1 Coding Scheme

Similarly to the work of (JAFARKHANI, 2001), the present work is derived from the full-rate full-diversity complex-valued space–time block code scheme proposed by Alamouti (ALAMOUTI, 1998). The transmission matrix proposed in (ALAMOUTI, 1998) is given by (SOARES, 2021)

$$\mathbf{A}_{i,j} = \begin{bmatrix} s[i] & s[j] \\ -s[j]^* & s[i]^* \end{bmatrix}, \tag{2.6}$$

in which $s[i]$ is the ith input symbol to be encoded.

Based on (ALAMOUTI, 1998), Jafarkhani (JAFARKHANI, 2001) proposed a quasi-orthogonal coding scheme using four antennas and consequently four encoded symbols as (SOARES, 2021)

$$\boldsymbol{S}_4^4 = \begin{bmatrix} \mathbf{A}_{1,2} & \mathbf{A}_{3,4} \\ -\left[\mathbf{A}_{3,4}\right]^* & \left[\mathbf{A}_{1,2}\right]^* \end{bmatrix} = \begin{bmatrix} s[1] & s[2] & s[3] & s[4] \\ -s[2]^* & s[1]^* & -s[4]^* & s[3]^* \\ -s[3]^* & -s[4]^* & s[1]^* & s[2]^* \\ s[4] & -s[3] & -s[2] & s[1] \end{bmatrix}, \tag{2.7}$$

where $\boldsymbol{S}$ is the quasi-orthogonal coding matrix. The main idea behind the work of (JAFARKHANI, 2001) is to build a 4×4 matrix from two 2×2 matrices, keeping a fixed transmission rate (SOARES, 2021).

In the present paper, we generalize the idea presented in (JAFARKHANI, 2001) to a new recursive method of generating coding schemes, as given by (SOARES, 2021)

$$\mathbf{S}_{M_s}^{M_T} = \begin{bmatrix} \mathbf{S}_{M_s-M_T/2}^{M_T/2} & \mathbf{S}_{M_s}^{M_T/2} \\ -[\mathbf{S}_{M_s}^{M_T/2}]^* & [\mathbf{S}_{M_s-M_T/2}^{M_T/2}]^* \end{bmatrix}, \tag{2.8}$$

in which $M_T = 2^n$, $\forall\, n \geq 1$ is the number of transmitting antennas and M_s is the number of encoded symbols. In the proposed scheme, $M_s \triangleq M_T$ and the code rate is $R = M_T/M_s = 1$ (SOARES, 2021). The recurrence is performed until we find $\mathbf{S}_n^1 = s[n]$, $\forall n \in [1, 2, \cdots, M_S]$ in Equation (2.8).

For example, with four transmitting antennas, Equation (2.8) results in (SOARES, 2021)

$$\mathbf{S}_4^4 = \begin{bmatrix} \mathbf{S}_{4-4/2}^{4/2} & \mathbf{S}_4^{4/2} \\ -[\mathbf{S}_4^{4/2}]^* & [\mathbf{S}_{4-4/2}^{4/2}]^* \end{bmatrix} = \begin{bmatrix} \mathbf{S}_2^2 & \mathbf{S}_4^2 \\ -[\mathbf{S}_4^2]^* & [\mathbf{S}_2^2]^* \end{bmatrix}. \tag{2.9}$$

From the recurrent structure of Equation (2.8), $\mathbf{S}_2^2$ and $\mathbf{S}_2^4$ are

$$\mathbf{S}_2^2 = \begin{bmatrix} \mathbf{S}_1^1 & \mathbf{S}_2^1 \\ -[\mathbf{S}_2^1]^* & [\mathbf{S}_1^1]^* \end{bmatrix}, \tag{2.10}$$

and

$$\mathbf{S}_4^2 = \begin{bmatrix} \mathbf{S}_3^1 & \mathbf{S}_4^1 \\ -[\mathbf{S}_4^1]^* & [\mathbf{S}_3^1]^* \end{bmatrix}. \tag{2.11}$$

Thus, substituting Equations (2.10) and (2.11) into Equation (2.9),

$$\mathbf{S}_4^4 = \begin{bmatrix} \begin{bmatrix} \mathbf{S}_1^1 & \mathbf{S}_2^1 \\ -[\mathbf{S}_2^1]^* & [\mathbf{S}_1^1]^* \end{bmatrix} & \begin{bmatrix} \mathbf{S}_3^1 & \mathbf{S}_4^1 \\ -[\mathbf{S}_4^1]^* & [\mathbf{S}_3^1]^* \end{bmatrix} \\ - \begin{bmatrix} \mathbf{S}_3^1 & \mathbf{S}_4^1 \\ -[\mathbf{S}_4^1]^* & [\mathbf{S}_3^1]^* \end{bmatrix}^* & \begin{bmatrix} \mathbf{S}_1^1 & \mathbf{S}_2^1 \\ -[\mathbf{S}_2^1]^* & [\mathbf{S}_1^1]^* \end{bmatrix}^* \end{bmatrix} = \begin{bmatrix} \mathbf{S}_1^1 & \mathbf{S}_2^1 & \mathbf{S}_3^1 & \mathbf{S}_4^1 \\ -\mathbf{S}_2^{1*} & \mathbf{S}_1^{1*} & -\mathbf{S}_4^{1*} & \mathbf{S}_3^{1*} \\ -\mathbf{S}_3^{1*} & -\mathbf{S}_4^{1*} & \mathbf{S}_1^{1*} & \mathbf{S}_2^{1*} \\ \mathbf{S}_4^1 & -\mathbf{S}_3^1 & -\mathbf{S}_2^1 & \mathbf{S}_1^1 \end{bmatrix}. \tag{2.12}$$

Replacing $\mathbf{S}_n^1 = s[n]$, $\forall n \in [1, 2, 3, 4]$, into Equation (2.12),

$$\mathbf{S}_4^4 = \begin{bmatrix} s[1] & s[2] & s[3] & s[4] \\ -s[2]^* & s[1]^* & -s[4]^* & s[3]^* \\ -s[3]^* & -s[4]^* & s[1]^* & s[2]^* \\ s[4] & -s[3] & -s[2] & s[1] \end{bmatrix}. \tag{2.13}$$

Note that Equation (2.13) is equal to the coding scheme proposed by (JAFARKHANI, 2001) with four antennas, as in Equation (2.4). However, in contrast to the work of (JAFARKHANI, 2001), our coding scheme, presented in Equation (2.8), can generate coding matrices for any $M_T = 2^n$, $\forall\, n \geq 1$, and $M_s \triangleq M_T$ (SOARES, 2021). For the case of $n = 1$, Equation (2.8) is equal to Equation (2.6), the full-rate full-diversity complex-valued space–time block code scheme proposed in (ALAMOUTI, 1998).

The main issue of the proposed coding scheme is that we cannot define a simplified ML decoding method as in the former cases. Then, it is here that the system proposed in this paper takes shape, with the MM-PTRBF decoding, making the joint solution feasible. We have observed, by extensive simulations, that Equation (2.8) achieves half of the diversity presented by the orthogonal coding schemes but keeps full-rate (i.e., $R = 1$), which is essentially the characteristics of the quasi-orthogonal scheme proposed by (SOARES, 2021; JAFARKHANI, 2001).

2.3.2 Complex MIMO-PTRBF Neural Network for Massive MIMO Decoding

In the proposed system, the maximum likelihood decoder is replaced by a neural network, the MIMO-PTRBF, to decode the received symbols, as shown in Figure 2.4. The

MIMO-PTRBF has a supervised learning stage, in which a training sequence is used to fit the hyper-parameters of the neural network. A pseudo-random generator creates this training sequence, which is known both at the transmitter and receiver sides. When the neural network output achieves the desired mean square error (MSE), it switches from the learning stage to the decoding stage. At this time, the information data are then effectively transmitted over the system, and the BER is computed. These two stages are implemented as in Figure 2.4, with the input switch of the MIMO STBC Encoder block and the output switch of the Neural Network Decoder block. The switches have two states represented by (a) and (b), which shift between the training and decoding stages (SOARES, 2021).

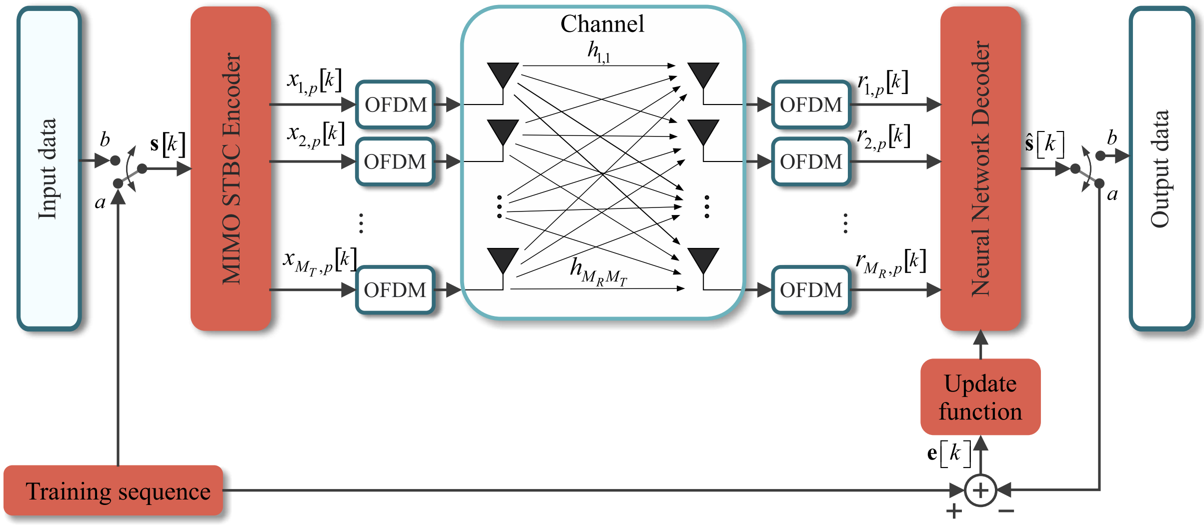

Figure 2.4 – Complete vision of the proposed MIMO-OFDM model (SOARES, 2021).

As in the maximum likelihood detector, the input signal to the MIMO-PTRBF algorithm is the set of received vectors $\mathbf{r}$, as shown in Figure 2.4. The MIMO-PTRBF architecture, with N neurons, has three free parameters: the matrix of synaptic weights $\mathbf{W} \in \mathbb{C}^{M_s \times N}$, the matrix of center vectors $\mathbf{\Gamma} \in \mathbb{C}^{M_R P \times N}$, and the vector of variances $\boldsymbol{\sigma^2} \in \mathbb{C}^{N \times 1}$. The MIMO-PTRBF is an extension of the PTRBF for multiple outputs. The key difference between both architectures is the multiple-output layer, which fits each output individually. Figure 2.5 shows a closer view of the receiver side using the MIMO-PTRBF neural network for decoding (SOARES, 2021).

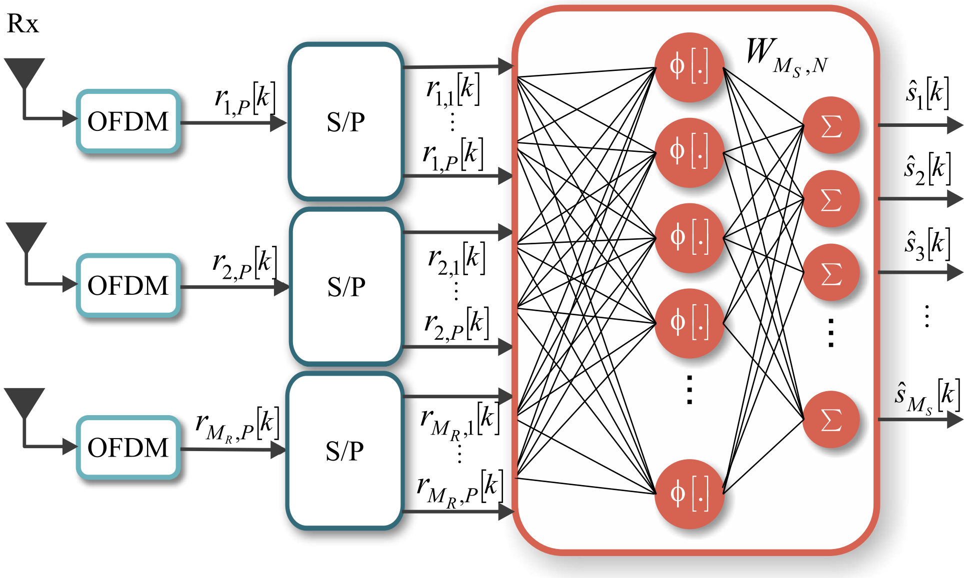

Figure 2.5 – Closer view of the system with neural network decoding (SOARES, 2021).

The output vector is thus given by

$$\hat{\mathbf{s}}[u] = \mathbf{W}[u]\boldsymbol{\phi}[u]. \tag{2.14}$$

Following the complex-valued radial basis function presented in (LOSS et al., 2007a), the nth neuron output of the MIMO-PTRBF (ϕ_n), for the pth output vector of $\mathbf{r}$, is (SOARES, 2021)

$$\phi_n = \exp\left(-\frac{||\text{Re}\{\mathbf{r}\} - \text{Re}\{\boldsymbol{\gamma}_n\}||_2^2}{\text{Re}\{\sigma_n^2\}}\right) + \jmath \exp\left(-\frac{||\text{Im}\{\mathbf{r}\} - \text{Im}\{\boldsymbol{\gamma}_n\}||_2^2}{\text{Im}\{\sigma_n^2\}}\right), \tag{2.15}$$

where $||\cdot||_2$ is the operator which returns the Euclidean norm of its argument, and $\text{Re}\{\cdot\}$ and $\text{Im}\{\cdot\}$ are the respective real and imaginary parts of their arguments. Additionally, as shown in Figure 2.6, the output of the neurons can be represented by the vector $\boldsymbol{\phi} = [\phi_1 \quad \phi_2 \quad \cdots \quad \phi_N]^T \in \mathbb{C}^{N\times 1}$. This kernel partitioning into real and imaginary components has an important role in avoiding any phase invariance at the output of the neurons (SOARES, 2021; MAYER; SOARES; ARANTES, 2020; LOSS et al., 2007a).

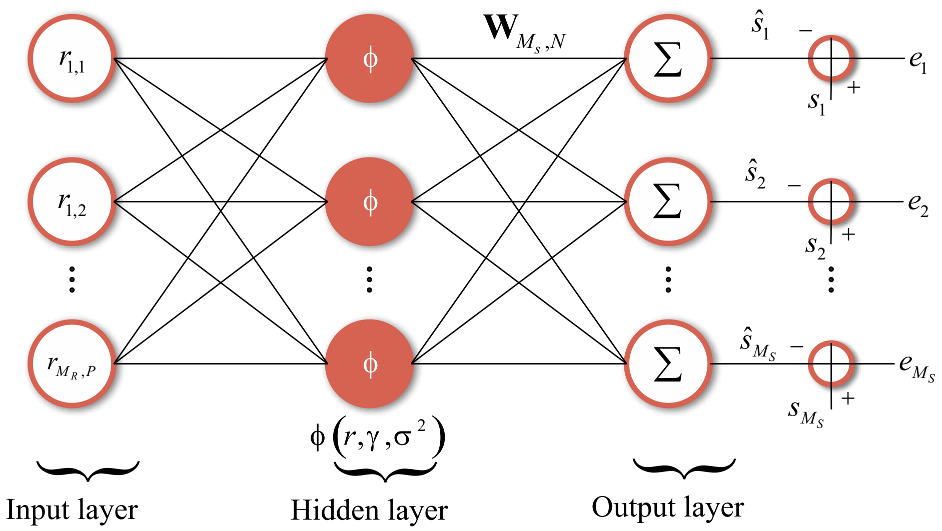

Figure 2.6 – MIMO phase transmittance radial basis function neural network architecture (SOARES, 2021).

Thus, by means of the steepest descent algorithm, the update of the MIMO-PTRBF free parameters is given by

$$\begin{aligned} w_{m_s,n}[u+1] &= w_{m_s,n}[u] - \eta_w \nabla^w J[u], \\ \boldsymbol{\gamma}_n[u+1] &= \boldsymbol{\gamma}_n[u] - \eta_\gamma \nabla^\gamma J[u], \\ \sigma_n^2[u+1] &= \sigma_n^2[u] - \eta_\sigma \nabla^\sigma J[u], \end{aligned} \tag{2.16}$$

in which η_w, η_γ, and η_σ are the adaptive steps of $w_{m_s,n}$, $\boldsymbol{\gamma}_n$, and σ_n^2, respectively. Furthermore, ∇^w, ∇^γ, and ∇^σ are the complex gradient operators of $w_{m_s,n}$, $\boldsymbol{\gamma}_n$, and σ_n^2, respectively.

Thus, with $\mathbf{r}$ and $\mathbf{s}$, the MIMO-PTRBF algorithm can be used to estimate the output vector $\hat{\mathbf{s}}$ at the uth training epoch by the minimization of the following cost function:

$$J[u] = \frac{1}{2}||\mathbf{s}[u] - \hat{\mathbf{s}}[u]||_2^2, \tag{2.17}$$

where $\mathbf{s}$ and $\hat{\mathbf{s}}$ are the training sequence and the output vector, respectively.

Applying the complex gradient operators (∇^w, ∇^γ, and ∇^σ) to (2.17) yields

$$\begin{aligned} \nabla^w J[u] &= -e_{m_s}[u]\phi_n^*[u], \\ \nabla^\gamma J_n[u] &= -\xi^*[u]\omega_n[u]\left(\mathrm{Re}\{\boldsymbol{\alpha}_n[u]\} - \mathrm{Im}\{\boldsymbol{\alpha}_n[u]\}\right) - \xi[u]\omega_n^*[u]\left(\mathrm{Re}\{\boldsymbol{\alpha}_n[u]\} + \mathrm{Im}\{\boldsymbol{\alpha}_n[u]\}\right), \\ \nabla^\sigma J_n[u] &= -\xi^*[u]\omega_n[u](\mathrm{Re}\{\beta_n[u]\} - \mathrm{Im}\{\beta_n[u]\}) - \xi[u]\omega_n^*[u](\mathrm{Re}\{\beta_n[u]\} + \mathrm{Im}\{\beta_n[u]\}), \end{aligned} \tag{2.18}$$

in which $e_{m_s}[u] = s_{m_s}[u] - \hat{s}_{m_s}[u]$ is the instantaneous error for the output $\hat{s}_{m_s}$ at the uth training epoch. Then, substituting Equation (2.18) in (2.16) yields

$$\begin{aligned} w_{m_s,n}[u+1] &= w_{m_s,n}[u] + \eta_w e_{m_s}[u]\phi_n^*[u], \\ \boldsymbol{\gamma}_n[u+1] &= \boldsymbol{\gamma}_n[u] + \eta_\gamma \left[\mathrm{Re}(\xi_n[u])\mathrm{Re}(\boldsymbol{\alpha}_n[u]) - \jmath\mathrm{Im}(\xi_n[u])\mathrm{Im}(\boldsymbol{\alpha}_n[u])\right], \\ \sigma_n[u+1] &= \sigma_n[u] + \eta_\sigma \left[\mathrm{Re}(\xi_n[u])[\mathrm{Re}(\beta_n[u]) - \jmath\mathrm{Im}(\xi_n[u])\mathrm{Im}(\beta_n[u])\right], \end{aligned} \tag{2.19}$$

in which $[\cdot]^*$ denotes the complex conjugate operator and $\xi_n[u]$ is the nth synaptic transmittance, given by

$$\xi_n[u] = \sum_{m_s=1}^{M_s} e_{m_s}^*[u] w_{m_s,n}[u]. \tag{2.20}$$

Furthermore, $\boldsymbol{\alpha}_n[u] \in \mathbb{C}^{\mathrm{R}}$ is the mth vector of the matrix of weighted centers ($\mathbf{A}[u] \in \mathbb{C}^{\mathrm{N}\times\mathrm{R}}$):

$$\boldsymbol{\alpha}_n[u] = \mathrm{Re}(\phi_n[u])\frac{[\mathrm{Re}(\mathbf{x}[u]) - \mathrm{Re}(\boldsymbol{\gamma}_n[u])]}{\mathrm{Re}(\sigma_n[u])} + \jmath\mathrm{Im}(\phi_n[u])\frac{[\mathrm{Im}(\mathbf{x}[u]) - \mathrm{Im}(\boldsymbol{\gamma}_n[u])]}{\mathrm{Im}(\sigma_n[u])}. \tag{2.21}$$

In a similar way, $\beta_n[u] \in \mathbb{C}$ is the nth element of the vector of weighted kernel ($\boldsymbol{\beta}[u] \in \mathbb{C}^{\mathrm{N}}$):

$$\beta_n[u] = \mathrm{Re}(\phi_n[u])\frac{\|\mathrm{Re}(\mathbf{x}[u]) - \mathrm{Re}(\boldsymbol{\gamma}_n[u])\|_2^2}{[\mathrm{Re}(\sigma_n[u])]^2} + \jmath\mathrm{Im}(\phi_n[u])\frac{\|\mathrm{Im}(\mathbf{x}[u]) - \mathrm{Im}(\boldsymbol{\gamma}_n[u])\|_2^2}{[\mathrm{Im}(\sigma_n[u])]^2}. \tag{2.22}$$

Generalizing Equation (2.19) to matrix structures results in

$$\begin{aligned} \mathbf{W}[u+1] &= \mathbf{W}[u] + \eta_w \mathbf{e}[u]\boldsymbol{\phi}^{\mathrm{H}}[u], \\ \boldsymbol{\Gamma}[u+1] &= \boldsymbol{\Gamma}[u] + \eta_\gamma \text{\AE}^*[u], \\ \boldsymbol{\sigma}[u+1] &= \boldsymbol{\sigma}[u] + \eta_\sigma \text{\ae}^*[u], \end{aligned} \tag{2.23}$$

where $\text{\AE}[u]$ and $\text{\ae}[u]$ are auxiliary variables used to reduce the computational complexity. $\text{\AE}[u]$ and $\text{\ae}[u]$ are given by

$$\begin{aligned} \text{\AE}[u] &= \mathrm{Re}(\boldsymbol{\Xi}[u])\mathrm{Re}(\mathbf{A}[u]) + \jmath\mathrm{Im}(\boldsymbol{\Xi}[u])\mathrm{Im}(\mathbf{A}[u]) \ \in \ \mathbb{C}^{\mathrm{N}\times\mathrm{R}}, \\ \text{\ae}[u] &= \mathrm{Re}(\boldsymbol{\Xi}[u])\mathrm{Re}(\boldsymbol{\beta}[u]) + \jmath\mathrm{Im}(\boldsymbol{\Xi}[u])\mathrm{Im}(\boldsymbol{\beta}[u]) \ \in \ \mathbb{C}^{\mathrm{N}}, \end{aligned} \tag{2.24}$$

in which $\boldsymbol{\Xi}[u]$ is the diagonal matrix of synaptic transmittance:

$$\boldsymbol{\Xi}[u] = \begin{bmatrix} \xi_1[u] & 0 & \cdots & 0 \\ 0 & \xi_2[u] & \cdots & 0 \\ \vdots & \vdots & \ddots & \vdots \\ 0 & 0 & \cdots & \xi_N[u] \end{bmatrix} \in \ \mathbb{C}^{\mathrm{N}\times\mathrm{N}}. \tag{2.25}$$

Each training update is given by Equation (2.23); however, for $u = 0$, the MIMO-PTRBF free parameters are initialized following some criterion defined by the user (e.g., based on the probability distribution of the input data). Although (2.23) minimizes the error between the output vector $\hat{\mathbf{s}}$ and the reference vector $\mathbf{s}$, as the neurons are dependent on exponential functions, a risk of instability is assumed if the exponential argument is positive. In order to circumvent this issue, based on Theorem A1 of (MAYER; SOARES; ARANTES, 2020), the real and imaginary parts of each scalar component of the vector of variances are lower-bounded by the limit $\mu > 0$, which, consequently, bounds the real and imaginary parts of the neurons output from 0 to 1 (SOARES, 2021). In addition, taking into account Theorem 2.2 (see Appendix 2.6), the adaptive step of the matrix of synaptic weights is limited by $\eta_w < 1/N$ for all simulations, to guarantee convergence in the mean. In addition, in the Appendix, Corollaries 2.1.1 and 2.1.2 are of utmost importance to prove Theorem A1. In addition, Definition 2..1 is used to prove Corollary 2.1.2.

2.4 SIMULATION RESULTS

Using the formerly mentioned OSTBC (TAROKH; JAFARKHANI; CALDERBANK, 1999) and QOSTBC (JAFARKHANI, 2001) coding schemes, several setups are compared with the proposed approach to validate and assess their performance in massive MIMO-OFDM. OSTBC and QOSTBC are simulated with the maximum likelihood (ML) decoding with perfect channel knowledge. This configuration achieves the maximum diversity gain $G_d = M_T M_R$ at the cost of half of the theoretical bandwidth efficiency, since $R = 1/2$ in this case. Considering a practical QOSTBC application, we also implement the EQOSTBC with the least-squares (ML-LS) channel estimation (SOARES, 2021). Figure 2.7 illustrates the simulated system.

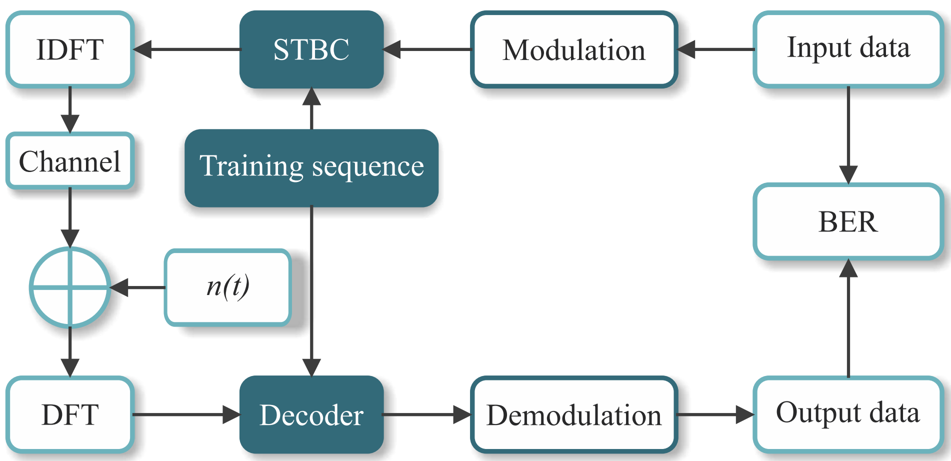

Figure 2.7 – Block model of the simulated systems.

In Figure 2.7, the binary input data are created by a pseudo-random generator with uniform distribution. The bit-stream is then modulated according to the M-QAM or M-PSK modulation scheme used in the simulation. Subsequently, using the coding scheme proposed in Section 2.3, the modulated symbols are encoded in the STBC block. In the IFFT block, the STBC symbols are frequency-multiplexed for OFDM transmission. At the receiver side, after the transmitted signal passes through the channel, the fast Fourier transform (FFT) is applied to demultiplex the STBC symbols. In the decoder, the proposed ANN-based technique presented in Section 2.3 and the ML algorithm (either with perfect channel knowledge at the receiver or with channel estimation by LS) are employed to assess the system performance. In the sequel, the decoder output symbols are demodulated, and BER is computed.

For the sake of comparison, the BER as a function of energy per bit to noise power spectral density ratio ($\mathrm{E_b/N_0}$) is used in the simulations. By adjusting the transmitting power for each antenna, the received signals are normalized by M_T transmitting antenna, by the receiver array gain M_R, and by the code rate gain R, implying

$$SNR_{(dB)} = E_b/N_{0(dB)} + 10\log_{10}\left(\frac{b}{RM_TM_R}\right), \tag{2.26}$$

in which b is the number of bits per QAM symbol.

In Figure 2.8, aiming to validate the simulator shown in Figure 2.7, we compare the obtained results with the theoretical performance of OSTBC for 4th, 8th, 16th, and 64th diversity orders using 4-QAM modulation for a Rayleigh channel with AWGN. For all OSTBC diversity orders, theoretical and simulated results were approximately the same, validating the framework. In addition, Figure 2.9 presents the reference results of (JAFARKHANI, 2001) with $M_T = 4$ antennas and $M_R = 1$ antenna for 16-QAM OSTBC and 4-QAM QOSTBC and the obtained results for the same scenarios. The simulated results are in line with theoretical results, which also corroborates the framework's reliability.

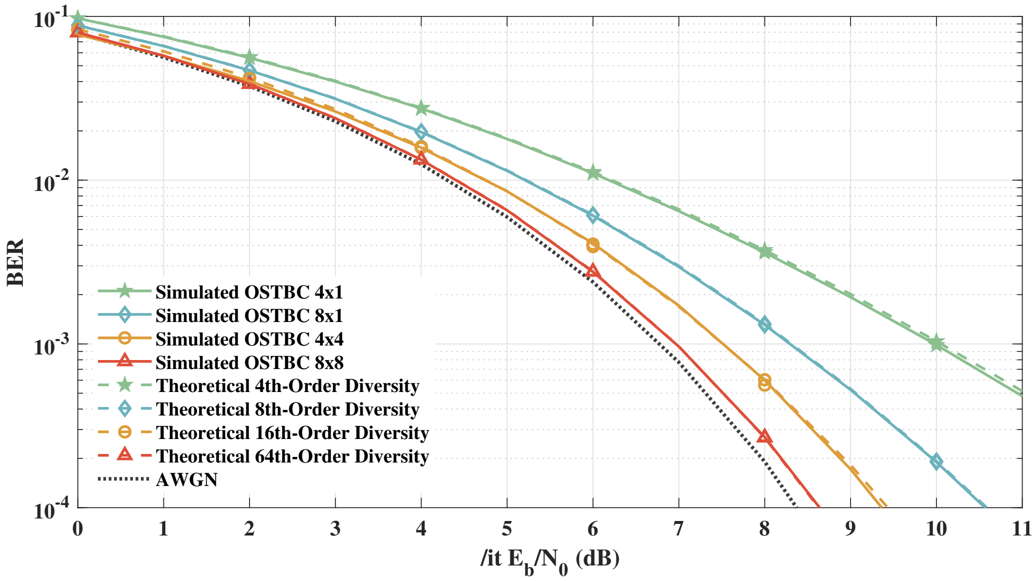

Figure 2.8 – Simulated and theoretical results for 4th, 8th, 16th, and 64th diversity orders.

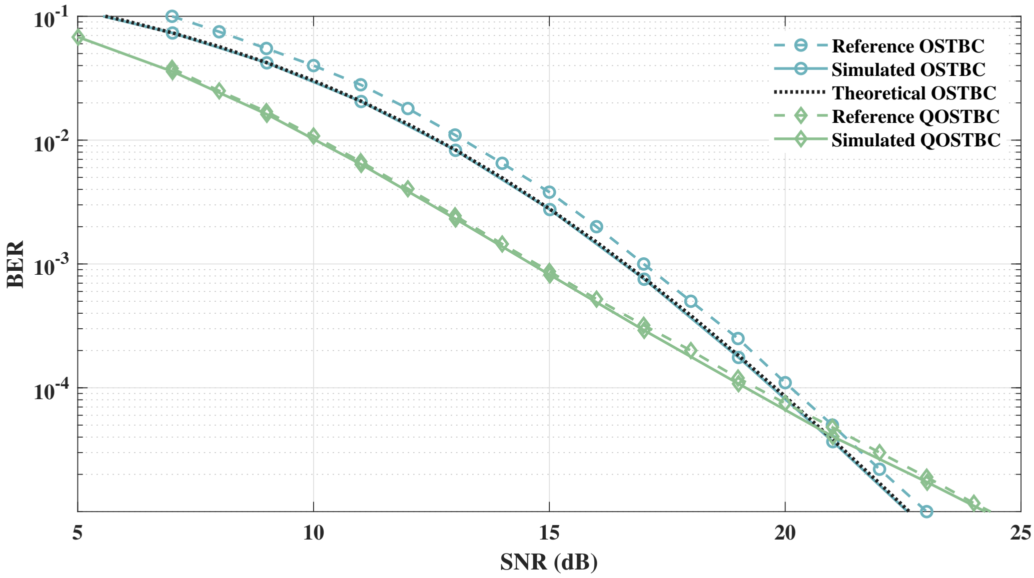

Figure 2.9 – Simulated, reference, and theoretical results for equal diversity order and bitrate (SOARES, 2021).

With the simulation framework validated, we can compare the proposed coding algorithm with results from the literature. Firstly, Figure 2.10 shows the results of the proposed coding algorithm and theoretical results for 2nd, 3rd, 4th, 5th, 8th, and 10th order diversity. As addressed by (JAFARKHANI, 2001), quasi-orthogonal transmitting schemes with four antennas achieve at least half of the theoretical diversity ($D_o = \frac{M_T}{2} = 2$) of the orthogonal four antenna scheme ($D_o = M_T = 4$). This can be seen in the solid blue curve with squares of Figure 2.10, which is located between the theoretical second and third-order curves. Using simulations, we extend the concept introduced by (JAFARKHANI, 2001) for QOSTBC with 8×1 and 16×1 antennas. In order to simulate these scenarios, we employ the proposed coding algorithm presented in Equation (2.8). As expected, the solid green curve with diamonds and the solid orange curve with circles are between the theoretical 4th and 5th order and the 8th and 10th order, respectively. Then, utilizing this analysis, we validate the proposed code algorithm and show that it is a suitable approach for generating QOSTBC matrices for at least 16 antennas. Higher-order QOSTBC architectures using Equation (2.8) are not simulated because of the extensive time required to perform maximum likelihood detection.

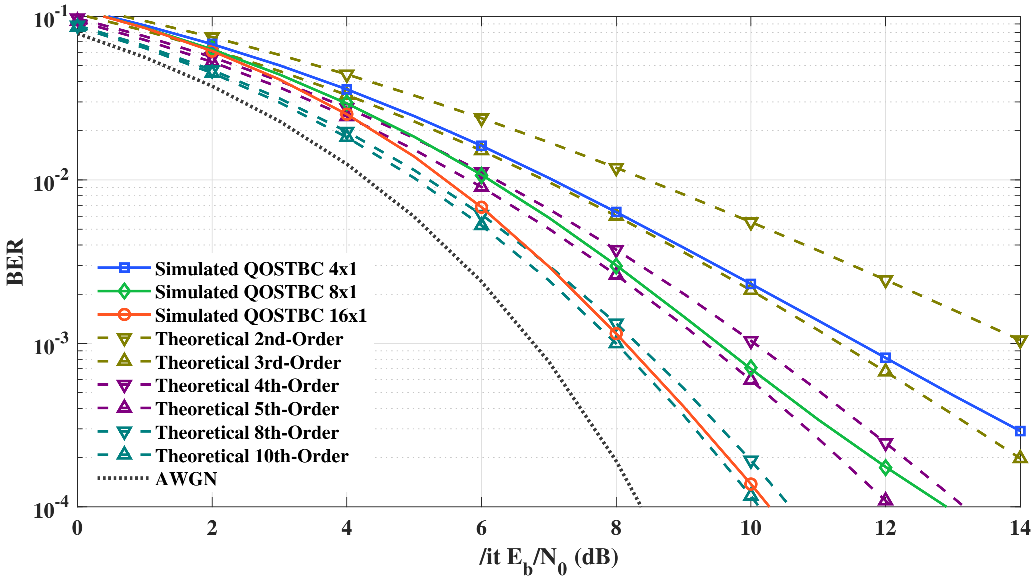

Figure 2.10 – Simulation for the proposed coding scheme against theoretical results for equal bitrate and $M_T = 4$ and 8 with $M_R = 1$ (SOARES, 2021).

In order to represent more practical scenarios, we set the simulation system with a 3GPP TS 38.211 specification (ETSI, 2022a) for 5G Physical channels and modulation. The Subcarrier Spacing (Δf) scales from 15 kHz to 240 kHz. The number of active carriers is 256, and the pilot sample rate (when applicable) is $M_T \times 8 \times f_{Doppler}$ with the conventional block-based pilot scheme (MEI et al., 2021). We perform simulations in the extremes to demonstrate the robustness of the proposed approach.

The radio channel realizations are created using the 3GPP TR 38.901 report on 5G: Study on channel model for frequencies from 0.5 GHz to 100 GHz (ETSI, 2022b). The 3GPP channel models (ETSI, 2022b) are applicable for frequency bands in the range of 0.5 GHz to 100 GHz. From Tapped Delay Line (TDL) models in (ETSI, 2022b), TDL-B is selected from Table 7.7.2-2 (depicted in Table 2.1) for the channel model simulated in this work.

Table 2.1 – Table 7.7.2-2. TDL-B.

Tap #	Normalized Delay	Power (dB)	Tap #	Normalized Delay	Power (dB)
1	0.0000	0.00	13	1.1021	−4.80
2	0.1072	−2.20	14	1.2756	−5.70
3	0.2155	−4.00	15	1.5474	−7.50
4	0.2095	−3.20	16	1.7842	−1.90
5	0.2870	−9.80	17	2.0169	−7.60
6	0.2986	−1.20	18	2.8294	−12.2
7	0.3752	−3.40	19	3.0219	−9.80
8	0.5055	−5.20	20	3.6187	−11.4
9	0.3681	−7.60	21	4.1067	−14.9
10	0.3697	−3.00	22	4.2790	−9.20
11	0.5700	−8.90	23	4.7834	−11.3
12	0.5283	−9.00			

In Table 2.1, as the channel model delays are normalized, they need to be scaled according to a desired delay spread in nanoseconds (ns):

$$\tau_{scaled} = \tau_{model} DS_{ns} \tag{2.27}$$

in which τ_{model} is the normalized delay value of the TDL model, τ_{scaled} is the new delay value (in [ns]), and DS_{ns} is the desired delay spread (in [ns]). From Table 7.7.3-1 (ETSI, 2022b), examples of scaling delay spreads are very short ($DS_{ns} = 10$ ns), short ($DS_{ns} = 30$ ns), nominal ($DS_{ns} = 100$ ns), long ($DS_{ns} = 300$ ns), and very long ($DS_{ns} = 1000$ ns). In this work, we use a delay spread of $DS_{ns} = 50$ ns.

From the channel model of Table 2.1, a Rayleigh distribution is used to compute each sub-channel of $\mathbf{H} \in \mathbb{C}^{M_T \times M_R}$ (MIMO channel matrix). The M-QAM BER figure for the AWGN channel is also used to define a lower bound on BER vs. E_b/N_0 performance. Additionally, it is assumed that all received signals are uncorrelated (SOARES, 2021).

A realistic scenario to assess the performance of a MIMO-OFDM system must also include the nonlinear effects of the transmitter power amplifiers (SOARES, 2021). This is necessary because the OFDM signal can have relatively high peak values (i.e., high PAPR) in the time domain since many subcarrier components are added via an IFFT operation. A high PAPR is one of the most detrimental aspects of the OFDM system, as it decreases the SQNR (signal-to-quantization noise ratio) of ADCs (analog-to-digital converters) and DACs (digital-to-analog converters), while also imposing a back-off that degrades the efficiency of the power amplifier in the transmitter. The PAPR issue is usually more critical in the uplink since the efficiency of the power amplifier is critical due to the limited battery power in a mobile terminal. For this purpose, from now on, the results assume mild amplifier nonlinearities, represented by a first-grade power amplifier or an appropriate back-off operating point (SOARES, 2021). Based on (LOSS et al., 2007a), the nonlinearity vector $\boldsymbol{\rho} = [\rho_1 \quad \rho_2 \quad \rho_3]^T = [0.9 \quad 0.1 \quad 0.05]^T$ implies 90%, 10%, and 5% first, second, and third-order coefficients, respectively.

With the model properly validated and the specified 5G channel model, we are now able to analyze the proposed complex-valued ANN-based decoder for MIMO-OFDM systems. First, we present the MSE convergence curves during the learning process. The MSE curves are averaged over 10 subsequent simulation traces, and a 4-QAM modulation with $E_b/N_0 = 12$ dB is employed. Figure 2.11a–d show the MSE evolution for $M_T = M_R = 4$, $M_T = M_R = 8$, $M_T = M_R = 16$, and $M_T = M_R = 32$ antennas, respectively. The red bottom and top curves in Figure 2.11 refer to the MSE standard deviations over the 10 subsequent simulation traces, and the green curves refer to the mean values. Although the steady-state MSEs decrease slightly as the number of antennas increases, one may notice that the decays of the standard deviations are more conspicuous as $M_T = M_R$ increases. This is due to the MIMO characteristics that mitigate the channel effects by sending several samples of the same signal to the receiver. Thus, sudden channel variations are smoothed, suggesting that the PTRBF learning process presents a robust and cohesive behavior.

The 4-QAM scatter plots presented in Figure 2.12 show the convergence of the proposed neural network decoder for the first 35 training epochs. For this sequence of scatter plots, each training epoch corresponds to one OFDM symbol; i.e., 256 4-QAM symbols. As shown in Figure 2.12, the proposed algorithm has a fast convergence rate since only 10 training epochs are sufficient to separate the 4-QAM constellation symbols efficiently (SOARES, 2021).

The 16-QAM scatter plots presented in Figure 2.13 show the convergence of the proposed neural network decoder for the first 140 training epochs, spaced in intervals of 20 OFDM symbols. In this case, the number of training epochs necessary for algorithm convergence is greater than for the 4-QAM case, given the intrinsic complexity of the higher-order constellation. Nevertheless, with only 20 training epochs, it is already possible to visually identify the 16-QAM constellation symbols and, with 80 training epochs, to see the correctly grouped symbols in the scatter plot (SOARES, 2021).

The 64-QAM scatter plots presented in Figure 2.14 show the convergence of the proposed neural network decoder for the first 7000 training epochs, spaced in intervals of 1000 OFDM symbols. In this case, the number of training epochs necessary for algorithm convergence is greater than for the former 16/4-QAM cases, in view of the intrinsic complexity of the much higher-order 64-QAM constellation. Nevertheless, with 3000 training epochs, it is already possible to visually identify the 64-QAM constellation symbols and, with 5000 training epochs, to see the correctly grouped symbols in the scatter plot (SOARES, 2021). Although an abrupt increase in training epochs occurs, when compared with 4-QAM in Figure 2.12, it represents a time interval of only 80 ms (5000 OFDM symbols with 240 kHz sub-carrier spacing).

After analyzing the MSE curves and constellations of the MMPTRBF, we can further investigate the BER vs. E_b/N_0 of the proposed approach. Figure 2.15 shows the BER vs. E_b/N_0 results of the QOSTBC, EQOSTBC, and MIMO-PTRBF systems operating with $M_T = M_R = 4$ antennas and 4-QAM modulation. The 4-QAM AWGN curve defines a lower bound for all MIMO systems that use 4-QAM modulation. The simulation results in Figure 2.15 indicate that the QOSTBC system outperforms the proposed work when perfect channel knowledge is available at the receiver, which is impractical. Although the EQOSTBC system is a feasible and practical version of the QOSTBC, due to the channel estimation block at the receiver, simulations using the least-squares channel estimation show that the EQOSTBC performance is degraded by more than 2.5 dB when compared with the QOSTBC (SOARES, 2021). Furthermore, even with a perfect channel estimator, it is computationally expensive to decode QOSTBC codes with maximum likelihood for more than four antennas, as addressed by (JAFARKHANI, 2001).

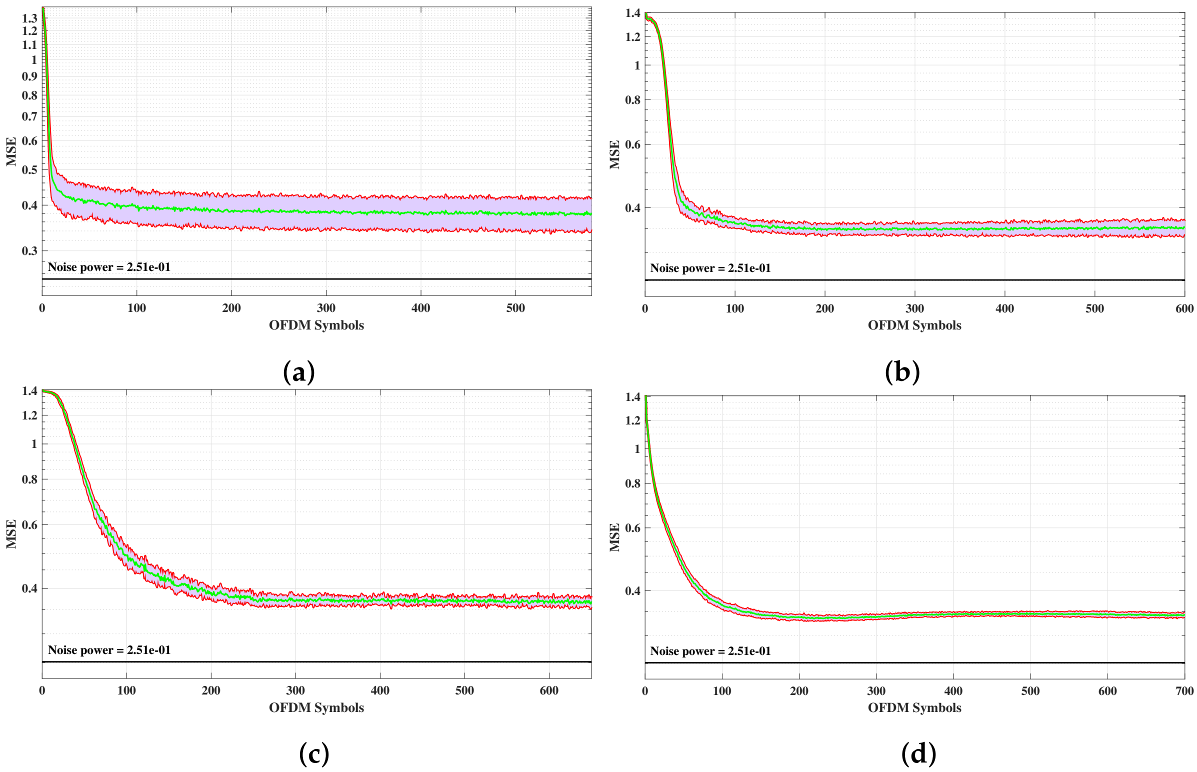

Figure 2.11 – Evolution of MSE values averaged over 10 realization sequences of the proposed MMPTRBF network decoder, using 4-QAM and $E_b/N_0 = 12$ dB for (**a**) $M_T = M_R = 4$ antennas, (**b**) $M_T = M_R = 8$ antennas, (**c**) $M_T = M_R = 16$ antennas, (**d**) $M_T = M_R = 32$ antennas.

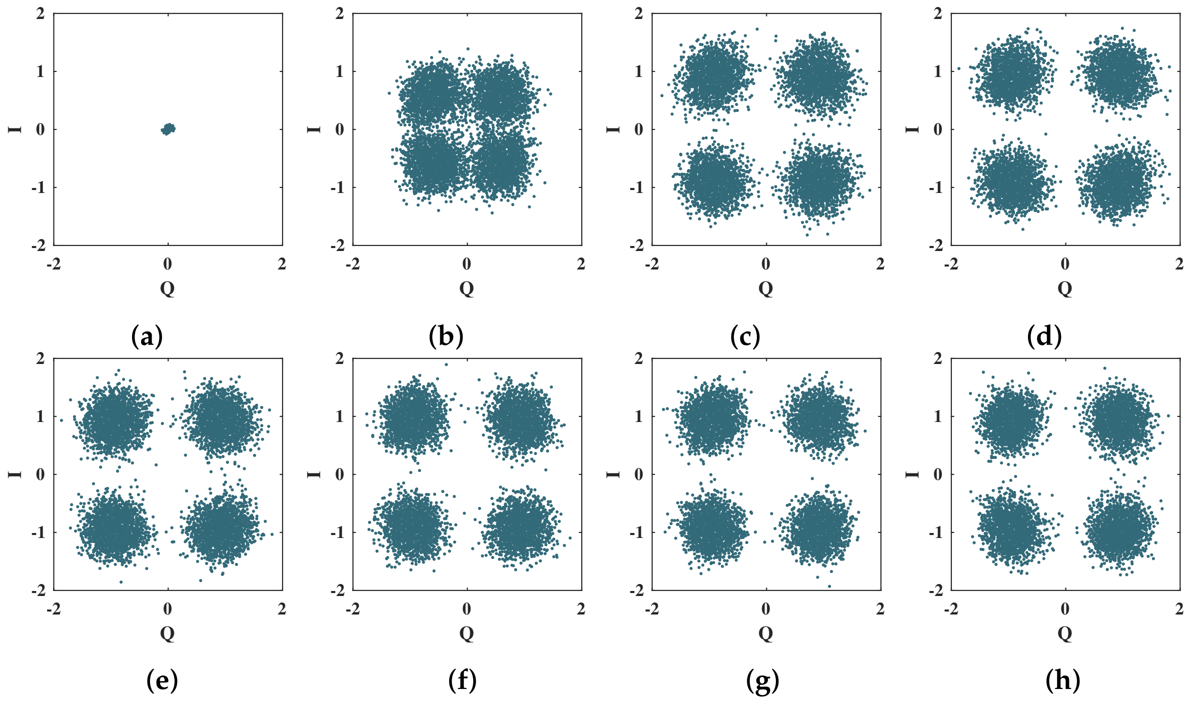

Figure 2.12 – Scatter plots for the 4-QAM symbols at the output of the MMPTRBF during the training period, for $M_T = M_R = 4$ antennas and $E_b/N_0 = 12$ dB. (**a**) 1 epoch, (**b**) 5 epochs, (**c**) 10 epochs, (**d**) 15 epochs, (**e**) 20 epochs, (**f**) 25 epochs, (**g**) 30 epochs, and (**h**) 35 epochs.

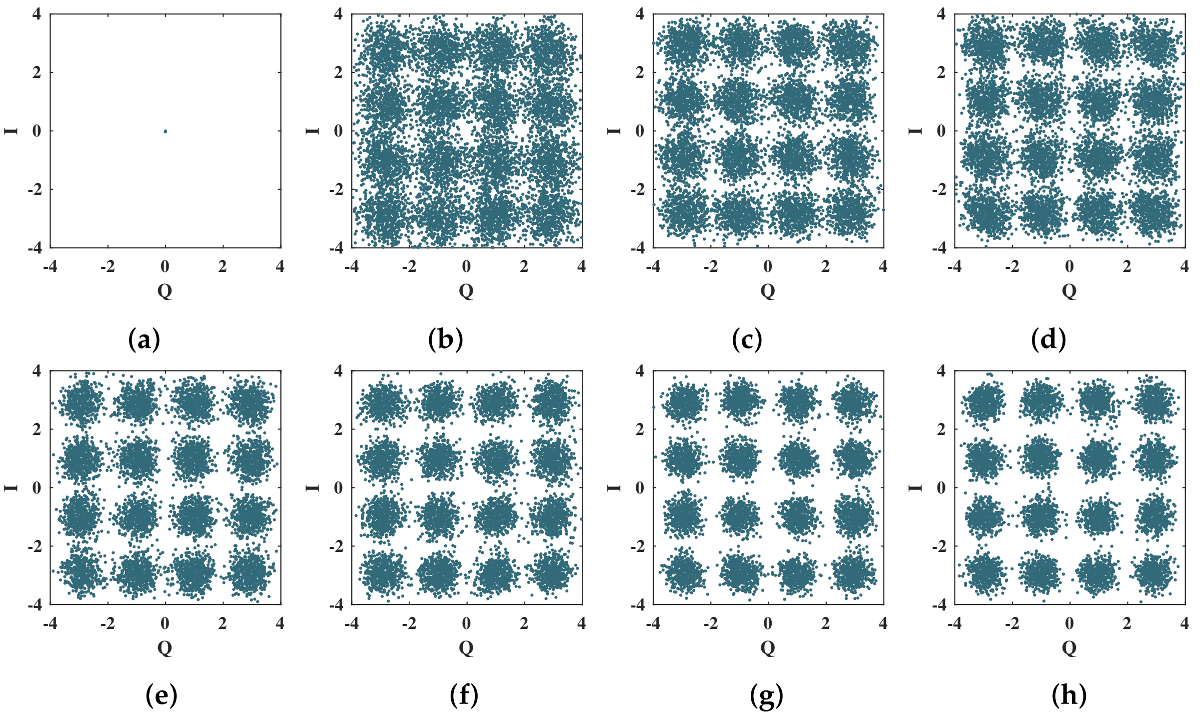

Figure 2.13 – Scatter plots for the 16-QAM symbols at the output of the MMPTRBF during the training period, for $M_T = M_R = 4$ antennas and $E_b/N_0 = 20$ dB. (**a**) 1 epoch, (**b**) 20 epochs, (**c**) 40 epochs, (**d**) 60 epochs, (**e**) 80 epochs, (**f**) 100 epochs, (**g**) 120 epochs, and (**h**) 140 epochs.

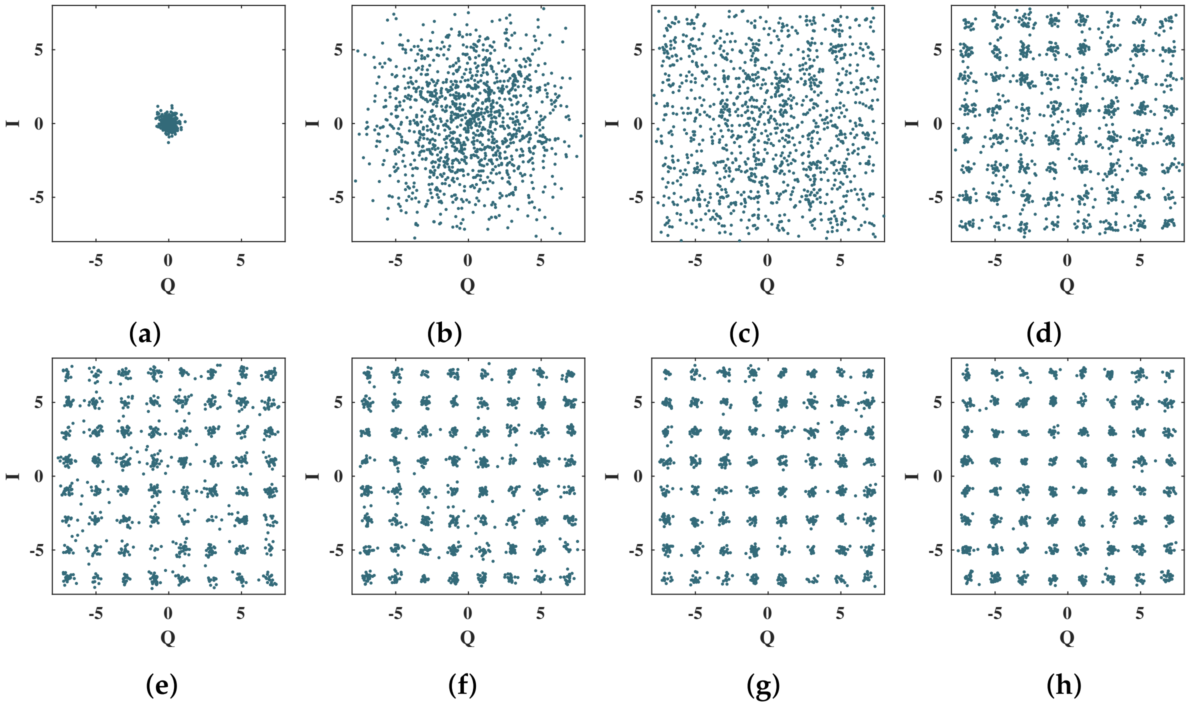

Figure 2.14 – Scatter plots for the 64-QAM symbols at the output of the MMPTRBF in the training phase, for $M_T = M_R = 4$ antennas and $E_b/N_0 = 26$ dB. (**a**) 1 epoch, (**b**) 1000 epochs, (**c**) 2000 epochs, (**d**) 3000 epochs, (**e**) 4000 epochs, (**f**) 5000 epochs, (**g**) 6000 epochs, and (**h**) 7000 epochs.

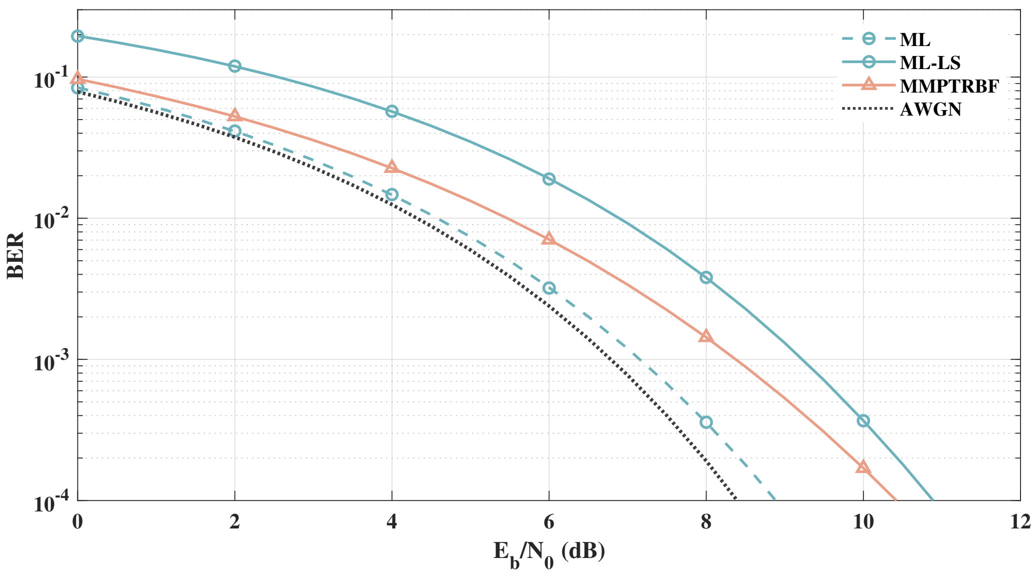

Figure 2.15 – Systems with $M_T = M_R = 4$ antennas for 4-QAM modulation.

Figures 2.16 and 2.17 show the BER×E_b/N_0 results of the QOSTBC, EQOSTBC, and MIMO-PTRBF systems operating with $M_T = 4$ and $M_T = 8$ with $M_R = 1$ antennas and 4-QAM modulation. Figures 2.16 and 2.17 highlight the diversity gain of the proposed system when compared with the EQOSTBC. Although the mathematical derivation of the proposed system diversity gain has not been obtained yet, simulations indicate a significant diversity gain (SOARES, 2021). Contrasting Figure 2.15 with Figure 2.16, one can see the increase in the diversity gain as the number of transmitting antennas increases.

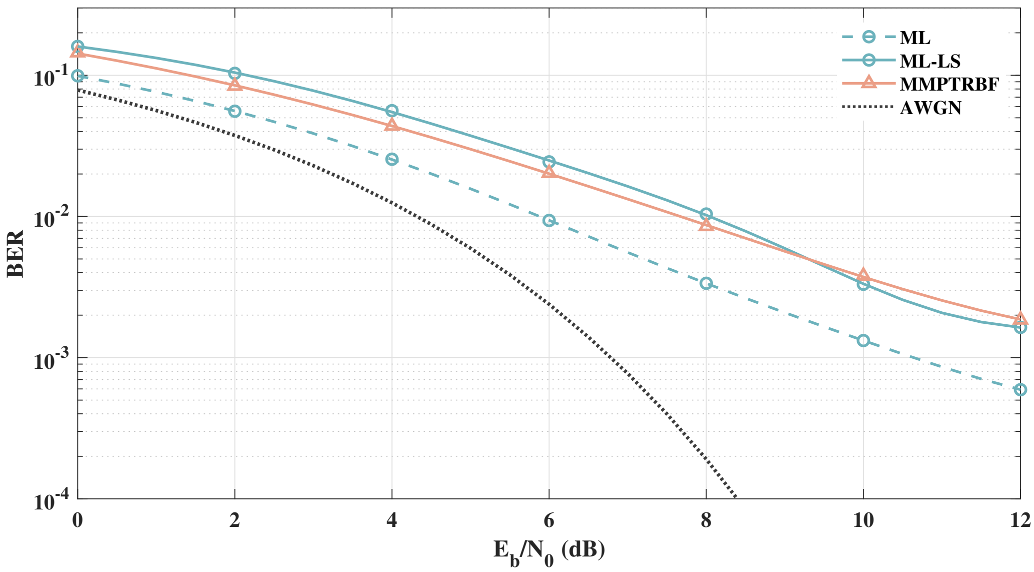

Figure 2.16 – Systems with $M_T = 4$ and $M_R = 1$ antennas for 4-QAM modulation.

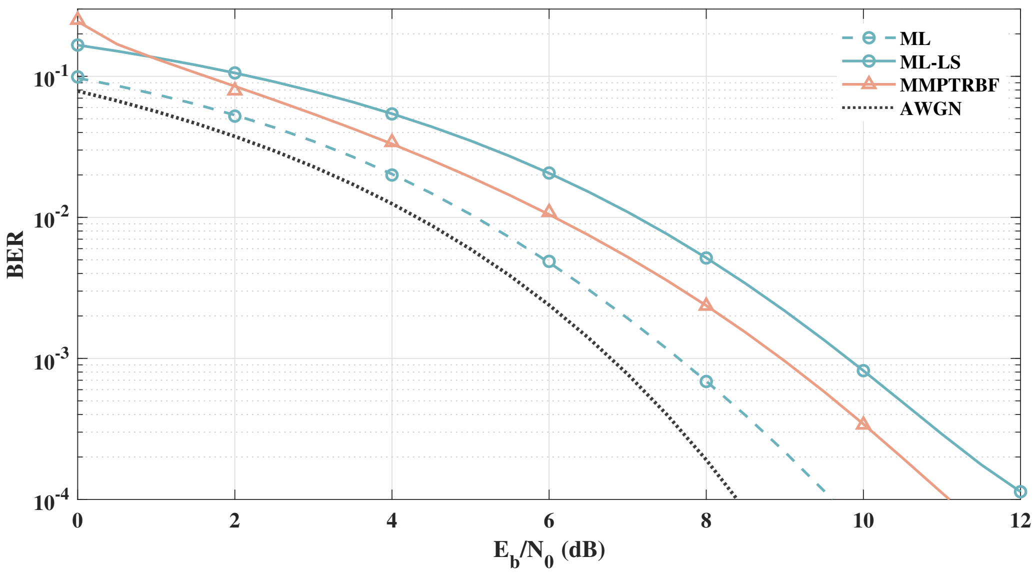

Figure 2.17 – Systems with $M_T = 8$ and $M_R = 1$ antennas for 4-QAM modulation.

Figure 2.18 shows the BER vs. E_b/N_0 results of the MMPTRBF systems operating with $M_T = 4$, 6, and 8 antennas for a 4-QAM modulation. Figure 2.18 also highlights the increase in the diversity gain as the number of transmitting antennas increases. For a BER $= 10^{-2}$, there is a gain of approximately 2 dB when doubling M_T.

To further investigate the effects of a larger number of transmitting and receiving antennas on the performances of BER, in Figure 2.19, we present the simulation results for a higher-order system with $M_T = M_R = 8$. It can be seen that the performance of the quasi-orthogonal code with channel estimation is worse for $M_T = 8$ than for $M_T = 4$

antennas, as shown in Figure 2.19. It is shown in (BIGUESH; GERSHMAN, 2006) that the performance of the linear estimator decreases proportionally with the number of transmitting antennas, which adds a constraint to the number of transmitting antennas for linearly decoded systems.

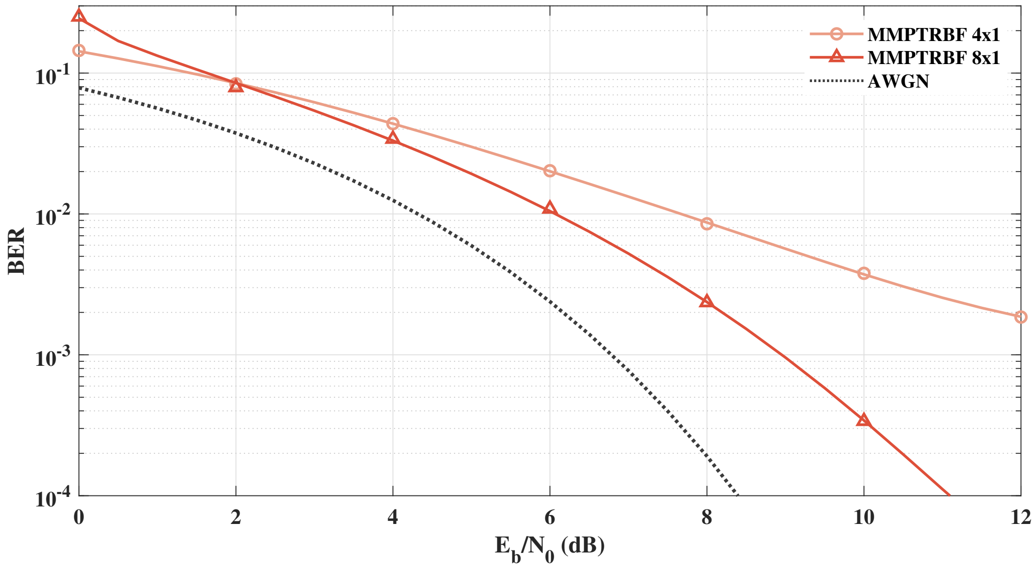

Figure 2.18 – MMPTRBF with $M_T = 4$, $M_T = 8$, and $M_R = 1$ antennas for 4-QAM modulation.

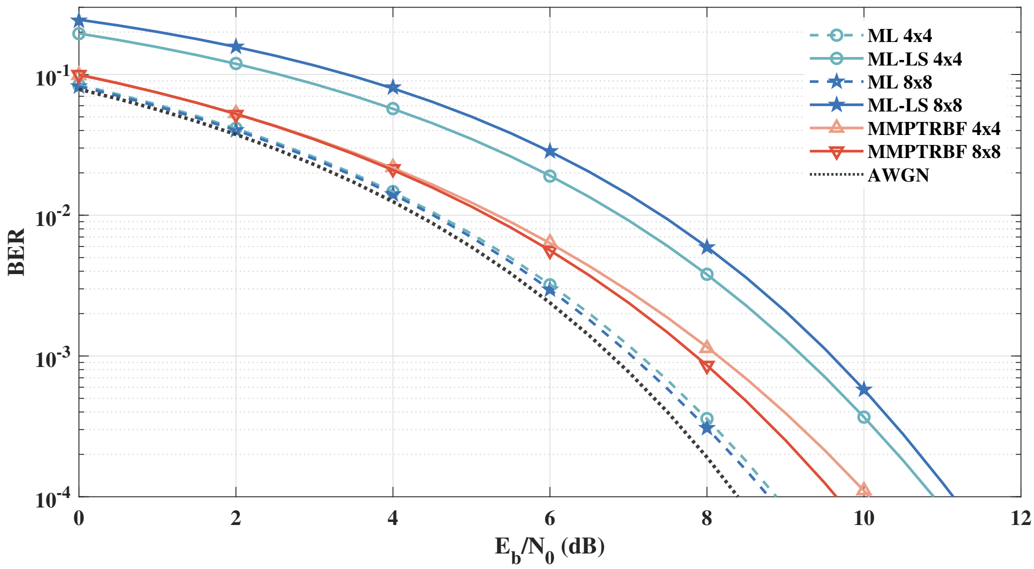

Figure 2.19 – Systems with $M_T = M_R = 4$, $M_T = M_R = 8$ antennas for 4-QAM modulation.

Figure 2.20 presents the simulation results for $M_T = M_R = 4$ $(N = 100)$, $M_T = M_R = 8$ $(N = 150)$, $M_T = M_R = 16$ $(N = 200)$, and $M_T = M_R = 32$ $(N = 600)$ to examine the extent of the proposed work for massive MIMO operations. These results show the potential of the proposed work to efficiently operate with a massive number of transmitting and receiving antennas. In addition, taking as reference the BER $= 10^{-3}$, one can notice that the gain increment is reduced when doubling the number of antennas as M_T increases. For instance, increasing from $M_T = M_R = 4$ to $M_T = M_R = 8$ yields a gain of 1.22 dB, while increasing from $M_T = M_R = 16$ to $M_T = M_R = 32$ yields a gain of only 0.2 dB.

It is important to highlight that, in contrast to the maximum likelihood detection, the proposed MMPTRBF decoding is able to operate with more than 16 antennas due to its reduced computational complexity, as discussed below in Section 2.5.

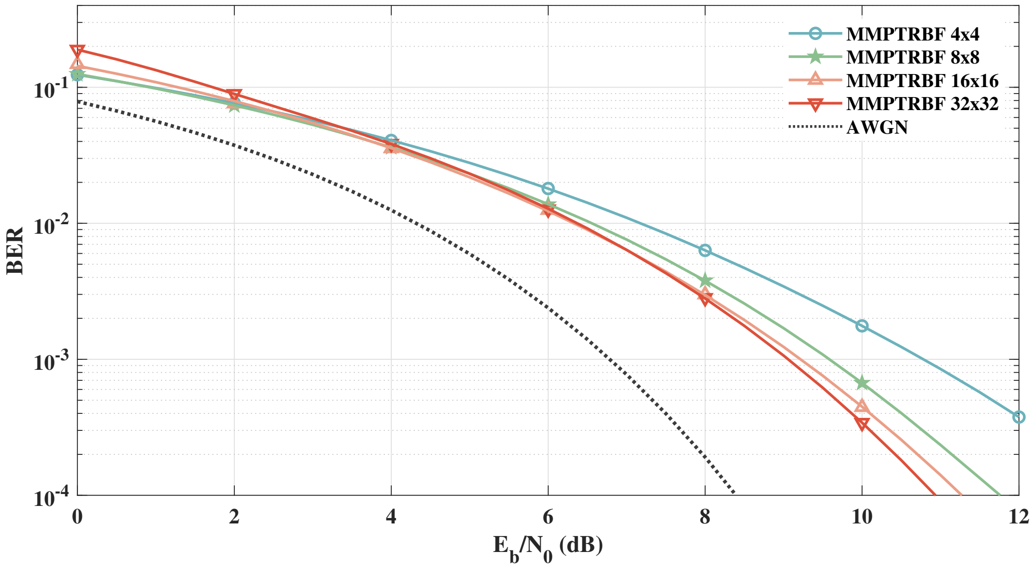

Figure 2.20 – MMPTRBF with $M_T = M_R = 4$, $M_T = M_R = 8$, $M_T = M_R = 16$, $M_T = M_R = 32$, antennas for 4-QAM modulation.

Figure 2.21 shows the BER vs. E_b/N_0 results of the ML-QOSTBC and ML-LS-QOSTBC with 16-PSK and MIMO-PTRBF with 16-QAM to further examine the extent of the proposed work for higher-order modulations with $M_T = M_R = 4$ antennas. This result shows that the proposed work operates efficiently with a higher modulation order of 16-QAM. It is important to note, however, that different modulation formats are used in this scenario because the maximum likelihood QOSTBC decoding is not capable of dealing with quadrature amplitude modulation, as addressed in (JAFARKHANI, 2001). For this reason, in order to keep 16-order modulation, a 16-PSK modulation format for QOSTBC is used. Figure 2.21 shows that the proposed work outperforms the QOSTBC using maximum likelihood (which is the optimal decoder for 16-PSK) by about 2 dB and outperforms the channel estimated scenario by more than 4 dB. Although this robust result seems to show a great advantage of using the proposed approach, we should be careful as it is not quite fair to compare 16-QAM and 16-PSK formats under the proposed nonlinear scenario.

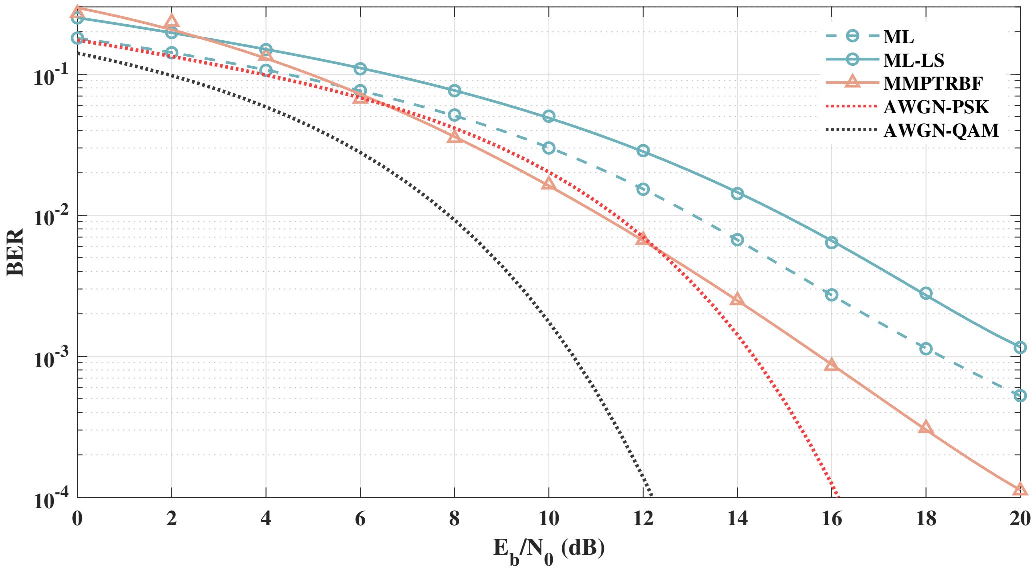

Figure 2.21 – Systems with $M_T = M_R = 4$ antennas operating at the same bitrate with 16-QAM (MMPTRBF) and 16-PSK (ML-QOSTBC and ML-LS-QOSTBC).

Figure 2.22 shows the BER vs. E_b/N_0 results of the MIMO-PTRBF systems operating with $M_T = M_R = 4$ and $M_T = M_R = 8$ for 16-QAM modulation. Figure 2.22 highlights the increase in the diversity gain as a result of the increase in the number of transmitting antennas. Although the MMPTRBF with $M_T = M_R = 8$ has the worst results for low values of E_b/N_0, for values above $E_b/N_0 = 10$ dB, the performance with $M_T = M_R = 8$ surpasses the $M_T = M_R = 4$ results by about 1.6 dB for BER $= 10^{-3}$.

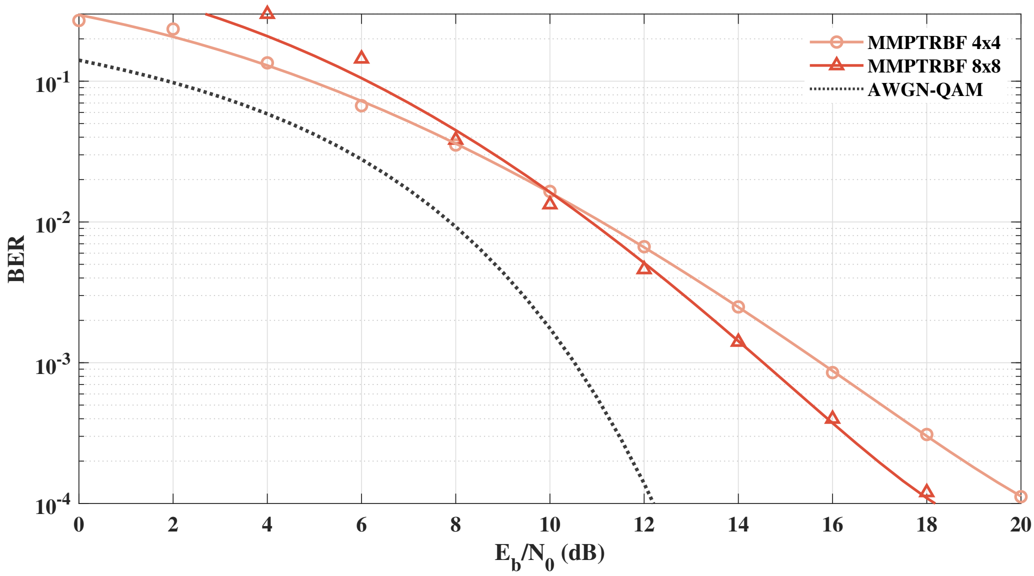

Figure 2.22 – MMPTRBF with $M_T = M_R = 4$ and $M_T = M_R = 8$ antennas operating at the same bitrate with 16-QAM modulation.

Figure 2.23 shows the BER vs. E_b/N_0 results of the MIMO-PTRBF with 64-QAM modulation to further investigate the proposed work for higher-order modulations with $M_T = M_R = 4$ antennas. Figure 2.23 shows the potential of the proposed approach of working with high-order modulation and highlights the gains over the QOSTBC with 64-PSK and perfect channel estimation, by about 5 dB, and for the channel estimated scenario by about 7 dB. It is important to emphasize, once again, that it is not quite fair to compare 64-QAM and 64-PSK formats under the proposed nonlinear scenario.

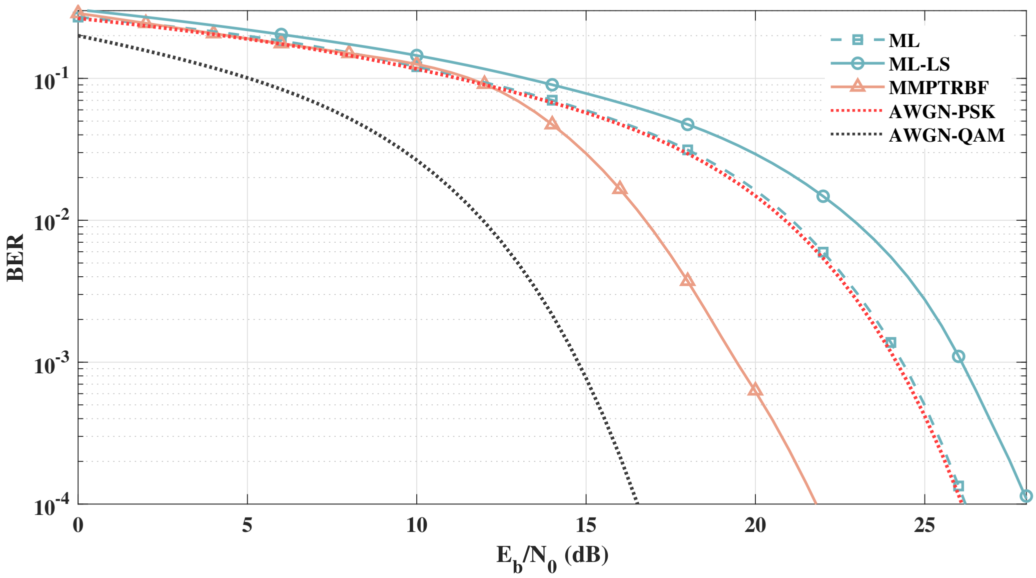

Figure 2.23 – Systems with $M_T = M_R = 4$ antennas operating at the same bitrate with 64-QAM (MMPTRBF) and 64-PSK (ML-QOSTBC and ML-LS-QOSTBC).

Figure 2.24 shows the BER vs. E_b/N_0 results of the MIMO-PTRBF systems operating with $M_T = M_R = 4$ and $M_T = M_R = 8$ for 64-QAM modulation. Figure 2.24 highlights the increase in the diversity gain as a result of the increase in transmitting antennas. When doubling the number of antennas from $M_T = M_R = 4$ to $M_T = M_R = 8$, the gain is about 0.87 dB for BER $= 10^{-3}$.

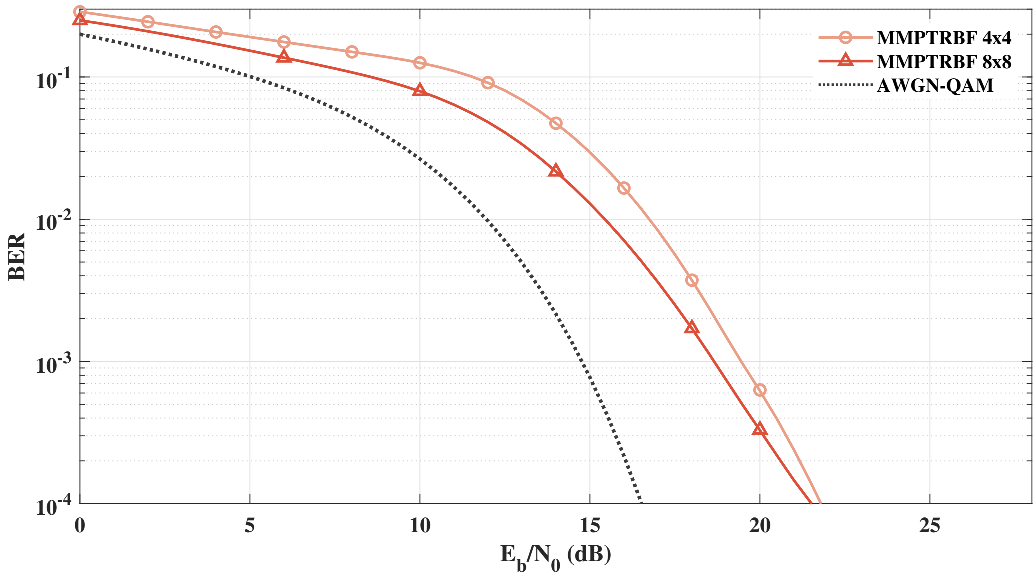

Figure 2.24 – MMPTRBF with $M_T = M_R = 4$ and 8 antennas operating at the same bitrate with 64-QAM modulation.

2.5 COMPUTATIONAL COMPLEXITIES

Table 2.2 presents the computational complexities of the OSTBC and EOSTBC with ML decoding, both with the additional complexity of channel estimation, and the proposed scheme with MIMO-PTRBF for training and decoding operation modes. M_T and M_R are the number of transmitting and receiving antennas, M_s is the number of transmitted symbols per MIMO block, P is the number of time samples per block of coded symbols, A is the constellation order (e.g., $A = 4$ in the case of 4-QAM), and N is the number of neurons used in the PTRBF neural network. Since the $\exp(\cdot)$ function can be easily implemented in hardware by lookup tables, multiplication is the most costly operation. One may note that, for $M_T \leq 8$, the complexity of the proposed algorithm is similar to the complexity of the OSTBC, for which no code exists for $M_T > 8$ (TAROKH; JAFARKHANI; CALDERBANK, 1999). The case of QOSTBC is similar, for which no simplified ML metric exists for $M_T \neq 4$ (SOARES, 2021; JAFARKHANI, 2001).

Table 2.2 – Computational complexities.

Decoder	**Multiplications**	**Additions**	$\exp(\cdot)$
OSTBC †	$(2PM_R + 4)M_sA + ch$	$(3PM_R + 3)M_sA + ch$	ch
QOSTBC †	$24M_R(M_s/2)A^2 + ch$	$16(M_R - 1)(M_s/2)A^2 + ch$	ch
ML* with $R = 1$	$M_RM_TP(A^{M_s}) + ch$	$M_RM_T(P-1)(A^{M_s}) + ch$	ch
MIMO-PTRBF (train)	$12NM_S + 12N + 8NM_RP + 2M_s$	$6NM_RP + 12NM_s - 2N$	$2N$
MIMO-PTRBF (decoding)	$2NM_RP + 2N + 4NM_s$	$4NM_RP + 4NM_s - 2N - 2M_s$	$2N$

† ch refers to the additional complexity of channel estimation.

Table 2.3 presents the computational complexities for the OSTBC, QOSTBC, and the proposed system, for $M_T = M_R = 4$. In Table 2.3, $N = 100$ neurons are used in the neural network, and maximum likelihood decoding is simulated with $R = 1$. Note that generic maximum likelihood decoding refers to the minimization of Equation (2.5) for a rate one ($R = 1$) coding scheme (e.g., it could decode the QOSTBC for the case $M_T = 4$ at a higher computational cost), and it will be assumed as an upper bound for the computational complexities of the other quasi-orthogonal systems. Furthermore, appropriate modulation schemes are used to provide the desired transmission rate for the evaluated systems; i.e., 4-QAM for rate one code ($R = 1$) and 16-QAM for half-rate code ($R = 1/2$) (SOARES, 2021).

Table 2.3 – Computational complexities for $M_T = M_R = 4$ and 2 bits/s/Hz.

Decoder	**Multiplications**	**Additions**	$\exp(\cdot)$
OSTBC †	$4.35 \times 10^3 + ch$	$6.34 \times 10^3 + ch$	ch
QOSTBC †	$3.07 \times 10^3 + ch$	$1.54 \times 10^3 + ch$	ch
ML for R = 1 †	$1.64 \times 10^4 + ch$	$1.23 \times 10^4 + ch$	ch
MIMO-PTRBF (train)	1.88×10^4	1.46×10^4	200
MIMO-PTRBF (test)	5.00×10^3	7.79×10^3	200

† ch refers to the additional complexity of channel estimation.

Table 2.4 displays the computational complexities for $M_T = M_R = 8$, when the PTRBF is equipped with $N = 150$ neurons. QOSTBC is defined as not applicable since no simplified ML decoding metric has been presented in the literature. Thus, we need to rely on the usual ML metric to perform decoding, which implies the limitation of using QOSTBC combined with ML for a higher number of antennas in practical approaches.

Table 2.4 – Computational complexities for $M_T = M_R = 8$ and 2 bits/s/Hz.

Decoder	**Multiplications**	**Additions**	**exp(·)**
OSTBC †	$3.33 \times 10^4 + ch$	$4.95 \times 10^4 + ch$	ch
QOSTBC †	Not applicable	Not applicable	Not applicable
ML for R = 1 †	$3.36 \times 10^7 + ch$	$2.94 \times 10^7 + ch$	ch
MIMO-PTRBF (train)	9.30×10^4	7.23×10^4	300
MIMO-PTRBF (test)	2.43×10^4	4.29×10^4	300

† ch refers to the additional complexity of channel estimation.

Table 2.5 displays the computational complexities for $M_T = M_R = 32$, when the PTRBF is equipped with $N = 600$ neurons. As the OSTBC coding matrix is limited to eight antennas (see (TAROKH; JAFARKHANI; CALDERBANK, 1999)), it is not applicable for $M_T = M_R = 32$. As already mentioned, since there is no simplified ML metric to perform ML decoding with QOSTBC, it results in an explosion of computational complexity for $M_T = M_R = 32$. On the other hand, the proposed approach can expand the number of antennas, maintaining a reasonable compromise between computational complexity and BER, as discussed in Section 2.4.

Table 2.5 – Computational complexities for $M_T = M_R = 32$ and 2 bits/s/Hz.

Decoder	**Multiplications**	**Additions**	**exp(·)**
OSTBC †	Not applicable	Not applicable	Not applicable
QOSTBC †	Not applicable	Not applicable	Not applicable
ML for R = 1 †	$6.04 \times 10^{23} + ch$	$5.86 \times 10^{23} + ch$	ch
MIMO-PTRBF (train)	5.15×10^6	3.92×10^6	1200
MIMO-PTRBF (test)	1.31×10^6	2.53×10^6	1200

† ch refers to the additional complexity of channel estimation.

The decoding computational complexities, shown in Figure 2.25, are addressed in terms of real-valued multiplications per MIMO symbol, as a function of $M_T = M_R$ antennas. The orthogonal and quasi-orthogonal systems are not illustrated for the entire simulation range in Figure 2.25 due to the absence of coding matrices and the simplification of the ML metric for configurations with $M_T = M_R > 8$ (SOARES, 2021).

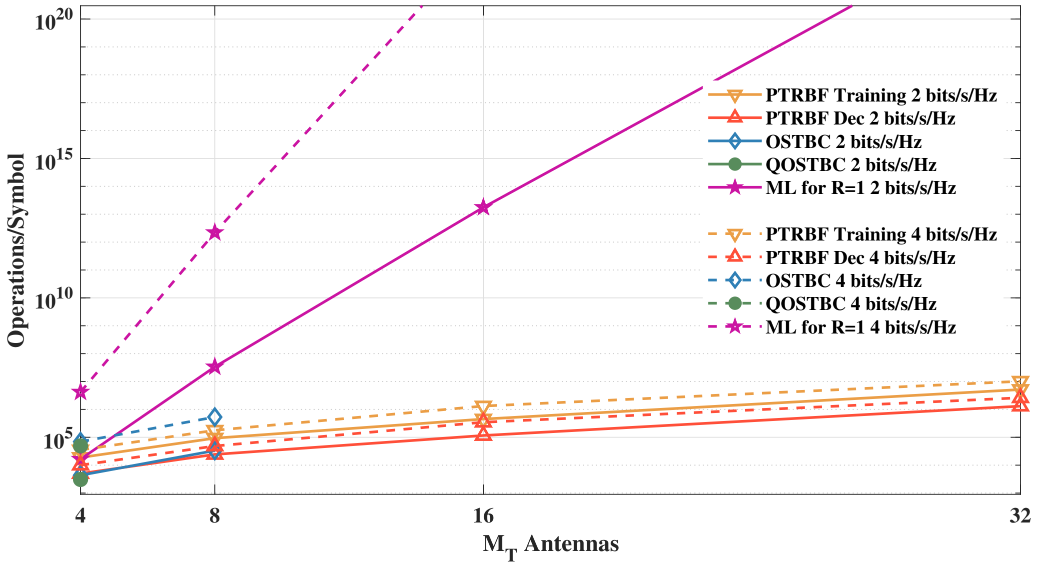

Figure 2.25 – Computational complexities as a function of $M_T = M_R$.

2.6 CONCLUSIONS

This work proposes a novel MIMO scheme for M-QAM systems that aims to achieve diversity gain for any number of antennas and at a lower computational cost when compared with traditional methods. The presented architecture is based on existing systems but with substantial improvements in the coding and decoding methods, based on conventional MIMO-OFDM systems with quasi-orthogonal coding but implemented with complex-valued Radial Basis Functions neural networks. The state-of-the-art algorithms and the proposed approach have been simulated in MATLAB to measure their relative performance under fading scenarios.

Based on the synergistic combination of the coding and decoding algorithms presented in Section 2.2, the proposed MIMO-PTRBF system is discussed and analyzed in Section 2.3. The main functional features of the proposed architecture can be summarized as follows: (1) the proposed coding algorithm generalizes the generation of quasi-orthogonal coding matrices, (2) the MIMO-PTRBF algorithm decodes the signal with satisfactory performance and feasible computational cost, presenting low steady-state MSE with fast convergence, and (3) the proposed approach seems practically feasible, at least for 32 x 32 MIMO systems, which are simulated in this work. We conjecture the practical feasibility of higher-order systems if faster hardware, such as FPGAs, is used.

The MIMO-PTRBF algorithm has been proposed in this work to implement massive MIMO schemes as an alternative to the classic MIMO-OSTBC systems under maximum likelihood detection. Simulations have shown that the proposed technique has a great potential to improve the signal-to-noise ratio at the receiver, with competitive computational complexity. Although there are recent works in the literature proposing techniques for MIMO decoding, they are focused on reducing computational complexity at the cost of performance and are limited by the simulated ML decoding. In this work, results show that the proposed approach achieves better results than ML decoding for higher-order modulation schemes with nonlinearities from power amplifiers, keeping a competitive computational complexity. Moreover, the proposed system is easily scalable in terms of the number of antennas, meaning that a wide range of transmitting and receiving antennas can be used. This is especially important for the next generations of mobile communications, such as 5G, 6G, and probably beyond.

The proposed architectures and algorithms find potential applications in some configurations of the next generations of wireless systems. For example, some specialized hardware improvements currently aim exclusively at real-time neural network algorithms. These are intended to be implemented in low-power graphical processing units (LPGPUs), favoring the speed and energy consumption of these algorithms. Therefore, the proposed architecture will be able to work with low-power consumption devices, with the ability to handle the distortions of nonlinear power amplifiers while maintaining a fast convergence rate. It should be emphasized that a fast convergence characteristic is essential for wireless channels with dynamic fluctuations.

This paper addresses some crucial aspects of MIMO-OFDM coding and decoding schemes for quasi-static channels. A complementary analysis of dynamic scenarios is also presented. We conjecture that the proposed work may be further improved using additional techniques, such as a mathematical approach for designing an optimum adaptive configuration.

Furthermore, it would be interesting to study and validate the proposed architecture for dynamic scenarios. In addition, as challenging and promising future work, the proposed algorithm can be adapted and implemented in advanced optical communication systems with Spatial Division Multiplexing (SDM), which is similar to a MIMO wireless system.

REFERENCES

ALAMOUTI, S. M. A simple transmit diversity technique for wireless communications. **IEEE Journal on Selected Areas in Communications**, v. 16, n. 8, p. 1451–1458, 1998. DOI: `10.1109/49.730453`. Cited on pages 48, 49, 144.

ASIF, R. M. et al. Energy efficiency augmentation in massive MIMO systems through linear precoding schemes and power consumption modeling. **Wireless Communications and Mobile Computing**, v. 2020, p. 1–13, 2020. DOI: `10.1155/2020/8839088`. Cited on pages 39, 141.

BIGUESH, M.; GERSHMAN, A. B. Training-based MIMO channel estimation: A study of estimator tradeoffs and optimal training signals. **IEEE Transactions on Signal**

Processing, v. 54, n. 3, p. 884–893, 2006. ISSN 1053587X. DOI: 10.1109/TSP.2005.863008. Cited on pages 45, 64.

CHO, Y. S. et al. **MIMO-OFDM Wireless Communications with MATLAB**. 1. ed. [S.l.]: Wiley, 2010. ISBN 9780470825617. Cited on page 47.

CHOPRA, S. R.; GUPTA, A. Error analysis of grouped multilevel space-time trellis coding with the combined application of massive MIMO and cognitive radio. **Wireless Personal Communications**, v. 117, n. 2, p. 461–482, 2021. DOI: 10.1007/s11277-020-07878-y. Cited on page 42.

CONDOLUCI, M. et al. Flexible Numerology in 5G NR: Interference Quantification and Proper Selection Depending on the Scenario. **Mobile Information Systems**, v. 2021, p. 1–9, 2021. DOI: 10.1155/2021/6651326. Cited on page 39.

DE SOUSA, T. F. B.; ARANTES, D. S.; FERNANDES, M. A. C. Adaptive Beamforming Applied to OFDM Systems. **Sensors**, v. 18, n. 10, p. 1–15, Oct. 2018. DOI: 10.3390/s18103558. Cited on page 40.

DE SOUSA, T. F. B.; FERNANDES, M. A. C. Butterfly Neural Equalizer Applied to Optical Communication Systems with Two-Dimensional Digital Modulation. **Optics Express**, v. 26, n. 23, p. 30837–30850, Nov. 2018. DOI: 10.1364/OE.26.030837. Cited on page 40.

DE SOUSA, T. F. B.; FERNANDES, M. A. C. Butterfly Neural Filter Applied to Beamforming. **IEEE Access**, v. 7, p. 96455–96469, July 2019. DOI: 10.1109/ACCESS.2019.2929590. Cited on page 40.

DILLI, R. Performance analysis of multi user massive MIMO hybrid beamforming systems at millimeter wave frequency bands. **Wireless Networks**, v. 27, n. 3, p. 1925–1939, 2021. DOI: 10.1007/s11276-021-02546-w. Cited on pages 39, 141.

DONG, Z.; HUANG, H. A training algorithm with selectable search direction for complex-valued feedforward neural networks. **Neural Netw.**, v. 137, p. 75–84, 2021. DOI: 10.1016/j.neunet.2021.01.014. Cited on pages 40, 96, 97.

DURGA, R. V.; MCLAUCHLIN, A. The proposed novel sphere decoder for MIMO detection. *In*: 2021 International Conference on Artificial Intelligence and Smart Systems (ICAIS). [S.l.: s.n.], 2021. P. 1240–1245. DOI: 10.1109/ICAIS50930.2021.9396022. Cited on page 41.

ELNAKEEB, A.; MITRA, U. Bilinear Channel Estimation for MIMO OFDM: Lower Bounds and Training Sequence Optimization. **IEEE Transactions on Signal Processing**, v. 69, p. 1317–1331, 2021. DOI: 10.1109/TSP.2021.3056591. Cited on page 40.

ENRICONI, M. P. et al. Phase transmittance RBF neural network beamforming for static and dynamic channels. **IEEE Antennas Wireless Propag. Lett.**, v. 19, n. 2, p. 243–247, Feb. 2020. Cited on pages 40, 83, 95–97, 155.

ETSI. 5G; NR; Physical channels and modulation (3GPP TS 38.211 version 17.2.0 Release 17). **3GPP**, 2022a. Cited on pages 57, 88.

ETSI. 5G; Study on channel model for frequencies from 0.5 to 100 GHz (3GPP TR 38.901 version 17.1.0 Release 17). **3GPP**, 2022b. Cited on pages 57, 58, 89.

GHZAOUI, M. E. et al. Compensation of non-linear distortion effects in MIMO-OFDM systems using constant envelope OFDM for 5G applications. **Journal of Circuits, Systems and Computers**, v. 29, n. 16, p. 1–21, 2020. DOI: 10.1142/S0218126620502576. Cited on page 39.

GONG, Y.; LETAIEF, K. B. Performance evaluation and analysis of space-time coding in unequalized multipath fading links. **IEEE Transactions on Communications**, v. 48, n. 11, p. 1778–1782, 2000. DOI: 10.1109/26.886466. Cited on page 43.

GUERREIRO, J.; DINIS, R.; CAMPOS, L. On the Achievable Capacity of MIMO-OFDM Systems in the CathLab Environment. **Sensors**, v. 20, n. 3, p. 1–16, 2020. DOI: 10.3390/s20030938. Cited on pages 40, 141.

HAN, M. et al. Efficient Hybrid Beamforming Design in mmWave Massive MU-MIMO DF Relay Systems With the Mixed-Structure. **IEEE Access**, v. 9, p. 66141–66153, 2021. DOI: 10.1109/ACCESS.2021.3073847. Cited on page 40.

HASSAN, A. Y. A Frequency-Diversity System With Diversity Encoder and OFDM Modulation. **IEEE Access**, v. 9, p. 2805–2818, 2021. DOI: 10.1109/ACCESS.2020.3047688. Cited on page 39.

HE, B.; SU, H.; HUANG, J. Joint beamforming and power allocation between a multistatic MIMO radar network and multiple targets using game theoretic analysis. **Digital Signal Processing**, v. 115, p. 1–13, 2021. DOI: 10.1016/j.dsp.2021.103085. Cited on page 39.

HU, Z.; ZHAO, H.; XUE, J. Error exponent for Nakagami-m fading massive MIMO channels. *In*: 2020 IEEE 6th International Conference on Computer and Communications (ICCC). [S.l.: s.n.], 2020. P. 59–63. DOI: 10.1109/ICCC51575.2020.9345091. Cited on pages 45, 143.

HWANG, S. et al. Compressive Sensing-Based Radar Imaging and Subcarrier Allocation for Joint MIMO OFDM Radar and Communication System. **Sensors**, v. 21, n. 7, p. 1–16, 2021. DOI: 10.3390/s21072382. Cited on page 39.

JAFARKHANI, H. A quasi-orthogonal space-time block code. **IEEE Transactions on Communications**, v. 49, n. 1, p. 1–4, 2001. DOI: 10.1109/26.898239. Cited on pages 46–49, 54–56, 60, 65, 68, 141, 143, 144.

JAMALI, V. et al. Intelligent Surface-Aided Transmitter Architectures for Millimeter-Wave Ultra Massive MIMO Systems. **IEEE Open Journal of the Communications Society**, v. 2, p. 144–167, 2021. DOI: 10.1109/OJCOMS.2020.3048063. Cited on page 39.

JANKIRAMAN, M. **Space-time Codes and MIMO Systems**. 1. ed. [S.l.]: Artech House, 2004. ISBN 9781580538664. Available from: <https://books.google.com.br/books?id=HU-T7y16AGEC>. Cited on pages 42, 43, 45, 47, 143.

KO, K. et al. Joint power allocation and scheduling techniques for BER minimization in multiuser MIMO systems. **IEEE Access**, v. 9, p. 66675–66686, 2021. DOI: 10.1109/ACCESS.2021.3074980. Cited on pages 39, 141.

LI, F. et al. Construction of Golay complementary matrices and its applications to MIMO omnidirectional transmission. **IEEE Transactions on Signal Processing**, v. 69, p. 2100–2113, 2021. DOI: 10.1109/TSP.2021.3067467. Cited on pages 39, 45, 143.

LI, Y. Optimum training sequences for OFDM systems with multiple transmit antennas. *In*: GLOBECOM '00 - IEEE. Global Telecommunications Conference. Conference Record (Cat. No.00CH37137). [S.l.: s.n.], 2000. v. 3, p. 1478–1482. DOI: 10.1109/GLOCOM.2000.891886. Cited on page 45.

LOSS, D. et al. Phase Transmittance RBF Neural Networks. **Electronics Letters**, v. 43, n. 16, p. 882–884, Aug. 2007a. DOI: 10.1049/el:20070016. Cited on pages 40, 41, 51, 59, 109, 111, 127.

MAJUMDER, M. et al. Optimal Bit Allocation-Based Hybrid Precoder-Combiner Design Techniques for mmWave MIMO-OFDM Systems. **IEEE Access**, v. 9, p. 54109–54125, 2021. DOI: 10.1109/ACCESS.2021.3070921. Cited on pages 40, 141.

MAREY, M.; MOSTAFA, H. Turbo Modulation Identification Algorithm for OFDM Software-Defined Radios. **IEEE Communications Letters**, v. 25, n. 5, p. 1707–1711, 2021. DOI: 10.1109/LCOMM.2021.3054590. Cited on page 39.

MAYER, K. S.; SOARES, J. A.; ARANTES, D. S. Complex MIMO RBF Neural Networks for Transmitter Beamforming over Nonlinear Channels. **Sensors**, v. 20, n. 2, p. 1–15, Jan. 2020. DOI: 10.3390/s20020378. Cited on pages 31, 40, 41, 51, 54, 79, 83, 95, 96, 109, 127.

MAYER, K. S. et al. A new CPFSK demodulation approach for software defined radio. **Journal of Circuits, Systems and Computers**, v. 28, n. 14, p. 1–14, 2019a. DOI: 10.1142/S0218126619502438. Cited on pages 40, 141.

MAYER, K. S. et al. High data-rates and high-order DP-QAM optical links can be efficiently implemented with concurrent equalization. *In*: 22ND Photonics North (PN). [S.l.: s.n.], 2020a. P. 1. DOI: 10.1109/PN50013.2020.9167008. Cited on pages 40, 141.

MAYER, K. S. et al. Nonlinear Modified Concurrent Equalizer. **Journal of Communication and Information Systems**, v. 34, n. 1, p. 201–205, Sept. 2019b. DOI: 10.14209/jcis.2019.21. Cited on page 40.

MAYER, K. S. et al. Soft failure localization using machine learning with SDN-based network-wide telemetry. *In*: 46TH European Conference on Optical Communication

(ECOC 2020). [S.l.: s.n.], 2020b. P. 1–4. DOI: 10.1109/ECOC48923.2020.9333313. Cited on page 40.

MAYER, K. S. et al. Blind Fuzzy Adaptation Step Control for a Concurrent Neural Network Equalizer. **Wireless Communications and Mobile Computing**, v. 2019, n. 1, p. 9082362, 2019c. DOI: https://doi.org/10.1155/2019/9082362. Cited on pages 40, 83, 95, 96, 109, 127, 161.

MAYER, K. S. et al. Machine-learning-based soft-failure localization with partial software-defined networking telemetry. **Journal of Optical Communications and Networking**, v. 13, n. 10, E122–E131, June 2021. Cited on page 40.

MEI, K. et al. A low complexity learning-based channel estimation for OFDM systems with online training. **IEEE Transactions on Communications**, v. 69, n. 10, p. 6722–6733, 2021. Cited on pages 57, 89.

MIRFARSHBAFAN, S. H. et al. Algorithm and VLSI design for 1-Bit data detection in massive MIMO-OFDM. **IEEE Open Journal of Circuits and Systems**, v. 1, p. 170–184, 2020. DOI: 10.1109/OJCAS.2020.3022514. Cited on page 39.

OSMAN, A. M. et al. A Modified Method of Filtering for FBMC Based 5G Communications on Minimizing Doppler Shift. *In*: 2021 6th International Conference for Convergence in Technology (I2CT). [S.l.: s.n.], 2021. P. 1–4. DOI: 10.1109/I2CT51068.2021.9417931. Cited on pages 40, 141.

PINTO, R. P. et al. Demonstration of machine-intelligent soft-failure localization using SDN telemetry. *In*: OPTICAL Fiber Communications Conference and Exhibition (OFC 2021). [S.l.: s.n.], 2021. P. 1–3. Cited on page 40.

SAAD, W.; BENNIS, M.; CHEN, M. A Vision of 6G Wireless Systems: Applications, Trends, Technologies, and Open Research Problems. **IEEE Network**, v. 34, n. 3, p. 134–142, 2020. Cited on page 40.

SHANG, B. et al. Spatial spectrum sensing in uplink two-tier user-centric deployed HetNets. **IEEE Transactions on Wireless Communications**, v. 19, n. 12, p. 7957–7972, 2020. DOI: 10.1109/TWC.2020.3018408. Cited on pages 39, 141.

SHIMIZU, D. Y. et al. A deep neural network model for link failure identification in multi-path ROADM based networks. *In*: 22ND Photonics North (PN). [S.l.: s.n.], 2020. P. 1. DOI: 10.1109/PN50013.2020.9166978. Cited on page 40.

SHR, K.-T.; CHEN, H.-D.; HUANG, Y.-H. A low-complexity Viterbi decoder for space-time trellis codes. **IEEE Transactions on Circuits and Systems I: Regular Papers**, v. 57, n. 4, p. 873–885, 2010. DOI: 10.1109/TCSI.2009.2027648. Cited on page 43.

SINDHU, P.; HAMEED, A. Efficient quasi-orthogonal space-time block codes for five and six transmit antennas. *In*: 2015 IEEE International Conference on Electronics, Computing and Communication Technologies (CONECCT). [S.l.: s.n.], 2015. P. 1–5. DOI: 10.1109/CONECCT.2015.7383923. Cited on pages 47, 144.

SOARES, J. A. **Complex phase-transmittance RBF neural network for massive MIMO-OFDM decoding**. Feb. 2021. MA thesis – Department of Communications, School of Electrical and Computer Engineering, University of Campinas. Available from: <http://acervus.unicamp.br/index.asp?codigo_sophia=1165045>. Cited on pages 39–52, 54, 56–60, 63, 68, 69.

SOKAL, B. et al. Tensor-Based Receiver for Joint Channel, Data, and Phase-Noise Estimation in MIMO-OFDM Systems. **IEEE Journal of Selected Topics in Signal Processing**, v. 15, n. 3, p. 803–815, 2021. DOI: 10.1109/JSTSP.2021.3061917. Cited on pages 40, 141.

SWAIN, R. R.; KHILAR, P. M.; DASH, T. Multifault diagnosis in WSN using a hybrid metaheuristic trained neural network. **Digital Communications and Networks**, v. 6, n. 1, p. 86–100, 2020. DOI: 10.1016/j.dcan.2018.02.001. Cited on page 40.

TAROKH, V.; JAFARKHANI, H.; CALDERBANK, A. R. Space-time block codes from orthogonal designs. **IEEE Transactions on Information Theory**, v. 45, n. 5, p. 1456–1467, 1999. DOI: 10.1109/18.771146. Cited on pages 45, 47, 54, 68, 69, 143.

TEMIZ, M.; ALSUSA, E.; BAIDAS, M. W. A dual-functional massive MIMO OFDM communication and radar transmitter architecture. **IEEE Transactions on Vehicular Technology**, v. 69, n. 12, p. 14974–14988, 2020. DOI: 10.1109/TVT.2020.3031686. Cited on page 39.

TIRKKONEN, O.; BOARIU, A.; HOTTINEN, A. Minimal non-orthogonality rate 1 space-time block code for 3+ Tx antennas. *In*: 2000 IEEE Sixth International Symposium on Spread Spectrum Techniques and Applications. ISSTA 2000. Proceedings (Cat. No.00TH8536). [S.l.: s.n.], 2000. v. 2, p. 429–432. DOI: 10.1109/ISSSTA.2000.876470. Cited on pages 47, 143.

TOKA, M.; KUCUR, O. Performance of MRT/RAS MIMO-NOMA with residual hardware impairments. **IEEE Wireless Communications Letters**, v. 10, n. 5, p. 1071–1074, 2021. DOI: 10.1109/LWC.2021.3057432. Cited on page 42.

WEIFENG SU; XIANG-GEN XIA. Quasi-orthogonal space-time block codes with full diversity. *In*: GLOBAL Telecommunications Conference, 2002. GLOBECOM '02. IEEE. [S.l.: s.n.], 2002. v. 2, p. 1098–1102. DOI: 10.1109/GLOCOM.2002.1188366. Cited on pages 47, 143, 144.

XU, H.; PILLAY, N. Multiple Complex Symbol Golden Space-Time Labeling Diversity. **IEEE Access**, v. 9, p. 70233–70241, 2021. DOI: 10.1109/ACCESS.2021.3078827. Cited on page 43.

YAO, G.; CHEN, H.; HU, J. An improved expectation propagation based detection scheme for MIMO systems. **IEEE Transactions on Communications**, v. 69, n. 4, p. 2163–2175, 2021. DOI: 10.1109/TCOMM.2020.3048942. Cited on page 42.

YERRAPRAGADA, A. K.; KELLEY, B. On the Application of K-User MIMO for 6G Enhanced Mobile Broadband. **Sensors**, v. 20, n. 21, p. 1–16, 2020. DOI: 10.3390/s20216252. Cited on pages 40, 141.

YOON, E. et al. LDPC Decoding With Low Complexity for OFDM Index Modulation. **IEEE Access**, v. 9, p. 68435–68444, 2021. DOI: 10.1109/ACCESS.2021.3077256. Cited on page 39.

ZHANG, H. et al. An optical neural chip for implementing complex-valued neural network. **Nat. Commun.**, v. 12, n. 457, p. 1–11, 2021a. Cited on pages 42, 95.

ZHAO, X. et al. Analysis of a distributed MIMO channel capacity under a special scenario. **EURASIP Journal on Wireless Communications and Networking**, v. 2019, n. 189, p. 1–7, 2019. Cited on page 42.

ZOU, F. et al. A novel PAPR reduction scheme for OFDM systems based on neural networks. **Wireless Communications and Mobile Computing**, v. 2021, p. 1–8, 2021. DOI: 10.1155/2021/5574807. Cited on pages 40, 141.

Appendix

Definition 2..1. A non-monotone and differentiable transformation $\mathbf{g} : \mathbb{R}^N \mapsto \mathbb{R}^N$, composed of M-real solutions, yields a multivariate change of probability density function:

$$f_{\mathbf{Y}}(\mathbf{y}) = \sum_{m=1}^{M} f_{\mathbf{X}}(\mathbf{x}) \left| J\left(\mathbf{g}_m^{-1}(\mathbf{y})\right)\right|,$$

in which $\mathbf{x}, \mathbf{y} \in \mathbb{R}^N$ are random vectors, $J(\cdot)$ is the determinant of the Jacobi operator, and $\mathbf{g}_m^{-1}$ is the inverse transformation of $\mathbf{g}$, regarding the mth real solution (see (HELD; BOVÉ, 2014), p. 322 and (DOLECEK, 2013), pp. 69–70).

Theorem 2.1. *If $\mathbf{x} \in \mathbb{R}^N$ is an input random vector of a kernel function $g(\mathbf{x}) = y \triangleq \exp\left\{-\frac{||\mathbf{x}-\boldsymbol{\gamma}||_2^2}{z}\right\}$, with constant $\boldsymbol{\gamma} \in \mathbb{R}^N$ and $z \in \mathbb{R}$; then, g performs a trans-dimensional transformation of probability density function from $f_{\mathbf{X}}(\mathbf{x})$ to $f_Y(y)$.*

Proof. Let the Gaussian kernel function $g(\mathbf{x}, \boldsymbol{\gamma}, z) \triangleq \exp\left\{-\frac{||\mathbf{x}-\boldsymbol{\gamma}||_2^2}{z}\right\}$, with constant center vector $\boldsymbol{\gamma}$ and variance z, be denoted by $y = g(\mathbf{x})$, since it is only dependent on the random vector $\mathbf{x} \in \mathbb{R}^N$. Furthermore, let $\mathbf{y} \triangleq [g(\mathbf{x}) \quad y_2 \ \cdots y_N]^{\mathrm{T}}$ be the auxiliary expanded vector of mapping. With Definition 2..1, we have the following transformation of the probability density function (PDF):

$$f_{\mathbf{Y}}(\mathbf{y}) = \sum_{m=1}^{M} f_{\mathbf{X}}(\mathbf{x}) \left| J\left(\mathbf{g}_m^{-1}(\mathbf{y})\right)\right|. \tag{2.28}$$

However, we need to marginalize the extra dimensions of $\mathbf{y}$ in (2.28) to obtain the PDF of the desired random variable $f_Y(y)$:

$$f_Y(y) = \sum_{m=1}^{M} \int f_{\mathbf{X}}(\mathbf{x}) \left| J\left(\mathbf{g}_m^{-1}(\mathbf{y})\right)\right| dy_2 \cdots dy_N. \tag{2.29}$$

Then, finding some non-monotone function $h(y) = h\left(g(\mathbf{x})\right) = f_{\mathbf{X}}(\mathbf{x})$, in which $h(y)$ is not a function of the expanded auxiliary terms y_2, y_3, $\cdots$, y_N, we can rewrite (2.29) as

$$f_Y(y) = \sum_{m=1}^{M} h_m(y) \int \left| J\left(\mathbf{g}_m^{-1}(\mathbf{y})\right)\right| dy_2 \cdots dy_N, \tag{2.30}$$

where the right-hand term under the integral is called integral Jacobian, and it is responsible for the volume correction (SAMBRIDGE et al., 2006) of the trans-dimensional transformation.

In addition, as the Gaussian kernel is a non-monotone function with two real solutions (due to the Euclidean norm), (2.30) results in

$$f_Y(y) = h_1(y) \int \left| J\left(\mathbf{g}_1^{-1}(\mathbf{y})\right)\right| dy_2 \cdots dy_N + h_2(y) \int \left| J\left(\mathbf{g}_2^{-1}(\mathbf{y})\right)\right| dy_2 \cdots dy_N, \tag{2.31}$$

which is the trans-dimensional transformation of PDF performed by a Gaussian kernel function. □

Corollary 2.1.1. *For any complex-valued vectors of same size* $\mathbf{x}, \mathbf{y} \in \mathbb{C}^N$ *and a scalar* $z \in \mathbb{C}$*, a kernel function* $f(\mathbf{x}, \mathbf{y}, z) \triangleq \exp\left\{-\frac{||\Re(\mathbf{x})-\Re(\mathbf{y})||_2^2}{\Re(z)}\right\} + \jmath \exp\left\{-\frac{||\Im(\mathbf{x})-\Im(\mathbf{y})||_2^2}{\Im(z)}\right\}$ *have real and imaginary boundaries between* 0 *and* 1*, if* $\Re(z) > 0$ *and* $\Im(z) > 0$*.*

Proof. The proof is straightforward using Theorem A1 of (MAYER; SOARES; ARANTES, 2020), where the real-valued analyses must be independently performed for the real and imaginary components of $\mathbf{x}$, $\mathbf{y}$, and z. □

Corollary 2.1.2. *If* $\mathbf{x} \in \mathbb{C}^N$ *is a complex-valued input random vector of a complex-valued kernel function* $g(\mathbf{x}) = y \triangleq \exp\left\{-\frac{||\Re(\mathbf{x})-\Re(\gamma)||_2^2}{\Re(z)}\right\} + \jmath \exp\left\{-\frac{||\Im(\mathbf{x})-\Im(\gamma)||_2^2}{\Im(z)}\right\}$*, with constant* $\boldsymbol{\gamma} \in \mathbb{C}^N$ *and* $z \in \mathbb{C}$*, then* g *performs a complex-valued trans-dimensional transformation of probability density function from* $f_{\Re(\mathbf{X})}\left(\Re\left(\mathbf{x}\right)\right) + \jmath f_{\Im(\mathbf{X})}\left(\Im\left(\mathbf{x}\right)\right)$ *to* $f_{\Re(Y)}\left(\Re\left(y\right)\right) + \jmath f_{\Im(Y)}\left(\Im\left(y\right)\right)$*, with independent real and imaginary components.*

Proof. The proof is straightforward using Theorem 2.1, where the real-valued analyses must be independently performed for the real and imaginary components of $\mathbf{x}$ and y. □

Theorem 2.2. *If* $\mathbf{x} \in \mathbb{C}^K$ *is a stationary complex-valued input random vector of a PT-RBF, then the matrix of synaptic weights* $\mathbf{W}[k] \in \mathbb{C}^{M\times N}$ *converges in the mean to the optimum matrix of synaptic weights* $\mathbf{W}_o$ *when* $k \to \infty$*, if the matrix of center vectors and the vector of variances are constants.*

Proof. Let the PT-RBF output $\mathbf{y}[k] = \mathbf{W}[k]\boldsymbol{\phi}[k] \in \mathbb{C}^M$, where $\boldsymbol{\phi}[k] \in \mathbb{C}^N$ is the vector of the neuron output. Furthermore, let the update function of the matrix of synaptic weights $\mathbf{W}[k+1] = \mathbf{W}[k] + \eta_w \mathbf{e}[k]\boldsymbol{\phi}^{\mathrm{H}}[k] \in \mathbb{C}^{M\times N}$, where η_w is the adaptive step and $\mathbf{e}[k] \in \mathbb{C}^M$ is the vector of errors. We can assume without loss in generality that the desired response is

$$\mathbf{d}[k] = \mathbf{W}_o\boldsymbol{\phi}[k] + \mathbf{q}[k] \in \mathbb{C}^M, \tag{2.32}$$

where $\mathbf{q}[k] \in \mathbb{C}^M$ is a complex-valued white Gaussian noise vector, with zero mean and variance $\boldsymbol{\sigma}_q^2$, which is uncorrelated with $\boldsymbol{\phi}[k]$. Then, substituting (2.32) into the error equation $\mathbf{e}[k] = \mathbf{d}[k] - \mathbf{y}[k]$, we have

$$\mathbf{e}[k] = \mathbf{W}_o\boldsymbol{\phi}[k] + \mathbf{q}[k] - \mathbf{W}[k]\boldsymbol{\phi}[k]. \tag{2.33}$$

Thus, replacing (2.33) into the update function of the matrix of synaptic weights:

$$\mathbf{W}[k+1] = \mathbf{W}[k] + \eta_w \mathbf{W}_o \boldsymbol{\phi}[k]\boldsymbol{\phi}^{\mathrm{H}}[k] + \eta_w \mathbf{q}[k]\boldsymbol{\phi}^{\mathrm{H}}[k] - \eta_w \mathbf{W}[k]\boldsymbol{\phi}[k]\boldsymbol{\phi}^{\mathrm{H}}[k]. \tag{2.34}$$

Subtracting $\mathbf{W}_o$ from both sides of (2.34), the synaptic weights error matrix $\mathbf{V}[k] = \mathbf{W}[k] - \mathbf{W}_o$ can be given by

$$\mathbf{V}[k+1] = \mathbf{V}[k] - \eta_w \mathbf{V}[k]\boldsymbol{\phi}[k]\boldsymbol{\phi}^{\mathrm{H}}[k] + \eta_w \mathbf{q}[k]\boldsymbol{\phi}^{\mathrm{H}}[k]. \tag{2.35}$$

Applying the expectation operator to both sides of (2.35):

$$\mathrm{E}\left(\mathbf{V}[k+1]\right) = \mathrm{E}\left(\mathbf{V}[k] - \eta_w \mathbf{V}[k]\boldsymbol{\phi}[k]\boldsymbol{\phi}^{\mathrm{H}}[k] + \eta_w \mathbf{q}[k]\boldsymbol{\phi}^{\mathrm{H}}[k]\right), \tag{2.36}$$

and employing the independence assumptions of $\mathbf{W}[k] \perp\!\!\!\perp \boldsymbol{\phi}[k]$ and $\mathbf{q}[k] \perp\!\!\!\perp \boldsymbol{\phi}[k]$:

$$\mathrm{E}\left(\mathbf{V}[k+1]\right) = \mathrm{E}\left(\mathbf{V}[k]\right) - \eta_w \mathrm{E}\left(\mathbf{V}[k]\right)\mathrm{E}\left(\boldsymbol{\phi}[k]\boldsymbol{\phi}^{\mathrm{H}}[k]\right) + \eta_w \mathrm{E}\left(\mathbf{q}[k]\right)\mathrm{E}\left(\boldsymbol{\phi}^{\mathrm{H}}[k]\right), \tag{2.37}$$

which results in:

$$\mathrm{E}\left(\mathbf{V}[k+1]\right) = \mathrm{E}\left(\mathbf{V}[k]\right)\left[\mathbf{I} - \eta_w \mathrm{E}\left(\boldsymbol{\phi}[k]\boldsymbol{\phi}^{\mathrm{H}}[k]\right)\right] = \mathrm{E}\left(\mathbf{V}[k]\right)\left[\mathbf{I} - \eta_w \mathbf{R}_{\phi\phi}\right], \tag{2.38}$$

where $\mathbf{I}$ is the identity matrix and $\mathbf{R}_{\phi\phi}$ is the correlation matrix of the neuron outputs. As $\mathbf{R}_{\phi\phi}$ is Hermitian and positive semidefinite (see (TENOUDJI, 2016), pp. 387, 469), it can be rotated into a diagonal matrix by the unitary transformation $\mathbf{R}_{\phi\phi} = \mathbf{Q}\boldsymbol{\Lambda}\mathbf{Q}^{\mathrm{H}}$, in which $\boldsymbol{\Lambda} = \mathrm{diag}\left(\lambda_1 \quad \lambda_2 \ \cdots \lambda_N\right)$ is the diagonal matrix of real and positive eigenvalues of $\mathbf{R}_{\phi\phi}$ (see (TENOUDJI, 2016), p. 471), in the form of $\lambda_1 \geq \lambda_2 \geq \cdots \geq \lambda_N$, and $\mathbf{Q} \in \mathbb{C}^{N \times N}$ is the orthonormal matrix of eigenvectors that diagonalizes $\mathbf{R}_{\phi\phi}$ through a similarity transformation (DINIZ, 2013).

Then, rotating $\mathrm{E}\left(\mathbf{V}[k]\right)$ by the matrix of eigenvectors $\mathbf{Q}$—i.e., $\bar{\mathbf{V}}[k] = \mathrm{E}\left(\mathbf{V}[k]\right)\mathbf{Q}$—decouples the evolution of its coefficients. By means of this rotation, we can express the modes of convergence (see (MANDIC; GOH, 2009), p. 77) of (2.38) as

$$\bar{\mathbf{V}}[k+1] = \bar{\mathbf{V}}[k]\left(\mathbf{I} - \eta_w \boldsymbol{\Lambda}\right). \tag{2.39}$$

As $\left(\mathbf{I} - \eta_w \boldsymbol{\Lambda}\right)$ is diagonal and the nth row of $\bar{\mathbf{V}}[k]$ represents the projection of $\mathrm{E}\left(\mathbf{V}[k]\right)$ onto the nth eigenvector of $\mathbf{R}_{\phi\phi}$, all elements of $\bar{\mathbf{V}}[k]$ evolve independently. Hence, (2.39) converges to zero if $|1 - \eta_w \lambda_n| < 1$ (see (DINIZ, 2013), p. 84). As the fastest mode of convergence corresponds to the maximum eigenvalue λ_{max}, using the identity $\lambda_1 = \lambda_{max} \leq \mathrm{tr}(\mathbf{R}_{\phi\phi})$ (see (MANDIC; GOH, 2009), p. 77), the condition for the convergence in the mean becomes

$$0 < \eta_w < \frac{2}{\lambda_{max}} \approx \frac{2}{\mathrm{tr}(\mathbf{R}_{\phi\phi})}. \tag{2.40}$$

As the trace of $\mathbf{R}_{\phi\phi}$ is equal to the product of the number of neurons outputs and the respective signal power, the adaptive step bound is given by

$$0 < \eta_w < \frac{2}{N\mathrm{E}\left(|\phi[k]|^2\right)}. \tag{2.41}$$

Note that the convergence in the mean of both PT-RBF and complex LMS is similar (see (MANDIC; GOH, 2009), p. 77), and it is natural in some way, considering that after the trans-dimensional transformation step of the PT-RBF, both algorithms have comparable architectures.

However, in view of Corollary 2.1.2, $\mathrm{E}(|\phi[k]|^2)$ can be difficult to obtain. To circumvent this issue, using Corollary 2.1.1, we can replace $\phi[k]$ by its maximum value $(1 + \jmath)$ into (2.41), which yields

$$0 < \eta_w < \frac{2}{N\,|1+\jmath|^2} = \frac{1}{N}, \tag{2.42}$$

which is the adaptive step bound for the convergence in the mean. □

Chapter 3

PCA-based Channel Estimation for MIMO Communications

Authors: Jonathan Aguiar Soares, Kayol Soares Mayer, Pedro Benevenuto Valadares, and Dalton Soares Arantes

Abstract

In multiple-input multiple-output communications, channel estimation is paramount to keep base stations and users on track. This paper proposes a novel PCA-based – principal component analysis – channel estimation approach for MIMO orthogonal frequency division multiplexing systems. The channel frequency response is firstly estimated with the least squares method, and then PCA is used to filter only the higher singular components of the channel impulse response, which is then converted back to frequency domain. The proposed approach is compared with the MMSE, the minimum mean square error estimation, in terms of bit error rate versus E_b/N_0.

Keywords: MIMO, OFDM, Channel Estimation, Principal Component Analysis.

This Chapter is a replica of the following manuscript: Jonathan Aguiar Soares, Kayol Soares Mayer, Pedro Benevenuto Valadares, and Dalton Soares Arantes, "PCA-based Channel Estimation for MIMO Communications" in XL Simpósio Brasileiro de Telecomunicações e Processamento de Sinais (SBrT2022), Sep. 2022, pp. 1–5, doi: 10.14209/sbrt.2022.1570825011.

3.1 INTRODUCTION

With the ever-increasing demand for wireless network capacity, multiple-input multiple-output (MIMO) communications have become essential in novel technologies to increase spectral efficiency and, consequently, network throughput (SOARES et al., 2021a). Among the MIMO technologies, space-time block coding (STBC) is fundamental to providing space diversity by supplying multiple independently faded replicas of the same information symbol, increasing communication reliability (KARA; KAYA; YANIKOMEROGLU, 2022). However, efficient channel estimation is still a challenging issue when increasing either the number of antennas or subcarriers in MIMOorthogonal frequency division multiplexing (OFDM), mainly in high mobility scenarios due to pilot overhead and complexity (ZHANG; GAO; ZHOU, 2022).

Under channel linearity and time-invariance constraints, the conventional minimum mean squared error (MMSE) is the optimal linear operator for channel estimation under jointly Gaussian distributed random variables (NEUMANN; WIESE; UTSCHICK, 2018). However, these constraints are unrealistic since even pedestrian channels are dynamic (YIN et al., 2016), and nonlinearities are common in power amplifiers (ENRICONI et al., 2020; MAYER et al., 2019c; MAYER; SOARES; ARANTES, 2020; MAYER et al., 2022). In addition, as the MMSE channel estimation relies on covariance matrix inversions, the computational complexity is extremely expensive (SHARIATI et al., 2013). Many different approaches focus on reducing MMSE computational complexity but still have reasonably high computational complexity for practical applications (ALI et al., 2020). In contrast to the MMSE, the conventional least squares (LS) algorithm has a lower computational complexity at the cost of less accurate channel estimation (BALEVI; DOSHI; ANDREWS, 2020).

In order to improve channel estimation of MIMO-OFDM systems, time filtering can be employed to cut channel components regarding delays longer than the channel delay spread. To accomplish this, after channel estimation (e.g., using LS or MMSE), inverse fast Fourier transform (IFFT) converts the channel frequency response to time domain, and a smoothing filter is applied to the maximum multipath delay which is within the cyclic prefix (CP) of the OFDM symbols. After subsequent filtering, the channel impulse response is converted back to frequency domain via a fast Fourier transform (FFT) (DIALLO; RABINEAU; CARIOU, 2009). Although it is a simple strategy, this is not able to filter noise components with delays shorter than the delay spread.

In this context, this work proposes a novel extension of the time domain MIMO-OFDM smoothing filter to mitigate noise components embedded in the channel impulses. The proposed approach is based on the principal component analysis (PCA) (ABDI; WILLIAMS, 2010) to filter the noise after the time domain smoothing filter. As the noise is orthogonal to the multipath components, for higher signal-to-noise ratio (SNR)s, we only keep the most significant components of the PCA transformation, which correspond to the channel components without noise. Then, in a MIMO-OFDM receiver, this filtering cascade is used after the low computational complexity LS channel estimator. Results are compared in terms of bit error rate (BER) versus energy per bit to noise power spectral density ratio (E_b/N_0) of the proposed approach and the conventional MSE with smoothing filter. To validate the proposed filtering robustness, results also consider dynamic channels with Doppler from 0 Hz to 40 Hz.

The paper notation is mostly standard. For example, $\mathbb{C}^{m\times m}$ is the $m \times m$ set of complex numbers. Matrices are denoted by boldface uppercase letters and vectors are denoted by boldface lowercase letters. The transpose, Hermitian, and inverse matrix operators are expressed as $[\cdot]^T$, $[\cdot]^H$, and $[\cdot]^{-1}$, respectively. The indexes $[n]$ and $[k]$ are related to the time and frequency domain, respectively.

The remainder of this paper is organized as follows. Section 3.2 presents a MIMO-OFDM communication scheme based on STBC. Section 3.3 describes channel estimation using MMSE and smoothing filter. Section 3.4 presents the proposed PCA-based channel estimation. Section 3.5 discusses the asymptotic computational complexities of the PCA-based and MMSE channel estimation algorithms. Lastly, Section 3.7 concludes the paper.

3.2 MIMO-OFDM SYSTEM MODEL

This paper considers the MIMO space-diversity scheme based on STBC and OFDM. STBC is responsible for increasing communication reliability by sending multiple signal copies via multiple antennas. Then, when increasing the number of antennas, the probability that all signal replicas are affected by deep fading is extremely low. On the other hand, OFDM enables broadband data transmission across multiple narrowband subchannels (which is essential for MIMO transmission), also known as subcarriers. By transmitting data through orthogonal subcarriers, OFDM mitigates intersymbol interference (ISI).

Fig. 3.2.1 presents a diagram of the considered MIMO-OFDM scheme. In the input data stream block, a sequence of bits is mapped into an M-QAM constellation. The transmitting Space Time Block Coder (STBC) converts the stream of QAM symbols, using a code matrix, to construct a transmitting matrix $\mathbf{X}[k] \in \mathbb{C}^{M_T\times P}$ where M_T represents the number of transmitting antennas and P the matrix code length. This procedure is repeated until the K OFDM subcarriers are filled. After the IFFT of the OFDM modulator, a cyclic prefix (CP) is added to mitigate OFDM symbol interference. In addition, at a specified time interval, the OFDM block channel state information reference signal (CSIRS) is sent to channel estimation at the receiver (Rx). The CSIRS signal is a pseudo-random sequence generated from the Zadoff-Chu (ZC) sequence (FIGUEIREDO et al., 2018).

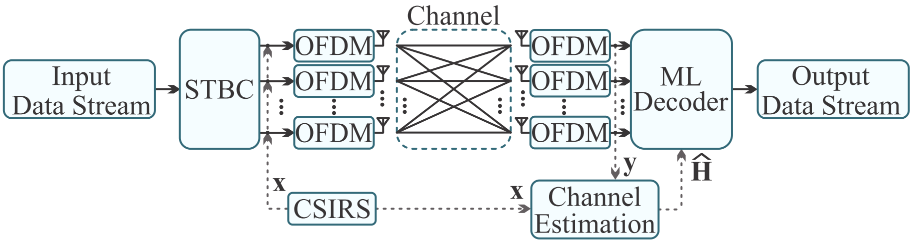

Figure 3.2.1 – STBC configuration for multiple-input multiple-output orthogonal frequency division multiplexing (STBC MIMO-OFDM).

Considering a time invariant channel in an MIMO-OFDM block, the received symbols, in the frequency domain, can be written as:

$$\mathbf{Y}[k] = \mathbf{H}[k]^T \mathbf{X}[k] + \mathbf{Z}[k] \ \in \mathbb{C}^{M_R \times P}, \tag{3.1}$$

where $\mathbf{Z}[k] \in \mathbb{C}^{M_R \times P}$ is the AWGN noise at the M_R receiving antennas, $\mathbf{H}[k] \in \mathbb{C}^{M_T \times M_R}$ is the frequency domain channel matrix, and $k \in [1, 2, \cdots K]^T$.

At Rx, the cyclic prefix is removed, and in each OFDM demodulator block, FFT is performed to convert the received signal to the frequency domain. Then, the received CSIRS and the CSIRS without channel interference are used to estimate the channel per subcarrier $\widehat{\mathbf{H}}[k] \in \mathbb{C}^{M_T \times M_R}$. The maximum likelihood (ML) decoder, with the estimated channel $\widehat{\mathbf{H}}[k]$, decodes the STBC matrices into QAM symbols to posterior demmaping into bits at the output data stream block.

3.3 MMSE CHANNEL ESTIMATION

The MMSE algorithm computes the channel estimation $\widehat{\mathbf{H}}_{\text{MMSE}}[k]$ as follows:

$$\widehat{\mathbf{H}}_{\text{MMSE}}[k] = \left(\frac{\mathbf{X}[k]\mathbf{X}[k]^H}{M_R \sigma_x^2} + \frac{\mathbf{I}_{M_T}}{M_R \sigma_h^2} \right)^{-1} \frac{\mathbf{X}[k]\mathbf{Y}[k]^H}{M_R \sigma_x^2}, \tag{3.2}$$

in which σ_x^2 and σ_h^2 are the variances of $\mathbf{X}[k]$ and $\mathbf{H}[k]$, respectively. As the MMSE channel estimation relies on CSIRS, I transmitted CSIRS MIMO-OFDM blocks need to be stored to compute (3.2).

The FFT-channel filtering (also known as smooth filtering) technique has been derived to improve the performance of the channel estimation, by eliminating the effect of noise outside the maximum channel delay. Taking the IFFT of the channel estimate for each component of $\widehat{\mathbf{H}}_{\text{MMSE}}[k]$:

$$\text{IFFT}\left\{ \widehat{h}_{m_T,m_R}[k] \right\} = \widehat{h}_{m_T,m_R}[n] + z_{m_T,m_R}[n], \tag{3.3}$$

where n denotes the time index, $\widehat{h}_{m_T,m_R}[n]$ is the estimated channel impulse response of the (m_T, m_R) component of $\widehat{\mathbf{H}}_{\text{MMSE}}[n]$, $m_T \in [1, 2, \cdots, M_T]$, and $m_R \in [1, 2, \cdots, M_R]$.

Ignoring the coefficients $\hat{h}[n]$ that contain only noise, let us define the coefficients for the maximum channel delay L as

$$\widetilde{h}_{m_T,m_R}[n] = \begin{cases} \widehat{h}_{m_T,m_R}[n] + z_{m_T,m_R}[n], & \text{if } n \leq L-1 \\ 0, & \text{if } n > L-1, \end{cases} \tag{3.4}$$

and transform the remaining L elements back to the frequency domain as follows:

$$\widetilde{h}_{m_T,m_R}[k] = \mathrm{FFT}\left\{\widetilde{h}_{m_T,m_R}[n]\right\}, \tag{3.5}$$

where $\widetilde{h}_{m_T,m_R}[k]$ is the (m_T, m_R) component of $\widetilde{\mathbf{H}}[k]$.

Note that the maximum channel delay L must be known in advance. Also note that smooth filtering method improves the performance of channel estimation. Figure 3.3.1 illustrates the MMSE estimator and smoothing filter.

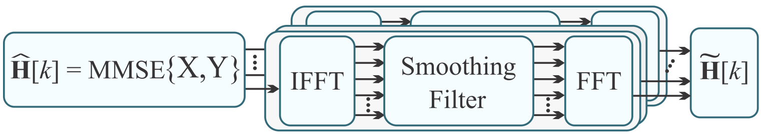

Figure 3.3.1 – MMSE channel estimation model of the k-th subcarrier.

3.4 PROPOSED PCA-BASED CHANNEL ESTIMATION

Least squares (LS) channel estimation is widely used in OFDM systems and has low computational complexity. This method requires CSIRS to obtain the channel coefficients. The LS channel estimation is given by

$$\widehat{\mathbf{H}}_{\mathrm{LS}}[k] = \mathbf{X}[k]\mathbf{Y}[k]^H. \tag{3.6}$$

Since the LS channel estimation is outperformed by the MMSE channel estimation approach, here we propose a PCA-based method for improving the LS channel estimation, as shown in Fig. 3.4.1.

Figure 3.4.1 – Proposed PCA channel estimation model of the k-th subcarrier.

The PCA is a method of denoising or filtering since noise is usually orthogonal to the signal. Therefore, we could use PCA denoising instead of performing smooth filtering, obtaining a performance similar to that of the MMSE. However, the computational complexities of both approaches would be the same.

Exploring the case where the IFFT components are set to zero when $n > L-1$, we place the PCA algorithm to remove the last portion of the noise in the $n \leq L-1$ elements. In other words,

$$\bar{h}_{m_T,m_R}[n] = \text{PCA}\left\{\widetilde{h}_{m_T,m_R}[n,i]\right\}, \tag{3.7}$$

where i is the number of stored channel realizations to perform the PCA denoising, and

$$\bar{h}_{m_T,m_R}[k] = \text{FFT}\left\{\bar{h}_{m_T,m_R}[n]\right\}, \tag{3.8}$$

is the final least squares principal component analysis (LSPCA) channel estimation of the (m_T, m_R) component of $\overline{\mathbf{H}}[k]$.

3.5 COMPUTATIONAL COMPLEXITIES

In this section, we evaluate the computational complexities of the MMSE and PCA algorithms mentioned above. Since these algorithms exhibit basic operations on complex matrices, such as multiplication, inversion and more complex transformations, such as the single-value decomposition (SVD), it is crucial to evaluate the computational costs involved in these calculations. The results can be summarized as follows:

- *Multiplications*: Considering $\mathbf{A} \in \mathbb{C}^{M\times N}$, and $\mathbf{B} \in \mathbb{C}^{N\times P}$, we have $4nmp$ multiplications and $(3n-1)mp$ additions. If we consider $m = n = p$, we clearly end up with an $O(n^3)$ asymptotic complexity.
- *Inversions*: A low complexity matrix inversion method for MIMO communications systems is proposed in (YU et al., 2015). The SDF-SGR based algorithm, for a complex square matrix $\mathbf{A} \in \mathbb{C}^{M\times M}$, contains $8n^3 + 4n^2 + 3n$ multiplications and $\frac{25}{3}n^3 - 4n^2 - \frac{1}{3}n$ additions, implying an $O(n^3)$ asymptotic complexity.
- *SVD*: SVD algorithms have $O(n^3)$ asymptotic complexity for an $n \times n$ input matrix.

From MMSE (3.2), we can notice that the algorithm complexity essentially lies in the computation of very expensive computational cost operations, such as matrix inversion and multiplication. Thus, the asymptotic complexity of this method is given by $O(n^3)$. Adjusting the dimension of the X^TX to match n with M_T dimension, we have that the asymptotic complexity $O(n^3)$ is then related to $O(M_T^3)$.

Since the SVD input matrix is $\widetilde{h}_{m_T,m_R}[n,i]$, where n is the n-th channel delay and i is the i-th buffered coefficients, i.e., constant size, the SVD complexity is negligible for asymptotic complexity. However these computations are performed for each independent single-input single-output (SISO)-channel in the MIMO-Channel $M_T \times M_R$ channel matrix $\mathbf{H}$. Therefore, the asymptotic complexity is given by $O(M_T \times M_R)$, i.e., $O(n^2)$. Thus the asymptotic complexity of this estimation method is given by the order of transmitting and receiving antennas.

Fig. 3.5.1 presents the evolution of the computational complexity of the MMSE (blue curve) and of the proposed LSPCA (red curve) as a function of the number N of antennas. As the MMSE and LSPCA computational complexities are $O(N^3)$ and $O(N^2)$, respectively, the MMSE computational complexity is always N times higher than for the LSPCA. Although for MIMO schemes with $N = 8$ antennas the MMSE could be implemented with 512 multiplications, when increasing the number of antennas to $N = 32$ (massive multiple-input multiple-output (mMIMO)), the computational complexity explodes to 32,768 multiplications, becoming prohibitive. On the other hand, the LSPCA complexity for N=32 antennas consists of only 1,024 multiplications. This clearly shows that the proposed scheme is much better suited for massive-MIMO systems.

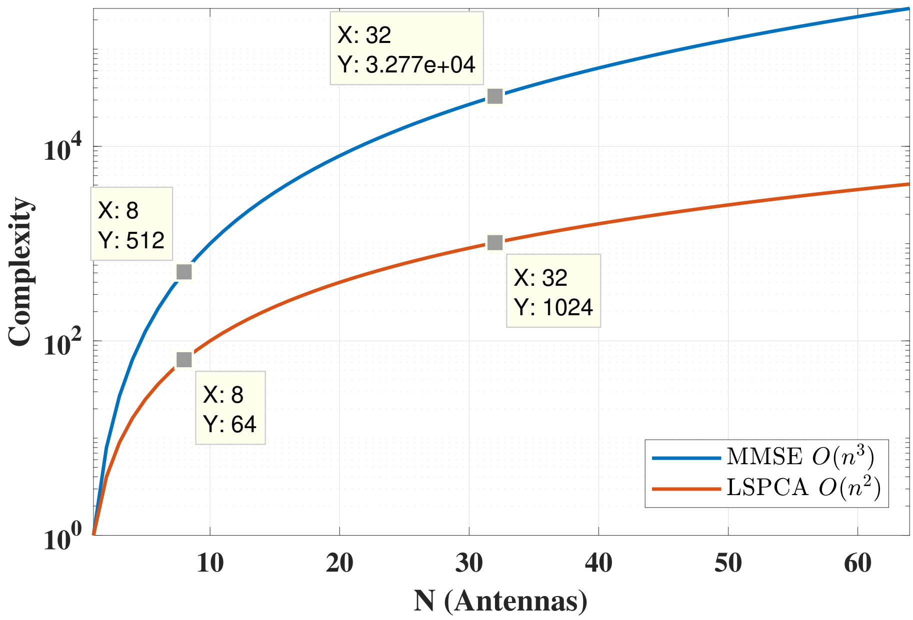

Figure 3.5.1 – MMSE and LSPCA asymptotic computational complexities. The MMSE and LSPCA computational complexities are shown in blue and red curves, respectively.

3.6 RESULTS

In order to represent more practical scenarios, we set the simulation system with a 3GPP TS 38.211 specification (ETSI, 2022a) for 5G Physical channels and modulation. The subcarrier spacing (Δf) scales from 30 kHz. The number of active subcarriers is 1024, and the CSIRS sample rate (when applicable) is 1/24 with the conventional block-based

CSIRS scheme (MEI et al., 2021). We perform simulations in the extremes of doppler shift to demonstrate the robustness of the proposed approach.

As the proposed transmitter (Tx) has eight antennas, the STBC encodes the received symbol sequence in intervals of eight symbols. It means that eight 4-QAM symbols are encoded into eight sequences composed of eight-time samples. In the Tx OFDM block, the STBC sequences are converted to the time domain for transmission, using 1,024 subcarriers. After sending 23 OFDM symbols per antenna, the OFDM block input is switched to send channel state information reference signal (CSIRS). To avoid OFDM symbol interference, a CP of duration L corresponding to 120% of the channel delay spread is appended to each OFDM symbol. In the process of channel propagation, the transmitted symbol will suffer from multipath fading and additive white Gaussian noise (AWGN). The channel environment will affect the correct signal reception. At the receiver (Rx), the serial OFDM symbols are transformed into parallel form in the serial-to-parallel (S/P) block. The CP is then removed from the parallel OFDM symbols. After removing the CP, the time-domain received OFDM symbols are transformed into the frequency domain via FFT.

The radio channel realizations are created using the "3GPP TR 38.901 report on 5G: Study on channel model for frequencies from 0.5 GHz to 100 GHz" (ETSI, 2022b). The 3GPP channel models (ETSI, 2022b) are applicable for frequency bands in the range from 0.5 GHz to 100 GHz. From Tapped Delay Line (TDL) models in (ETSI, 2022b), TDL-B is selected from Table 7.7.2-2 for the channel model simulated in this work.

Simulation results are shown in Fig. 3.6.1 by setting channel to be quasistatic, i.e., Doppler $f_d = 0.5$ Hz and Fig. 3.6.2 by setting channel to have Doppler $f_d = 10$ Hz both using 20 realizations to perform channel estimation for the following estimators: LSPCA $\lambda_{max} = 3$ performing PCA with 3 principal components, LSPCA $\lambda_{max} = 5$ performing PCA with 5 principal components and MMSE. Additional curves of Theoretical BER for 8x8 diversity gain and perfect channel knowledge are plotted as reference.

Fig. 3.6.1 presents results for a quasi-static channel (i.e., $f_d = 0.5$ Hz). Although the MMSE reached the perfect channel estimation performance, the LSPCA with $\lambda_{max} = 5$ and $\lambda_{max} = 3$ achieved similar results but with much lower computational complexity.

For a more realistic scenario, considering a dynamic channel with a Doppler frequency of 10 Hz, Fig. 3.6.2 illustrates that the proposed algorithm presents superior performance when compared with the MMSE. For example, for a BER $= 10^{-4}$, both LSPCA with $\lambda_{max} = 3$ and $\lambda_{max} = 5$ achieved a gain of 0.4 dB when compared with the MMSE.

Fig. 3.6.3 presents simulation results for a range of Doppler frequency f_d varying from 0 Hz (static channel) to 40 Hz (dynamic channel), in steps of 5 Hz and with a fixed

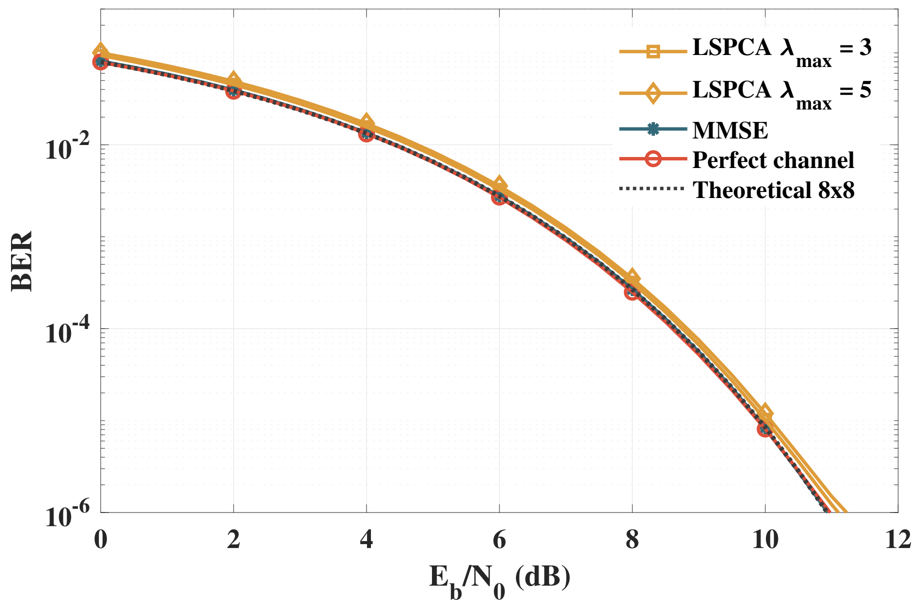

Figure 3.6.1 – Simulation results for the MIMO-OFDM system with Doppler $f_d = 0.5$ Hz using the following estimators: LSPCA $\lambda_{max} = 3$, LSPCA $\lambda_{max} = 5$ and MMSE. Additional curves of Theoretical BER for 8x8 diversity gain and perfect channel knowledge are plotted as reference.

pilot ratio. The simulation stops at 40 Hz, since the LSPCA and MMSE channel estimation results tend to the BER upper limit of 5×10^{-1}. For $f_d > 5$ Hz, the proposed LSPCA presented a significantly better performance, surpassing the MMSE in almost one order of magnitude for $f_d = 20$ Hz. This result shows that the proposed approach is more robust to channel variations than the MMSE, which is only optimal for static channels under jointly Gaussian distributed random variables (NEUMANN; WIESE; UTSCHICK, 2018).

3.7 CONCLUSIONS

This paper presents a PCA-based filtering approach to improve the efficiency of MIMO-OFDM channel estimation. The proposed approach outperformed the MMSE channel estimation regarding BER versus $\mathrm{E_b/N_0}$ when operating with Doppler frequencies higher than 10 Hz, keeping the same pilot ratio. For Doppler frequencies lower than 10 Hz, both PCA-based and MMSE channel estimation presented similar results, but the PCA-based channel estimation was evaluated with much lower computational complexity ($O(N^3)$ for the MMSE and only $O(N^2)$ for the LSPCA). With the computational complexity defined in terms of transmitting and receiving antennas, it is evident that the proposed work has much more potential to work with mMIMO architectures. In future works, this method could be validated for massive MIMO and also for nonlinear PCA using neural network denoising autoencoders to encompass nonlinear channel estimation.

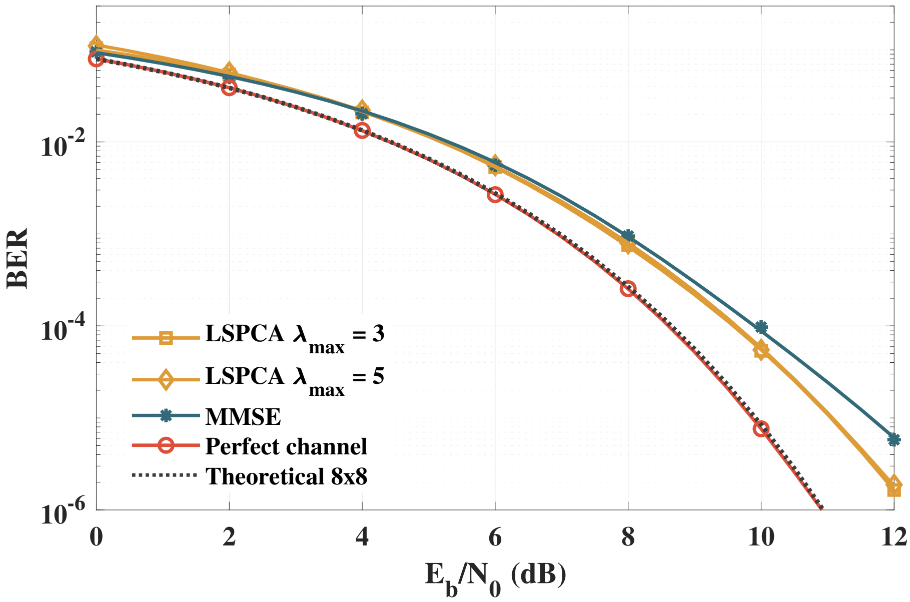

Figure 3.6.2 – Simulation results for the MIMO-OFDM system with Doppler $f_d = 10$ Hz using the following estimators: LSPCA $\lambda_{max} = 3$, LSPCA $\lambda_{max} = 5$ and MMSE. Additional curves of Theoretical BER for 8x8 diversity gain and perfect channel knowledge are plotted as reference.

REFERENCES

ABDI, H.; WILLIAMS, L. J. Principal component analysis. **WIREs Computational Statistics**, v. 2, n. 4, p. 433–459, July 2010. Cited on page 83.

ALI, M. S. et al. On improved DFT-based low-complexity channel estimation algorithms for LTE-based uplink NB-IoT systems. **Computer Communications**, v. 149, p. 214–224, Jan. 2020. Cited on page 83.

BALEVI, E.; DOSHI, A.; ANDREWS, J. G. Massive MIMO channel estimation with an untrained deep neural network. **IEEE Trans. Wireless Commun.**, v. 19, n. 3, p. 2079–2090, Mar. 2020. Cited on pages 83, 95.

DIALLO, M.; RABINEAU, R.; CARIOU, L. Robust DCT based channel estimation for MIMO-OFDM system. *In*: 2009 IEEE Wireless Communications and Networking Conference. [S.l.: s.n.], Apr. 2009. P. 1–5. Cited on page 83.

ENRICONI, M. P. et al. Phase transmittance RBF neural network beamforming for static and dynamic channels. **IEEE Antennas Wireless Propag. Lett.**, v. 19, n. 2, p. 243–247, Feb. 2020. Cited on pages 40, 83, 95–97, 155.

ETSI. 5G; NR; Physical channels and modulation (3GPP TS 38.211 version 17.2.0 Release 17). **3GPP**, 2022a. Cited on pages 57, 88.

ETSI. 5G; Study on channel model for frequencies from 0.5 to 100 GHz (3GPP TR 38.901 version 17.1.0 Release 17). **3GPP**, 2022b. Cited on pages 57, 58, 89.

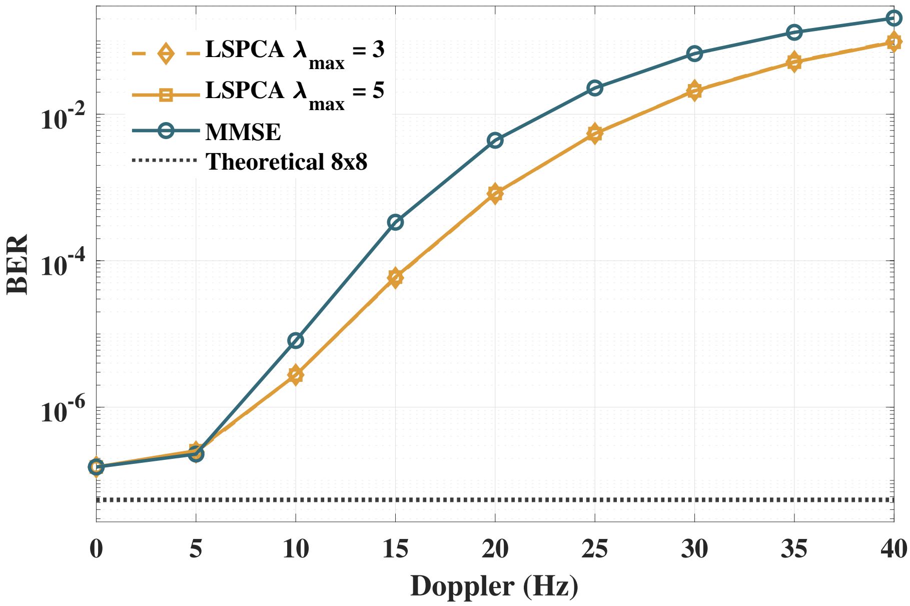

Figure 3.6.3 – Simulation results for the MIMO-OFDM system for a range of Doppler f_d varying from 0 Hz to 40 Hz, in steps of 5 Hz using the following estimators: LSPCA $\lambda_{max} = 3$, LSPCA $\lambda_{max} = 5$ and MMSE. An additional curve of Theoretical BER for 8x8 diversity gain is plotted as reference.

FIGUEIREDO, F. A. P. de et al. Channel estimation for massive MIMO TDD systems assuming pilot contamination and flat fading. **Eurasip Journal on Wireless Communications and Networking**, v. 2018, 1 2018. Cited on page 84.

KARA, F.; KAYA, H.; YANIKOMEROGLU, H. Power-time channel diversity (PTCD): A novel resource-efficient diversity technique for 6G and beyond. **IEEE Wireless Communications Letters**, p. 1–5, 2022. Cited on page 83.

MAYER, K. S.; SOARES, J. A.; ARANTES, D. S. Complex MIMO RBF Neural Networks for Transmitter Beamforming over Nonlinear Channels. **Sensors**, v. 20, n. 2, p. 1–15, Jan. 2020. DOI: `10.3390/s20020378`. Cited on pages 31, 40, 41, 51, 54, 79, 83, 95, 96, 109, 127.

MAYER, K. S. et al. Blind Fuzzy Adaptation Step Control for a Concurrent Neural Network Equalizer. **Wireless Communications and Mobile Computing**, v. 2019, n. 1, p. 9082362, 2019c. DOI: `https://doi.org/10.1155/2019/9082362`. Cited on pages 40, 83, 95, 96, 109, 127, 161.

MAYER, K. S. et al. Deep Phase-Transmittance RBF Neural Network for Beamforming With Multiple Users. **IEEE Wireless Communications Letters**, v. 11, n. 7, p. 1498–1502, 2022. DOI: `10.1109/LWC.2022.3177162`. Cited on pages 30, 83, 95–97, 109, 127, 142, 145, 155, 156, 161–163.

MEI, K. et al. A low complexity learning-based channel estimation for OFDM systems with online training. **IEEE Transactions on Communications**, v. 69, n. 10, p. 6722–6733, 2021. Cited on pages 57, 89.

NEUMANN, D.; WIESE, T.; UTSCHICK, W. Learning the MMSE channel estimator. **IEEE Transactions on Signal Processing**, v. 66, n. 11, p. 2905–2917, June 2018. Cited on pages 83, 90.

SHARIATI, N. et al. Low-complexity channel estimation in large-scale MIMO using polynomial expansion. *In*: 2013 IEEE 24th Annual International Symposium on Personal, Indoor, and Mobile Radio Communications (PIMRC). [S.l.: s.n.], Sept. 2013. P. 1157–1162. Cited on page 83.

SOARES, J. A. et al. Complex-valued phase transmittance RBF neural networks for massive MIMO-OFDM receivers. **Sensors**, v. 21, n. 24, p. 1–31, Dec. 2021a. ISSN 1424-8220. DOI: 10.3390/s21248200. Available from: <https://www.mdpi.com/1424-8220/21/24/8200>. Cited on pages 83, 95–99, 109, 127, 142–145, 148.

YIN, X. et al. Modeling city-canyon pedestrian radio channels based on passive sounding in in-service networks. **IEEE Transactions on Vehicular Technology**, v. 65, n. 10, p. 7931–7943, Oct. 2016. Cited on page 83.

YU, D. et al. Low complexity complex matrix inversion method for MIMO communication systems. *In*: 2015 International Conference on Wireless Communications & Signal Processing (WCSP). [S.l.: s.n.], Oct. 2015. P. 1–5. Cited on page 87.

ZHANG, S.-Q.; GAO, W.; ZHOU, Z.-H. Towards understanding theoretical advantages of complex-reaction networks. **Neural Netw.**, v. 151, p. 80–93, 2022. Cited on pages 83, 95, 109, 127.

Chapter 4

Semi-supervised ML-based Joint Channel Estimation and Decoding for m-MIMO with Gaussian Inference Learning

Authors: Jonathan Aguiar Soares, Kayol Soares Mayer, and Dalton Soares Arantes

Abstract

This letter proposes the use of quasi-orthogonal space-time block codes (QOSTBC) to enhance link quality and reliability in massive multiple-input multiple-output (m-MIMO) systems subject to independent fading in dynamic channels. It has been shown, however, that the computational complexity of classical decoding algorithms, such as maximum likelihood (ML), can hinder the adoption of QOSTBC codes in systems with many antennas and high-order modulation schemes. complex-valued neural networks (CVNNs) offer a promising alternative for joint decoding and channel estimation with competitive computational complexity. This work presents an extension of our previously proposed CVNN with supervised training, which incorporates two semi-supervised learning techniques: hard inference learning (HIL) and Gaussian inference learning (GIL). By leveraging non-pilot-aided data, HIL and GIL enable the CVNNs to self-learn from useful information, increasing their tracking ability and robustness in dynamic channels.

Keywords: Massive-MIMO, MIMO-OFDM, inference learning, complex-valued neural networks, machine learning.

This Chapter is a replica of the following manuscript: Jonathan Aguiar Soares, Kayol Soares Mayer, and Dalton Soares Arantes, "Semi-supervised ML-based Joint Channel Estimation and Decoding for m-MIMO with Gaussian Inference Learning" in IEEE Wireless Communications Letters, vol. 12, no. 12, pp. 2123-2127, Dec. 2023, doi: 10.1109/LWC.2023.3309479.

4.1 INTRODUCTION

Within the context of m-MIMO schemes, spatial diversity assumes a critical role when the transmitter (Tx) lacks channel knowledge. In these schemes, space-time block codes (STBC) are employed to transmit orthogonal or quasi-orthogonal signals via independent fading paths in multiple-input multiple-output (MIMO) links (MORSALI et al., 2019; FAZAL-E-ASIM et al., 2022). Additionally, orthogonal frequency-division multiplexing (OFDM) is usually implemented with STBC to avoid channel equalization and to multiplex users into closely spaced subchannels (CHEN et al., 2017; CHEN; JIANG, 2019; SOARES et al., 2021a).

In m-MIMO, channel estimation, decoding, and beamforming can be efficiently implemented with neural networks (NNs), handling nonlinearities from radiofrequency (RF) amplifiers, spatial and stochastic variations of dynamic channels, and even noise in millimeter-wave (mmWave) systems (HE et al., 2018; MAYER; SOARES; ARANTES, 2020; MAYER et al., 2022; SOARES et al., 2021a). Among these impairments, channel tracking in dynamic scenarios shows promise when using NNs. This is due to their universal approximation capabilities, which can help to overcome some of the challenging issues presented by classical algorithms, such as noise enhancement. Besides that, the class of CVNNs has been demonstrating an excellent potential for wireless communications (MAYER; SOARES; ARANTES, 2020; MAYER et al., 2022; SOARES et al., 2021a; MAYER et al., 2019c; ENRICONI et al., 2020), since their intrinsic complex structures can naturally manipulate complex-valued data (ZHANG et al., 2021a; ALAPURANEN; SCHROEDER, 2021). CVNNs circumvent phase-recovery issues of real-valued neural networks (RVNNs), increasing functionality, improving performance, and reducing the training time (HIROSE; YOSHIDA, 2012a; ZHANG; GAO; ZHOU, 2022; ZHAO; HUANG, 2023; XU et al., 2022; LEE; HASEGAWA; GAO, 2022; VOIGTLAENDER, 2023).

Recently, several NN-based algorithms have been successfully employed for m-MIMO channel estimation and decoding (SOARES et al., 2021a; BALEVI; DOSHI; ANDREWS, 2020; ZHENG; LAU, 2021; GAO et al., 2022; ELBIR; COLERI, 2022; JIA; CHENG; ZHANG, 2019; YANG et al., 2020; KUMAR; SINGH; MAHAPATRA, 2022). Balevi *et al.* (BALEVI; DOSHI; ANDREWS, 2020) employed real-valued deep learning (DL) and least-squares (LS) algorithms for channel estimation of multi-cell interference-limited m-MIMO systems. Zheng and Lau (ZHENG; LAU, 2021) proposed a real-valued deep neural network (DNN) for mmWave m-MIMO channel estimation, based on real-time received pilot samples and without channel knowledge. Gao *et al.* (GAO et al., 2022) implemented real-valued DL with an integrated attention mechanism to improve channel estimation at the cost of a small complexity overhead. Elbir and Coleri (ELBIR; COLERI, 2022) adopted a federated learning approach to train a real-valued convolutional neural network (CNN) for channel estimation of both conventional and reconfigurable intelligent surfaces (RISs). Jia *et al.* (JIA; CHENG; ZHANG, 2019) proposed a partial learning scheme to train RVNNs for m-MIMO decoding, achieving a bit error rate (BER) lower than for ML detection. Yang *et al.* (YANG et al., 2020) adopted real-valued graph neural networks (GNNs) for channel estimation under high mobility scenarios. Kumar and Singh (KUMAR; SINGH; MAHAPATRA, 2022) implemented a real-valued DNN decoder resorting to the uplink Rayleigh and correlated channels perfectly known at the receiver.

Some studies have addressed the issue of joint channel estimation and decoding for m-MIMO communications in the literature (WU et al., 2016; VERENZUELA et al., 2020; SANOOPKUMAR; MUNEER; SAMEER, 2022). However, when considering m-MIMO-OFDM with QOSTBC, the topic has received scarce attention. This lack of focus is possibly due to the challenges of creating quasi-orthogonal matrices and formulating decoding algorithms for m-MIMO and M-ary quadrature amplitude modulation (M-QAM). To the best of our knowledge, the phase-transmittance radial basis function (PT-RBF) neural network, proposed in (SOARES et al., 2021a), is the only work that addresses this issue.

This letter proposes an extension of the work of Soares *et al.* (SOARES et al., 2021a), incorporating semi-supervised training with the novel HIL and GIL approaches. These methods enable CVNNs to continue learning during the inference phase (i.e., without pilot data). After the pilot-aided training step, HIL or GIL is activated, controlling the error magnitude used to update the CVNN. Additionally, this letter extends the results to other well-known CVNNs, including the complex-valued feedforward neural network (CVFNN) (DONG; HUANG, 2021; KIM; ADALI, 2002), the split complex feedforward neural network (SCFNN) (SCARDAPANE et al., 2020; KIM; ADALI, 2002), and the complex-valued RBF (C-RBF) (ENRICONI et al., 2020). Robust results are depicted in terms of Doppler shifts on a dynamic 5G channel.

4.2 ML-BASED JOINT CHANNEL ESTIMATION AND DECODING FOR MASSIVE MIMO

4.2.1 Complex-valued Neural Networks

Complex-valued Neural Networks (CVNNs) can directly operate as powerful nonlinear filters in the complex domain, surpassing the results of classical RVNNs (HIROSE; YOSHIDA, 2012a). In recent works, CVNNs have been successfully employed in communication systems for channel equalization (MAYER et al., 2019c), beamforming (MAYER; SOARES; ARANTES, 2020; MAYER et al., 2022; ENRICONI et al., 2020), channel estimation, and decoding (SOARES et al., 2021a). For example, in the case of joint channel estimation and decoding, CVNNs not only offer superior performance, but also present lower computational complexity compared to classical algorithms, as outlined in references (SOARES et al., 2021a; MAYER, 2022).

CVNNs are mainly divided into shallow (e.g., C-RBF and FC-RBF) and deep (e.g., CVFNN, SCFNN, and PT-RBF) neural networks. The well-known CVFNN (DONG; HUANG, 2021; KIM; ADALI, 2002) is similar to the classical real-valued DL model (SCHMIDHUBER, 2015), but it distinctively operates with complex values for various elements such as input, output, synaptic weights, bias, and activation functions. The SCFNN is a particular case of CVFNNs, in which the activation function independently processes its real and imaginary inputs (SCARDAPANE et al., 2020; KIM; ADALI, 2002). The C-RBF is a natural extension of the radial basis function (RBF) neural network into the complex domain. In this domain, outputs, center vectors, and synaptic weights are all complex-valued (ENRICONI et al., 2020; MAYER et al., 2022). Designed to circumvent phase issues intrinsically related to the phase vanishing of C-RBF Gaussian kernels, the PT-RBF has a Gaussian activation function originally designed in a split-complex architecture. The split-complex activation function takes the real and imaginary components of the neuron input separately, keeping the phase information at the output (MAYER et al., 2022).

4.2.2 System Architecture

Fig. 4.2.1 presents the architecture of the massive MIMO-OFDM system incorporating QOSTBC spatial diversity. Here, N_{tx} and N_{rx} represent the number of transmitting and receiving antennas, respectively. On the Tx side, the QAM symbols q are parallelized into the vector $\mathbf{q}[k] \in \mathbb{C}^{N_s}$ in the serial to parallel (S/P) block, where N_s is the number of QAM symbols to be encoded, and k is the subcarrier index. Subsequently, $\mathbf{q}[k]$ is encoded spatially and temporally via the QOSTBC encoding block (see Eq. 8 in (SOARES et al., 2021a)) to create the QOSTBC matrix $\mathbf{S}[k] \in \mathbb{C}^{N_{tp} \times N_{tx}}$, where N_{tp} is the number of time encoded symbols. Next, each column $\mathbf{s}_{n_{tx}}[k] \in \mathbb{C}^{N_{tp}}$ of $\mathbf{S}[k]$ feeds into the OFDM modulator blocks of each transmitting antenna. In each OFDM modulator block, the input signal is first parallelized by an S/P block, mapping $\mathbb{C} \mapsto \mathbb{C}^K$, where K is the number of subcarriers. Then, an inverse fast Fourier transform (IFFT) block converts data from the frequency domain to the time domain. In the sequel, a cyclic prefix (CP) of length N_{cp} is inserted at the beginning of each IFFT output to mitigate the inter-symbol interference (ISI) (YE; LI; JUANG, 2018). Finally, the resultant signal is serialized (i.e., $\mathbb{C}^{K+N_{cp}} \mapsto \mathbb{C}$) in the parallel

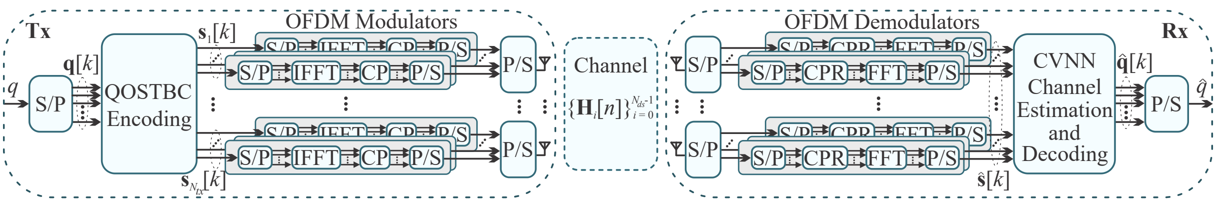

Figure 4.2.1 – Massive MIMO-OFDM system with QOSTBC.

to serial (P/S) block. As each antenna must transmit the OFDM symbols in sequence, another P/S block serializes the income data from the N_{tp}-OFDM modulators, to convey one at a time.

Considering a sample-spaced multipath channel with N_{ds} samples $\{\mathbf{H}_i[n]\}_{i=0}^{N_{ds}-1} \in \mathbb{C}^{N_{rx}\times N_{tx}}$, the received signal is

$$\mathbf{y}[n] = \sum_{i=0}^{N_{ds}-1} \mathbf{H}_i[n]\mathbf{x}[n-i] + \mathbf{w}[n], \tag{4.1}$$

where n is the discrete-time index, $\mathbf{x}[n] \in \mathbb{C}^{N_{tx}}$ is the vector of transmitted data, and $\mathbf{w}[n] \sim \mathcal{CN}(0,\, \sigma_w^2) \in \mathbb{C}^{N_{rx}}$ is the vector of complex additive white Gaussian noise (AWGN) at the receiver, with zero mean and variance σ_w^2.

On the receiver side, the signal received at each antenna is parallelized by an S/P block to feed N_{tp}-OFDM demodulators. In an OFDM demodulator, the input signal is firstly parallelized by an S/P block, mapping $\mathbb{C} \mapsto \mathbb{C}^{K+N_{cp}}$. Subsequently, the cyclic prefix is removed in the CPR block, and the resultant signal of dimension $\mathbb{C}^K$ is converted to the frequency domain by a fast Fourier transform (FFT) block. The FFT output is then serialized by a P/S block, creating the OFDM demodulator output. Consequently, the input to the CVNN channel estimation and decoding block is the received QOSTBC vector $\hat{\mathbf{s}}[k] \in \mathbb{C}^{N_{tp}N_{rx}}$ for the k-th subcarrier. The CVNN output is the estimated vector $\hat{\mathbf{q}}[k] \in \mathbb{C}^{N_s}$, which is serialized by a P/S block to produce the estimated outputs $\hat{q}$. In order to improve the decoded CVNN output, we also adjust $\hat{\mathbf{q}}[k]$ to match the QAM constellation.

We have proposed this system architecture, based on CVNNs, to enable channel decoding of QOSTBC in m-MIMO-OFDM with high-order M-QAM. Therefore, differently from previous works limited to M-ary phase-shift keying (PSK), the work proposed here offers greater flexibility and competitive computational complexity, as already demonstrated by Soares et al. (SOARES et al., 2021a).

4.2.3 Training Model

An adequate training model is mandatory for supervised machine learning algorithms to achieve satisfactory performance. To train the CVNN block shown in Fig. 4.2.1, we have adopted the training model proposed in (SOARES et al., 2021a). In this scheme, part of the transmitted information comprises pilots known to the receiver. Utilizing these pilots, the CVNN can update its free parameters using a quadratic cost function

$$J[k] = \frac{1}{2}\|\mathbf{e}[k]\|_2^2 = \frac{1}{2}\|\mathbf{q}_p[k] - \hat{\mathbf{q}}[k]\|_2^2, \tag{4.2}$$

in which $\|\cdot\|_2$ is the Euclidean norm, $\mathbf{q}_p[k] \in \mathbb{C}^{N_s}$ is the vector of pilots, $\hat{\mathbf{q}}[k] \in \mathbb{C}^{N_s}$ is the estimated vector, and $\mathbf{e}[k] \in \mathbb{C}^{N_s}$ is the vector of estimation error.

Through this training model, the CVNN learns how the channel impacts each independent subcarrier and acquires the ability to decode QOSTBC vectors, regardless of the number of transmitting and receiving antennas.

4.2.4 Hard Inference Learning

Mobile wireless channels usually vary over time and frequency, affected by large- and small-scale fading (CHA; NOH, 2019). Due to this highly dynamic nature, channel estimation and tracking can be challenging. For instance, the training approach proposed in (SOARES et al., 2021a) can efficiently estimate the channel information in a given time but, as the channel is dynamic, the estimation error increases over time, degrading the decoding process.

In this context, our first proposition is a hard inference learning (HIL) technique, aimed at tracking channel variations over time. HIL is initiated once the supervised training phase concludes, allowing the CVNN to adjust its parameters based on the hard error estimation obtained from useful information (i.e., non-pilot-aided). Consequently, HIL bolsters the learning capabilities of the CVNN without diminishing the rate of useful information.

Firstly, in the HIL algorithm, the CVNN output vector (after mean and magnitude corrections, as in Section 4.2.2) is approximated to the reference constellation symbols as

$$\bar{\mathbf{q}}[k] = \mathcal{Q}\left\{\hat{\mathbf{q}}[k]\right\}, \tag{4.3}$$

where $\mathcal{Q}\{\cdot\}$ is the constellation quantizer, which is a complex-valued nearest neighbor operator. The vector $\bar{\mathbf{q}}[k] \in \mathbb{C}^{N_s}$ is the CVNN approximated output, a coarse estimation of $\mathbf{q}[k]$.

The HIL error vector, which is used to update the CVNN parameters, is then computed as

$$\bar{\mathbf{e}}[k] = \bar{\mathbf{q}}[k] - \hat{\mathbf{q}}[k]. \tag{4.4}$$

Despite its improved performance, this semi-supervised hard-decision learning scheme is susceptible to noise. If a decision is incorrect, it leads to error propagation, which can subsequently degrade the convergence of the CVNN. This is similar to what happens in turbo equalization with hard-decision feedback (ZHANG; ZAKHAROV; LI, 2018).

4.2.5 Gaussian Inference Learning

As an extension to HIL, this letter also introduces a more efficient scheme, the Gaussian inference learning (GIL), which is designed specifically for semi-supervised soft-decision learning. GIL enables CVNNs to learn from non-pilot-aided data with a reduced impact on error propagation during training. The GIL is designed as a heuristic that refines coarse error estimations based on knowledge of the error distribution. Assuming that CVNNs are able to mitigate most channel imperfections, only Gaussian noise will remain present at the output of the joint channel estimation and decoding. This noise can then be modeled as a Gaussian distribution around the reference symbols, with a variance that can be estimated. As a result, we can weigh the GIL error vector as

$$\tilde{\mathbf{e}}[k] = \left(\boldsymbol{\alpha}[k] \oslash \sqrt{\mathbf{P}_{\boldsymbol{\alpha}}[k]}\right) \odot \bar{\mathbf{e}}[k], \tag{4.5}$$

in which $\boldsymbol{\alpha}[k] \in \mathbb{R}^{N_s}$ is the GIL weight vector, and $\mathbf{P}_{\boldsymbol{\alpha}}[k] \in \mathbb{R}^{N_s}$ is its respective power vector used for normalization. The normalized vector $\boldsymbol{\alpha}[k] \oslash \sqrt{\mathbf{P}_{\boldsymbol{\alpha}}[k]}$ softly controls the amount of error passed to the CVNN cost function. The operator $\sqrt{\cdot}$ denotes the element-wise square root, and $\odot$ and $\oslash$ denote the Hadamard product and division, respectively.

The i-th component of the normalization power $\mathbf{P}_{\boldsymbol{\alpha}}[k]$ is

$$P_{\alpha_i}[k] = \begin{cases} \frac{1}{K}\sum\limits_{l=0}^{K-1} \alpha_i^2[k-l], & \forall\ k/K \in \mathbb{N}, \\ P_{\alpha_i}[k-1], & \forall\ k/K \notin \mathbb{N}, \end{cases} \tag{4.6}$$

where $\mathbb{N}$ is the set of natural numbers and $i \in [1,\, 2,\, \cdots,\, N_s]$. The i-th component of the vector $\boldsymbol{\alpha}[k]$ is

$$\alpha_i[k] = \exp\left[-\frac{1}{2}\frac{|\bar{e}_i[k]|^2}{\sigma_{e_i}^2[k]}\right], \tag{4.7}$$

in which $|\cdot|$ is the modulus function, and $\sigma_{e_i}^2[k]$ is the i-th component of the estimated error variance vector $\boldsymbol{\sigma}_e^2[k] \in \mathbb{R}^{N_s}$, given by

$$\sigma_{e_i}^2[k] = \begin{cases} \frac{1}{KN_f-1}\sum\limits_{l=0}^{KN_f-1} \bar{e}_i^2[k-l], & \forall\ k/K \in \mathbb{N}, \\ \sigma_{e_i}^2[k-1], & \forall\ k/K \notin \mathbb{N}, \end{cases} \tag{4.8}$$

where N_f is the number of MIMO-OFDM frames used to compute $\sigma_{e_i}^2[k]$.

To visualize the GIL weighting, we establish a fixed value for the GIL variance, $\sigma_{\alpha_i}^2 = 1/3$, in a 16-QAM modulation, as depicted in Fig. 4.2.2. It is notable that the closer the CVNN estimate is to a reference symbol (represented by a black cross), the closer the GIL weight is to one. This implies that almost all of the error information is conveyed to the CVNN update. Conversely, the further the CVNN estimate is from the reference symbols, the closer the GIL weight becomes to zero, subsequently reducing the impact of this estimation on the CVNN update.

Note that the computational complexities of HIL and GIL are insignificant when juxtaposed with channel estimation and decoding. It is because the most onerous operations, performed in (4.6) and (4.8), are only executed at intervals of K subcarriers, effectively distributing the complexity per subcarrier.

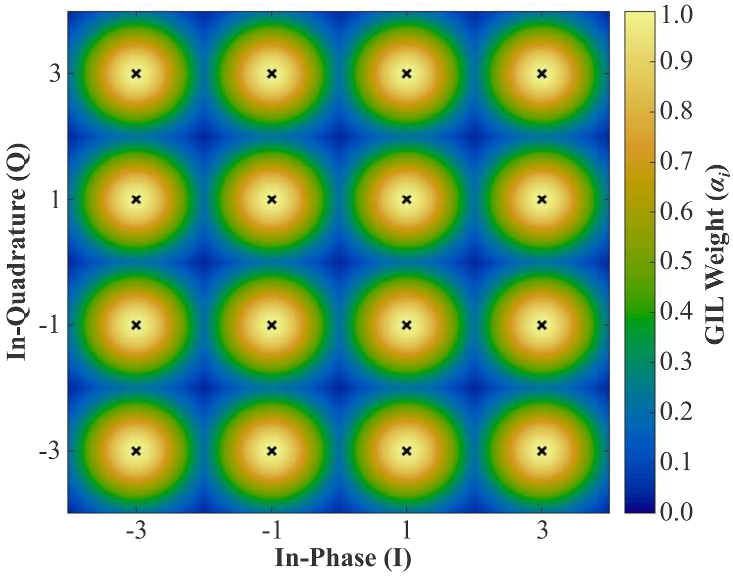

Figure 4.2.2 – Heat map of the GIL weight distribution for a 16-QAM modulation with $\sigma^2_{\alpha_i} = 1/3$. The black crosses regard the reference symbols.

4.3 RESULTS

In order to represent a practical scenario, we consider a simulation system with the 3GPP TS 38.211 specification for 5G physical channels and modulation (5G. . . , 2022). The OFDM is defined with 60-kHz subcarrier spacing, $K = 256$ active subcarriers, and a block-based pilot scheme. Symbols are modulated with 16-QAM and, for the massive MIMO setup, 32 antennas are employed both at the transmitter and receiver.

Based on the tapped delay line-A (TDL-A) from the 3GPP TR 38.901 5G channel models (5G. . . , 2022), the massive MIMO channel follows the TDLA from the 3GPP TR 38.104 5G radio base station transmission and reception (5G. . . , 2022). The TDLA is described with 12 taps, with varying delays from 0.0 ns to 290 ns and powers from -26.2 dB to 0 dB. A Rayleigh distribution is used to compute each sub-channel of $\{\mathbf{H}_i[n]\}_{i=0}^{N_{ds}-1}$ (see Table G.2.1.2-2 (5G. . . , 2022)). The Doppler frequency (f_D) is simulated in the range from 0 Hz to 200 Hz.

The CVNNs operate with 1024 inputs and 32 outputs. The inputs are taken from the OFDM demodulator outputs, one at a time, i.e., $\hat{\mathbf{s}}[k]$ for $k \in [1, 2, \ldots, 256]$. Each frame comprised of K subcarriers is dealt with as one training epoch. In the training phase, the desired output vector of the k-th subcarrier is $\mathbf{q}[k]$. Notwithstanding, a training upsampling of thirty times, with subcarrier shuffle, was employed to improve convergence. The CVFNN and SCFNN were constructed with two layers of neurons and arctanh$(\cdot)$ and tanh$(\cdot)$ activation functions in the hidden layer and linear activation functions in the output layer. The PT-RBF and C-RBF were built in shallow architectures. The CVNNs hyperparameters, summarized in Table 4.3.1, were empirically obtained by trial and error, for 0-Hz Doppler. The CVNNs adaptive steps are denoted by η_w, η_b, η_γ, and η_σ, and the

Table 4.3.1 – CVNNs optimized hyperparameters.

Algorithm	η_w	η_b	η_γ	η_σ	N_1	N_2
CVFNN	0.005	0.005	–	–	168	32
SCFNN	0.050	0.050	–	–	168	32
C-RBF	0.050	0.050	0.050	0.050	200	–
PT-RBF	0.050	0.050	0.030	0.050	200	–

(–) not applicable.

Table 4.3.2 – Adaptive step compensation factor (ρ) depending on f_D.

	Doppler frequency (f_D) [Hz]										
Algorithm	0	20	40	60	80	100	120	140	160	180	200
CVFNN (HIL)	1	1	5	–	–	–	–	–	–	–	–
CVFNN (GIL)	1	2	5	5	–	–	–	–	–	–	–
SCFNN (HIL)	1	1	6	6	–	–	–	–	–	–	–
SCFNN (GIL)	1	1	6	6	6	–	–	–	–	–	–
PT-RBF (HIL)	1	6	6	8	8	8	10	10	–	–	–
PT-RBF (GIL)	1	4	6	6	8	8	8	8	9	–	–
C-RBF (HIL)	1	6	6	6	6	8	8	8	10	–	–
C-RBF (GIL)	1	4	6	6	6	6	8	8	8	8	–

(–) The algorithm did not converge for the corresponding f_D.

number of neurons per layer are N_1 and N_2. However, depending on the Doppler frequency, it is necessary to increase the adaptive steps to keep the channel estimation on track. Thus, the adaptive steps of Table 4.3.1 are compensated by a factor ρ, depending on the Doppler effect, as depicted in Table 4.3.2.

Fig. 4.3.1 presents the inference results for the required bit energy to noise power spectral density ratio ($\mathrm{E_b/N_0}$) to achieve a target pre-forward error correction (pre-FEC) bit error rate (BER) of 2×10^{-2} (CASTRO et al., 2019) in dynamic channels. Considering the range of application around $\mathrm{E_b/N_0} = 25$ dB, the SCFNN and CVFNN presented quite similar results, operating up to approximately 40 Hz (HIL) and 50 Hz (GIL) of Doppler. On the other hand, the more robust CVNNs, the PT-RBF and C-RBF, presented satisfactory results up to 150 Hz. The best result was achieved with the C-RBF, for which the GIL extended its range of application up to 180 Hz. Compared to the C-RBF and PT-RBF, the CVFNN and SCFNN show poorer performance, primarily due to their susceptibility to noise, as discussed in (MAYER, 2022).

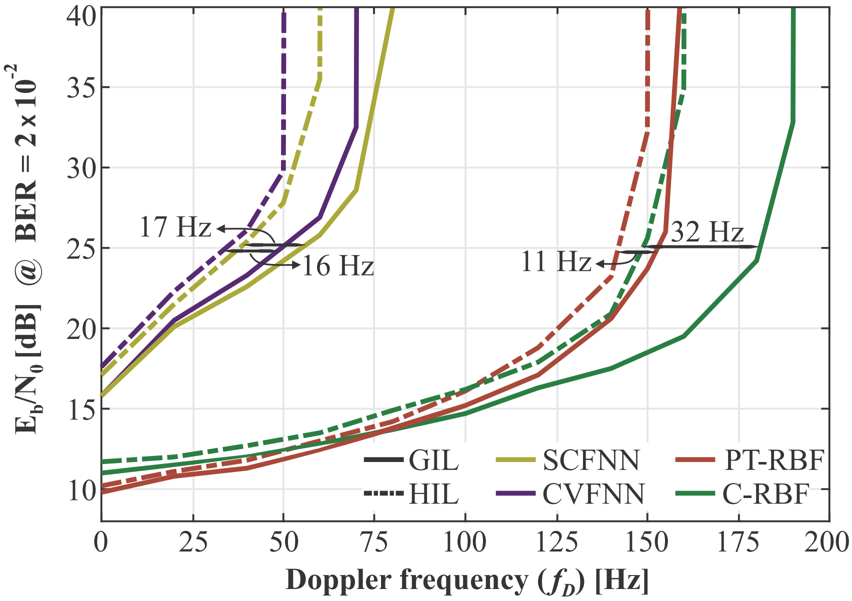

Figure 4.3.1 – Joint CVNN channel estimation and decoding performance with HIL and GIL, depending on the Doppler frequency f_D on the TDLA channel (5G scenario). Result of the required $\mathrm{E_b/N_0}$ to achieve a target pre-FEC BER $= 2 \times 10^{-2}$, i.e., before an advanced FEC decoder, as in low-density parity check (LDPC) and turbo codes. Dashed and solid lines correspond to HIL and GIL semi-supervised learning, respectively.

4.4 CONCLUSIONS

This letter introduces two semi-supervised learning techniques for complex-valued neural networks (CVNNs): hard inference learning (HIL) and Gaussian inference learning (GIL). These proposed techniques weigh the error utilized in CVNN cost functions, thus enabling parameter updates with non-pilot aided data, or "useful data". Simulation results demonstrate that both HIL and GIL training approaches significantly improve joint m-MIMO channel estimation and decoding in dynamic channels. While the SCFNN and CVFNN only achieved satisfactory results up to 50 Hz of Doppler frequency, both PT-RBF and C-RBF performed quite well up to approximately 150 Hz. Remarkably, with the application of GIL, the performance of C-RBF could be extended up to 180 Hz. While they have been used for QOSTBC, the proposed HIL and GIL are suitable learning heuristics for any CVNN applications that have well-defined outputs from a finite alphabet, such as those found in digital communication systems.

REFERENCES

5G; NR; BASE STATION (BS) RADIO TRANSMISSION AND RECEPTION. Sophia Antipolis, France, Oct. 2022. (3GPP technical specification 38.104; version 17.7.0; release 17). Cited on pages 101, 114, 133, 146.

5G; NR; PHYSICAL CHANNELS AND MODULATION. Sophia Antipolis, France, Sept. 2022. (3GPP technical specification 38.211; version 17.3.0; release 17). Cited on pages 101, 114, 133, 146.

5G; STUDY ON CHANNEL MODEL FOR FREQUENCIES FROM 0.5 TO 100 GHZ. Sophia Antipolis, France, Apr. 2022. (3GPP technical report 38.901; version 17.0.0; release 17). Cited on pages 101, 114, 133, 146.

ALAPURANEN, P.; SCHROEDER, J. Complex artificial neural network with applications to wireless communications. **Digit. Signal Process.**, v. 119, p. 1–6, 2021. Cited on page 95.

BALEVI, E.; DOSHI, A.; ANDREWS, J. G. Massive MIMO channel estimation with an untrained deep neural network. **IEEE Trans. Wireless Commun.**, v. 19, n. 3, p. 2079–2090, Mar. 2020. Cited on pages 83, 95.

CASTRO, C. et al. 100 Gbit/s terahertz-wireless real-time transmission using a broadband digital-coherent modem. *In*: PROC. 5G World Forum. Dresden: IEEE, Nov. 2019. P. 399–402. Cited on page 102.

CHA, B.; NOH, S.-K. Learning using LTE RSRP and NARNET in the same indoor area. *In*: PROC. Inter. Comput. Sci. Eng. Conf. Phuket: IEEE, Nov. 2019. P. 261–264. Cited on page 99.

CHEN, L. et al. Performance analysis and compensation of joint TX/RX I/Q imbalance in differential STBC-OFDM. **IEEE Trans. Veh. Technol.**, v. 66, n. 7, p. 6184–6200, 2017. Cited on page 95.

CHEN, X.; JIANG, M. Enhanced adaptive polar-linear interpolation aided channel estimation. **IEEE Wireless Commun. Lett.**, v. 8, n. 3, p. 693–696, 2019. Cited on page 95.

DONG, Z.; HUANG, H. A training algorithm with selectable search direction for complex-valued feedforward neural networks. **Neural Netw.**, v. 137, p. 75–84, 2021. DOI: `10.1016/j.neunet.2021.01.014`. Cited on pages 40, 96, 97.

ELBIR, A. M.; COLERI, S. Federated learning for channel estimation in conventional and RIS-assisted massive MIMO. **IEEE Trans. Wireless Commun.**, v. 21, n. 6, p. 4255–4268, 2022. Cited on page 95.

ENRICONI, M. P. et al. Phase transmittance RBF neural network beamforming for static and dynamic channels. **IEEE Antennas Wireless Propag. Lett.**, v. 19, n. 2, p. 243–247, Feb. 2020. Cited on pages 40, 83, 95–97, 155.

FAZAL-E-ASIM et al. Kronecker product-based space-time block codes. **IEEE Wireless Commun. Lett.**, v. 11, n. 2, p. 386–390, 2022. Cited on page 95.

GAO, J. et al. An attention-aided deep learning framework for massive MIMO channel estimation. **IEEE Trans. Wireless Commun.**, v. 21, n. 3, p. 1823–1835, 2022. Cited on page 95.

HE, H. et al. Deep learning-based channel estimation for beamspace mmWave massive MIMO systems. **IEEE Wireless Commun. Lett.**, v. 7, n. 5, p. 852–855, 2018. Cited on page 95.

HIROSE, A.; YOSHIDA, S. Generalization characteristics of complex-valued feedforward neural networks in relation to signal coherence. **IEEE Trans. Neural Netw. Learn. Syst.**, v. 23, n. 4, p. 541–551, 2012a. Cited on pages 95, 96, 109, 127.

JIA, Z.; CHENG, W.; ZHANG, H. A partial learning-based detection scheme for massive MIMO. **IEEE Wireless Commun. Lett.**, v. 8, n. 4, p. 1137–1140, 2019. Cited on pages 95, 96.

KIM, T.; ADALI, T. Fully complex multi-layer perceptron network for nonlinear signal processing. **J. VLSI Signal Process. Syst. Signal Image Video Technol.**, v. 32, p. 29–43, 2002. Cited on pages 96, 97.

KUMAR, S.; SINGH, A.; MAHAPATRA, R. DLNet: Deep learning-aided massive MIMO decoder. **AEU-Int. J. Electron. Commun.**, p. 154350, 2022. Cited on pages 95, 96.

LEE, C.; HASEGAWA, H.; GAO, S. Complex-valued neural networks: A comprehensive survey. **IEEE/CAA J. Autom. Sin.**, v. 9, n. 8, p. 1406–1426, 2022. Cited on page 95.

MAYER, K. S.; SOARES, J. A.; ARANTES, D. S. Complex MIMO RBF Neural Networks for Transmitter Beamforming over Nonlinear Channels. **Sensors**, v. 20, n. 2, p. 1–15, Jan. 2020. DOI: `10.3390/s20020378`. Cited on pages 31, 40, 41, 51, 54, 79, 83, 95, 96, 109, 127.

MAYER, K. S. et al. Blind Fuzzy Adaptation Step Control for a Concurrent Neural Network Equalizer. **Wireless Communications and Mobile Computing**, v. 2019, n. 1, p. 9082362, 2019c. DOI: `https://doi.org/10.1155/2019/9082362`. Cited on pages 40, 83, 95, 96, 109, 127, 161.

MAYER, K. S. **Complex-valued neural networks and applications in telecommunications**. 2022. Ph.D. Thesis – University of Campinas. Cited on pages 97, 102, 163.

MAYER, K. S. et al. Deep Phase-Transmittance RBF Neural Network for Beamforming With Multiple Users. **IEEE Wireless Communications Letters**, v. 11, n. 7, p. 1498–1502, 2022. DOI: `10.1109/LWC.2022.3177162`. Cited on pages 30, 83, 95–97, 109, 127, 142, 145, 155, 156, 161–163.

MORSALI, A. et al. Design criteria for omnidirectional STBC in massive MIMO systems. **IEEE Wireless Commun. Lett.**, v. 8, n. 5, p. 143–1439, 2019. Cited on page 95.

SANOOPKUMAR, P. S.; MUNEER, P.; SAMEER, S. M. A joint equalization and decoding technique for multiuser massive MIMO uplink system with transmitter and receiver RF impairments under doubly selective channels. **IEEE Syst. J.**, p. 1–11, 2022. Cited on page 96.

SCARDAPANE, S. et al. Complex-valued neural networks with nonparametric activation functions. **IEEE Trans. Emerg. Topics Comput. Intell.**, v. 4, n. 2, p. 140–150, 2020. Cited on pages 96, 97.

SCHMIDHUBER, J. Deep learning in neural networks: An overview. **Neural Netw.**, v. 61, p. 85–117, 2015. Cited on page 97.

SOARES, J. A. et al. Complex-valued phase transmittance RBF neural networks for massive MIMO-OFDM receivers. **Sensors**, v. 21, n. 24, p. 1–31, Dec. 2021a. ISSN 1424-8220. DOI: 10.3390/s21248200. Available from: <https://www.mdpi.com/1424-8220/21/24/8200>. Cited on pages 83, 95–99, 109, 127, 142–145, 148.

VERENZUELA, D. et al. Massive-MIMO iterative channel estimation and decoding (MICED) in the uplink. **IEEE Trans. Commun.**, v. 68, n. 2, p. 854–870, 2020. Cited on page 96.

VOIGTLAENDER, F. The universal approximation theorem for complex-valued neural networks. **Applied and Computational Harmonic Analysis**, v. 64, p. 33–61, 2023. ISSN 1063-5203. DOI: https://doi.org/10.1016/j.acha.2022.12.002. Available from: <https://www.sciencedirect.com/science/article/pii/S1063520322001014>. Cited on pages 29, 95.

WU, S. et al. Message-passing receiver for joint channel estimation and decoding in 3D massive MIMO-OFDM systems. **IEEE Trans. Wireless Commun.**, v. 15, n. 12, p. 8122–8138, 2016. Cited on page 96.

XU, J. et al. The performance analysis of complex-valued neural network in radio signal recognition. **IEEE Access**, v. 10, p. 48708–48718, 2022. Cited on pages 95, 109, 127.

YANG, Y. et al. Graph neural network-based channel tracking for massive MIMO networks. **IEEE Commun. Lett.**, v. 24, n. 8, p. 1747–1751, 2020. Cited on pages 95, 96.

YE, H.; LI, G. Y.; JUANG, B.-H. Power of deep learning for channel estimation and signal detection in OFDM systems. **IEEE Wireless Commun. Lett.**, v. 7, n. 1, p. 114–117, 2018. DOI: 10.1109/LWC.2017.2757490. Cited on pages 97, 147, 155.

ZHANG, H. et al. An optical neural chip for implementing complex-valued neural network. **Nat. Commun.**, v. 12, n. 457, p. 1–11, 2021a. Cited on pages 42, 95.

ZHANG, S.-Q.; GAO, W.; ZHOU, Z.-H. Towards understanding theoretical advantages of complex-reaction networks. **Neural Netw.**, v. 151, p. 80–93, 2022. Cited on pages 83, 95, 109, 127.

ZHANG, Y.; ZAKHAROV, Y. V.; LI, J. Soft-decision-driven sparse channel estimation and turbo equalization for MIMO underwater acoustic communications. **IEEE Access**, v. 6, p. 4955–4973, 2018. Cited on page 99.

ZHAO, W.; HUANG, H. Adaptive orthogonal gradient descent algorithm for fully complex-valued neural networks. **Neurocomputing**, v. 546, p. 1–8, 2023. Cited on page 95.

ZHENG, X.; LAU, V. K. N. Online deep neural networks for mmWave Massive MIMO channel estimation with arbitrary array geometry. **IEEE Trans. Signal Process.**, v. 69, p. 2010–2025, 2021. Cited on page 95.

Chapter 5

On the Parameter Selection of Phase-transmittance Radial Basis Function Neural Networks for Communication Systems

Authors: Jonathan Aguiar Soares, Kayol Soares Mayer, and Dalton Soares Arantes

Abstract

In the ever-evolving field of digital communication systems, complex-valued neural networks (CVNNs) have become a cornerstone, delivering exceptional performance in tasks like equalization, channel estimation, beamforming, and decoding. Among the myriad of CVNN architectures, the phase-transmittance radial basis function neural network (PT-RBF) stands out, especially when operating in noisy environments such as 5G MIMO systems. Despite its capabilities, achieving convergence in multi-layered, multi-input, and multi-output PT-RBFs remains a daunting challenge. Addressing this gap, this paper presents a novel Deep PT-RBF parameter initialization technique. Through rigorous simulations conforming to 3GPP TS 38 standards, our method not only outperforms conventional initialization strategies like random, K-means, and constellation-based methods but is also the only approach to achieve successful convergence in deep PT-RBF architectures. These findings pave the way to more robust and efficient neural network deployments in complex digital communication systems.

Keywords: Neural Networks, Complex-valued Neural Networks, Radial Basis Function, Initialization.

This Chapter is a replica of the following manuscript: Jonathan Aguiar Soares, Kayol Soares Mayer, and Dalton Soares Arantes, "On the Parameter Selection of Phase-transmittance Radial Basis Function Neural Networks for Communication Systems" in International Conference on Machine Learning for Communication and Networking, May 2024, doi: 10.1109/ICMLCN59089.2024.10624891.

5.1 INTRODUCTION

Recently, in communication systems, complex-valued neural networks (CVNNs) have been studied in several applications, such as equalization, channel estimation, beamforming, and decoding (MAYER et al., 2019c; DING; HIROSE, 2020; ZHANG et al., 2021b; LI et al., 2022; MAYER; SOARES; ARANTES, 2020; KAMIYAMA; KOBAYASHI; IWASHITA, 2021; FREIRE et al., 2021; SOARES et al., 2021a; XU et al., 2022; CHU; GAO; LIU, et al., 2022; MAYER et al., 2022; YANG et al., 2022; XIAO; YANG; FENG, 2023). This growing interest is related to enhanced functionality, improved performance, and reduced training time when compared with real-valued neural networks (RVNNs) (HIROSE; YOSHIDA, 2012a; BARRACHINA et al., 2021; CRUZ; MAYER; ARANTES, 2022; ZHANG; GAO; ZHOU, 2022).

The effectiveness of neural networks is critically dependent on several factors, such as initialization, regularization, and optimization (HUMBIRD; PETERSON; MCCLARREN, 2019). Although regularization and optimization techniques are vital to speed up the training process and reduce steady-state error (HU et al., 2021), depending on the initial parameter selection, the neural network can get stuck at local minima, achieving suboptimal solutions (NARKHEDE; BARTAKKE; SUTAONE, 2022). For radial basis function (RBF)-based neural networks, this problem is even worse since, for each layer, there are four parameters (synaptic weight, bias, center vectors, and center variances) in contrast to two parameters (synaptic weights and bias) of usual multilayer perceptron neural networks.

In this context, with a focus on the phase-transmittance radial basis function (PT-RBF) neural network (MAYER et al., 2022), we propose a novel parameter selection scheme. This scheme aims to initialize synaptic weights, biases, center vectors, and center variances in the complex domain. Notably, existing literature offers limited guidance on initialization techniques for multilayer RBF-based CVNNs. Despite this gap, our study compares the proposed approach against well-known methods such as random initialization (WALLACE; TSAPATSOULIS; KOLLIAS, 2005), K-means clustering (TURNBULL; ELKAN, 2005), and constellation-based initialization (LOSS et al., 2007a). To the best of our knowledge, this is the first work that handles this initialization challenge for multi-layered PT-RBFs.

5.2 COMPLEX-VALUED PT-RBF NEURAL NETWORKS

Following the notation used by (MAYER et al., 2022), the deep PT-RBF is defined with L hidden layers (excluding the input layer), where the superscript $l \in [0, 1, \cdots, L]$ denotes the layer index and $l = 0$ is the input layer. The l-th layer (excluding the input layer $l = 0$) is composed by $I^{\{l\}}$ neurons, $O^{\{l\}}$ outputs, and has a matrix of synaptic weights

$\mathbf{W}^{\{l\}} \in \mathbb{C}^{O^{\{l\}} \times I^{\{l\}}}$, a bias vector $\mathbf{b}^{\{l\}} \in \mathbb{C}^{O^{\{l\}}}$, a matrix of center vectors $\mathbf{\Gamma}^{\{l\}} \in \mathbb{C}^{I^{\{l\}} \times O^{\{l-1\}}}$, and a variance vector $\boldsymbol{\sigma}^{\{l\}} \in \mathbb{C}^{I^{\{l\}}}$. Notice that $\bar{\mathbf{x}} \in \mathbb{C}^{P}$ is the deep PT-RBF normalized input vector (P inputs) and $\mathbf{y}^{\{L\}} \in \mathbb{C}^{R}$ is the deep PT-RBF output vector (R outputs). The l-th hidden layer output vector $\mathbf{y}^{\{l\}} \in \mathbb{C}^{O^{\{l\}}}$ is given by

$$\mathbf{y}^{\{l\}} = \mathbf{W}^{\{l\}} \boldsymbol{\phi}^{\{l\}} + \mathbf{b}^{\{l\}}, \tag{5.1}$$

where $\boldsymbol{\phi}^{\{l\}} \in \mathbb{C}^{I^{\{l\}}}$ is the vector of Gaussian kernels.

The m-th Gaussian kernel of the l-th hidden layer is formulated as

$$\phi_m^{\{l\}} = \exp\left[-\Re\left(v_m^{\{l\}}\right)\right] + \jmath \exp\left[-\Im\left(v_m^{\{l\}}\right)\right], \tag{5.2}$$

in which $v_m^{\{l\}}$ is the m-th Gaussian kernel input of the l-th hidden layer, described as

$$v_m^{\{l\}} = \frac{\left\| \Re\left(\mathbf{y}^{\{l-1\}}\right) - \Re\left(\boldsymbol{\gamma}_m^{\{l\}}\right) \right\|_2^2}{\Re\left(\sigma_m^{\{l\}}\right)} + \jmath \frac{\left\| \Im\left(\mathbf{y}^{\{l-1\}}\right) - \Im\left(\boldsymbol{\gamma}_m^{\{l\}}\right) \right\|_2^2}{\Im\left(\sigma_m^{\{l\}}\right)}, \tag{5.3}$$

where $\mathbf{y}^{\{l-1\}} \in \mathbb{C}^{O^{\{l-1\}}}$ is the output vector of the $(l-1)$-th hidden layer (except for the first hidden layer that $\mathbf{y}^{\{0\}} = \bar{\mathbf{x}}$), $\boldsymbol{\gamma}_m^{\{l\}} \in \mathbb{C}^{O^{\{l-1\}}}$ is the m-th vector of Gaussian centers of the l-th hidden layer, $\sigma_m^{\{l\}} \in \mathbb{C}$ is the respective m-th variance, and $\Re(\cdot)$ and $\Im(\cdot)$ return the real and imaginary components, respectively.

5.3 INITIALIZATION OF COMPLEX-VALUED RADIAL BASIS FUNCTION NEURAL NETWORKS

5.3.1 Random Initialization

Based on real-valued initialization (WALLACE; TSAPATSOULIS; KOLLIAS, 2005), one of the simplest and easiest ways to initialize the parameters of a complex-valued RBF-based neural network is setting $\mathbf{\Gamma}^{\{l\}}$ and $\mathbf{W}^{\{l\}}$ randomly, as

$$\mathbf{\Gamma}^{\{l\}} \sim \mathcal{CG}\left(0, \sigma^2_{\mathbf{\Gamma}^{\{l\}}}\right), \tag{5.4}$$

$$\mathbf{W}^{\{l\}} \sim \mathcal{CG}\left(0, 1\right), \tag{5.5}$$

in which $\mathcal{CG}(\cdot)$ is a generic complex-valued distribution function, and $\sigma^2_{\mathbf{\Gamma}^{\{l\}}}$ is the desired variance of $\mathbf{\Gamma}^{\{l\}}$.

On the other hand, the bias and center variances are initialized as constant values

$$\mathbf{b}^{\{l\}} = \mathbf{0} + \jmath \mathbf{0}, \tag{5.6}$$

$$\boldsymbol{\sigma}^{\{l\}} = \frac{\sigma^2_{\boldsymbol{\Gamma}^{\{l\}}}}{2} \left(\mathbf{1} + \jmath \mathbf{1}\right), \tag{5.7}$$

where $\mathbf{0}$ and $\mathbf{1}$ are vectors of zeros and ones with the same dimensions of $\mathbf{b}^{\{l\}}$ and $\boldsymbol{\sigma}^{\{l\}}$, respectively.

5.3.2 K-means Clustering

For shallow RBF-based neural networks, a more sophisticated approach of initialization relies on a clustering algorithm, such as K-means, to find $K = I^{\{1\}}$ cluster centers. Then, these cluster centers as the initial center vectors of RBFs ensure that the centers are distributed along the dataset's inherent structure. However, as the PT-RBF Gaussian neurons operate with a split-complex design, the K-means must be applied for the real and imaginary components of the input dataset $\mathcal{X} \supset \mathbf{x}$, separately, creating a set of cluster centers $\mathbf{C}_{\mathcal{X}} = \mathbf{C}_{\Re(\mathcal{X})} + \jmath \mathbf{C}_{\Im(\mathcal{X})}$. The m-th center vector of the hidden layer is $\boldsymbol{\gamma}_m^{\{1\}} \in \mathbf{C}_{\mathcal{X}}$, randomly selected without replacement.

The center variances are chosen based on the in-cluster distances from K-means. Thus, the PT-RBF m-th center variance of the hidden layer is

$$\begin{aligned}\sigma_m^{\{1\}} = &\frac{1}{\left|\mathcal{X}_{\Re\left(\boldsymbol{\gamma}_m^{\{1\}}\right)}\right|} \sum_{\Re(\mathbf{x}) \in \mathcal{X}_{\Re\left(\boldsymbol{\gamma}_m^{\{1\}}\right)}} \left\|\Re\left(\mathbf{x}\right) - \Re\left(\boldsymbol{\gamma}_m^{\{1\}}\right)\right\|_2^2 \\ &+ \jmath \frac{1}{\left|\mathcal{X}_{\Im\left(\boldsymbol{\gamma}_m^{\{1\}}\right)}\right|} \sum_{\Im(\mathbf{x}) \in \mathcal{X}_{\Im\left(\boldsymbol{\gamma}_m^{\{1\}}\right)}} \left\|\Im\left(\mathbf{x}\right) - \Im\left(\boldsymbol{\gamma}_m^{\{1\}}\right)\right\|_2^2,\end{aligned} \tag{5.8}$$

in which $\mathcal{X}_{\Re\left(\boldsymbol{\gamma}_m^{\{1\}}\right)} \subset \Re\left(\mathcal{X}\right)$ and $\mathcal{X}_{\Im\left(\boldsymbol{\gamma}_m^{\{1\}}\right)} \subset \Im\left(\mathcal{X}\right)$ are subsets of the input dataset vectors nearest to $\Re\left(\boldsymbol{\gamma}_m^{\{1\}}\right)$ and $\Im\left(\boldsymbol{\gamma}_m^{\{1\}}\right)$, respectively. The operator $|\cdot|$ returns the subset cardinality.

The synaptic weights and bias initializations are equal to the random initialization scheme.

5.3.3 Constellation-based initialization

As an alternative in finite alphabet outputs, the center vectors can be randomly selected from the output dataset (LOSS et al., 2007a). For example, when the output dataset is a constellation containing M-ary quadrature amplitude modulation (M-QAM), all center vector components are initialized with randomly selected M-QAM symbols. The

PT-RBF m-th center variance of the l-th hidden layer is

$$\sigma_m^{\{l\}} = \frac{1}{2} \max_{1 \leq i,k \leq I^{\{l\}}} \left[\left\| \Re\left(\boldsymbol{\gamma}_i^{\{l\}}\right) - \Re\left(\boldsymbol{\gamma}_k^{\{l\}}\right) \right\|_2 \right]$$
$$\jmath \frac{1}{2} \max_{1 \leq i,k \leq I\{l\}} \left[\left\| \Im\left(\boldsymbol{\gamma}_i^{\{l\}}\right) - \Im\left(\boldsymbol{\gamma}_k^{\{l\}}\right) \right\|_2 \right]. \quad (5.9)$$

The synaptic weights and bias are initialized with zeros.

5.4 DEEP PT-RBF PARAMETER INITIALIZATION

To properly initialize the deep PT-RBF parameters, we first need to understand the relationship between the input vector $\mathbf{x}$ and the Gaussian center vectors $\boldsymbol{\gamma}_m^{\{1\}}$. In (5.2), regarding (5.3), and keeping $\sigma_m^{\{1\}}$ constant, the closer $\boldsymbol{\gamma}_m^{\{1\}}$ is to $\mathbf{x}$, the higher is the value of the real and imaginary parts of $\phi_m^{\{1\}}$. For example, if $\boldsymbol{\gamma}_m^{\{1\}} = \mathbf{x}$ then $\phi_m^{\{1\}} = 1 + \jmath 1$. On the other hand, if $\boldsymbol{\gamma}_m^{\{1\}}$ is set far from $\mathbf{x}$, then $\phi_m^{\{1\}} \to 0$. In this context, in order to not saturate or vanish $\phi_m^{\{1\}}$, we assume $\mu_{\bar{\mathbf{x}}} = \mu_{\boldsymbol{\gamma}^{\{1\}}} = 0$ and $\sigma^2_{\bar{\mathbf{x}}} = \sigma^2_{\boldsymbol{\gamma}^{\{1\}}}$, where $\bar{\mathbf{x}}$ is the normalized input dataset. Furthermore, we expect that depending on the dataset inputs, $\phi_m^{\{1\}}$ varies reasonably. For example, considering $v_m^{\{1\}} = 5$ and $v_m^{\{1\}} = 10$, the variation in $\phi_m^{\{1\}}$ is only 4.54×10^{-5}. In contrast, considering $v_m^{\{1\}} = 0$ and $v_m^{\{1\}} = 3$, the variation in $\phi_m^{\{1\}}$ is 0.95. Then, it is desirable that $\mu_{v^{\{1\}}}$ is not too large. Based on Appendix 5.A, the expected value of $v^{\{1\}}$ is

$$\mu_{\mathbf{v}^{\{1\}}} = \frac{P}{c_\sigma} \left[\sigma^2_{\Re(\bar{\mathbf{x}})} + \jmath \sigma^2_{\Im(\bar{\mathbf{x}})} + \sigma^2_{\Re\left(\boldsymbol{\gamma}_m^{\{1\}}\right)} + \jmath \sigma^2_{\Im\left(\boldsymbol{\gamma}_m^{\{1\}}\right)} \right], \quad (5.10)$$

in which $\sigma^2_{\bar{\mathbf{x}}} = 2\sigma^2_{\Re(\bar{\mathbf{x}})} = 2\sigma^2_{\Im(\bar{\mathbf{x}})}$ is the variance of $\bar{\mathbf{x}}$, $\sigma^2_{\boldsymbol{\gamma}_m^{\{1\}}} = 2\sigma^2_{\Re\left(\boldsymbol{\gamma}_m^{\{1\}}\right)} = 2\sigma^2_{\Im\left(\boldsymbol{\gamma}_m^{\{1\}}\right)}$ is the variance of $\boldsymbol{\gamma}_m^{\{1\}}$, $c_\sigma = \Re\left(\sigma_m^{\{1\}}\right) = \Im\left(\sigma_m^{\{1\}}\right)\ \forall\ m$, and c_σ is a positive and nonzero constant.

As $\sigma^2_{\bar{\mathbf{x}}} = \sigma^2_{\boldsymbol{\gamma}^{\{1\}}}$, from (5.10), we have

$$\sigma^2_{\bar{\mathbf{x}}} = \frac{c_\sigma \mu_{\Re\left(\mathbf{v}^{\{1\}}\right)}}{P}. \quad (5.11)$$

Based on (5.11), the normalized input is given as

$$\bar{\mathbf{x}} = \frac{(\mathbf{x} - \mu_{\mathbf{x}})}{\sqrt{\sigma^2_{\mathbf{x}}}} \sqrt{\frac{c_\sigma \mu_{\Re\left(\mathbf{v}^{\{1\}}\right)}}{P}}, \quad (5.12)$$

where $\mu_{\mathbf{x}}$ and $\sigma^2_{\mathbf{x}}$ are applied to adjust the mean and variance of $\bar{\mathbf{x}}$ before the normalization by (5.11).

Similarly, in the first hidden layer, the normalized matrix of center vectors is

$$\boldsymbol{\Gamma}^{\{1\}} \sim \mathcal{CG}\left(0, \frac{c_\sigma \mu_{\Re\left(\mathbf{v}^{\{1\}}\right)}}{P}\right). \quad (5.13)$$

In order to normalize the output dataset $\mathbf{d}$, we need to compute the variance of the output vector $\mathbf{y}^{\{L\}}$, by

$$\sigma^2_{\mathbf{y}^{\{L\}}} = \mathrm{Var}\left[\mathbf{W}^{\{L\}}\boldsymbol{\phi}^{\{L\}} + \mathbf{b}^{\{L\}}\right]. \tag{5.14}$$

However, as $\mathbf{W}^{\{L\}}$ is a complex-valued matrix and performs a linear combination with $\boldsymbol{\phi}^{\{L\}}$, which is a complex-valued vector, the real and imaginary components are handled at the same time, in the complex domain. Moreover, we assume that $\mathbf{b}^{\{l\}}$ is initialized with zeros, for all layers. Thus, based on Appendix 5.C, (5.14) results in

$$\sigma^2_{\mathbf{y}^{\{L\}}} = \frac{12}{5} c_\sigma^{-2} \exp(-2\mu_{\mathbf{v}^{\{L\}}}) I^{\{L\}} \mathrm{O}^{\{\mathrm{L}-1\}} \sigma^2_{\mathbf{W}^{\{L\}}} \sigma^4_{\gamma^{\{L\}}}, \tag{5.15}$$

where $\sigma^2_{\mathbf{W}^{\{\mathbf{L}\}}}$ is the variance of $\mathbf{W}^{\{L\}}$, and $\mu_{\mathbf{v}^{\{L\}}}$ is the expected value of $\mathbf{v}^{\{L\}}$. Choosing $\sigma^2_{\mathbf{y}^{\{L\}}} = \sigma^2_{\bar{\mathbf{d}}}$, i.e., the variance of the PT-RBF output equal to the variance of the normalized output dataset, yields the initialization of $\mathbf{W}^{\{L\}}$ as

$$\mathbf{W}^{\{L\}} \sim \mathcal{CG}\left(0, \frac{5\exp(2\mu_{\mathbf{v}^{\{L\}}})\sigma^2_{\bar{\mathbf{d}}}}{12 c_\sigma^{-2} I^{\{L\}} \mathrm{O}^{\{\mathrm{L}-1\}} \sigma^2_{\mathbf{W}^{\{L\}}} \sigma^4_{\gamma^{\{L\}}}}\right), \tag{5.16}$$

in which the output dataset can be normalized by

$$\bar{\mathbf{d}} = \frac{(\mathbf{d} - \mu_{\mathbf{d}})}{\sqrt{\sigma^2_{\mathbf{d}}}} \sqrt{\sigma^2_{\mathbf{y}^{\{L\}}}} = \frac{(\mathbf{d} - \mu_{\mathbf{d}})}{\sqrt{\sigma^2_{\mathbf{d}}}} \sqrt{\frac{c_\sigma \mu_{\Re\left(\mathbf{v}^{\{L\}}\right)}}{R}}. \tag{5.17}$$

Relying on (5.13), we can generalize the initialization of $\boldsymbol{\Gamma}^{\{l\}}$, as

$$\boldsymbol{\Gamma}^{\{l\}} \sim \mathcal{CG}\left(0, \frac{c_\sigma \mu_{\Re\left(\mathbf{v}^{\{l\}}\right)}}{O^{\{l-1\}}}\right). \tag{5.18}$$

From (5.11), the variance of the output hidden layers can be considered as

$$\sigma^2_{\mathbf{y}^{\{l\}}} = \frac{c_\sigma \mu_{\Re\left(\mathbf{v}^{\{l+1\}}\right)}}{O^{\{l\}}}, \tag{5.19}$$

where, replacing $\sigma^4_{\gamma^{\{L\}}}$ by (5.18) and $\sigma^2_{\bar{\mathbf{d}}}$ by (5.19) into (5.16), yields

$$\mathbf{W}^{\{l\}} \sim \mathcal{CG}\left(0, \frac{5 c_\sigma \exp(-2\mu_{\mathbf{v}^{\{L\}}}) O^{\{l-1\}}}{12 I^{\{l\}} O^{\{l\}} \mu_{\mathbf{v}^{\{l\}})}}\right), \tag{5.20}$$

It is important to note that, (5.12) and (5.17) only hold for $\sigma^2_{\mathbf{x}} = 2\sigma^2_{\Re(\mathbf{x})} = 2\sigma^2_{\Im(\mathbf{x})}$ and $\sigma^2_{\mathbf{d}} = 2\sigma^2_{\Re(\mathbf{d})} = 2\sigma^2_{\Im(\mathbf{d})}$, respectively. For the particular case of $\sigma^2_{\Re(\mathbf{x})} \neq \sigma^2_{\Im(\mathbf{x})}$ and $\sigma^2_{\Re(\mathbf{d})} \neq \sigma^2_{\Im(\mathbf{d})}$, then (5.12) and (5.17) become

$$\bar{\mathbf{x}} = \left[\frac{(\Re(\mathbf{x}) - \mu_{\Re(\mathbf{x})})}{\sqrt{2\sigma^2_{\Re(\mathbf{x})}}} + \jmath \frac{(\Im(\mathbf{x}) - \mu_{\Im(\mathbf{x})})}{\sqrt{2\sigma^2_{\Im(\mathbf{x})}}}\right] \times \sqrt{\frac{c_\sigma \mu_{\Re\left(\mathbf{v}^{\{1\}}\right)}}{P}}, \tag{5.21}$$

$$\bar{\mathbf{d}} = \left[\frac{\left(\Re\left(\mathbf{d}\right) - \mu_{\Re(\mathbf{d})}\right)}{\sqrt{2\sigma^2_{\Re(\mathbf{d})}}} + \jmath\frac{\left(\Im\left(\mathbf{d}\right) - \mu_{\Im(\mathbf{d})}\right)}{\sqrt{2\sigma^2_{\Im(\mathbf{d})}}}\right] \times \sqrt{\frac{c_\sigma \mu_{\Re\left(\mathbf{v}^{\{L\}}\right)}}{R}}. \quad (5.22)$$

5.5 RESULTS

For the sake of simplification, in the proposed approach, the parameters c_σ and $\mu_{\mathbf{v}^{\{l\}}}$ were set to 1, for all layers. Then, the initializations and normalizations become

$$\mathbf{b}^{\{l\}} = \mathbf{0} + \jmath\mathbf{0}, \quad (5.23)$$

$$\boldsymbol{\sigma}^{\{l\}} = \mathbf{1} + \jmath\mathbf{1}, \quad (5.24)$$

$$\boldsymbol{\Gamma}^{\{l\}} \sim \mathcal{CG}\left(0, \frac{1}{O^{\{l-1\}}}\right), \quad (5.25)$$

$$\mathbf{W}^{\{l\}} \sim \mathcal{CG}\left(0, \frac{5\exp(-2)O^{\{l-1\}}}{12I^{\{l\}}O^{\{l\}}}\right), \quad (5.26)$$

$$\bar{\mathbf{x}} = \frac{(\mathbf{x} - \mu_{\mathbf{x}})}{\sqrt{\sigma^2_{\mathbf{x}}}}\sqrt{\frac{1}{P}}, \quad (5.27)$$

$$\bar{\mathbf{d}} = \frac{(\mathbf{d} - \mu_{\mathbf{d}})}{\sqrt{\sigma^2_{\mathbf{d}}}}\sqrt{\frac{1}{R}}. \quad (5.28)$$

For the random initialization, we defined $\sigma^2_{\boldsymbol{\Gamma}^{\{l\}}} = 1$. The K-means and constellation-based initializations are obtained from the input and output datasets, respectively.

Based on (SOARES; MAYER; ARANTES, 2023), we consider a space-time block coding (STBC) simulation system with the 3GPP TS 38.211 specification for 5G physical channels and modulation (5G. . . , 2022). The orthogonal frequency-division multiplexing (OFDM) is defined with 60-kHz subcarrier spacing, 256 active subcarriers, and a block-based pilot scheme. Symbols are modulated with 16-QAM and, for the MIMO setup, 4 antennas are employed both at the transmitter and receiver. Based on the tapped delay line-A (TDLA) from the 3GPP TR 38.901 5G channel models (5G. . . , 2022), the MIMO channel follows the TDLA from the 3GPP TR 38.104 5G radio base station transmission and reception (5G. . . , 2022). The TDLA is described with 12 taps, with varying delays from 0.0 ns to 290 ns and powers from -26.2 dB to 0 dB. A Rayleigh distribution is used to compute each sub-channel. To avoid influencing the learning curves, we do not take into account the Doppler effect, and we do not employ the inference learning techniques proposed in (SOARES; MAYER; ARANTES, 2023). The CVNNs operate with 16 inputs and 4 outputs. The inputs are taken from the OFDM demodulator outputs, one at a time (see (SOARES; MAYER; ARANTES, 2023), Fig. 1). Training and validation

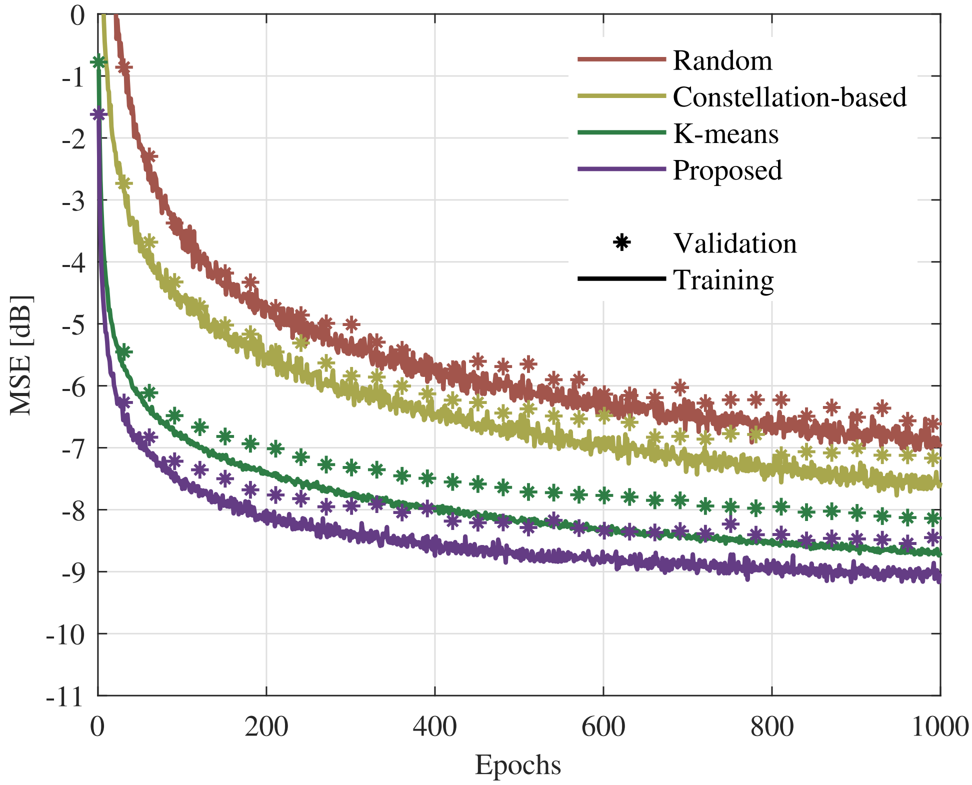

Figure 5.5.1 – MSE convergence results of training (solid lines) and validation (asterisks) of the PT-RBF initialization with a hidden layer ($I^{\{1\}} = 64$ neurons) for joint channel estimation and decoding in a MIMO-OFDM 4×4 system, operating with 16-QAM and 256 subcarriers. Results were averaged over 100 subsequent simulations with $\mathrm{E_b/N_0} = 26$ dB.

were performed for $3,840$ and $1,280$ instances, respectively. To assess performance, we calculated the Mean Squared Error (MSE), defined as $\mathrm{MSE} = \frac{1}{n}\sum_{i=1}^{n}(y_i - \hat{y}_i)^2$, where y_i represents the total transmitted constellation symbols over 100 simulations. Each output training instance corresponds to 4 symbols, resulting in a total of 15,360 and 5,120 16-QAM symbols for training and validation phases, respectively.

Fig. 5.5.1 illustrates the MSE convergence for 1000 epochs of training (solid lines) and validation (asterisks) of the PT-RBF with a hidden layer ($I^{\{1\}} = 64$ neurons). Results were averaged over 100 simulations with a bit energy to noise power spectral density ratio $\mathrm{E_b/N_0} = 26$ dB. Table 5.5.1 depicts the PT-RBF hyperparameters empirically optimized for each initialization scheme. None of the algorithms presented under- or over-fitting. The random initialization presented the poorest convergence results, with a steady-state error of -6 dB. On the other hand, the constellation-based and K-means initializations achieved a steady-state error of -6 dB and -8.8 dB, respectively. The best results were obtained with the proposed approach, with -9.1 dB of steady-state error. For comparison results regarding the convergence rate, considering $\mathrm{MSE} = -5$ dB, the proposed approach reaches this mark in five training epochs, followed by the K-means (11 epochs), constellations-based (80 epochs), and random initialization (165 epochs).

For further comparison, we have also employed the initialization schemes for PT-

Table 5.5.1 – Single layer PT-RBF optimized hyperparameters.

Algorithm	η_w	η_b	η_γ	η_σ
Random	0.5	0.5	0.5	0.5
Constellation-based	0.5	0.5	0.5	0.5
K-means	0.1	0.1	0.4	0.2
Proposed Approach	0.1	0.1	0.4	0.2

Table 5.5.2 – Deep PT-RBF optimized hyperparameters for the proposed approach.

Algorithm	η_w	η_b	η_γ	η_σ
first layer	0.100	0.100	0.100	0.100
second layer	0.050	0.050	0.050	0.050
third layer	0.033	0.033	0.033	0.033
fourth layer	0.025	0.025	0.025	0.025

These hyperparameters were optimized for the proposed initialization of the deep PT-RBFs. For example, in a deep PT-RBF with two hidden layers, only the first and second rows of hyperparameters are necessary. In a shallow architecture, the optimization is available in Table 5.5.1.

RBFs with two, three, and four hidden layers. However, the K-means was not considered since it is only suitable for shallow RBFs. In addition, although several trials were attempted, no convergence was achieved for the random and constellation-based initializations. Thus, Fig. 5.5.2 shows the convergence results for the proposed approach for the PT-RBFs with one ($I^{\{1\}} = 64$ neurons), two ($I^{\{1\}} = 48$ and $I^{\{2\}} = 16$ neurons), three ($I^{\{1\}} = 24$, $I^{\{2\}} = 24$, and $I^{\{3\}} = 16$ neurons), and four ($I^{\{1\}} = 16$, $I^{\{2\}} = 16$, $I^{\{3\}} = 16$, and $I^{\{4\}} = 16$ neurons) hidden layers[1]. Table 5.5.2 depicts the deep PT-RBF hyperparameters empirically optimized for each hidden layer. Unlike the other initialization schemes, the proposed approach achieves reasonable convergence for all architectures. One may note that all multilayered PT-RBFs architectures achieved the same steady-state MSE results. This result is due to the number of neurons utilized to create the PT-RBF layers. For the three- and four-layered PT-RBFs, the layers with the lowest number of neurons performed bottlenecks, impacting results. In order to circumvent this issue, more neurons could be adopted per layer; nonetheless, it does not affect the convergence verification.

[1] For the sake of comparison, we chose a total number of neurons $N_T = 64$, which was split depending on the number of layers.

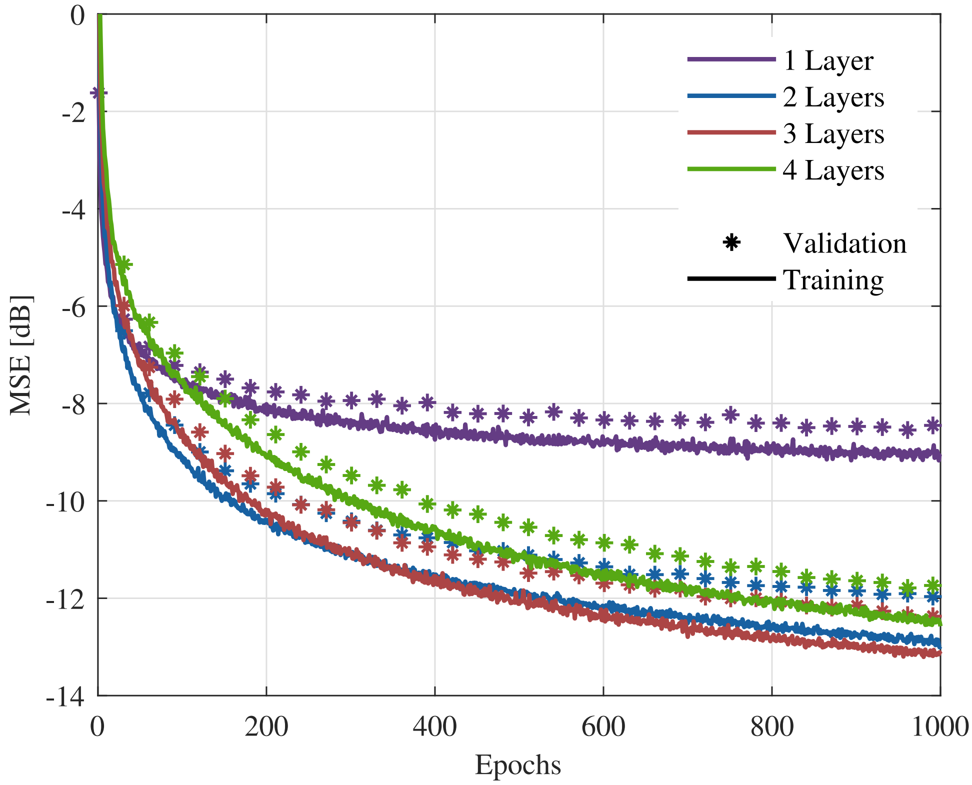

Figure 5.5.2 – MSE convergence results of training (solid lines) and validation (stars) of the proposed initialization approach with one ($I^{\{1\}} = 64$ neurons), two ($I^{\{1\}} = 48$ and $I^{\{2\}} = 16$ neurons), three ($I^{\{1\}} = 24$, $I^{\{2\}} = 24$, and $I^{\{3\}} = 16$ neurons), and four ($I^{\{1\}} = 16$, $I^{\{2\}} = 16$, $I^{\{3\}} = 16$, and $I^{\{4\}} = 16$ neurons) hidden layers for joint channel estimation and decoding in a MIMO-OFDM 4×4 system, operating with 16-QAM and 256 subcarriers. Results were averaged over 100 subsequent simulations with $\mathrm{E_b/N_0} = 26$ dB.

5.6 CONCLUSION

This paper presents an in-depth analysis of the initialization process in phase-transmittance radial basis function (PT-RBF) neural networks. Our findings have elucidated the intricate dependencies involved in the initialization process. Specifically, the normalization between layers which is dependent on the number of inputs, outputs and neurons. This reveals that synaptic weights initialization is influenced by the layer-wise configuration of inputs, neurons, and outputs. Consequently, our proposed approach demonstrates robustness to variations in the number of inputs, outputs, hidden layers, and neurons.

This innovation is particularly impactful for deploying these networks in real-world scenarios, which require robustness for a wide range of different configurations, with no room for ad hoc adjustments. In a carefully designed simulation environment, our proposed deep PT-RBF parameter initialization exhibited superior convergence performance compared to existing methods such as random, K-means, and constellation-based initialization. Notably, for multi-layer architecture, our method was the only one that achieved successful convergence, highlighting its unique efficacy and adaptability.

The results of our study have important implications. Firstly, they introduce a robust and effective initialization method that can significantly improve the convergence rate and steady state MSE of PT-RBF neural networks. Additionally, offering the potential for extending our framework to other RBF neural network architectures. In future works, we plan to validate the robustness of our proposed approach through more exhaustive experiments. We also aim to explore the applicability of our initialization framework to other neural network architectures, thereby contributing to the broader advancement of neural network-based solutions in digital communications.

ACKNOWLEDGMENTS

This study was supported in part by the Coordenação de Aperfeiçoamento de Pessoal de Nível Superior — Brasil (CAPES) — Finance Code 001.

REFERENCES

5G; NR; BASE STATION (BS) RADIO TRANSMISSION AND RECEPTION. Sophia Antipolis, France, Oct. 2022. (3GPP technical specification 38.104; version 17.7.0; release 17). Cited on pages 101, 114, 133, 146.

5G; NR; PHYSICAL CHANNELS AND MODULATION. Sophia Antipolis, France, Sept. 2022. (3GPP technical specification 38.211; version 17.3.0; release 17). Cited on pages 101, 114, 133, 146.

5G; STUDY ON CHANNEL MODEL FOR FREQUENCIES FROM 0.5 TO 100 GHZ. Sophia Antipolis, France, Apr. 2022. (3GPP technical report 38.901; version 17.0.0; release 17). Cited on pages 101, 114, 133, 146.

BARRACHINA, J. A. et al. Complex-valued vs. real-valued neural networks for classification perspectives: An example on non-circular data. *In*: 2021 IEEE International Conference on Acoustics, Speech and Signal Processing (ICASSP). [S.l.: s.n.], 2021. P. 2990–2994. Cited on pages 109, 127.

CHU, J.; GAO, M.; LIU, X., et al. Channel estimation based on complex-valued neural networks in IM/DD FBMC/OQAM transmission system. **Journal of Lightwave Technology**, v. 40, n. 4, p. 1055–1063, 2022. Cited on pages 109, 127.

CRUZ, A. A.; MAYER, K. S.; ARANTES, D. S. RosenPy: An open source python framework for complex-valued neural networks. **SSRN**, p. 1–18, 2022. Available from: <https://ssrn.com/abstract=4252610>. Cited on pages 109, 127.

DING, T.; HIROSE, A. Online regularization of complex-valued neural networks for structure optimization in wireless-communication channel prediction. **IEEE Access**, v. 8, p. 143706–143722, 2020. Cited on pages 109, 127.

FREIRE, P. J. et al. Complex-valued neural network design for mitigation of signal distortions in optical links. **Journal of Lightwave Technology**, v. 39, n. 6, p. 1696–1705, 2021. Cited on pages 109, 127, 155.

HIROSE, A.; YOSHIDA, S. Generalization characteristics of complex-valued feedforward neural networks in relation to signal coherence. **IEEE Trans. Neural Netw. Learn. Syst.**, v. 23, n. 4, p. 541–551, 2012a. Cited on pages 95, 96, 109, 127.

HU, T. et al. Regularization matters: A nonparametric perspective on overparametrized neural network. *In*: PROCEEDINGS of The 24th International Conference on Artificial Intelligence and Statistics. [S.l.: s.n.], 2021. P. 829–837. Cited on pages 109, 127.

HUMBIRD, K. D.; PETERSON, J. L.; MCCLARREN, R. G. Deep neural network initialization with decision trees. **IEEE Transactions on Neural Networks and Learning Systems**, v. 30, n. 5, p. 1286–1295, 2019. Cited on pages 109, 127.

KAMIYAMA, T.; KOBAYASHI, H.; IWASHITA, K. Neural network nonlinear equalizer in long-distance coherent optical transmission systems. **IEEE Photonics Technology Letters**, v. 33, n. 9, p. 421–424, 2021. Cited on pages 109, 127.

LI, H. et al. CVLNet: A complex-valued lightweight network for CSI feedback. **IEEE Wireless Communications Letters**, v. 11, n. 5, p. 1092–1096, 2022. Cited on pages 109, 127.

LOSS, D. et al. Phase Transmittance RBF Neural Networks. **Electronics Letters**, v. 43, n. 16, p. 882–884, Aug. 2007a. DOI: `10.1049/el:20070016`. Cited on pages 40, 41, 51, 59, 109, 111, 127.

MAYER, K. S.; SOARES, J. A.; ARANTES, D. S. Complex MIMO RBF Neural Networks for Transmitter Beamforming over Nonlinear Channels. **Sensors**, v. 20, n. 2, p. 1–15, Jan. 2020. DOI: `10.3390/s20020378`. Cited on pages 31, 40, 41, 51, 54, 79, 83, 95, 96, 109, 127.

MAYER, K. S. et al. Blind Fuzzy Adaptation Step Control for a Concurrent Neural Network Equalizer. **Wireless Communications and Mobile Computing**, v. 2019, n. 1, p. 9082362, 2019c. DOI: `https://doi.org/10.1155/2019/9082362`. Cited on pages 40, 83, 95, 96, 109, 127, 161.

MAYER, K. S. et al. Deep Phase-Transmittance RBF Neural Network for Beamforming With Multiple Users. **IEEE Wireless Communications Letters**, v. 11, n. 7, p. 1498–1502, 2022. DOI: `10.1109/LWC.2022.3177162`. Cited on pages 30, 83, 95–97, 109, 127, 142, 145, 155, 156, 161–163.

NARKHEDE, M. V.; BARTAKKE, P. P.; SUTAONE, M. S. A review on weight initialization strategies for neural networks. **Artificial Intelligence Review**, v. 55, p. 291–322, 2022. Cited on pages 109, 127.

SOARES, J. A. et al. Complex-valued phase transmittance RBF neural networks for massive MIMO-OFDM receivers. **Sensors**, v. 21, n. 24, p. 1–31, Dec. 2021a. ISSN 1424-8220. DOI: `10.3390/s21248200`. Available from:

<https://www.mdpi.com/1424-8220/21/24/8200>. Cited on pages 83, 95–99, 109, 127, 142–145, 148.

SOARES, J. A.; MAYER, K. S.; ARANTES, D. S. Semi-Supervised ML-Based Joint Channel Estimation and Decoding for m-MIMO With Gaussian Inference Learning. **IEEE Wireless Communications Letters**, v. 12, n. 12, p. 2123–2127, 2023. DOI: 10.1109/LWC.2023.3309479. Cited on pages 30, 114, 133, 146, 155, 161, 162.

TURNBULL, D.; ELKAN, C. Fast recognition of musical genres using RBF networks. **IEEE Transactions on Knowledge and Data Engineering**, v. 17, n. 4, p. 580–584, 2005. Cited on pages 109, 127.

WALLACE, M.; TSAPATSOULIS, N.; KOLLIAS, S. Intelligent initialization of resource allocating RBF networks. **Neural Networks**, v. 18, n. 2, p. 117–122, 2005. Cited on pages 109, 110, 127.

XIAO, C.; YANG, S.; FENG, Z. Complex-valued depthwise separable convolutional neural network for automatic modulation classification. **IEEE Transactions on Instrumentation and Measurement**, v. 72, p. 1–10, 2023. Cited on pages 109, 127.

XU, J. et al. The performance analysis of complex-valued neural network in radio signal recognition. **IEEE Access**, v. 10, p. 48708–48718, 2022. Cited on pages 95, 109, 127.

YANG, X. et al. Automatic modulation mode recognition of communication signals based on complex-valued neural network. *In*: 2022 International Conference on Computing, Communication, Perception and Quantum Technology (CCPQT). [S.l.: s.n.], 2022. P. 32–37. Cited on pages 109, 127.

ZHANG, S.-Q.; GAO, W.; ZHOU, Z.-H. Towards understanding theoretical advantages of complex-reaction networks. **Neural Netw.**, v. 151, p. 80–93, 2022. Cited on pages 83, 95, 109, 127.

ZHANG, Y. et al. CV-3DCNN: Complex-valued deep learning for CSI prediction in FDD massive MIMO systems. **IEEE Wireless Communications Letters**, v. 10, n. 2, p. 266–270, 2021b. Cited on pages 109, 127.

Appendix

5.A EXPECTED VALUE OF $\mathbf{v}^{\{l\}}$

Taking the Gaussian kernel input $\mathbf{v}^{\{l\}}$ of a layer l, its expected value is

$$\mu_{\mathbf{v}^{\{l\}}} = \mathrm{E}\left[\frac{\left\|\Re\left(\mathbf{y}^{\{l-1\}}\right) - \Re\left(\boldsymbol{\gamma}_m^{\{l\}}\right)\right\|_2^2}{\Re\left(\sigma_m^{\{l\}}\right)} + \jmath \frac{\left\|\Im\left(\mathbf{y}^{\{l-1\}}\right) - \Im\left(\boldsymbol{\gamma}_m^{\{l\}}\right)\right\|_2^2}{\Im\left(\sigma_m^{\{l\}}\right)} \right], \quad (5.29)$$

where $m \in [1, 2, \cdots, I^{\{l\}}]$.

Due to the split-complex kernel of PT-RBFs, the expected value of the real and imaginary components can be computed separately. Focusing on the real part

$$\Re\left(\mu_{\mathbf{v}^{\{l\}}}\right) = \mathrm{E}\left[\frac{\left\|\Re\left(\mathbf{y}^{\{l-1\}}\right) - \Re\left(\boldsymbol{\gamma}_m^{\{l\}}\right)\right\|_2^2}{\Re\left(\sigma_m^{\{l\}}\right)} \right]. \quad (5.30)$$

Assuming $\Re\left(\sigma_m^{\{l\}}\right) = \Im\left(\sigma_m^{\{l\}}\right) = c_\sigma \;\; \forall m, \{l\}$, with $c_\sigma > 0$, then

$$\Re\left(\mu_{\mathbf{v}^{\{l\}}}\right) = c_\sigma^{-1} \mathrm{E}\left[\left\|\Re\left(\mathbf{y}^{\{l-1\}}\right) - \Re\left(\boldsymbol{\gamma}_m^{\{l\}}\right)\right\|_2^2 \right], \quad (5.31)$$

which is

$$\Re\left(\mu_{\mathbf{v}^{\{l\}}}\right) = c_\sigma^{-1} \sum_{i=1}^{O^{\{l-1\}}} \mathrm{E}\left[\Re\left(y_i^{\{l-1\}}\right)^2\right] + \mathrm{E}\left[\Re\left(\gamma_{m,i}^{\{l\}}\right)^2\right] - 2\mathrm{E}\left[\Re\left(y_i^{\{l-1\}}\right)\Re\left(\gamma_{m,i}^{\{l\}}\right)\right], \quad (5.32)$$

where $\gamma_{m,i}^{\{l\}}$ and $y_i^{\{l-1\}}$ are the i-th elements of $\boldsymbol{\gamma}_m^{\{l\}}$ and $\mathbf{y}^{\{l-1\}}$, respectively.

As $\boldsymbol{\gamma}_m^{\{l\}}$ and $\mathbf{y}^{\{l-1\}}$ are independent, and assuming $\boldsymbol{\gamma}_m^{\{l\}}$ and $\mathbf{y}^{\{l-1\}}$ with zeros mean, then

$$\mathrm{E}\left[\Re\left(y_i^{\{l-1\}}\right)\Re\left(\gamma_{m,i}^{\{l\}}\right)\right] = 0, \quad (5.33)$$

which results in

$$\Re\left(\mu_{\mathbf{v}^{\{l\}}}\right) = c_\sigma^{-1} \sum_{i=1}^{O^{\{l-1\}}} \mathrm{E}\left[\Re\left(y_i^{\{l-1\}}\right)^2\right] + \mathrm{E}\left[\Re\left(\gamma_{m,i}^{\{l\}}\right)^2\right]. \quad (5.34)$$

Furthermore, the variances of $\Re\left(\mathbf{y}^{\{l-1\}}\right)$ and $\Re\left(\boldsymbol{\gamma}_m^{\{l\}}\right)$ are

$$\sigma^2_{\Re\left(\mathbf{y}^{\{l-1\}}\right)} = \frac{1}{O^{\{l-1\}}} \sum_{i=1}^{O^{\{l-1\}}} \Re\left(y_i^{\{l-1\}}\right)^2, \quad (5.35)$$

$$\sigma^2_{\Re\left(\boldsymbol{\gamma}_m^{\{l\}}\right)} = \frac{1}{O^{\{l-1\}}} \sum_{i=1}^{O^{\{l-1\}}} \Re\left(\gamma_i^{\{l\}}\right)^2, \tag{5.36}$$

thus, in (5.34), applying the summation to the expected value arguments, yields

$$\Re\left(\mu_{\mathbf{v}^{\{l\}}}\right) = c_\sigma^{-1} O^{\{l-1\}} \mathrm{E}\left[\sigma^2_{\Re\left(\mathbf{y}^{\{l-1\}}\right)} + \sigma^2_{\Re\left(\boldsymbol{\gamma}_m^{\{l\}}\right)}\right]. \tag{5.37}$$

However, as the variances $\sigma^2_{\Re\left(\mathbf{y}^{\{l-1\}}\right)}$ and $\sigma^2_{\Re\left(\boldsymbol{\gamma}_m^{\{l\}}\right)}$ are constants, $\Re\left(\mu_{\mathbf{v}^{\{l\}}}\right)$ can be expressed as

$$\Re\left(\mu_{\mathbf{v}^{\{l\}}}\right) = c_\sigma^{-1} O^{\{l-1\}} \left[\sigma^2_{\Re\left(\mathbf{y}^{\{l-1\}}\right)} + \sigma^2_{\Re\left(\boldsymbol{\gamma}_m^{\{l\}}\right)}\right]. \tag{5.38}$$

Applying these computations to $\Re\left(\mu_{\mathbf{v}^{\{l\}}}\right)$, and adding it to $\Re\left(\mu_{\mathbf{v}^{\{l\}}}\right)$, we obtain the expected value of $\mathbf{v}^{\{l\}}$ as

$$\begin{aligned}\mu_{\mathbf{v}^{\{l\}}} = c_\sigma^{-1} O^{\{l-1\}} \Bigg[&\sigma^2_{\Re\left(\mathbf{y}^{\{l-1\}}\right)} + \jmath\sigma^2_{\Im\left(\mathbf{y}^{\{l-1\}}\right)} \\ &+ \sigma^2_{\Re\left(\boldsymbol{\gamma}_m^{\{l\}}\right)} + \jmath\sigma^2_{\Im\left(\boldsymbol{\gamma}_m^{\{l\}}\right)}\Bigg].\end{aligned} \tag{5.39}$$

5.B VARIANCE OF $\mathbf{v}^{\{l\}}$

The variance of $\mathbf{v}^{\{l\}}$ is

$$\sigma^2_{\mathbf{v}^{\{l\}}} = \mathrm{Var}\left[\Re\left(\mathbf{v}^{\{l\}}\right)\right] + \mathrm{Var}\left[\Im\left(\mathbf{v}^{\{l\}}\right)\right], \tag{5.40}$$

because the PT-RBF split-complex kernel.

First, considering the term $\mathrm{Var}\left[\Re\left(\mathbf{v}^{\{l\}}\right)\right]$, we have

$$\begin{aligned}\mathrm{Var}\left[\Re\left(\mathbf{v}^{\{l\}}\right)\right] = \left(\frac{O^{\{l-1\}}}{c_\sigma}\right)^2 \mathrm{Var}\Bigg[&\mathrm{E}\left[\Re\left(y_i^{\{l-1\}}\right)^2\right] \\ &+\mathrm{E}\left[\Re\left(\gamma_m^{\{l\}}\right)^2\right] - \mathrm{E}\left[2\Re\left(y_i^{\{l-1\}}\gamma_m^{\{l\}}\right)\right]\Bigg]\end{aligned} \tag{5.41}$$

Theoretically $\mathrm{Var}\left[\mathrm{E}\left[\Re\left(\gamma_m^{\{l\}}\right)^2\right] - \mathrm{E}\left[2\Re\left(y_i^{\{l-1\}}\gamma_m^{\{l\}}\right)\right]\right]$ should be zero, since $\mathrm{E}\left[\Re\left(\gamma_m^{\{l\}}\right)^2\right]$ is the variance of $\gamma_m^{\{l\}}$ and for $\mathrm{E}\left[2\Re\left(y_i^{\{l-1\}}\gamma_m^{\{l\}}\right)\right]$ both $\gamma_m^{\{l\}}$ and $y_i^{\{l-1\}}$ have zero mean. However, in practice, as our vector is limited in size, we will have an approximation with a small value. In fact, $\mathrm{Var}\left[\mathrm{E}\left[2\Re\left(y_i^{\{l-1\}}\gamma_m^{\{l\}}\right)\right]\right]$ is the variance of the sample mean, which is given by $\sigma^2(\mu_{\overline{x}}) = \frac{\sigma_x^2}{n}$. Thus, considering the variance of $y_i^{\{l-1\}}\gamma_m^{\{l\}}$ as the product of the variances of $y_i^{\{l-1\}}$ and $\gamma_m^{\{l\}}$, denoted as $\sigma^2_{y_i^{\{l-1\}}}$ and $\sigma^2_{\gamma_m^{\{l\}}}$ respectively, which is valid since they are independent, we have,

$$\mathrm{Var}\left[\mathrm{E}\left[2\Re\left(y_i^{\{l-1\}}\gamma_m^{\{l\}}\right)\right]\right] = \frac{4\Re\left(\sigma^2_{y_i^{\{l-1\}}}\sigma^2_{\gamma_m^{\{l\}}}\right)}{O^{\{l-1\}}} \tag{5.42}$$

and similarly $\mathrm{Var}\left[\mathrm{E}\left[\Re\left(\gamma_m^{\{l\}}\right)^2\right]\right]$ is the variance of the sample variance given by$\mathrm{Var}\left(\hat{\sigma}^2\right) = \frac{\mu_4 - \frac{n-3}{n-1}\sigma^4}{n}$, where μ_4 is the fourth central moment, given by $\mu_4 = \frac{\left(\sqrt{12\sigma^2}\right)^4}{80}$for $\mathcal{U}\left(0, \sigma^2\right)$, then,

$$\mathrm{Var}\left[\mathrm{E}\left[\Re\left(\gamma_m^{\{l\}}\right)^2\right]\right] = \left(\frac{\left(\sqrt{12\Re\left(\sigma^2_{\gamma_m^{\{l\}}}\right)}\right)^4}{80} - \frac{O^{\{l-1\}}-3}{O^{\{l-1\}}-1}\left(\sqrt{\Re\left(\sigma^2_{\gamma_m^{\{l\}}}\right)}\right)^4\right)\frac{1}{O^{\{l-1\}}} \quad (5.43)$$

which simplifies to,

$$\mathrm{Var}\left[\mathrm{E}\left[\Re\left(\gamma_m^{\{l\}}\right)^2\right]\right] = \frac{4\Re\left(\sigma^2_{\gamma_m^{\{l\}}}\right)^2}{5O^{\{l-1\}}} \quad (5.44)$$

In view of $\mathrm{Var}\left[\Re\left(y_i^{\{l-1\}}\right)^2\right]$ is a constant in regard to m, then $\mathrm{Var}\left[\mathrm{E}\left[\Re\left(y_i^{\{l-1\}}\right)^2\right]\right] = 0$, and $\mathrm{Var}\left[\Re\left(\mathbf{v}^{\{l\}}\right)\right] = \mathrm{Var}\left[\Im\left(\mathbf{v}^{\{l\}}\right)\right]$ and substituting (5.42), and (5.44) into (5.41), we obtain,

$$\mathrm{Var}\left[\left(\mathbf{v}^{\{l\}}\right)\right] = 2\left(\frac{O^{\{l-1\}}}{c_\sigma}\right)^2\left(\frac{4\Re\left(\sigma^2_{y_i^{\{l-1\}}}\sigma^2_{\gamma_m^{\{l\}}}\right)}{O^{\{l-1\}}} + \frac{4\left(\Re\left(\sigma^2_{\gamma_m^{\{l\}}}\right)\right)^2}{5O^{\{l-1\}}}\right) \quad (5.45)$$

Since $\sigma^2_{\bar{\mathbf{x}}} = \sigma^2_{y_i^{\{l-1\}}} = \sigma^2_{\gamma_m^{\{1\}}}$, from (5.10), we have,

$$\mathrm{Var}\left[\left(\mathbf{v}^{\{l\}}\right)\right] = \frac{12}{5}c_\sigma^{-2}O^{\{l-1\}}\sigma^4_{\gamma_m^{\{l\}}} \quad (5.46)$$

5.C VARIANCE OF $\mathbf{y}^{\{l\}}$

The variance of $\mathbf{y}^{\{l\}}$ is

$$\sigma^2_{\mathbf{y}^{\{l\}}} = \mathrm{Var}\left[\left(\mathbf{w}_m^{\{l\}}\right)^T\boldsymbol{\phi}^{\{l\}}\right],$$

where $m \in [1, 2, \cdots, I^{\{l\}}]$. Differently from (5.40), we cannot compute the expected value of the real and imaginary components separately since $\mathbf{y}^{\{l\}}$ is a linear combination result of a complex-valued vector $\boldsymbol{\phi}^{\{l\}}$ and a complex-valued matrix $\mathbf{W}^{\{l\}}$. Expanding (5.C)

$$\sigma^2_{\mathbf{y}^{\{l\}}} = \mathrm{Var}\left[\sum_{m=1}^{I^{\{l\}}}\phi_m^{\{l\}}w_{i,m}^{\{l\}}\right],$$

where $\phi_m^{\{l\}}$ and $w_{i,m}^{\{l\}}$ are the m-th elements of $\boldsymbol{\phi}^{\{l\}}$ and $\mathbf{w}_i^{\{l\}}$ respectively, and i is the i-th elements of $\mathbf{y}^{\{l\}}$, further to,

$$\sigma^2_{\mathbf{y}^{\{l\}}} = {I^{\{l\}}}^2 \mathrm{Var}\left[\mathrm{E}\left[\boldsymbol{\phi}^{\{l\}}\mathbf{w}_i^{\{l\}}\right]\right].$$

From (5.C) the variance $\sigma^2_{\mathbf{y}^{\{l\}}}$ incurs in the variance of the sample mean, since they are independent, we have, $\mathrm{Var}\left[\boldsymbol{\phi}^{\{l\}}\mathbf{w}_i^{\{l\}}\right] = \sigma^2_{\mathbf{w}_i^{\{l\}}}\sigma^2_{\boldsymbol{\phi}^{\{l\}}}$, therefore,

$$\mathrm{Var}\left[\mathrm{E}\left[\boldsymbol{\phi}^{\{l\}}\mathbf{w}_i^{\{l\}}\right]\right] = \frac{\sigma^2_{\mathbf{w}^{\{l\}}}\sigma^2_{\boldsymbol{\phi}^{\{l\}}}}{I^{\{l\}}} \tag{5.47}$$

Substituting this into (5.C), we arrive at the expression:

$$\sigma^2_{\mathbf{y}^{\{l\}}} = \mathrm{I}^{\{\mathrm{l}\}}\sigma^2_{\mathbf{w}^{\{l\}}}\sigma^2_{\boldsymbol{\phi}^{\{l\}}}.$$

From (5.2), and in view of $\Re\left(\mathbf{v}^{\{l\}}\right) = \Im\left(\mathbf{v}^{\{l\}}\right)$, thus $\sigma^2_{\boldsymbol{\phi}^{\{l\}}} = 2\mathrm{Var}\left\{\exp\left[-\Re\left(\mathbf{v}^{\{l\}}\right)\right]\right\}$, In order to calculate $\mathrm{Var}\left\{\exp\left[-\Re\left(\mathbf{v}^{\{l\}}\right)\right]\right\} = \mathrm{E}\left\{\exp\left[-\Re\left(\mathbf{v}^{\{l\}}\right)\right]^2\right\} - \mathrm{E}\left\{\exp\left[-\Re\left(\mathbf{v}^{\{l\}}\right)\right]\right\}^2$ we can assume $\Re\left(\mathbf{v}^{\{l\}}\right)$ with a normal distribution with mean $\mu_{\Re\left(\mathbf{v}^{\{l\}}\right)}$ and variance $\sigma^2_{\Re\left(\mathbf{v}^{\{l\}}\right)}$. Note that, it is an adequate assumption for a large dataset, due to the central limit theorem. Thus

$$\mathrm{E}\left\{\exp\left[-\Re\left(v_i^{\{l\}}\right)\right]\right\} = \frac{1}{\sqrt{2\pi\sigma^2_{\Re\left(\mathbf{v}^{\{l\}}\right)}}} \times \int_0^\infty \exp\left[-\Re\left(v_i^{\{l\}}\right)\right]\psi\left[\Re\left(v_i^{\{l\}}\right)\right]\, d\Re\left(v_i^{\{l\}}\right), \tag{5.48}$$

where $\psi\left(\cdot\right)$ is

$$\psi\left[\Re\left(v_i^{\{l\}}\right)\right] = \exp\left\{-\frac{\left[\Re\left(v_i^{\{l\}}\right) - \mu_{\Re\left(\mathbf{v}^{\{l\}}\right)}\right]^2}{2\sigma^2_{\Re\left(\mathbf{v}^{\{l\}}\right)}}\right\}. \tag{5.49}$$

Solving (5.48), yields

$$\mathrm{E}\left[\Re\left(\mathbf{v}^{\{l\}}\right)\right] = \frac{1}{2}\exp\left[\frac{\sigma^2_{\Re\left(\mathbf{v}^{\{l\}}\right)}}{2} - 2\mu_{\Re\left(\mathbf{v}^{\{l\}}\right)}\right] \times \left[\mathrm{erf}\left(\frac{\mu_{\Re\left(\mathbf{v}^{\{l\}}\right)} - 2\sigma^2_{\Re\left(\mathbf{v}^{\{l\}}\right)}}{\sqrt{2\sigma^2_{\Re\left(\mathbf{v}^{\{l\}}\right)}}}\right) + 1\right], \tag{5.50}$$

in which $\mathrm{erf}(\cdot)$ is the error function.

Relying on the results of Appendix 5.B, we consider that $\mu_{\Re\left(\mathbf{v}^{\{l\}}\right)} \gg \sigma^2_{\Re\left(\mathbf{v}^{\{l\}}\right)}$, which is acceptable when the center vectors of $\boldsymbol{\Gamma}^{\{l\}}$ are chosen near to $\mathbf{y}^{\{l-1\}}$. Then, (5.50) can be simplified to

$$\mathrm{E}\left\{\exp\left[-\Re\left(\mathbf{v}^{\{l\}}\right)\right]\right\} = \exp\left(\frac{\sigma^2_{\Re\left(\mathbf{v}^{\{l\}}\right)}}{2} - \mu_{\Re\left(\mathbf{v}^{\{l\}}\right)}\right), \tag{5.51}$$

similarly

$$\mathrm{E}\left\{\exp\left[-\Re\left(\mathbf{v}^{\{l\}}\right)\right]^2\right\} = \exp\left(2\sigma^2_{\Re\left(\mathbf{v}^{\{l\}}\right)} - 2\mu_{\Re\left(\mathbf{v}^{\{l\}}\right)}\right). \tag{5.52}$$

Then,

$$\begin{aligned}\mathrm{Var}\left\{\exp\left[-\Re\left(\mathbf{v}^{\{l\}}\right)\right]\right\} = \exp&\left(2\sigma^2_{\Re\left(\mathbf{v}^{\{l\}}\right)} - 2\mu_{\Re\left(\mathbf{v}^{\{l\}}\right)}\right)\\ &- \exp\left(\frac{\sigma^2_{\Re\left(\mathbf{v}^{\{l\}}\right)}}{2} - \mu_{\Re\left(\mathbf{v}^{\{l\}}\right)}\right)^2\end{aligned} \tag{5.53}$$

Which, can be simplified to

$$\sigma^2_{\boldsymbol{\phi}^{\{l\}}} = \sigma^2_{\mathbf{v}^{\{l\}}} \exp\left(-2\mu_{\mathbf{v}^{\{l\}}}\right) \tag{5.54}$$

Replacing (5.54) into (5.C), results in

$$\sigma^2_{\mathbf{y}^{\{l\}}} = I^{\{l\}}\sigma^2_{\mathbf{w}^{\{l\}}}\sigma^2_{\mathbf{v}^{\{l\}}} \exp\left(-2\mu_{\mathbf{v}^{\{l\}}}\right).$$

Then, finally, replacing (5.46), results in

$$\sigma^2_{\mathbf{y}^{\{l\}}} = \frac{12}{5} c_\sigma^{-2} \exp(-2\mu_{\mathbf{v}^{\{l\}}}) I^{\{l\}} O^{\{l-1\}} \sigma^2_{\mathbf{w}^{\{l\}}} \sigma^4_{\gamma^{\{l\}}},$$

Chapter 6

Deep Complex-valued Radial Basis Function Neural Networks and Parameter Selection

Authors: Jonathan Aguiar Soares, Vinícius H. Luiz, Dalton Soares Arantes, and Kayol Soares Mayer

Abstract

In the ever-evolving field of artificial neural networks and learning systems, complex-valued neural networks (CVNNs) have become a cornerstone, achieving exceptional performance in image processing and telecommunications. More precisely, in digital communication systems, CVNNs have been delivering significant results in tasks like equalization, channel estimation, beamforming, and decoding. Among the CVNN architectures, the complex-valued radial basis function neural network (C-RBF) stands out, especially when operating in noisy environments such as 5G multiple-input multiple-output (MIMO) systems. In such a context, this paper extends the classical shallow C-RBF to deep architectures, increasing its flexibility for a wider range of applications. Also, based on the parameter selection of the phase transmittance radial basis function (PT-RBF) neural network, we propose an initialization scheme for the deep C-RBF. Via rigorous simulations conforming to 3GPP TS 38 standards for digital communications, our method not only outperforms conventional initialization strategies like random, K-means, and constellation-based methods but it also seems to be the only approach to achieve successful convergence for deep C-RBF architectures. These findings pave the way to more robust and efficient neural network deployments in complex-valued digital communication systems.

Keywords: Neural Networks, Complex-valued Neural Networks, Radial Basis Function, Deep Learning, Initialization.

This Chapter is a replica of the following manuscript: Jonathan Aguiar Soares, Vinícius H. Luiz, Dalton Soares Arantes, and Kayol Soares Mayer, "Deep Complex-valued Radial Basis Function Neural Networks and Parameter Selection" in 19th International Symposium on Wireless Communication Systems, July 2024, doi: 10.1109/ISWCS61526.2024.10639101.

6.1 INTRODUCTION

Recently, in communication systems, CVNNs have been studied in several applications, such as equalization, channel estimation, beamforming, and decoding (MAYER et al., 2019c; DING; HIROSE, 2020; ZHANG et al., 2021b; LI et al., 2022; MAYER; SOARES; ARANTES, 2020; KAMIYAMA; KOBAYASHI; IWASHITA, 2021; FREIRE et al., 2021; SOARES et al., 2021a; XU et al., 2022; CHU; GAO; LIU, et al., 2022; MAYER et al., 2022; YANG et al., 2022; XIAO; YANG; FENG, 2023). This growing interest is related to enhanced functionality, improved performance, and reduced training time when compared with real-valued neural networks (RVNNs) (HIROSE; YOSHIDA, 2012a; BARRACHINA et al., 2021; CRUZ; MAYER; ARANTES, 2022; ZHANG; GAO; ZHOU, 2022).

The effectiveness of neural networks is critically dependent on several factors, such as initialization, regularization, and optimization (HUMBIRD; PETERSON; MCCLARREN, 2019). Although regularization and optimization techniques are vital to speed up the training process and reduce steady-state error (HU et al., 2021), depending on the initial parameter selection the neural network can get stuck at local minima, achieving suboptimal solutions (NARKHEDE; BARTAKKE; SUTAONE, 2022). For radial basis function (RBF)-based neural networks, this problem is even worse since, for each layer, there are four parameters (synaptic weight, bias, center vectors, and center variances) in contrast to two parameters (synaptic weights and bias) of usual multilayer perceptron neural networks.

In this context, with a focus on the C-RBF neural network (MAYER et al., 2022), we propose an extension for deep learning and a novel parameter selection scheme. This scheme aims to initialize synaptic weights, biases, center vectors, and center variances in the complex domain. Notably, existing literature offers limited guidance on initialization techniques for multilayer RBF-based CVNNs. Despite this gap, our study compares the proposed approach against well-known methods such as random initialization (WALLACE; TSAPATSOULIS; KOLLIAS, 2005), K-means clustering (TURNBULL; ELKAN, 2005), and constellation-based initialization (LOSS et al., 2007a). To the best of our knowledge, this is the first work proposing the architecture, training algorithm, and parameter selection for a multi-layered C-RBF.

6.2 C-RBF NEURAL NETWORKS

The complex-valued Gaussian neuron is a natural extension of the well-known Gaussian neuron for the complex domain (CHEN; MCLAUGHLIN; MULGREW, 1994). Similarly to its real-valued version, the output of the C-RBF neuron is described as

$$y[n] = w[n]\phi[n] + b[n], \tag{6.1}$$

in which $\phi[n] \in \mathbb{R}$ is the Gaussian kernel output

$$\phi[n] = \exp\left(-\frac{\|\mathbf{x}[n] - \boldsymbol{\gamma}[n]\|_2^2}{\sigma[n]}\right), \tag{6.2}$$

and $\boldsymbol{\gamma}[n] \in \mathbb{C}^P$ is the Gaussian center, $\sigma[n] \in \mathbb{R}$ is the variance. Note that the bias $b[n] \in \mathbb{C}$ is a linear complex-valued synaptic weight like $w[n] \in \mathbb{C}$, but considering the Gaussian output equals one. Unlike the RBF neuron, the C-RBF neuron Gaussian center, synaptic weight, and bias are complex-valued free parameters, which are essential to map a complex-valued input $\mathbf{x}[n] \in \mathbb{C}^P$ into a complex-valued output $y[n] \in \mathbb{C}$. By (6.2), the complex-valued input is firstly mapped into a real-valued scalar via the Euclidean norm of the Gaussian kernel. As the variance is also a real-valued parameter, the Gaussian kernel output is consequently a real-valued scalar. Thus, the complex mapping to the output is only possible because of the synaptic weights and bias.

6.2.1 Shallow C-RBF

The main differences between the C-RBF and RBF regard the free parameters domains and the backpropagation training. In a C-RBF neural network with P inputs, R outputs, and M Gaussian neurons, the vector of outputs $\mathbf{y}[n] \in \mathbb{C}^R$ is given by

$$\mathbf{y}[n] = \mathbf{W}[n]\boldsymbol{\phi}[n] + \mathbf{b}[n], \tag{6.3}$$

where $\mathbf{W}[n] \in \mathbb{C}^{R\times M}$ is the matrix of synaptic weights, $\boldsymbol{\phi}[n] \in \mathbb{R}^M$ is the vector of Gaussian kernels, and $\mathbf{b}[n] \in \mathbb{C}^R$ is the vector of bias.

The m-th Gaussian kernel of $\boldsymbol{\phi}[n]$ is formulated as

$$\phi_m[n] = \exp\left(-\frac{\|\mathbf{x}[n] - \boldsymbol{\gamma}_m[n]\|_2^2}{\sigma_m[n]}\right), \tag{6.4}$$

in which $\boldsymbol{\gamma}_m[n] \in \mathbb{C}^P$ and $\sigma_m[n] \in \mathbb{R}$ are the m-th vectors of Gaussian Centers and variances, respectively.

Albeit $\mathbf{b}[n]$ and $\mathbf{W}[n]$ can be considered as only one free parameter, for the sake of simplicity we assume it as separate free parameters. Therefore, the C-RBF is a shallow ANN with four free parameters (i.e., matrix of synaptic weights $\mathbf{W}[n]$; vector of bias $\mathbf{b}[n]$; matrix of Gaussian centers $\boldsymbol{\Gamma}[n] \in \mathbb{C}^{M\times P}$; and vector of variances $\boldsymbol{\sigma}[n] \in \mathbb{R}^M$), whose updates are performed via the steepest descent algorithm as

$$\begin{aligned}
w_{r,m}[n+1] &= w_{r,m}[n] - \eta_w \nabla_w J[n],\\
b_r[n+1] &= b_r[n] - \eta_b \nabla_b J[n],\\
\boldsymbol{\gamma}_m[n+1] &= \boldsymbol{\gamma}_m[n] - \eta_\gamma \nabla_\gamma J[n],\\
\sigma_m[n+1] &= \sigma_m[n] - \eta_\sigma \nabla_\sigma J[n],
\end{aligned} \tag{6.5}$$

where η_w, η_b, η_γ, and η_σ are the respective adaptive steps of $w_{r,m}$, b_r, $\boldsymbol{\gamma}_m$, and σ_m. Also, ∇_w, ∇_b, ∇_γ, and ∇_σ are the complex gradient operators of $w_{r,m}$, b_r, $\boldsymbol{\gamma}_m$, and σ_m, respectively. Furthermore, $J[n]$ is the quadratic cost function

$$J[n] = \frac{1}{2} \|\mathbf{e}[n]\|_2^2 = \frac{1}{2} \|\mathbf{d}[n] - \mathbf{y}[n]\|_2^2, \tag{6.6}$$

in which $\mathbf{e}[n] = \mathbf{d}[n] - \mathbf{y}[n] \in \mathbb{C}^R$ is the error vector and $\mathbf{d}[n] \in \mathbb{C}^R$ is the vector of desired outputs.

Solving the gradients in (6.5), and organizing the equations in matrix structures, we obtain

$$\begin{gathered}
\mathbf{W}[n+1] = \mathbf{W}[n] + \eta_w \mathbf{e}[n] \boldsymbol{\phi}^T[n], \\
\mathbf{b}[n+1] = \mathbf{b}[n] + \eta_b \mathbf{e}[n], \\
\boldsymbol{\Gamma}[n+1] = \boldsymbol{\Gamma}[n] + \eta_{\boldsymbol{\gamma}} \mathrm{diag}\left(\boldsymbol{\xi}[n] \odot \boldsymbol{\beta}[n]\right) \left(\mathbf{X}[n] - \boldsymbol{\Gamma}[n]\right), \\
\boldsymbol{\sigma}[n+1] = \boldsymbol{\sigma}[n] + \eta_\sigma \boldsymbol{\xi}[n] \odot \boldsymbol{\beta}[n] \odot \mathbf{v}[n],
\end{gathered} \tag{6.7}$$

where $\boldsymbol{\xi}[n] = \Re\left(\mathbf{W}[n]\right)^T \Re\left(\mathbf{e}[n]\right) + \Im\left(\mathbf{W}[n]\right)^T \Im\left(\mathbf{e}[n]\right) \in \mathbb{R}^M$ is the vector of synaptic transmittance, and $\boldsymbol{\beta}[n] \in \mathbb{R}^M$ is the vector of Gaussian weighted kernel, with the m-th component $\beta_m[n] = \phi_m[n]/\sigma_m[n]$. The expanded input matrix $\mathbf{X}[n] \in \mathbb{C}^{M \times P}$ is

$$\mathbf{X}[n] = \begin{bmatrix} — & \mathbf{x}^T[n] & — \\ — & \mathbf{x}^T[n] & — \\ & \vdots & \\ — & \mathbf{x}^T[n] & — \end{bmatrix}. \tag{6.8}$$

6.2.2 Proposed Deep C-RBF

The deep C-RBF is defined with L hidden layers (excluding the input layer), where the superscript $l \in [0, 1, \cdots, L]$ denotes the layer index and $l = 0$ is the input layer. The l-th layer (excluding the input layer $l = 0$) is composed by $I^{\{l\}}$ neurons, $O^{\{l\}}$ outputs, and has a matrix of synaptic weights $\mathbf{W}^{\{l\}} \in \mathbb{C}^{O^{\{l\}} \times I^{\{l\}}}$, a bias vector $\mathbf{b}^{\{l\}} \in \mathbb{C}^{O^{\{l\}}}$, a matrix of center vectors $\boldsymbol{\Gamma}^{\{l\}} \in \mathbb{C}^{I^{\{l\}} \times O^{\{l-1\}}}$, and a variance vector $\boldsymbol{\sigma}^{\{l\}} \in \mathbb{R}^{I^{\{l\}}}$. Notice that $\bar{\mathbf{x}} \in \mathbb{C}^P$ is the deep C-RBF normalized input vector (P inputs) and $\mathbf{y}^{\{L\}} \in \mathbb{C}^R$ is the deep C-RBF output vector (R outputs). The l-th hidden layer output vector $\mathbf{y}^{\{l\}} \in \mathbb{C}^{O^{\{l\}}}$ is given by

$$\mathbf{y}^{\{l\}} = \mathbf{W}^{\{l\}} \boldsymbol{\phi}^{\{l\}} + \mathbf{b}^{\{l\}}, \tag{6.9}$$

where $\boldsymbol{\phi}^{\{l\}} \in \mathbb{R}^{I^{\{l\}}}$ is the vector of Gaussian kernels.

The m-th Gaussian kernel of the l-th hidden layer is formulated as

$$\phi_m^{\{l\}} = \exp\left[-v_m^{\{l\}}\right], \tag{6.10}$$

in which $v_m^{\{l\}}$ is the m-th Gaussian kernel input of the l-th hidden layer, described as

$$v_m^{\{l\}} = \frac{\left\| \mathbf{y}^{\{l-1\}} - \boldsymbol{\gamma}_m^{\{l\}} \right\|_2^2}{\sigma_m^{\{l\}}}, \tag{6.11}$$

where $\mathbf{y}^{\{l-1\}} \in \mathbb{C}^{O^{\{l-1\}}}$ is the output vector of the $(l-1)$-th hidden layer (except for the first hidden layer that $\mathbf{y}^{\{0\}} = \bar{\mathbf{x}}$), $\boldsymbol{\gamma}_m^{\{l\}} \in \mathbb{C}^{O^{\{l-1\}}}$ is the m-th vector of Gaussian centers of the l-th hidden layer, $\sigma_m^{\{l\}} \in \mathbb{R}$ is the respective m-th variance.

Similarly to (6.5), we can define a generalized steepest descent algorithm to the l-th layer, as

$$\begin{aligned}
w_{r,m}^{\{l\}}[n+1] &= w_{r,m}^{\{l\}}[n] - \eta_w \nabla_w^{\{l\}} J[n], \\
b_r^{\{l\}}[n+1] &= b_r^{\{l\}}[n] - \eta_b \nabla_b^{\{l\}} J[n], \\
\boldsymbol{\gamma}_m^{\{l\}}[n+1] &= \boldsymbol{\gamma}_m^{\{l\}}[n] - \eta_\gamma \nabla_\gamma^{\{l\}} J[n], \\
\sigma_m^{\{l\}}[n+1] &= \sigma_m^{\{l\}}[n] - \eta_\sigma \nabla_\sigma^{\{l\}} J[n].
\end{aligned} \tag{6.12}$$

Solving the gradients in (6.12), and organizing the resulting equations in matrix structures, we obtain

$$\begin{aligned}
\mathbf{W}^{\{l\}}[n+1] &= \mathbf{W}^{\{l\}}[n] + \eta_w^{\{l\}} \boldsymbol{\psi}^{\{l\}}[n] \left(\boldsymbol{\phi}^{\{l\}}[n] \right)^T, \\
\mathbf{b}^{\{l\}}[n+1] &= \mathbf{b}^{\{l\}}[n] + \eta_b^{\{l\}} \boldsymbol{\psi}^{\{l\}}[n], \\
\boldsymbol{\Gamma}^{\{l\}}[n+1] &= \boldsymbol{\Gamma}^{\{l\}}[n] - \eta_{\boldsymbol{\gamma}}^{\{l\}} \boldsymbol{\delta}^{\{l\}}[n] \left(\mathbf{Y}^{\{l-1\}}[n] - \boldsymbol{\Gamma}^{\{l\}}[n] \right), \\
\boldsymbol{\sigma}^{\{l\}}[n+1] &= \boldsymbol{\sigma}^{\{l\}}[n] - \eta_\sigma^{\{l\}} \boldsymbol{\delta}^{\{l\}}[n] \mathbf{v}^{\{l\}}[n],
\end{aligned} \tag{6.13}$$

where $\boldsymbol{\psi}^{\{l\}}$ and $\boldsymbol{\delta}^{\{l\}}[n]$ are presented at the bottom of the next page, and $\boldsymbol{\beta}^{\{l\}}[n] \in \mathbb{R}^{I^{\{l\}}}$ is the vector of Gaussian weighted kernel of the l-th hidden layer, with the m-th component $\beta_m^{\{l\}}[n] = \phi_m^{\{l\}}[n]/\sigma_m^{\{l\}}[n]$. The vector $\mathbf{1}_{\mathbf{I}^{\{l+1\}}}$ is composed of $I^{\{l+1\}}$ ones, and $\mathbf{Y}^{\{l\}}[n] \in \mathbb{C}^{I^{\{l+1\}} \times O^{\{l\}}}$ is the expanded matrix of layer's outputs, in which each row is given by

$$\mathbf{Y}^{\{l\}}[n] = \begin{bmatrix} — & \left(\mathbf{y}^{\{l\}}[n]\right)^T & — \\ — & \left(\mathbf{y}^{\{l\}}[n]\right)^T & — \\ & \vdots & \\ — & \left(\mathbf{y}^{\{l\}}[n]\right)^T & — \end{bmatrix}. \tag{6.14}$$

$$\boldsymbol{\psi}^{\{l\}}[n] = \begin{cases} \left[\mathbf{Y}^{\{l\}}[n] - \boldsymbol{\Gamma}^{\{l+1\}}[n] \right]^T \boldsymbol{\delta}^{\{l+1\}}[n] \mathbf{1}_{\mathbf{I}^{\{l+1\}}}, & \text{for } 0 < l < L, \\ \mathbf{d}[n] - \mathbf{y}[n] = \mathbf{e}[n], & \text{for } l = L, \end{cases} \tag{6.15}$$

$$\boldsymbol{\delta}^{\{l\}}[n] = -\operatorname{diag}\left\{ \left[\Re\left(\mathbf{W}^{\{l\}}[n]\right)^T \Re\left(\boldsymbol{\psi}^{\{l\}}[n]\right) + \Im\left(\mathbf{W}^{\{l\}}[n]\right)^T \Im\left(\boldsymbol{\psi}^{\{l\}}[n]\right) \right] \odot \boldsymbol{\beta}^{\{l\}}[n] \right\}. \tag{6.16}$$

6.3 PROPOSED DEEP C-RBF PARAMETER INITIALIZATION

Based on (SOARES; MAYER; ARANTES, 2024), to properly initialize the deep C-RBF parameters, we first need to understand the relationship between the input vector $\mathbf{x}$ and the Gaussian center vectors $\boldsymbol{\gamma}_m^{\{1\}}$. In (6.10), regarding (6.11), and keeping $\sigma_m^{\{1\}}$ constant, the closer $\boldsymbol{\gamma}_m^{\{1\}}$ is to $\mathbf{x}$, higher is the value of $\phi_m^{\{1\}}$. For example, if $\boldsymbol{\gamma}_m^{\{1\}} = \mathbf{x}$ then $\phi_m^{\{1\}} = 1$. On the other hand, if $\boldsymbol{\gamma}_m^{\{1\}}$ is set far from $\mathbf{x}$, then $\phi_m^{\{1\}} \to 0$. In this context, to not saturate or vanish $\phi_m^{\{1\}}$, we assume $\mu_{\bar{\mathbf{x}}} = \mu_{\boldsymbol{\gamma}^{\{1\}}} = 0$ and $\sigma_{\bar{\mathbf{x}}}^2 = \sigma_{\boldsymbol{\gamma}^{\{1\}}}^2$, where $\bar{\mathbf{x}}$ is the normalized input dataset. Furthermore, we expect that depending on the dataset inputs, $\phi_m^{\{1\}}$ varies reasonably. For example, considering $v_m^{\{1\}} = 5$ and $v_m^{\{1\}} = 10$, the variation in $\phi_m^{\{1\}}$ is only 4.54×10^{-5}. In contrast, considering $v_m^{\{1\}} = 0$ and $v_m^{\{1\}} = 3$, the variation in $\phi_m^{\{1\}}$ is 0.95. Then, it is desirable that $\mu_{v^{\{1\}}}$ is not too large. Based on Appendix A of (SOARES; MAYER; ARANTES, 2024), the expected value of $v^{\{1\}}$ is

$$\mu_{\mathbf{v}^{\{1\}}} = \frac{P}{c_\sigma}\left[\sigma^2_{\Re(\bar{\mathbf{x}})} + \sigma^2_{\Im(\bar{\mathbf{x}})} + \sigma^2_{\Re\left(\boldsymbol{\gamma}_m^{\{1\}}\right)} + \sigma^2_{\Im\left(\boldsymbol{\gamma}_m^{\{1\}}\right)}\right], \tag{6.17}$$

in which $\sigma_{\bar{\mathbf{x}}}^2 = 2\sigma^2_{\Re(\bar{\mathbf{x}})} = 2\sigma^2_{\Im(\bar{\mathbf{x}})}$ is the variance of $\bar{\mathbf{x}}$, $\sigma^2_{\boldsymbol{\gamma}_m^{\{1\}}} = 2\sigma^2_{\Re\left(\boldsymbol{\gamma}_m^{\{1\}}\right)} = 2\sigma^2_{\Im\left(\boldsymbol{\gamma}_m^{\{1\}}\right)}$ is the variance of $\boldsymbol{\gamma}_m^{\{1\}}$, $c_\sigma = \sigma_m^{\{1\}}\ \forall\ m$, and c_σ is a positive and nonzero constant.

As $\sigma_{\bar{\mathbf{x}}}^2 = \sigma^2_{\boldsymbol{\gamma}^{\{1\}}}$, from (6.17), we have

$$\sigma_{\bar{\mathbf{x}}}^2 = \frac{c_\sigma \mu_{\mathbf{v}^{\{1\}}}}{2P}. \tag{6.18}$$

Based on (6.18), the normalized input is given as

$$\bar{\mathbf{x}} = \frac{(\mathbf{x} - \mu_{\mathbf{x}})}{\sqrt{\sigma_{\mathbf{x}}^2}}\sqrt{\frac{c_\sigma \mu_{\mathbf{v}^{\{1\}}}}{2P}}, \tag{6.19}$$

where $\mu_{\mathbf{x}}$ and $\sigma_{\mathbf{x}}^2$ are applied to adjust the mean and variance of $\bar{\mathbf{x}}$ before the normalization by (6.18).

Similarly, in the first hidden layer, the normalized matrix of center vectors is

$$\boldsymbol{\Gamma}^{\{1\}} \sim \mathcal{CG}\left(0, \frac{c_\sigma \mu_{\mathbf{v}^{\{1\}}}}{2P}\right). \tag{6.20}$$

In order to normalize the output dataset $\mathbf{d}$, we need to compute the variance of the output vector $\mathbf{y}^{\{L\}}$, by

$$\sigma^2_{\mathbf{y}^{\{L\}}} = \mathrm{Var}\left[\mathbf{W}^{\{L\}}\boldsymbol{\phi}^{\{L\}} + \mathbf{b}^{\{L\}}\right]. \tag{6.21}$$

We assume that $\mathbf{b}^{\{l\}}$ is initialized with zeros, for all layers. Thus, based on Appendix C of (SOARES; MAYER; ARANTES, 2024), (6.21) results in

$$\sigma^2_{\mathbf{y}^{\{l\}}} = \frac{12}{5}\left(\frac{\sigma^2_{\gamma_m^{\{l\}}}}{c_\sigma \exp\left(\mu_{\mathbf{v}^{\{l\}}}\right)}\right)^2 I^{\{l\}} O^{\{l-1\}} \sigma^2_{\mathbf{W}^{\{l\}}}, \tag{6.22}$$

where $\sigma^2_{\mathbf{W}\{\mathbf{L}\}}$ is the variance of $\mathbf{W}^{\{L\}}$, and $\mu_{\mathbf{v}^{\{L\}}}$ is the expected value of $\mathbf{v}^{\{L\}}$. Choosing $\sigma^2_{\mathbf{y}^{\{L\}}} = \sigma^2_{\bar{\mathbf{d}}}$, i.e., the variance of the C-RBF output equal to the variance of the normalized output dataset, yields the initialization of $\mathbf{W}^{\{L\}}$ as

$$\mathbf{W}^{\{L\}} \sim \mathcal{CG}\left(0, \frac{\sigma^2_{\bar{\mathbf{d}}}}{\frac{12}{5}\left(\frac{\sigma^2_{\gamma_m^{\{l\}}}}{c_\sigma \exp\left(\mu_{\mathbf{v}^{\{l\}}}\right)}\right)^2 I^{\{l\}} O^{\{l-1\}}}\right), \tag{6.23}$$

in which the output dataset can be normalized by

$$\bar{\mathbf{d}} = \frac{(\mathbf{d} - \mu_{\mathbf{d}})}{\sqrt{\sigma^2_{\mathbf{d}}}} \sqrt{\sigma^2_{\mathbf{y}^{\{L\}}}} = \frac{(\mathbf{d} - \mu_{\mathbf{d}})}{\sqrt{\sigma^2_{\mathbf{d}}}} \sqrt{\frac{c_\sigma \mu_{\mathbf{v}^{\{L\}}}}{2R}}. \tag{6.24}$$

Relying on (6.20), we can generalize the initialization of $\boldsymbol{\Gamma}^{\{l\}}$, as

$$\boldsymbol{\Gamma}^{\{l\}} \sim \mathcal{CG}\left(0, \frac{c_\sigma \mu_{\mathbf{v}^{\{l\}}}}{2O^{\{l-1\}}}\right). \tag{6.25}$$

From (6.18), the variance of the output hidden layers can be considered as

$$\sigma^2_{\mathbf{y}^{\{l\}}} = \frac{c_\sigma \mu_{\mathbf{v}^{\{l+1\}}}}{2O^{\{l\}}}, \tag{6.26}$$

where, replacing $\sigma^2_{\bar{\mathbf{d}}}$ by (6.26) into (6.23), yields

$$\mathbf{W}^{\{L\}} \sim \mathcal{CG}\left(0, \frac{5 c_\sigma O^{\{l-1\}}}{6 I^{\{l\}} O^{\{l\}} \mu_{\mathbf{v}^{\{l+1\}}} \exp(-2\mu_{\mathbf{v}^{\{l\}}})}\right). \tag{6.27}$$

It is important to note that, (6.19) and (6.24) only hold for $\sigma^2_{\mathbf{x}} = 2\sigma^2_{\Re(\mathbf{x})} = 2\sigma^2_{\Im(\mathbf{x})}$ and $\sigma^2_{\mathbf{d}} = 2\sigma^2_{\Re(\mathbf{d})} = 2\sigma^2_{\Im(\mathbf{d})}$, respectively. For the particular case of $\sigma^2_{\Re(\mathbf{x})} \neq \sigma^2_{\Im(\mathbf{x})}$ and $\sigma^2_{\Re(\mathbf{d})} \neq \sigma^2_{\Im(\mathbf{d})}$, then (6.19) and (6.24) become

$$\bar{\mathbf{x}} = \left[\frac{(\Re(\mathbf{x}) - \mu_{\Re(\mathbf{x})})}{\sqrt{2\sigma^2_{\Re(\mathbf{x})}}} + \jmath \frac{(\Im(\mathbf{x}) - \mu_{\Im(\mathbf{x})})}{\sqrt{2\sigma^2_{\Im(\mathbf{x})}}}\right] \sqrt{\frac{c_\sigma \mu_{\mathbf{v}^{\{1\}}}}{2P}}, \tag{6.28}$$

$$\bar{\mathbf{d}} = \left[\frac{(\Re(\mathbf{d}) - \mu_{\Re(\mathbf{d})})}{\sqrt{2\sigma^2_{\Re(\mathbf{d})}}} + \jmath \frac{(\Im(\mathbf{d}) - \mu_{\Im(\mathbf{d})})}{\sqrt{2\sigma^2_{\Im(\mathbf{d})}}}\right] \sqrt{\frac{c_\sigma \mu_{\mathbf{v}^{\{L\}}}}{2R}}. \tag{6.29}$$

6.4 RESULTS

For the sake of simplification, in the proposed approach the parameters c_σ and $\mu_{\mathbf{v}^{\{l\}}}$ were set to 1, for all layers. Then, the initializations and normalizations become

$$\mathbf{b}^{\{l\}} = \mathbf{0} + \jmath \mathbf{0}, \tag{6.30}$$

$$\boldsymbol{\sigma}^{\{l\}} = \mathbf{1} + \jmath\mathbf{1}, \tag{6.31}$$

$$\boldsymbol{\Gamma}^{\{l\}} \sim \mathcal{CG}\left(0, \frac{1}{2O^{\{l-1\}}}\right), \tag{6.32}$$

$$\mathbf{W}^{\{l\}} \sim \mathcal{CG}\left(0, \frac{5O^{\{l-1\}}\exp(2)}{6\mathrm{I}^{\{l-1\}}O^{\{l\}}}\right), \tag{6.33}$$

$$\bar{\mathbf{x}} = \frac{(\mathbf{x} - \mu_{\mathbf{x}})}{\sqrt{\sigma^2_{\mathbf{x}}}}\sqrt{\frac{1}{2P}}, \tag{6.34}$$

$$\bar{\mathbf{d}} = \frac{(\mathbf{d} - \mu_{\mathbf{d}})}{\sqrt{\sigma^2_{\mathbf{d}}}}\sqrt{\frac{1}{2R}}. \tag{6.35}$$

For the random initialization, we defined $\sigma^2_{\boldsymbol{\Gamma}^{\{l\}}} = 1$. The K-means and constellation-based initializations are obtained from the input and output datasets, respectively (see (SOARES; MAYER; ARANTES, 2024)).

Based on (SOARES; MAYER; ARANTES, 2023), we consider a space-time block coding (STBC) simulation system with the 3GPP TS 38.211 specification for 5G physical channels and modulation (5G..., 2022). The orthogonal frequency-division multiplexing (OFDM) is defined with 60-kHz subcarrier spacing, 256 active subcarriers, and a block-based pilot scheme. Symbols are modulated with 16-QAM and, for the multiple-input multiple-output (MIMO) setup, 4 antennas are employed both at the transmitter and receiver. Based on the tapped delay line-A (TDL-A) from the 3GPP TR 38.901 5G channel models (5G..., 2022), the MIMO channel follows the TDLA from the 3GPP TR 38.104 5G radio base station transmission and reception (5G..., 2022). The TDLA is described with 12 taps, with varying delays from 0.0 ns to 290 ns and powers from -26.2 dB to 0 dB. A Rayleigh distribution is used to compute each sub-channel. To avoid influencing the learning curves, we do not take into account the Doppler effect, and we do not employ the inference learning techniques proposed by (SOARES; MAYER; ARANTES, 2023). The CVNNs operate with 16 inputs and 4 outputs. The inputs are taken from the OFDM demodulator outputs, one at a time (see (SOARES; MAYER; ARANTES, 2023), Fig. 1). Training and validation were performed for $3,840$ and $1,280$ instances, respectively. To assess performance, we calculated the Mean Squared Error (MSE), defined as $\mathrm{MSE} = \frac{1}{n}\sum_{i=1}^{n}(y_i - \hat{y}_i)^2$, where y_i represents the total transmitted constellation symbols over all 20 simulations and $\hat{y}_i$ represents the respective estimated symbol from the C-RBF.

Fig. 6.4.1 illustrates the mean squared error (MSE) convergence results for 1000 epochs of training (solid lines) and validation (asterisks) of the C-RBF with a hidden layer ($I^{\{1\}} = 64$ neurons). Results were averaged over 20 subsequent simulations with a bit energy to noise power spectral density ratio $\mathrm{E_b/N_0} = 26$ dB. Table 6.4.1 depicts the C-RBF hyperparameters empirically optimized for each initialization scheme. None of the algorithms presented under- or over-fitting. The random initialization presented the

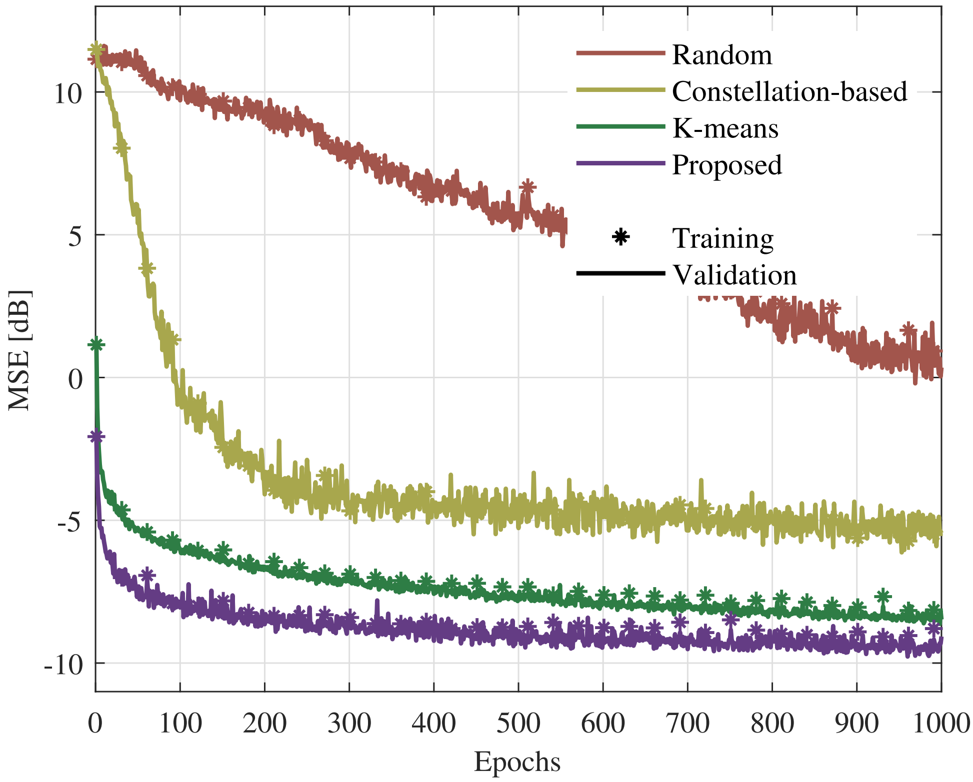

Figure 6.4.1 – MSE convergence results of training (solid lines) and validation (asterisks) of the C-RBF initialization with a hidden layer ($I^{\{1\}} = 64$ neurons) for joint channel estimation and decoding in a MIMO-OFDM 4×4 system, operating with 16-QAM and 256 subcarriers. Results were averaged over 20 subsequent simulations with $\mathrm{E_b/N_0} = 26$ dB. The lower the steady state MSE, the better the performance.

Table 6.4.1 – Single layer C-RBF optimized hyper-parameters.

Algorithm	η_w	η_b	η_γ	η_σ
Random	0.5	0.5	0.5	0.5
Constellation-based	0.5	0.5	0.5	0.5
K-means	0.1	0.1	0.4	0.2
Proposed Approach	0.1	0.1	0.4	0.2

poorest convergence results, with a steady-state error of -6 dB. On the other hand, the constellation-based and K-means initializations achieved a steady-state error of -6 dB and -7.5 dB, respectively. The best results were obtained with the proposed approach, with -9.5 dB of steady-state error. For comparison results regarding the convergence rate, considering MSE $= -5$ dB, the proposed approach reaches this mark in five training epochs, followed by the K-means (11 epochs), constellations-based (80 epochs), and random initialization (165 epochs).

For further comparison, we have also employed the initialization schemes for C-RBFs with two, three, and four hidden layers. However, the K-means was not considered since it is only suitable for shallow RBFs. In addition, although several trials were attempted,

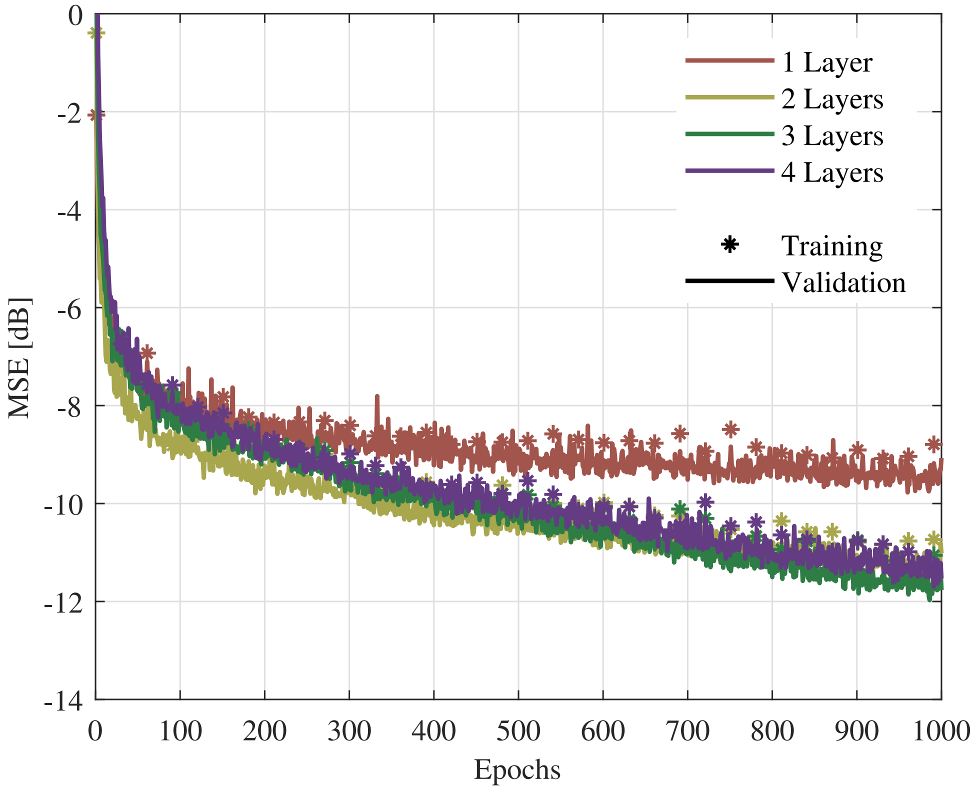

Figure 6.4.2 – MSE convergence results of training (solid lines) and validation (stars) of the proposed initialization approach with one ($I^{\{1\}} = 64$ neurons), two ($I^{\{1\}} = 48$ and $I^{\{2\}} = 16$ neurons), three ($I^{\{1\}} = 24$, $I^{\{2\}} = 24$, and $I^{\{3\}} = 16$ neurons), and four ($I^{\{1\}} = 16$, $I^{\{2\}} = 16$, $I^{\{3\}} = 16$, and $I^{\{4\}} = 16$ neurons) hidden layers for joint channel estimation and decoding in a MIMO-OFDM 4×4 system, operating with 16-QAM and 256 subcarriers. Results were averaged over 20 subsequent simulations with $\mathrm{E_b/N_0} = 26$ dB. The lower the steady state MSE, the better the performance.

no convergence was achieved for the random and constellation-based initializations. Thus, Fig. 6.4.2 shows the convergence results for the proposed approach for the C-RBFs with one ($I^{\{1\}} = 64$ neurons), two ($I^{\{1\}} = 48$ and $I^{\{2\}} = 16$ neurons), three ($I^{\{1\}} = 24$, $I^{\{2\}} = 24$, and $I^{\{3\}} = 16$ neurons), and four ($I^{\{1\}} = 16$, $I^{\{2\}} = 16$, $I^{\{3\}} = 16$, and $I^{\{4\}} = 16$ neurons) hidden layers[1]. Table 6.4.2 depicts the deep C-RBF hyperparameters empirically optimized for each hidden layer. Unlike the other initialization schemes, the proposed approach achieves reasonable convergence for all architectures. One may note that the steady-state MSE results converged to the same value by the multi-layered architecture. This result is due to the number of neurons utilized to create the C-RBF layers. For the layers with the lowest number of neurons performed bottlenecks, impacting results. In order to circumvent this issue, more neurons could be adopted per layer; nonetheless, it does not affect the convergence verification.

[1] For the sake of comparison, we chose a total number of neurons $N_T = 64$, which was split depending on the number of layers.

Table 6.4.2 – Deep C-RBF optimized hyperparameters for the proposed approach.

Algorithm	η_w	η_b	η_γ	η_σ
first layer	0.100	0.100	0.100	0.100
second layer	0.050	0.050	0.050	0.050
third layer	0.033	0.033	0.033	0.033
fourth layer	0.025	0.025	0.025	0.025

These hyperparameters were optimized for the proposed initialization of the deep C-RBFs. For example, in a deep C-RBF with two hidden layers, only the first and second rows of hyperparameters are necessary. In a shallow architecture, the optimization is available in Table 6.4.1.

6.5 CONCLUSION

This paper presents an in-depth analysis of the initialization process in complex-valued radial basis function (C-RBF) neural networks. Our findings have elucidated the intricate dependencies involved in the initialization process. Specifically, the normalization of the input and output datasets depends on the number of inputs and outputs, respectively. Furthermore, synaptic weights are influenced by the number of neurons and outputs per layer, whereas center vectors are dependent on the number of inputs per layer. Therefore, the proposed approach is robust to changes in the neural network architecture, such as the number of inputs, outputs, hidden layers, and neurons. This innovation is particularly impactful for deploying these networks in real-world scenarios, which require robustness for a wide range of different configurations with no room for ad hoc adjustments. In a carefully designed simulation environment, conforming to 3GPP TS 38 standards, our proposed deep C-RBF parameter initialization technique exhibited superior convergence performance when compared to existing methods such as random initialization, K-means, and constellation-based initialization. Notably, for deep C-RBF architectures, our method was the only one that achieved successful convergence, highlighting its unique efficacy and adaptability. The implications of these results are manifold. First, they introduce a robust and effective initialization method that can significantly improve the training and performance of C-RBF neural networks, particularly in challenging 5G MIMO systems. Secondly, they lay the foundation for future research, opening avenues for the exploration of adaptive initialization techniques and offering the potential for extending our framework to other neural network architectures. In future works, we plan to validate the robustness of our proposed approach through more exhaustive experiments. We also aim to explore the applicability of our initialization framework to other neural network architectures, thereby contributing to the broader advancement of neural network-based solutions in digital communications.

REFERENCES

5G; NR; BASE STATION (BS) RADIO TRANSMISSION AND RECEPTION. Sophia Antipolis, France, Oct. 2022. (3GPP technical specification 38.104; version 17.7.0; release 17). Cited on pages 101, 114, 133, 146.

5G; NR; PHYSICAL CHANNELS AND MODULATION. Sophia Antipolis, France, Sept. 2022. (3GPP technical specification 38.211; version 17.3.0; release 17). Cited on pages 101, 114, 133, 146.

5G; STUDY ON CHANNEL MODEL FOR FREQUENCIES FROM 0.5 TO 100 GHZ. Sophia Antipolis, France, Apr. 2022. (3GPP technical report 38.901; version 17.0.0; release 17). Cited on pages 101, 114, 133, 146.

BARRACHINA, J. A. et al. Complex-valued vs. real-valued neural networks for classification perspectives: An example on non-circular data. *In*: 2021 IEEE International Conference on Acoustics, Speech and Signal Processing (ICASSP). [S.l.: s.n.], 2021. P. 2990–2994. Cited on pages 109, 127.

CHEN, S.; MCLAUGHLIN, S.; MULGREW, B. Complex-valued radial basic function network, part I: Network architecture and learning algorithms. **Signal Processing**, v. 35, n. 1, p. 19–31, 1994. Cited on page 127.

CHU, J.; GAO, M.; LIU, X., et al. Channel estimation based on complex-valued neural networks in IM/DD FBMC/OQAM transmission system. **Journal of Lightwave Technology**, v. 40, n. 4, p. 1055–1063, 2022. Cited on pages 109, 127.

CRUZ, A. A.; MAYER, K. S.; ARANTES, D. S. RosenPy: An open source python framework for complex-valued neural networks. **SSRN**, p. 1–18, 2022. Available from: <https://ssrn.com/abstract=4252610>. Cited on pages 109, 127.

DING, T.; HIROSE, A. Online regularization of complex-valued neural networks for structure optimization in wireless-communication channel prediction. **IEEE Access**, v. 8, p. 143706–143722, 2020. Cited on pages 109, 127.

FREIRE, P. J. et al. Complex-valued neural network design for mitigation of signal distortions in optical links. **Journal of Lightwave Technology**, v. 39, n. 6, p. 1696–1705, 2021. Cited on pages 109, 127, 155.

HIROSE, A.; YOSHIDA, S. Generalization characteristics of complex-valued feedforward neural networks in relation to signal coherence. **IEEE Trans. Neural Netw. Learn. Syst.**, v. 23, n. 4, p. 541–551, 2012a. Cited on pages 95, 96, 109, 127.

HU, T. et al. Regularization matters: A nonparametric perspective on overparametrized neural network. *In*: PROCEEDINGS of The 24th International Conference on Artificial Intelligence and Statistics. [S.l.: s.n.], 2021. P. 829–837. Cited on pages 109, 127.

HUMBIRD, K. D.; PETERSON, J. L.; MCCLARREN, R. G. Deep neural network initialization with decision trees. **IEEE Transactions on Neural Networks and Learning Systems**, v. 30, n. 5, p. 1286–1295, 2019. Cited on pages 109, 127.

KAMIYAMA, T.; KOBAYASHI, H.; IWASHITA, K. Neural network nonlinear equalizer in long-distance coherent optical transmission systems. **IEEE Photonics Technology Letters**, v. 33, n. 9, p. 421–424, 2021. Cited on pages 109, 127.

LI, H. et al. CVLNet: A complex-valued lightweight network for CSI feedback. **IEEE Wireless Communications Letters**, v. 11, n. 5, p. 1092–1096, 2022. Cited on pages 109, 127.

LOSS, D. et al. Phase Transmittance RBF Neural Networks. **Electronics Letters**, v. 43, n. 16, p. 882–884, Aug. 2007a. DOI: `10.1049/el:20070016`. Cited on pages 40, 41, 51, 59, 109, 111, 127.

MAYER, K. S.; SOARES, J. A.; ARANTES, D. S. Complex MIMO RBF Neural Networks for Transmitter Beamforming over Nonlinear Channels. **Sensors**, v. 20, n. 2, p. 1–15, Jan. 2020. DOI: `10.3390/s20020378`. Cited on pages 31, 40, 41, 51, 54, 79, 83, 95, 96, 109, 127.

MAYER, K. S. et al. Blind Fuzzy Adaptation Step Control for a Concurrent Neural Network Equalizer. **Wireless Communications and Mobile Computing**, v. 2019, n. 1, p. 9082362, 2019c. DOI: `https://doi.org/10.1155/2019/9082362`. Cited on pages 40, 83, 95, 96, 109, 127, 161.

MAYER, K. S. et al. Deep Phase-Transmittance RBF Neural Network for Beamforming With Multiple Users. **IEEE Wireless Communications Letters**, v. 11, n. 7, p. 1498–1502, 2022. DOI: `10.1109/LWC.2022.3177162`. Cited on pages 30, 83, 95–97, 109, 127, 142, 145, 155, 156, 161–163.

NARKHEDE, M. V.; BARTAKKE, P. P.; SUTAONE, M. S. A review on weight initialization strategies for neural networks. **Artificial Intelligence Review**, v. 55, p. 291–322, 2022. Cited on pages 109, 127.

SOARES, J. A. et al. Complex-valued phase transmittance RBF neural networks for massive MIMO-OFDM receivers. **Sensors**, v. 21, n. 24, p. 1–31, Dec. 2021a. ISSN 1424-8220. DOI: `10.3390/s21248200`. Available from: <`https://www.mdpi.com/1424-8220/21/24/8200`>. Cited on pages 83, 95–99, 109, 127, 142–145, 148.

SOARES, J. A.; MAYER, K. S.; ARANTES, D. S. On the Parameter Selection of Phase-transmittance Radial Basis Function Neural Networks for Communication Systems. *In*: IEEE International Conference on Machine Learning for Communication and Networking (ICMLCN). [S.l.: s.n.], 2024. P. 530–536. DOI: `10.1109/ICMLCN59089.2024.10624891`. Cited on pages 131, 133, 142, 172.

SOARES, J. A.; MAYER, K. S.; ARANTES, D. S. Semi-Supervised ML-Based Joint Channel Estimation and Decoding for m-MIMO With Gaussian Inference Learning.

IEEE Wireless Communications Letters, v. 12, n. 12, p. 2123–2127, 2023. DOI: `10.1109/LWC.2023.3309479`. Cited on pages 30, 114, 133, 146, 155, 161, 162.

TURNBULL, D.; ELKAN, C. Fast recognition of musical genres using RBF networks. **IEEE Transactions on Knowledge and Data Engineering**, v. 17, n. 4, p. 580–584, 2005. Cited on pages 109, 127.

WALLACE, M.; TSAPATSOULIS, N.; KOLLIAS, S. Intelligent initialization of resource allocating RBF networks. **Neural Networks**, v. 18, n. 2, p. 117–122, 2005. Cited on pages 109, 110, 127.

XIAO, C.; YANG, S.; FENG, Z. Complex-valued depthwise separable convolutional neural network for automatic modulation classification. **IEEE Transactions on Instrumentation and Measurement**, v. 72, p. 1–10, 2023. Cited on pages 109, 127.

XU, J. et al. The performance analysis of complex-valued neural network in radio signal recognition. **IEEE Access**, v. 10, p. 48708–48718, 2022. Cited on pages 95, 109, 127.

YANG, X. et al. Automatic modulation mode recognition of communication signals based on complex-valued neural network. *In*: 2022 International Conference on Computing, Communication, Perception and Quantum Technology (CCPQT). [S.l.: s.n.], 2022. P. 32–37. Cited on pages 109, 127.

ZHANG, S.-Q.; GAO, W.; ZHOU, Z.-H. Towards understanding theoretical advantages of complex-reaction networks. **Neural Netw.**, v. 151, p. 80–93, 2022. Cited on pages 83, 95, 109, 127.

ZHANG, Y. et al. CV-3DCNN: Complex-valued deep learning for CSI prediction in FDD massive MIMO systems. **IEEE Wireless Communications Letters**, v. 10, n. 2, p. 266–270, 2021b. Cited on pages 109, 127.

Chapter 7

Neural Network-based Subcarrier-level Joint Channel Estimation and Decoding for MIMO-OFDM Receivers

Authors: Jonathan Aguiar Soares, Kayol Soares Mayer, and Dalton Soares Arantes

Abstract

The increasing demands of modern telecommunications require improvements in spectral efficiency and system throughput. In this context, our study introduces a novel decoding method for MIMO-OFDM systems employing parallel neural networks, which markedly enhances decoding speed and accuracy over previous models. Unlike serial decoding, which fails to address the unique characteristics of individual subcarriers, our method employs distinct phase-transmittance radial basis function (PT-RBF) neural networks for each subcarrier. This parallel processing approach significantly reduces decoding time and increases system adaptability by effectively managing nonlinear impairments and intersymbol interference. Simulation results show that our method outperforms conventional decoding techniques in reducing bit error rate (BER) across both linear and nonlinear scenarios.

Keywords: Neural Networks, MIMO-OFDM, Complex-valued Neural Networks, Parallel Processing.

This Chapter is a replica of the following manuscript: Jonathan Aguiar Soares, Kayol Soares Mayer, and Dalton Soares Arantes, "Neural Network-based Subcarrier-level Joint Channel Estimation and Decoding for MIMO-OFDM Receivers" in IEEE Latin-American Conference on Communications, November 2024, doi: 10.1109/LATINCOM62985.2024.10770650.

7.1 INTRODUCTION

The exponential surge in global data consumption, driven by advancements such as 5G networks, cloud computing, and an ever-growing Internet of Things (IoT) ecosystem, underscores the critical need for enhanced spectral efficiency, robust telecommunications infrastructure, and improved reliability. The integration of multiple-input multiple-output (MIMO) technology with orthogonal frequency-division multiplexing (OFDM), especially in massive multiple-input multiple-output (mMIMO) systems, markedly increases channel capacity without additional bandwidth or power, forming the backbone of next-generation networks like 5G (KO et al., 2021; DILLI, 2021; SOKAL et al., 2021; SACI et al., 2017; MAJUMDER et al., 2021; YERRAPRAGADA; KELLEY, 2020; GUERREIRO; DINIS; CAMPOS, 2020). Despite their potential, the performance of these systems frequently suffers due to multipath propagation, additive white Gaussian noise (AWGN), and nonlinear impairments like the high peak-to-average power ratio (PAPR) in transmitter amplifiers (MAYER et al., 2020a, 2019a; OSMAN et al., 2021; ZOU et al., 2021). One promising solution to overcome these performance challenges in mMIMO systems is the implementation of transmitting diversity through Space-Time Block Coding (STBC). STBC enhances signal robustness against fading and mitigates issues such as multipath propagation and the peak-to-average power ratio effects. By encoding the transmitted data across multiple antennas, STBC allows the system to exploit spatial redundancy, thereby significantly improving the reliability and quality of the communication. This approach not only compensates for channel impairments but also optimizes the use of available bandwidth and power, further enhancing the efficacy of modern telecommunication infrastructures (ASIF et al., 2020; SHANG et al., 2020).

STBC is utilized in various communication technologies to enhance system performance. It supports high mobility scenarios with Orthogonal Time Frequency Space Modulation, contributing to increased transmission rates and diversity in MIMO systems (QIAN; XIAO; JIANG, 2022). In visible light communications (VLC), STBC is used to improve reliability in light-based data transmission (NASER et al., 2022), and it aids in boosting spectral efficiency in MIMO transmissions using quasi-orthogonal structures (WU et al., 2022a). Additionally, STBC is employed in cognitive radios to assist in modulation recognition (MAREY; DOBRE; MOSTAFA, 2022) and in challenging underwater and marine environments to help enhance communication reliability and performance (NAIK et al., 2023; HE; SHEN, 2022). Additionally, STBC is applicable in a broad range of other areas (XIU et al., 2022; MAREY et al., 2022; SINGH; KUMAR, 2022; ZHONG; XIAO; NIU, 2022), illustrating its diverse utility in modern telecommunications.

One significant challenge in implementing STBC is the complexity involved in deriving orthogonal space time coding (OSTBC) schemes for systems with a high number of transmitting antennas (JAFARKHANI, 2001). While OSTBC offers the benefit of high diversity gain, its application is limited by the difficulty in achieving orthogonal designs as the number of antennas increases. An alternative, quasi-orthogonal space-time block coding (QOSTBC), although providing better spectral efficiency due to its lower code rates, sacrifices some diversity gain compared to OSTBC. Additionally, QOSTBC introduces greater computational demands during decoding, as it requires processing groups of transmitted symbols using maximum likelihood (ML) decoders. Moreover, QOSTBC's compatibility issues with quadrature amplitude modulation (QAM) constellations further detract from its spectral efficiency.

To overcome these limitations, Soares et al. (SOARES et al., 2021a) enhanced decoder performance through the application of machine learning techniques, specifically employing PT-RBF neural networks. This method effectively manages the complexities associated with QOSTBC, providing a solution that not only addresses the decoding challenges but also achieves competitive performance. The findings from this study demonstrate that incorporating machine learning into the decoding process successfully mitigates many of the inherent difficulties encountered with QOSTBC, thereby validating the effectiveness of this innovative approach. However, this method relied on a single neural network operating as a serial decoder for the entire symbol, a design choice made to utilize a larger dataset for training, thus reducing the time required for model convergence.

This paper introduces a new approach utilizing parallel neural networks to decode MIMO-OFDM signals, a significant evolution from the previous serial decoding method. This approach exploits the recent advancements in neural network technologies, particularly via the application of deep PT-RBF neural networks (MAYER et al., 2022) and initialization methods (SOARES; MAYER; ARANTES, 2024). By deploying individual networks for each subcarrier, the system not only enhances decoding speeds through parallel processing, but also significantly improves decoding accuracy by allowing each network to specialize based on the unique characteristics of its respective subcarrier. This presents a substantial advancement in the decoding process for MIMO-OFDM systems.

The remainder of this paper is organized as follows: Section 7.2 provides a brief review of STBC systems. The proposed parallel channel estimation and decoding strategy for MIMO-OFDM systems is detailed in Section 7.3. Simulation results demonstrating the efficacy of our approach compared with traditional methods are presented in Section 7.4. Conclusions are discussed in Section 7.5.

7.2 BACKGROUND

Space-time code is a digital communication technique used to transmit multiple copies of a data stream via multiple antennas to compensate for fading and AWGN. On the receiver side, these multiple copies of the signal are received by one or more antennas, improving communication reliability.

7.2.1 Space-Time Block Coding and OFDM

A generalized coding scheme referred to as space-time block codes (STBCs) (JANKIRAMAN, 2004; TAROKH; JAFARKHANI; CALDERBANK, 1999; LI et al., 2021), based on the theory of orthogonal matrix designs, can achieve the full-transmit diversity of $N_{tx}N_{rx}$ employing the maximum likelihood (ML) decoding algorithm at the receiver (JANKIRAMAN, 2004). The idea is to transmit N_{tx} orthogonal streams, which implies that the receiver antennas receive N_{tx} orthogonal streams. This special class of space-time block codes is the so-called OSTBC (SOARES et al., 2021a; TAROKH; JAFARKHANI; CALDERBANK, 1999; HU; ZHAO; XUE, 2020). Besides diversity gain, the OSTBC leads to a secondary linear coding gain $G_c = 10\log(R)$ at the receiver due to the coherent detection of multiple signal copies over time, and an array gain $G_a = 10\log(N_{rx})$ due to the coherent combination of multiple received signals over the receiving antennas (SOARES et al., 2021a).

One of the disadvantages of OSTBC is the code rate. Let N_{tp} represent the number of time samples to convey one block of coded symbols and N_s represent the number of symbols transmitted per block. The space-time block code rate is defined as the ratio between the number of symbols that the encoder receives at its input and the number of space-time coded symbols transmitted from each antenna, given by $R = N_s/N_{tp}$. For example, an OSTBC coding matrix for $N_{tx} = 4$ implies a code rate $R = 1/2$, reducing spectral efficiency.

In order to increase the spectral efficiency in orthogonal codes, Jafarkhani (JAFARKHANI, 2001) proposed QOSTBC of rate one, relaxing the requirement of orthogonality. However, when compared with orthogonal codes, the diversity gain is reduced by a factor of two. In contrast to orthogonally designed codes that process one symbol at a time on the decoder, quasi-orthogonal codes process pairs of transmitted symbols, which exponentially increases the computational complexity of decoding (SOARES et al., 2021a). Jafarkhani (JAFARKHANI, 2001) proposed a coding matrix of rate one for $N_{tx} = 4$, given by

$$\mathbf{QOSTBC_{4,4}} = \begin{bmatrix} s[1] & s[2] & s[3] & s[4] \\ -s[2]^* & s[1]^* & -s[4]^* & s[3]^* \\ -s[3]^* & -s[4]^* & s[1]^* & s[2]^* \\ s[4] & -s[3] & -s[2] & s[1] \end{bmatrix}. \tag{7.1}$$

In the literature, related approaches with a maximum of $N_{tx} = 6$ antennas were proposed for quasi-orthogonal codes (TIRKKONEN; BOARIU; HOTTINEN, 2000;

WEIFENG SU; XIANG-GEN XIA, 2002; SINDHU; HAMEED, 2015). In (WEIFENG SU; XIANG-GEN XIA, 2002), the authors developed an architecture similar to (JAFARKHANI, 2001); however, it presents full diversity at the cost of more processing and is limited to $N_{tx} = 4$ antennas. In the same way, by increasing the decoding processing, Sindhu and Hameed (SINDHU; HAMEED, 2015) proposed two quasi-orthogonal schemes with $N_{tx} = 5$ and 6 antennas (SOARES et al., 2021a).

7.2.2 Quasi-Orthogonal Coding Scheme

In the present paper, we use the generalized recursive method proposed in (SOARES et al., 2021a) for generating QOSTBC coding schemes:

$$\mathbf{S}_{N_s}^{N_{tx}} = \begin{bmatrix} \mathbf{S}_{N_s-N_{tx}/2}^{N_{tx}/2} & \mathbf{S}_{N_s}^{N_{tx}/2} \\ -[\mathbf{S}_{N_s}^{N_{tx}/2}]^* & [\mathbf{S}_{N_s-N_{tx}/2}^{N_{tx}/2}]^* \end{bmatrix}, \tag{7.2}$$

in which $N_{tx} = 2^n$, $\forall\, n \in \mathbb{N}^+$, is the number of transmitting antennas and N_s is the number of encoded symbols. In this encoding approach, $N_s \triangleq N_{tx}$ and the code rate is $R = N_{tx}/N_s = 1$ (SOARES et al., 2021a). The recurrence is employed until $\mathbf{S}_n^1 = s[n]$, $\forall n \in [1, 2, \cdots, N_s]$ in (7.2).

With four transmitting antennas, (7.2) results in:

$$\mathbf{S}_4^4 = \begin{bmatrix} s[1] & s[2] & s[3] & s[4] \\ -s[2]^* & s[1]^* & -s[4]^* & s[3]^* \\ -s[3]^* & -s[4]^* & s[1]^* & s[2]^* \\ s[4] & -s[3] & -s[2] & s[1] \end{bmatrix}. \tag{7.3}$$

Note that (7.3) is equal to the coding scheme proposed by (JAFARKHANI, 2001) with four antennas, as in (7.1). However, in contrast to the work of (JAFARKHANI, 2001), this scheme can generate coding matrices for any $N_{tx} = 2^n$, $\forall\, n \in \mathbb{N}^+$, and $N_s \triangleq N_{tx}$ (SOARES et al., 2021a). For the case of $n = 1$, (7.2) is equal to the Alamouti coding, the full-rate full-diversity complex-valued space-time block code proposed in (ALAMOUTI, 1998).

7.3 PROPOSED PT-RBF-BASED SUBCARRIER-LEVEL JOINT CHANNEL ESTIMATION AND DECODING

The main issue of the coding scheme proposed by Soares et al. (SOARES et al., 2021a) is that it is impossible to define a simplified ML decoding method for $n > 2$. Given that limitation, and relying on the approximation capabilities of artificial neural networks (ANNs), Soares et al. (SOARES et al., 2021a) proposed a joint channel estimation and decoding approach based on the PT-RBF neural network. As presented in (SOARES et al., 2021a), compared to the ML decoding, the PT-RBF has a lower computational complexity and allows the decoding of high-order QAM modulation with a massive number of transmitting and receiving antennas.

Fig. 7.3.1 shows an mMIMO receiver with QOSTBC decoding using a PT-RBF (SOARES et al., 2021a). First, the signals received from the N_{rx} antennas are parallelized in the serial to parallel (S/P) block to feed N_{tp}-OFDM demodulators. In each OFDM demodulator, the input signal is parallelized by an S/P block to subsequently remove the cyclic prefix in the CPR block. The resulting signal is transformed to the frequency domain via a FFT block. The FFT output is serialized by a parallel to serial (P/S) block, yielding the OFDM demodulator output. The PT-RBF Channel Estimation and Decoding block receives as input a QOSTBC vector $\hat{\mathbf{s}}[k] \in \mathbb{C}^{N_{tp}N_{rx}}$, one at a time (i.e., subcarrier per subcarrier, with $k \in [1, 2, \ldots, K]$). The PT-RBF output is the estimated vector $\hat{\mathbf{q}}[k] \in \mathbb{C}^{N_s}$.

Although the PT-RBF enables the decoding of massive MIMO QOSTBC systems, the training becomes challenging with the increasing number of subcarriers, affecting both convergence rate and accuracy. In mild scenarios (i.e., without deep fading), as the channel does not vary significantly in frequency, the estimation of a given subcarrier is very useful for any other, regardless of the frequency separation. On the other hand, if the channel has many fluctuations, it is not valid anymore. In order to circumvent this issue, a higher number of neurons can be used in the PT-RBF, at the cost of a higher computational complexity. Nonetheless, even increasing the number of neurons (or layers in a deep architecture (MAYER et al., 2022)), there is a penalty compared with the QOSTBC with ML decoding.

In this context, we propose a new architecture for subcarrier-level joint channel estimation and decoding of mMIMO QOSTBC based on the well-known PT-RBF. As shown in Fig. 7.3.2, the receiving and OFDM demodulation process is equal to the one illustrated in Fig. 7.3.1. However, unlike Soares et al. (SOARES et al., 2021a), the proposed approach comprises K PT-RBFs, one employed for each subcarrier. The subcarrier allocation is

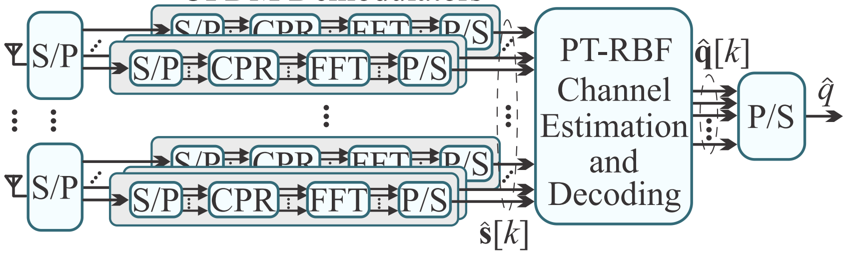

Figure 7.3.1 – Receiver architecture of a massive MIMO-OFDM system with PT-RBF-based channel estimation and decoding (SOARES et al., 2021a).

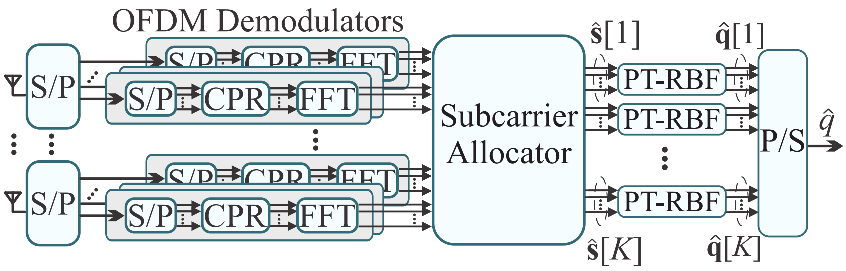

Figure 7.3.2 – Proposed receiver architecture in a massive MIMO-OFDM system with parallelized PT-RBF neural networks. The OFDM demodulation process is followed by subcarrier-specific channel estimation and decoding using multiple PT-RBF neural networks, each handling a distinct subcarrier for improved parallel processing.

performed by the Subcarrier Allocator block, which parallelizes K QOSTBC vectors $\hat{\mathbf{s}}[k]$. Then, in the training phase, the k-th PTRBF neural network is only fed with $\hat{\mathbf{s}}[k]$ and $\hat{\mathbf{q}}[k]$ vectors, becoming an expert in the k-th subcarrier. As a result, it reduces the PT-RBF computational complexity by reducing the number of neurons, and also splits the processing into K parts, increasing the parallelism.

7.4 RESULTS

Based on (SOARES; MAYER; ARANTES, 2023), we consider a space-time block coding (STBC) simulation system with the 3GPP TS 38.211 specification for 5G physical channels and modulation (5G..., 2022). The orthogonal frequency-division multiplexing (OFDM) is defined with 60-kHz subcarrier spacing, 256 active subcarriers, and a block-based pilot scheme. Symbols are modulated with 4QAM, 16QAM, and 16PSK, and for the MIMO setup, four antennas are employed at the transmitter and one at the receiver. Based on the tapped delay line-A (TDLA) from the 3GPP TR 38.901 5G channel models (5G..., 2022), the MIMO channel follows the TDLA from the 3GPP TR 38.104 5G radio base station transmission and reception (5G..., 2022). The TDLA is described with 12 taps, with varying delays from 0.0 ns to 290 ns and powers from -26.2 dB to 0 dB. A Rayleigh distribution is used to compute each sub-channel. To avoid influencing the learning curves, we do not take into account the Doppler effect, and we do not employ the inference learning techniques proposed in (SOARES; MAYER; ARANTES, 2023). The CVNNs operate with four inputs and four outputs, accounting for the coding with $N_s = N_{tx} = 4$. The inputs are taken from the OFDM demodulator outputs, one at a time (see Figs. 7.3.1 and 7.3.2). Training and inference were performed for $4,000$ and $1,000$ instances, respectively. Each output training instance corresponds to four QAM symbols, resulting in 16,000 and 4,000 QAM symbols for the training and inference phases, for each PT-RBF. Performance was assessed via bit error rate (BER) results. The PT-RBF hyperparameters were empirically optimized and the best performance was achieved with three ($I^{\{1\}} = 32$, $I^{\{2\}} = 32$, and $I^{\{3\}} = 32$ neurons), hidden layers. The best results were

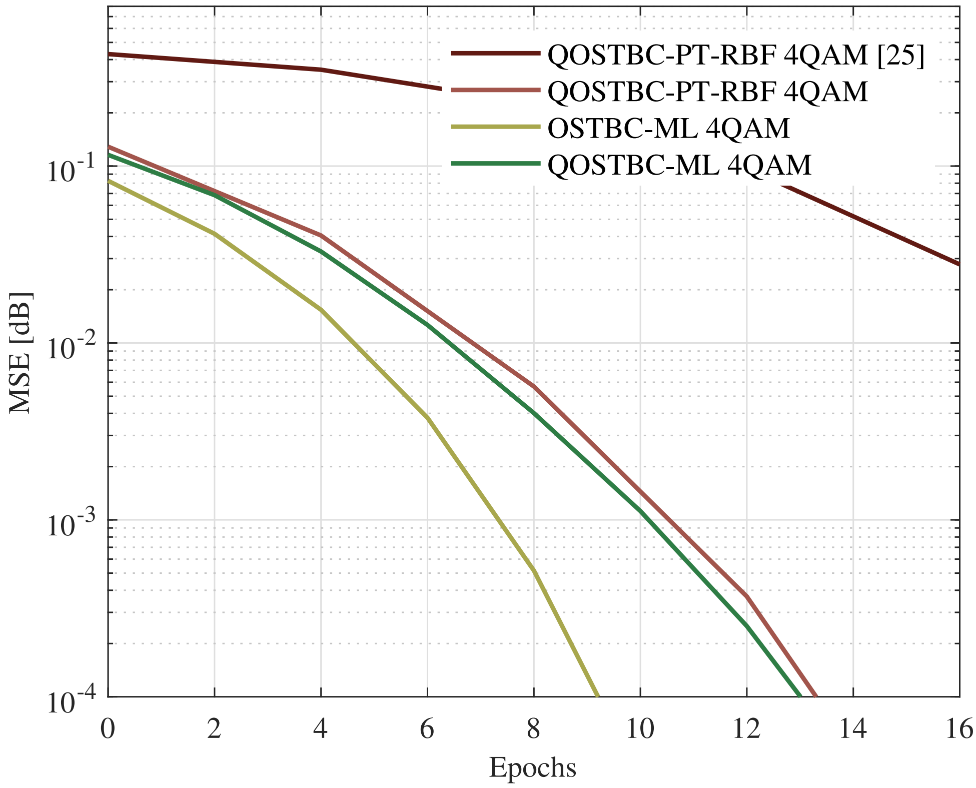

Figure 7.4.1 – BER results of the PT-RBF (proposed approach – red line) with three hidden layers ($I^1 = 32$, $I^2 = 32$, and $I^3 = 32$neurons) for subcarrier joint channel estimation and decoding in a MIMO-OFDM 4×1 system, operating with 4-QAM and 256 subcarriers. Additionally, results from the former serial decoding method using three hidden layers($I^1 = 128$, $I^2 = 128$, and $I^3 = 128$ neurons) are shown in dark red for comparison. All results were averaged over 10 subsequent simulations with $\mathrm{E_b/N_0}$ in a range of 0 dB to 16dB, in steps of 2dB. QOSTB-ML(green line) and OSTBC-ML(yellow line) are also simulated for comparison.

obtained with the learning rates $\eta_w^{\{1\}} = \eta_w^{\{2\}} = \eta_w^{\{3\}} = 0.01$, $\eta_b^{\{1\}} = \eta_b^{\{2\}} = \eta_b^{\{3\}} = 0.01$, $\eta_\gamma^{\{1\}} = \eta_\gamma^{\{2\}} = \eta_\gamma^{\{3\}} = 0.04$, and $\eta_\sigma^{\{1\}} = \eta_\sigma^{\{2\}} = \eta_\sigma^{\{3\}} = 0.01$ of weights, bias, center vectors, and variances, respectively.

Fig. 7.4.1 illustrates the BER convergence for QOSTB coding scheme and decoding with PT-RBF (QOSTBC-PT-RBF) and maximum likelihood (QOSTBC-ML), and OSTBC coding scheme with maximum likelihood decoding (OSTBC-ML). Although in such a scenario the ML decoding is the optimal decoder, the proposed decoder achieves almost the same performance, with a loss of approximately only 0.375 dB. Additionally, we have included results from the former serial decoding approach, updated with a deep architecture of three hidden layers and extensively optimized through trial and error. Despite these enhancements, this former method was unable to achieve satisfactory performance for the chosen channel environment, illustrating the superiority of our proposed approach.

Additionally, we have also employed nonlinear effects in the system introducing clipping on the transmitter side, thus adding nonlinearities in the transmitted signal (YE; LI; JUANG, 2018). Fig. 7.4.2 depicts BER results when the clipping ratio ($CR = A/\alpha$, in which α is the root mean square of signal) is 1. In this nonlinear scenario, the proposed

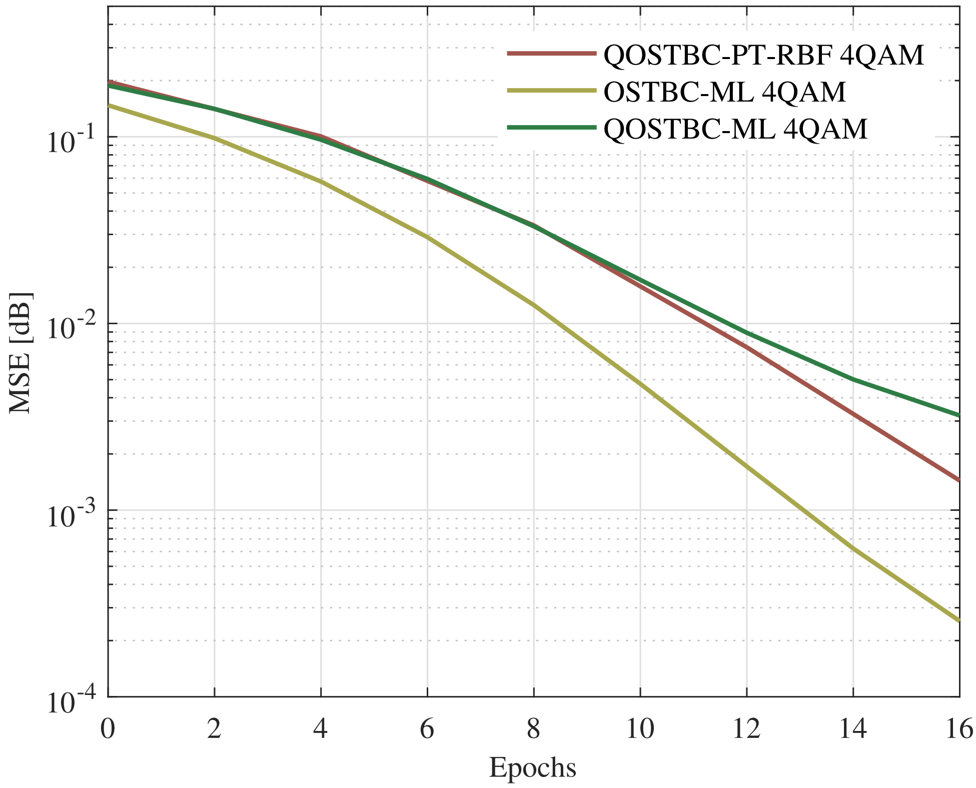

Figure 7.4.2 – BER results of the PT-RBF (proposed approach – red line) with three hidden layers ($I^{\{1\}} = 32$, $I^{\{2\}} = 32$, and $I^{\{3\}} = 32$ neurons) for subcarrier joint channel estimation and decoding in a MIMO-OFDM 4×1 system, operating with 4QAM and 256 subcarriers. A nonlinear effect is introduced in the transmitter using clipping in the transmitted signal. Results were averaged over 10 subsequent simulations with $\mathrm{E_b/N_0}$ in a range of 0 dB to 16 dB, in steps of 2 dB. QOSTB-ML (green line) and OSTBC-ML (yellow line) are simulated for comparison.

decoder achieves better results compared with the ML decoder for $\mathrm{E_b/N_0} > 10$ dB, showing the robustness of the proposed decoder when nonlinear impairments are considered. Furthermore, for $\mathrm{E_b/N_0} = 14$ dB, the proposed decoder achieves 2 dB of gain to achieve the same BER compared with the ML decoder.

For further comparison, we employed 16QAM modulation in Fig. 7.4.3. However, QOSTB-ML also considers 16PSK modulation, as decoding is only suitable for PSK modulations (SOARES et al., 2021a). Additionaly, we have retained the QOSTB-ML 16QAM result for reference. Unlike the QOSTB-ML decoder, the proposed approach achieves reasonable convergence for a high-order QAM modulation, enabling its application in more challenging applications, such as the ones discussed in (SOARES et al., 2021a). Additionally, the proposed PT-RBF decoder achieved better BER results than QOSTB-ML considering the same bitrate (regardless of the modulation schemes). This is because MPSK has lower minimal symbol distances than MQAM, which results in a BER penalty.

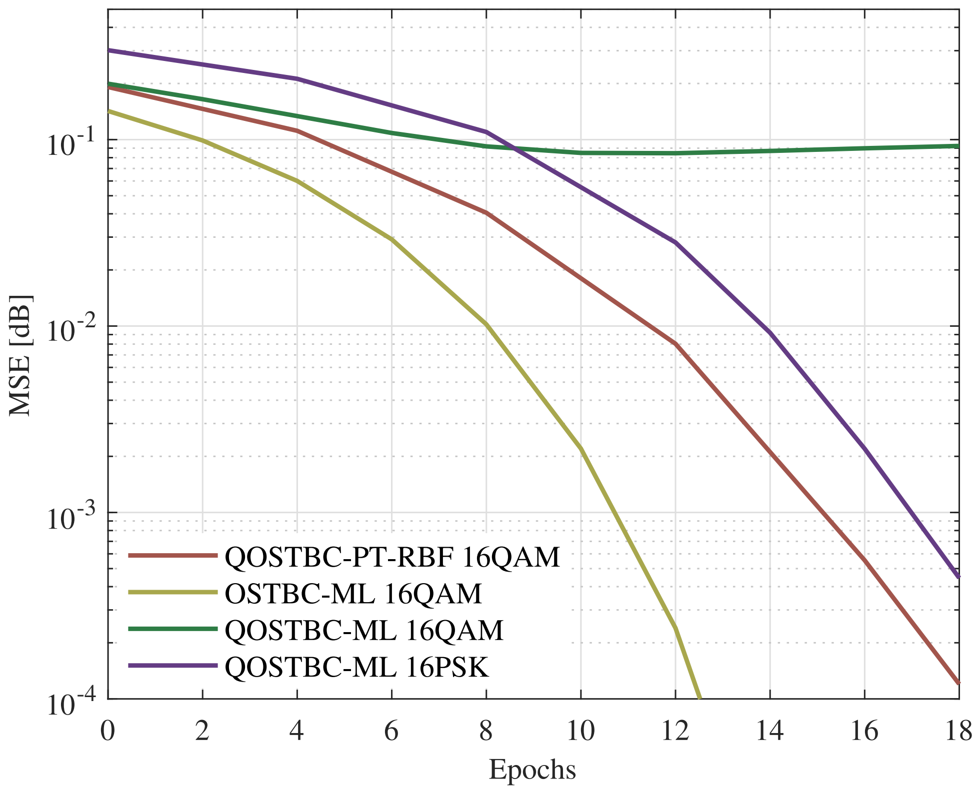

Figure 7.4.3 – BER results of the PT-RBF (proposed approach – red line) with three hidden layers ($I^{\{1\}} = 32$, $I^{\{2\}} = 32$, and $I^{\{3\}} = 32$ neurons) for subcarrier joint channel estimation and decoding in a MIMO-OFDM 4×1 system, operating with 16QAM and 256 subcarriers. Results were averaged over 10 subsequent simulations with E_b/N_0 in a range of 0 dB to 18 dB, in steps of 2 dB. 16QAM QOSTB-ML (green line), 16PSK QOSTB-ML (purple line), and OSTBC-ML (yellow line) are simulated for comparison.

7.5 CONCLUSIONS

This paper introduces a novel PT-RBF-based subcarrier-level joint channel estimation and decoding approach for MIMO-OFDM systems that leverage parallel neural networks for enhanced channel estimation. By deploying separate neural networks to process individual subcarriers in parallel, the proposed method significantly improves decoding speed and robustness compared to traditional techniques. The empirical results demonstrate that the proposed decoder not only meets but, in some cases, also exceeds the performance of the maximum likelihood decoding, especially in scenarios with nonlinear distortions (transmitter clipping). Despite the success of the current study, there is room for further research. First, exploring the scalability of the proposed PT-RBF networks to systems with a higher number of antennas and subcarriers could provide insights into their performance in ultra-massive MIMO setups. Second, optimizing the training algorithms and further refining the neural network initialization procedures could enhance the efficiency and accuracy of the decoding process. Third, testing the proposed approach under a wider range of channel conditions and modulation schemes would help to understand its robustness and reliability in real-world scenarios.

REFERENCES

5G; NR; BASE STATION (BS) RADIO TRANSMISSION AND RECEPTION. Sophia Antipolis, France, Oct. 2022. (3GPP technical specification 38.104; version 17.7.0; release 17). Cited on pages 101, 114, 133, 146.

5G; NR; PHYSICAL CHANNELS AND MODULATION. Sophia Antipolis, France, Sept. 2022. (3GPP technical specification 38.211; version 17.3.0; release 17). Cited on pages 101, 114, 133, 146.

5G; STUDY ON CHANNEL MODEL FOR FREQUENCIES FROM 0.5 TO 100 GHZ. Sophia Antipolis, France, Apr. 2022. (3GPP technical report 38.901; version 17.0.0; release 17). Cited on pages 101, 114, 133, 146.

ALAMOUTI, S. M. A simple transmit diversity technique for wireless communications. **IEEE Journal on Selected Areas in Communications**, v. 16, n. 8, p. 1451–1458, 1998. DOI: `10.1109/49.730453`. Cited on pages 48, 49, 144.

ASIF, R. M. et al. Energy efficiency augmentation in massive MIMO systems through linear precoding schemes and power consumption modeling. **Wireless Communications and Mobile Computing**, v. 2020, p. 1–13, 2020. DOI: `10.1155/2020/8839088`. Cited on pages 39, 141.

DILLI, R. Performance analysis of multi user massive MIMO hybrid beamforming systems at millimeter wave frequency bands. **Wireless Networks**, v. 27, n. 3, p. 1925–1939, 2021. DOI: `10.1007/s11276-021-02546-w`. Cited on pages 39, 141.

GUERREIRO, J.; DINIS, R.; CAMPOS, L. On the Achievable Capacity of MIMO-OFDM Systems in the CathLab Environment. **Sensors**, v. 20, n. 3, p. 1–16, 2020. DOI: `10.3390/s20030938`. Cited on pages 40, 141.

HE, R.; SHEN, Z. System Design and Performance of Ship-borne Satellite High-speed Data Reliable Transportation Based on Coded STBC-OFDM. *In*: 2022 7th International Conference on Intelligent Computing and Signal Processing (ICSP). [S.l.: s.n.], 2022. P. 1302–1306. DOI: `10.1109/ICSP54964.2022.9778435`. Cited on page 141.

HU, Z.; ZHAO, H.; XUE, J. Error exponent for Nakagami-m fading massive MIMO channels. *In*: 2020 IEEE 6th International Conference on Computer and Communications (ICCC). [S.l.: s.n.], 2020. P. 59–63. DOI: `10.1109/ICCC51575.2020.9345091`. Cited on pages 45, 143.

JAFARKHANI, H. A quasi-orthogonal space-time block code. **IEEE Transactions on Communications**, v. 49, n. 1, p. 1–4, 2001. DOI: `10.1109/26.898239`. Cited on pages 46–49, 54–56, 60, 65, 68, 141, 143, 144.

JANKIRAMAN, M. **Space-time Codes and MIMO Systems**. 1. ed. [S.l.]: Artech House, 2004. ISBN 9781580538664. Available from: <`https://books.google.com.br/books?id=HU-T7y16AGEC`>. Cited on pages 42, 43, 45, 47, 143.

KO, K. et al. Joint power allocation and scheduling techniques for BER minimization in multiuser MIMO systems. **IEEE Access**, v. 9, p. 66675–66686, 2021. DOI: `10.1109/ACCESS.2021.3074980`. Cited on pages 39, 141.

LI, F. et al. Construction of Golay complementary matrices and its applications to MIMO omnidirectional transmission. **IEEE Transactions on Signal Processing**, v. 69, p. 2100–2113, 2021. DOI: `10.1109/TSP.2021.3067467`. Cited on pages 39, 45, 143.

MAJUMDER, M. et al. Optimal Bit Allocation-Based Hybrid Precoder-Combiner Design Techniques for mmWave MIMO-OFDM Systems. **IEEE Access**, v. 9, p. 54109–54125, 2021. DOI: `10.1109/ACCESS.2021.3070921`. Cited on pages 40, 141.

MAREY, M.; DOBRE, O. A.; MOSTAFA, H. Cognitive Radios Equipped With Modulation and STBC Recognition Over Coded Transmissions. **IEEE Wireless Communications Letters**, v. 11, n. 7, p. 1513–1517, 2022. DOI: `10.1109/LWC.2022.3177638`. Cited on page 141.

MAREY, M. et al. STBC Recognition for OFDM Transmissions: Channel Decoder Aided Algorithm. **IEEE Communications Letters**, v. 26, n. 7, p. 1658–1662, 2022. DOI: `10.1109/LCOMM.2022.3170524`. Cited on page 141.

MAYER, K. S. et al. A new CPFSK demodulation approach for software defined radio. **Journal of Circuits, Systems and Computers**, v. 28, n. 14, p. 1–14, 2019a. DOI: `10.1142/S0218126619502438`. Cited on pages 40, 141.

MAYER, K. S. et al. High data-rates and high-order DP-QAM optical links can be efficiently implemented with concurrent equalization. *In*: 22ND Photonics North (PN). [S.l.: s.n.], 2020a. P. 1. DOI: `10.1109/PN50013.2020.9167008`. Cited on pages 40, 141.

MAYER, K. S. et al. Deep Phase-Transmittance RBF Neural Network for Beamforming With Multiple Users. **IEEE Wireless Communications Letters**, v. 11, n. 7, p. 1498–1502, 2022. DOI: `10.1109/LWC.2022.3177162`. Cited on pages 30, 83, 95–97, 109, 127, 142, 145, 155, 156, 161–163.

NAIK, R. P. et al. Performance of Orthogonal and Non-Orthogonal Space Time Block Code Through the Underwater Wireless Optical Channels. *In*: 2023 IEEE International Conference on Advanced Networks and Telecommunications Systems (ANTS). [S.l.: s.n.], 2023. P. 373–378. DOI: `10.1109/ANTS59832.2023.10469512`. Cited on page 141.

NASER, S. et al. Space-Time Block Coded Spatial Modulation for Indoor Visible Light Communications. **IEEE Photonics Journal**, v. 14, n. 1, p. 1–11, 2022. DOI: `10.1109/JPHOT.2021.3126873`. Cited on page 141.

OSMAN, A. M. et al. A Modified Method of Filtering for FBMC Based 5G Communications on Minimizing Doppler Shift. *In*: 2021 6th International Conference for Convergence in Technology (I2CT). [S.l.: s.n.], 2021. P. 1–4. DOI: `10.1109/I2CT51068.2021.9417931`. Cited on pages 40, 141.

QIAN, Y.; XIAO, L.; JIANG, T. SM-STBC aided Orthogonal Time Frequency Space Modulation. *In*: 2022 IEEE Wireless Communications and Networking Conference

(WCNC). [S.l.: s.n.], 2022. P. 2172–2177. DOI: 10.1109/WCNC51071.2022.9771767. Cited on page 141.

SACI, A. et al. One-Shot Blind Channel Estimation for OFDM Systems Over Frequency-Selective Fading Channels. **IEEE Transactions on Communications**, v. 65, n. 12, p. 5445–5458, 2017. DOI: 10.1109/TCOMM.2017.2740925. Cited on page 141.

SHANG, B. et al. Spatial spectrum sensing in uplink two-tier user-centric deployed HetNets. **IEEE Transactions on Wireless Communications**, v. 19, n. 12, p. 7957–7972, 2020. DOI: 10.1109/TWC.2020.3018408. Cited on pages 39, 141.

SINDHU, P.; HAMEED, A. Efficient quasi-orthogonal space-time block codes for five and six transmit antennas. *In*: 2015 IEEE International Conference on Electronics, Computing and Communication Technologies (CONECCT). [S.l.: s.n.], 2015. P. 1–5. DOI: 10.1109/CONECCT.2015.7383923. Cited on pages 47, 144.

SINGH, S. K.; KUMAR, A. Modified design of STBC Encoder for reducing Non-Linear distortions in OFDM Channel Estimation. *In*: 2022 Second International Conference on Advances in Electrical, Computing, Communication and Sustainable Technologies (ICAECT). [S.l.: s.n.], 2022. P. 1–5. DOI: 10.1109/ICAECT54875.2022.9807993. Cited on page 141.

SOARES, J. A. et al. Complex-valued phase transmittance RBF neural networks for massive MIMO-OFDM receivers. **Sensors**, v. 21, n. 24, p. 1–31, Dec. 2021a. ISSN 1424-8220. DOI: 10.3390/s21248200. Available from: <https://www.mdpi.com/1424-8220/21/24/8200>. Cited on pages 83, 95–99, 109, 127, 142–145, 148.

SOARES, J. A.; MAYER, K. S.; ARANTES, D. S. On the Parameter Selection of Phase-transmittance Radial Basis Function Neural Networks for Communication Systems. *In*: IEEE International Conference on Machine Learning for Communication and Networking (ICMLCN). [S.l.: s.n.], 2024. P. 530–536. DOI: 10.1109/ICMLCN59089.2024.10624891. Cited on pages 131, 133, 142, 172.

SOARES, J. A.; MAYER, K. S.; ARANTES, D. S. Semi-Supervised ML-Based Joint Channel Estimation and Decoding for m-MIMO With Gaussian Inference Learning. **IEEE Wireless Communications Letters**, v. 12, n. 12, p. 2123–2127, 2023. DOI: 10.1109/LWC.2023.3309479. Cited on pages 30, 114, 133, 146, 155, 161, 162.

SOKAL, B. et al. Tensor-Based Receiver for Joint Channel, Data, and Phase-Noise Estimation in MIMO-OFDM Systems. **IEEE Journal of Selected Topics in Signal Processing**, v. 15, n. 3, p. 803–815, 2021. DOI: 10.1109/JSTSP.2021.3061917. Cited on pages 40, 141.

TAROKH, V.; JAFARKHANI, H.; CALDERBANK, A. R. Space-time block codes from orthogonal designs. **IEEE Transactions on Information Theory**, v. 45, n. 5, p. 1456–1467, 1999. DOI: 10.1109/18.771146. Cited on pages 45, 47, 54, 68, 69, 143.

TIRKKONEN, O.; BOARIU, A.; HOTTINEN, A. Minimal non-orthogonality rate 1 space-time block code for 3+ Tx antennas. *In*: 2000 IEEE Sixth International Symposium on Spread Spectrum Techniques and Applications. ISSTA 2000. Proceedings (Cat. No.00TH8536). [S.l.: s.n.], 2000. v. 2, p. 429–432. DOI: 10.1109/ISSSTA.2000.876470. Cited on pages 47, 143.

WEIFENG SU; XIANG-GEN XIA. Quasi-orthogonal space-time block codes with full diversity. *In*: GLOBAL Telecommunications Conference, 2002. GLOBECOM '02. IEEE. [S.l.: s.n.], 2002. v. 2, p. 1098–1102. DOI: 10.1109/GLOCOM.2002.1188366. Cited on pages 47, 143, 144.

WU, C. et al. Quasi-Orthogonal Space-Time Block Coded Spatial Modulation. **IEEE Transactions on Communications**, v. 70, n. 12, p. 7872–7885, 2022a. DOI: 10.1109/TCOMM.2022.3216805. Cited on page 141.

XIU, H. et al. A DFDD Based Detector for Space-Time Block Coded Differential Spatial Modulation Under Time-Selective Channels. **IEEE Communications Letters**, v. 26, n. 2, p. 359–363, 2022. DOI: 10.1109/LCOMM.2021.3132697. Cited on page 141.

YE, H.; LI, G. Y.; JUANG, B.-H. Power of deep learning for channel estimation and signal detection in OFDM systems. **IEEE Wireless Commun. Lett.**, v. 7, n. 1, p. 114–117, 2018. DOI: 10.1109/LWC.2017.2757490. Cited on pages 97, 147, 155.

YERRAPRAGADA, A. K.; KELLEY, B. On the Application of K-User MIMO for 6G Enhanced Mobile Broadband. **Sensors**, v. 20, n. 21, p. 1–16, 2020. DOI: 10.3390/s20216252. Cited on pages 40, 141.

ZHONG, Y.; XIAO, Y.; NIU, H. Transmit Antenna Selection and Artificial Noise Design for Secure STBC-SM Transmission. *In*: 2022 IEEE 95th Vehicular Technology Conference: (VTC2022-Spring). [S.l.: s.n.], 2022. P. 1–6. DOI: 10.1109/VTC2022-Spring54318.2022.9860380. Cited on page 141.

ZOU, F. et al. A novel PAPR reduction scheme for OFDM systems based on neural networks. **Wireless Communications and Mobile Computing**, v. 2021, p. 1–8, 2021. DOI: 10.1155/2021/5574807. Cited on pages 40, 141.

Chapter 8

Complex-valued NN-based End-to-end Learning in Massive-MIMO Communications

Authors: Jonathan Aguiar Soares, Kayol Soares Mayer, and Dalton Soares Arantes

Abstract

This paper presents a novel end-to-end (E2E) learning architecture for massive MIMO communication systems using complex-valued neural networks (CVNNs). Our approach leverages CVNNs to process complex signals directly, eliminating the need to split real and imaginary components, thereby preserving the natural structure of wireless signals. The proposed architecture integrates both the encoding and decoding stages, optimized for flat-fading Rayleigh channel conditions, focusing on improving transmission efficiency. A key contribution is the extension of the approach to multi-user MIMO scenarios, where the system is designed to orthogonalize data streams for several user equipment, improving spectral efficiency with federated learning. We show that it is possible to effectively transmit a number of data streams that exceed the channel matrix rank. Additionally, a power control mechanism based on regularization is introduced to ensure stable transmission power. The effectiveness of the proposed approach is rigorously validated through simulations across a range of scenarios, demonstrating significant improvements in the mutual information. The results are compared with theoretical limits and classical approaches, highlighting the potential of CVNN-based architectures for advancing future wireless communication systems in both single and multi-user contexts.

Keywords: MIMO, MU-MIMO, End-to-end Learning, Autoencoder, Federated Learning, Complex-valued Neural Networks.

This Chapter is a replica of the following manuscript: Jonathan Aguiar Soares, Kayol Soares Mayer, and Dalton Soares Arantes, "Complex-valued NN-based End-to-end Learning in Massive-MIMO Communications" submitted to IEEE TRANSACTIONS ON WIRELESS COMMUNICATIONS, October 2024, doi: –.

8.1 INTRODUCTION

multiple-input multiple-output (MIMO) systems have become a paramount technology in modern wireless communications (BJÖRNSON et al., 2023), enabling significant improvements in both data throughput and link reliability by leveraging multiple antennas at the transmitter and receiver. By exploiting spatial diversity, MIMO systems enhance communication capacity and spectral efficiency, which is essential for current and emerging wireless technologies like 5G and beyond. As the demand for high-capacity wireless networks continues to grow, innovations in MIMO technologies are critical to meet the ever-increasing need for faster and more reliable communication (WANG et al., 2023).

The evolution of deep learning (DL) techniques is boosting the advancement of MIMO systems (QIN et al., 2019). For example, Ye et al. (YE; LI; JUANG, 2018) demonstrate how DL can enhance channel estimation and decoding in orthogonal frequency-division multiplexing (OFDM) systems. Wang et al. (WANG et al., 2022) implemented a reliable intelligent space-time block coding (STBC) receiver with convolutional neural networks (CNNs). Albreem et al. (ALBREEM et al., 2022) discuss using DL for MIMO detection, including the application in cell-free massive MIMO. Yuan et al. (YUAN et al., 2023) proposed a wideband hybrid precoding network for Terahertz massive MIMO. He et al. (HE et al., 2020) employed a model-driven DL approach that outperforms a traditional iterative MIMO detector considering 4×4 to 32×32 antenna setups.

Although these promising approaches achieve significant results in digital communication systems, most rely on real-valued DL techniques, even when handling inherently complex-valued data. This simplification can lead to information loss, particularly when handling wireless signals, which are naturally complex-valued. In contrast, complex-valued neural networks (CVNNs) process data directly in the complex domain, preserving signal integrity (CRUZ; MAYER; ARANTES, 2024). Hirose and Yoshida (HIROSE; YOSHIDA, 2012b) emphasized the advantages of CVNNs in tasks such as equalization and channel estimation, particularly in maintaining coherence and enhancing generalization in signal processing. This pioneering work demonstrated that CVNNs provide a more accurate model of signal behavior in communication systems, resulting in better performance for decoding and signal reconstruction tasks. Additional CVNN use cases include nonlinear compensation (FREIRE et al., 2021), channel equalization (XU et al., 2024) and prediction (WU et al., 2021), beamforming (ENRICONI et al., 2020; MAYER et al., 2022), and joint channel estimation and decoding (SOARES et al., 2021b; SOARES; MAYER; ARANTES, 2023). For instance, Wang et al. (WANG et al., 2022) and Soares et al. (SOARES et al., 2021b) independently tackled the same reliable communication problem. While the real-valued neural networks (RVNNs) of Wang et al. (WANG et al., 2022) were limited to systems with 4×4 antennas and 4-QAM (quadrature amplitude modulation), the CVNN of Soares et al. (SOARES et al., 2021b) could handle 32×32 antennas and 64-QAM, marking the first work to address quasi-orthogonal STBC (QOSTBC) systems with more than 4×4 antennas and higher-order QAM modulations.

One promising approach in MIMO systems is using autoencoders, which have demonstrated significant potential in optimizing the communication process from transmission to reception (SONG et al., 2022). Autoencoders, a class of artificial neural networks (ANNs), are trained to learn efficient data representations, leading to more effective encoding and decoding (LI; PEI; LI, 2023). When applied to MIMO systems, these deep learning models offer improved performance over traditional methods, particularly in handling complex and nonlinear channel conditions.

Recent works have explored autoencoders in communication systems. O'Shea and Hoydis (O'SHEA; HOYDIS, 2017) introduced deep learning for the physical layer, showing that autoencoders can learn robust and efficient E2E communication schemes. Dörner *et al.* (DÖRNER et al., 2018) extended this by implementing a neural network-based over-the-air communication system using software-defined radios, proving the practicality of such approaches. Aoudia and Hoydis (AOUDIA; HOYDIS, 2019) tackled the issue of unknown channels by proposing a model-free training method that removes the need for a differentiable channel model. Further advancing the field, Ye *et al.* (YE et al., 2020; YE; LI; JUANG, 2021) developed deep learning-based systems that operate without explicit channel estimation or pilot signals, leveraging generative adversarial networks (GANs) to model channel effects. Song *et al.* (SONG et al., 2022) explored E2E learning for MIMO and multi-user systems, demonstrating the potential of autoencoders to mitigate interference in multi-user scenarios.

Despite these advancements, most current autoencoder-based methods rely on real-valued ANNs, which process complex-valued signals by splitting them into real and imaginary parts. However, communication signals are inherently complex, and this approach can introduce inefficiencies and inaccuracies. CVNNs are specifically designed to process complex signals directly, providing clear advantages to digital signal processing (DSP) in communication systems (MAYER et al., 2022).

In this paper, we propose a novel E2E learning architecture for MIMO systems using complex-valued autoencoders. By employing CVNNs, our approach fully utilizes the complex nature of the signals, improving the system's overall efficiency and simplifying the signal processing chain. Moreover, we introduce a robust power control mechanism through regularization to address potential issues with output signal power, such as signal distortion, which are common challenges in high-throughput MIMO systems. Additionally, we extend the autoencoder framework with federated learning to a multi-user MIMO (MU-MIMO) scheme, in which multiple data streams can be transmitted and received simultaneously, tackling interference and boosting mutual information (MI). This is a key advancement over traditional single-user models, addressing the challenges of multi-user interference. Simulations are performed over stochastic flat-fading Rayleigh channels.

The remainder of this paper is organized as follows. Section 8.2 discusses the related work on E2E communication systems and MU-MIMO. Section 8.3 presents the system model, explaining the MIMO setup. Section 8.4 details the proposed approach, including the CVNN design, multi-user scheme with federated learning, and transmission power control. Section 8.5 provides the results and performance evaluation of the proposed model. Finally, Section 8.6 concludes the paper, discussing the implications of the findings and potential future work.

8.2 RELATED WORK

8.2.1 End-to-End Communication Systems

The seminal work by O'Shea and Hoydis (O'SHEA; HOYDIS, 2017) pioneered the use of autoencoders in the physical layer, demonstrating the potential of deep learning to learn robust communication schemes by interpreting communication systems as E2E reconstruction tasks. Following this, there has been a significant interest in leveraging neural networks for optimizing both transmitter and receiver design in wireless communications (O'SHEA; HOYDIS, 2017; DÖRNER et al., 2018; FELIX et al., 2018; AOUDIA; HOYDIS, 2018, 2019; ZHANG; ZHANG; JIANG, 2019; LETIZIA; TONELLO, 2021; YE et al., 2020; YE; LI; JUANG, 2021; AN et al., 2023; AIT AOUDIA; HOYDIS, 2022; GUO et al., 2024; WU et al., 2022b; SAGDUYU; ULUKUS; YENER, 2023; SONG et al., 2022; SINGH et al., 2024; ZHANG; VAEZI, 2024; JI et al., 2024).

Building upon this foundation, Dörner *et al.* (DÖRNER et al., 2018) implemented an E2E communication system using software-defined radios (SDRs) for single-input single-output (SISO) and single-carrier systems. Their work demonstrated the practical feasibility of neural network-based transceivers and introduced methods to handle synchronization issues in continuous data transmission. Felix *et al.* (FELIX et al., 2018) extended this concept to OFDM systems. They proposed an OFDM-based autoencoder that enables reliable communication over frequency-selective fading channels and inherently learns to cope with hardware impairments, such as nonlinear amplifiers.

Aoudia and Hoydis contributed significantly to the field by addressing the challenge of unknown channel models (AOUDIA; HOYDIS, 2018, 2019). In (AOUDIA; HOYDIS, 2018), they introduced a learning algorithm that iterates between supervised training of the receiver and reinforcement learning-based training of the transmitter, enabling E2E learning without a differentiable channel model. This work was further expanded in (AOUDIA; HOYDIS, 2019), where they demonstrated the practical viability of their approach through hardware implementation on SDRs, achieving state-of-the-art performance over real channels.

In 2019, Zhang *et al.* (ZHANG; ZHANG; JIANG, 2019) analyzed the phenomena of overfitting and underfitting in deep learning-based E2E communication systems. They proposed using regularization techniques to alleviate overfitting, thereby improving the communication systems' reliability and error rate performance. Letizia and Tonello (LETIZIA; TONELLO, 2021) proposed an approach to maximize MI as a loss function in autoencoder training. By incorporating the channel into the loss function, they aimed to construct capacity-approaching codes and mitigate overfitting issues, enhancing the explainability and performance of machine learning models in communications.

Ye *et al.* (YE et al., 2020; YE; LI; JUANG, 2021) made notable contributions by introducing methods to handle unknown channel conditions. In (YE et al., 2020), they employed conditional generative adversarial networks (GANs) to model channel effects in a data-driven manner, allowing for E2E learning without explicit channel estimation. Later, in (YE; LI; JUANG, 2021), they developed pilot-free E2E communication systems for frequency-selective and MIMO channels, where the transmitter and receiver are jointly optimized using DL. In more recent works, An *et al.* (AN et al., 2023) proposed a learning-based E2E wireless communication system utilizing a deep neural network channel module. Their approach models unknown channels more accurately, leading to performance gains over traditional systems and those using GAN-based channel modeling.

In 2022, Aoudia and Hoydis (AIT AOUDIA; HOYDIS, 2022) explored E2E learning for OFDM systems over frequency- and time-selective fading channels. They showed that a neural network-based receiver could reduce the reliance on pilot signals without loss of bit error rate (BER) performance, effectively increasing throughput by 7%. Guo *et al.* (GUO et al., 2024) introduced a learning-based framework integrating CSI feedback and localization in massive MIMO systems. Their approach allows the feedback codeword to be used directly for localization without requiring reconstruction, improving both CSI feedback accuracy and localization performance.

Wu *et al.* (WU et al., 2022b) presented a channel-adaptive joint source and channel coding scheme for wireless image transmission over multipath fading channels. By employing OFDM and a dual-attention mechanism, their model adapts to channel variations and judiciously allocates transmission power, achieving state-of-the-art performance among existing schemes. Sagduyu *et al.* (SAGDUYU; ULUKUS; YENER, 2023) discussed task-oriented communications for next-generation (NextG) networks, focusing on E2E, DL, and artificial intelligence (AI) security aspects. They considered wireless signal classification as a task and addressed the security threats posed by adversarial machine learning attacks on deep learning-based communication systems.

Song *et al.* (SONG et al., 2022) benchmarked and interpreted E2E learning for

MIMO and multi-user communication systems. They highlighted potential pitfalls when interpreting learned communication schemes and demonstrated that autoencoders could learn to avoid interference in multi-user scenarios. Singh *et al.* (SINGH et al., 2024) proposed an autoencoder-based E2E orthogonal time frequency space (OTFS) system design that accounts for hardware impairments (HIs). By considering HIs in the design, their model significantly enhances error performance in doubly dispersive channels, outperforming conventional OTFS systems with state-of-the-art signal detectors.

Despite the extensive research on autoencoders and E2E learning, comparatively fewer works address multi-user schemes using these techniques. Song *et al.* (SONG et al., 2022) benchmarked and interpreted E2E learning for MIMO and multi-user communication systems. They considered both point-to-point scenarios, such as the Alamouti STBC, limited to two transmitting antennas and a single user, and singular value decomposition (SVD)-based schemes, also limited to single-user systems. For multi-user scenarios, they examined MIMO broadcast channels using zero-forcing (ZF) precoding. Still, their analysis was restricted to single-antenna users, with an indication that an extension to multiple antennas was left for future work. They demonstrated that autoencoders could learn to mitigate interference in multi-user scenarios but also pointed out that the learned schemes sometimes corresponded to conventional methods in a transformed domain. This outcome is expected and validates neural networks' capability as universal approximators (HORNIK; STINCHCOMBE; WHITE, 1989), inherently converging to optimal or global solutions in linear and controlled simulation scenarios. However, in practical systems where multiple complex effects are present, neural networks can demonstrate their true potential by extrapolating solutions in systems with very high degrees of freedom, as is the case in E2E approaches.

Zhang and Vaezi (ZHANG; VAEZI, 2024) focused on a two-user z-interference channel (ZIC) with perfect and imperfect channel state information (CSI). They designed a deep autoencoder-based structure that jointly optimizes the encoder and decoder pairs for both users. Their model generates interference-aware constellations that dynamically adapt their shape based on interference intensity to minimize the bit error rate (BER). An in-phase/quadrature-phase (I/Q) power allocation layer was introduced to enable the generation of non-uniform constellations, bringing further gains compared to standard uniform constellations like QAM. However, their analysis was limited to two users and specific interference scenarios, which may not generalize to more complex multi-user environments.

Ji *et al.* (JI et al., 2024) addressed dynamic interference in E2E communication systems with multi-user Gaussian interference channels. They proposed an adaptive learning algorithm for predicting and mitigating dynamic interference, allowing the system to estimate uncertain interference intensity through an adaptive training loop at the receiver. Since existing deep learning-based autoencoders are unable to train E2E systems without channel knowledge, they introduced a GAN-based training scheme to imitate real channels. Their approach enables effective communication without prior knowledge of the channel model. While their method shows significant improvements over traditional modulation schemes like phase-shift keying (PSK) and QAM in terms of block error rate (BLER), the study primarily focuses on scenarios with dynamic interference and does not extensively explore other multi-user aspects such as user scalability or resource allocation.

8.3 SYSTEM MODEL

In a MIMO communication system, multiple antennas on both the transmitter and receiver sides enable significant improvements in data rates and reliability. The system depicted in Fig. 8.3.1a can be described by the equation:

$$\mathbf{y}[k] = \mathbf{H}[k]\mathbf{x}[k] + \boldsymbol{\eta}[k], \tag{8.1}$$

in which $\mathbf{x}[k] \in \mathbb{C}^{N_{\text{tx}}}$ is the transmitted signal, $\mathbf{y}[k] \in \mathbb{C}^{N_{\text{rx}}}$ is the received signal, $\mathbf{H}[k] \in \mathbb{C}^{N_{\text{rx}} \times N_{\text{tx}}}$ is the channel matrix, $\boldsymbol{\eta}[k] \in \mathbb{C}^{N_{\text{rx}}}$ is the additive white Gaussian noise (AWGN) vector, and $k = 0, 1, \cdots, \infty$ is the discrete time index.

The matrix $\mathbf{H}[k]$ describes the fading channel between the N_{tx} transmit antennas and N_{rx} receive antennas, with elements drawn from a complex Gaussian distribution in the case of a flat fading Rayleigh channel. The noise $\boldsymbol{\eta}[k]$ has independent and identically distributed (i.i.d.) complex Gaussian entries with variance N_0.

When CSI is available at the transmitter, the capacity of the MIMO system can be achieved using singular value decomposition (SVD) and the water-filling algo-

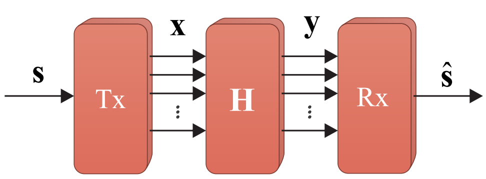

(a)

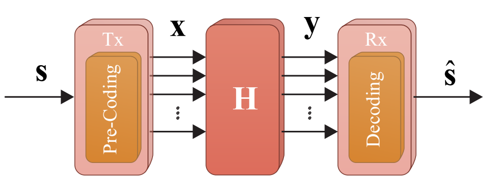

(b)

Figure 8.3.1 – MIMO communication systems. (a) Classical. (b) MIMO system with precoding and decoding.

rithm (RALEIGH; CIOFFI, 1998). The capacity expression is based on the transmitted signal's correlation matrix $\mathbf{R}_{xx} = \mathbb{E}\{\mathbf{x}[k]\mathbf{x}^H[k]\}$.

The channel decomposition is given by

$$\mathbf{H} = \mathbf{U}\boldsymbol{\Sigma}\mathbf{V}^H, \tag{8.2}$$

in which $\mathbf{U} \in \mathbb{C}^{N_{\mathrm{rx}} \times N_{\mathrm{rx}}}$ and $\mathbf{V} \in \mathbb{C}^{N_{\mathrm{tx}} \times N_{\mathrm{tx}}}$ are unitary matrices, and $\boldsymbol{\Sigma} \in \mathbb{C}^{N_{\mathrm{rx}} \times N_{\mathrm{tx}}}$ is a diagonal matrix containing the singular values λ_i of $\mathbf{H}$. Considering the MIMO system illustrated in Fig. 8.3.1b, the precoding is performed by processing $\mathbf{V}$, resulting in the transmitted signal $\mathbf{x}(k) = \mathbf{V}\mathbf{s}(k)$. The received signal after decoding with $\mathbf{U}$ is

$$\hat{\mathbf{s}} = \boldsymbol{\Sigma}\mathbf{s} + \mathbf{U}^H\boldsymbol{\eta}. \tag{8.3}$$

To achieve the channel capacity, the power allocated to each sub-channel is determined using the water-filling algorithm. The power P_i allocated to each sub-channel is

$$P_i = \left(\mu - \frac{N_0}{\lambda_i^2}\right)^+, \tag{8.4}$$

in which $(\cdot)^+$ is the rectifying function and μ is the water-filling level, chosen to satisfy the total average power constraint $P_{\mathrm{total}} = \sum_i P_i$.

The achievable capacity for CSI known at the transmitter and with the transmitted signal optimally precoded is given by

$$C = \sum_{i=1}^{\min(N_{\mathrm{tx}}, N_{\mathrm{rx}})} \log_2\left(1 + \frac{P_i\lambda_i^2}{N_0}\right) \quad [\text{bits/s/Hz}], \tag{8.5}$$

which is equivalently expressed in bits/channel use.

8.4 PROPOSED APPROACH

In this work, we propose a transmission model designed to improve the performance and robustness of communication systems. The objective is to refine the signal encoding, transmission, and decoding processes using complex-valued neural network-based models. CVNNs can directly operate as powerful nonlinear filters in the complex domain, surpassing the results of classical RVNNs (HIROSE; YOSHIDA, 2012b). In recent works, CVNNs have been successfully employed in communication systems for a wide range of applications, such as channel equalization (MAYER et al., 2019c), beamforming (MAYER et al., 2022), channel estimation and decoding (SOARES; MAYER; ARANTES, 2023). For example, in the case of joint channel estimation and decoding, CVNNs not only achieve superior performance but also present lower computational complexity compared with classical algorithms. Among the class of CVNNs, the phase-transmittance radial basis function (PT-RBF) has been extensively studied for communications systems due to its better performance in noisy scenarios, as outlined in references (SOARES; MAYER; ARANTES, 2023; MAYER et al., 2022). Fig 8.4.1 illustrates the proposed E2E architecture comprised of PT-RBFs (i.e., encoder and decoder) and a de-embedded channel for gradient transmission.

8.4.1 Complex-valued PT-RBF Neural Networks

Following the notation used in (MAYER et al., 2022), the PT-RBF is defined with L hidden layers (excluding the input layer), where the superscript $l \in [0, 1, \cdots, L]$ denotes the layer index and $l = 0$ is the input layer. The l-th layer (excluding the input layer $l = 0$) is comprised by $I^{\{l\}}$ neurons, $O^{\{l\}}$ outputs, and has a matrix of synaptic weights $\mathbf{W}^{\{l\}} \in \mathbb{C}^{O^{\{l\}} \times I^{\{l\}}}$, a bias vector $\mathbf{b}^{\{l\}} \in \mathbb{C}^{O^{\{l\}}}$, a matrix of center vectors $\mathbf{\Gamma}^{\{l\}} \in \mathbb{C}^{I^{\{l\}} \times O^{\{l-1\}}}$, and a variance vector $\boldsymbol{\sigma}^{\{l\}} \in \mathbb{C}^{I^{\{l\}}}$. Notice that $\bar{\mathbf{x}} \in \mathbb{C}^{N_{\text{inp}}}$ is the PT-RBF normalized input vector (N_{inp} inputs) and $\mathbf{y}^{\{L\}} \in \mathbb{C}^{N_{\text{out}}}$ is the PT-RBF output vector (N_{out} outputs). The l-th hidden layer output vector $\mathbf{y}^{\{l\}} \in \mathbb{C}^{O^{\{l\}}}$ is given by

$$\mathbf{y}^{\{l\}} = \mathbf{W}^{\{l\}} \boldsymbol{\phi}^{\{l\}} + \mathbf{b}^{\{l\}}, \tag{8.6}$$

where $\boldsymbol{\phi}^{\{l\}} \in \mathbb{C}^{I^{\{l\}}}$ is the vector of Gaussian kernels.

The m-th Gaussian kernel of the l-th hidden layer is formulated as

$$\phi_m^{\{l\}} = \exp\left[-\Re\left(v_m^{\{l\}}\right)\right] + \jmath \exp\left[-\Im\left(v_m^{\{l\}}\right)\right], \tag{8.7}$$

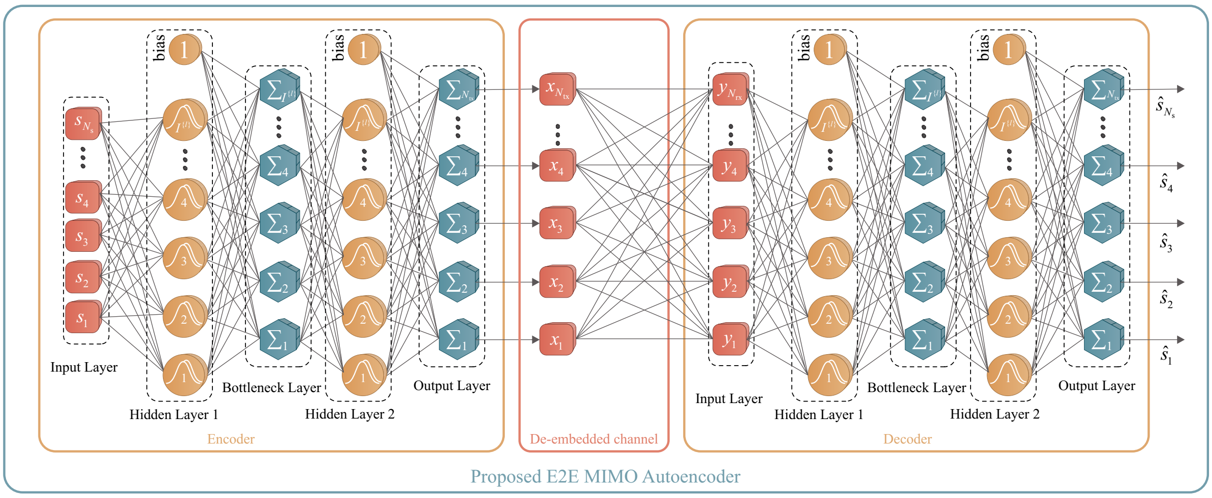

Figure 8.4.1 – Proposed E2E system architecture.

in which $v_m^{\{l\}}$ is the m-th Gaussian kernel input of the l-th hidden layer, described as

$$v_m^{\{l\}} = \frac{\left\| \Re\left(\mathbf{y}^{\{l-1\}}\right) - \Re\left(\boldsymbol{\gamma}_m^{\{l\}}\right) \right\|_2^2}{\Re\left(\sigma_m^{\{l\}}\right)} + \jmath \frac{\left\| \Im\left(\mathbf{y}^{\{l-1\}}\right) - \Im\left(\boldsymbol{\gamma}_m^{\{l\}}\right) \right\|_2^2}{\Im\left(\sigma_m^{\{l\}}\right)}, \quad (8.8)$$

where $\mathbf{y}^{\{l-1\}} \in \mathbb{C}^{O^{\{l-1\}}}$ is the output vector of the $(l-1)$-th hidden layer (except for the first hidden layer that $\mathbf{y}^{\{0\}} = \bar{\mathbf{x}}$), $\boldsymbol{\gamma}_m^{\{l\}} \in \mathbb{C}^{O^{\{l-1\}}}$ is the m-th vector of Gaussian centers of the l-th hidden layer, $\sigma_m^{\{l\}} \in \mathbb{C}$ is the respective m-th variance, and $\Re(\cdot)$ and $\Im(\cdot)$ return the real and imaginary components, respectively.

8.4.2 Backpropagation and Channel De-embedding

The overall system, depicted in Fig. 8.4.1, can be analyzed by three blocks: an encoder that transforms the input data into a transmitted signal; a channel $\mathbf{H} \in \mathbb{C}^{N_{\text{rx}} \times N_{\text{tx}}}$ that interacts with the transmitted signal; and a decoder that reconstructs the original data from the received signal. To construct such a system, considering the transmitting model in (8.1), we employ two PT-RBFs, one for encoding and the other for decoding. In the transmission process (i.e., forward step), the input signal $\mathbf{s} \in \mathbb{C}^{N_{\text{s}}}$ feeds the encoder, creating $\mathbf{x} \in \mathbb{C}^{N_{\text{tx}}}$. After passing through the channel, the received signal ($\mathbf{y} \in \mathbb{C}^{N_{\text{rx}}}$) feeds the decoder, resulting in $\hat{\mathbf{s}} \in \mathbb{C}^{N_{\text{s}}}$. In the training process (i.e., backward step), a local gradient is transmitted from the decoder to the encoder. However, since there is a channel in the middle, we need to consider how the channel affects the transmitted signal and incorporate this dynamic into the gradient computations.

During backpropagation, the loss function gradient $\nabla_\theta J$ is computed for any parameter θ as described in (MAYER et al., 2022). Nevertheless, it is necessary to take the channel into account, to update the encoder parameters. Then, at the encoder, the backpropagation chain rule leads to

$$\nabla_\theta J = \frac{\partial J}{\partial \hat{\mathbf{s}}} \cdots \frac{\partial \mathbf{y}}{\partial \mathbf{x}} \frac{\partial \mathbf{x}}{\partial \theta}, \quad (8.9)$$

in which the ellipses are used to omit the rest of the chain rule derivatives that can be different depending on the neural network architecture. For an in-depth study on the backpropagation in CVNNs, see (MAYER, 2022).

In view of (8.9), the channel effect is given by derivative $\partial \mathbf{y} / \partial \mathbf{x} = \mathbf{H}^T$, which couples the chain rule from the decoder to the encoder. Consequently, the local gradients at the encoder become

$$\nabla_\theta J = \frac{\partial J}{\partial \hat{\mathbf{s}}} \cdots \mathbf{H}^T \frac{\partial \mathbf{x}}{\partial \theta}. \quad (8.10)$$

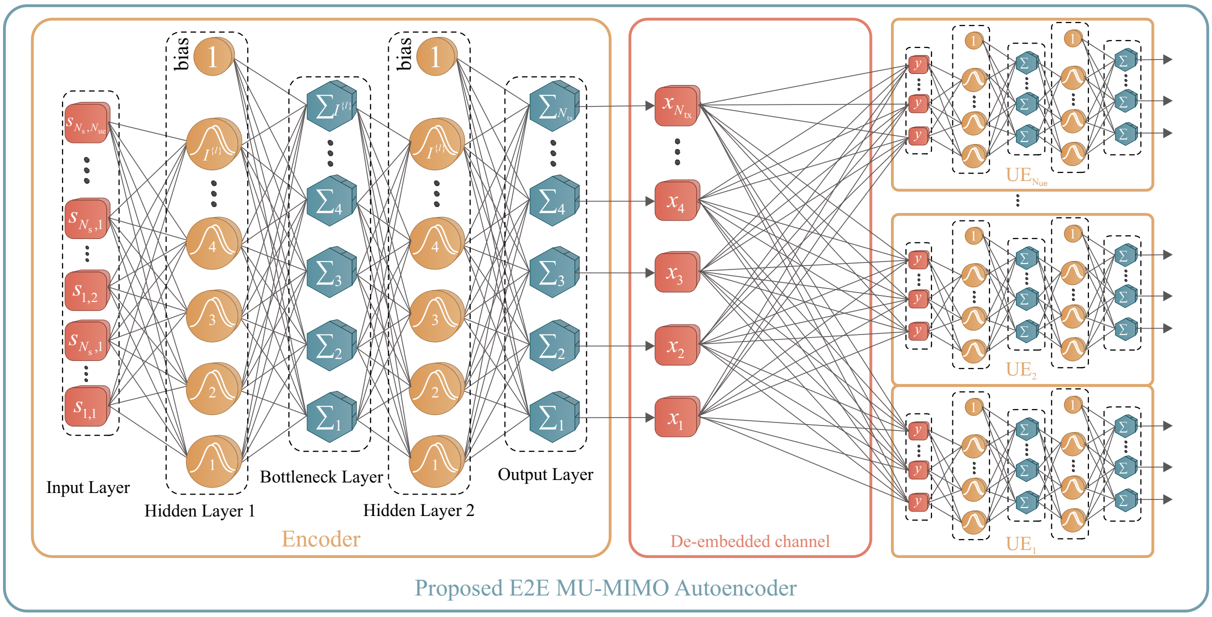

Figure 8.4.2 – Proposed multi-user E2E system architecture.

Regarding the specific case of the PT-RBF, the encoder gradient coupling is given by

$$\boldsymbol{\psi}_{\text{enc}}^{\{L\}} = \mathbf{H}^T \boldsymbol{\psi}_{\text{dec}}^{\{0\}}, \tag{8.11}$$

in which $\boldsymbol{\psi}_{\text{enc}}^{\{L\}}$ and $\boldsymbol{\psi}_{\text{dec}}^{\{0\}}$ are the gradient vectors at the encoder output and decoder input, respectively. The remaining parameter update equations for the encoder follow the standard gradient descent approach, where the error is backpropagated through the network until it reaches the encoder's input.

Note that the gradient coupling method of (8.10) can be applied to any complex-valued neural network by linearly combining the gradient at the decoder input by the channel matrix. This gradient at the decoder input can be transferred to the encoder via a low-capacity feedback channel.

By incorporating the channel transpose $\mathbf{H}$ into the gradient computations, we effectively de-embed the channel from the backpropagation process. This allows the gradient information to flow from the decoder back to the encoder, enabling the encoder to adjust its parameters to mitigate the channel effects and enhance system performance. It ensures that the encoder learns signal representations that are robust to channel impairments, thereby improving data and user multiplexing capabilities. This approach requires knowledge of the channel matrix $\mathbf{H}$ during training, which is feasible in supervised learning scenarios where the CSI is available. In practical implementations with time-varying channels, online learning methods can be employed to update the network parameters and maintain performance.

8.4.3 Multi-user Autoencoder

Extending the proposed complex-valued PT-RBF neural network to an MU-MIMO scenario involves accommodating multiple user equipments (UEs), each with its decoder while maintaining a shared encoder at the transmitter. This architecture allows efficient data and user multiplexing in a MIMO system serving multiple users simultaneously, as shown in Fig. 8.4.2.

8.4.3.1 System Model

Consider a MIMO system with N_{ue} UEs, in which the n-th UE (UE_n) has $N_{\text{rx},n}$ receiving antennas. The transmitter (e.g., base station) is equipped with N_{tx} transmitting antennas and employs a single neural network encoder to serve all UEs. Each UE operates its neural network decoder, which resides within the UE and is independent of other UEs.

For the UE_n, the received signal $\mathbf{y}_n \in \mathbb{C}^{N_{\text{rx},n}}$ is given by

$$\mathbf{y}_n = \mathbf{H}_n \mathbf{x} + \boldsymbol{\eta}_n, \tag{8.12}$$

in which $\mathbf{x} \in \mathbb{C}^{N_{\text{tx}}}$ is the transmitted signal, $\mathbf{H}_n \in \mathbb{C}^{N_{\text{rx},n} \times N_{\text{tx}}}$ is the UE_n channel matrix, $\boldsymbol{\eta}_n \in \mathbb{C}^{N_{\text{rx},n}}$ is the UE_n noise vector.

8.4.3.2 Training Process

Each UE employs its neural network decoder and uses a unique pseudo-random pilot sequence for training, eliminating the need to share training sequences among UEs and reducing computational overhead. The encoder at the transmitter is responsible for nullifying inter-UE interference by learning to encode signals that are distinguishable at each UE's decoder.

During the training phase, UE_n computes the quadratic loss function based on its received pilots

$$J_n = \frac{1}{2} \|\mathbf{s}_n - \hat{\mathbf{s}}_n\|_2^2, \tag{8.13}$$

in which $\mathbf{s}_n \in \mathbb{C}^{N_{\text{s},n}}$ and $\hat{\mathbf{s}}_n \in \mathbb{C}^{N_{\text{s},n}}$ are the pilot and estimated vectors, respectively.

8.4.3.3 Backpropagation and Federated Learning

Following the strategy proposed in Section 8.4.2, the UE_n computes its local gradient and estimates the channel $\mathbf{H}_n$, transmitting these pieces of information to the encoder. Then, at the receiver, a global channel matrix $\mathbf{H} = [\mathbf{H}_1 \; \mathbf{H}_2 \cdots \mathbf{H}_{N_{\text{ue}}}]^T \in \mathbb{C}^{(N_{\text{rx},n} N_{\text{ue}}) \times N_{\text{tx}}}$ can be stacked to encompass all UEs. Similarly, the same stacking can be employed on the local gradients, which, for the PT-RBF, yields $\boldsymbol{\psi}_{\text{dec}}^{\{0\}} = \left[\boldsymbol{\psi}_{\text{dec},0}^{\{0\}} \; \boldsymbol{\psi}_{\text{dec},1}^{\{0\}} \cdots \boldsymbol{\psi}_{\text{dec},N_{\text{ue}}}^{\{0\}}\right]^T \in \mathbb{C}^{N_{\text{rx},n} N_{\text{ue}}}$. Finally, the aggregated gradient at the transmitter can be computed as in (8.11).

This method accurately accounts for all UEs in a single operation. However, it requires each UE to feedback both its estimated channel $\mathbf{H}_n$ and its local decoder gradient (i.e., $\boldsymbol{\psi}_{\text{dec},n}^{\{0\}}$ for the PT-RBF) to the transmitter, which may not be practical due to feedback bandwidth constraints.

To address this issue, we propose a federated learning approach in which each UE computes its local gradient and sends it to the transmitter via a feedback channel. This approach reduces the feedback overhead, as each UE_n only needs to transmit a gradient vector $\nabla_{\mathbf{x}} J_n$ of length $N_{\text{tx},n}$, without requiring the full channel matrix. Specifically, for UE_n

$$\nabla_{\mathbf{x}} J_n = \frac{\partial J_n}{\partial \hat{\mathbf{s}}_n} \cdots \frac{\partial \mathbf{y}_n}{\partial \mathbf{x}} = \frac{\partial J_n}{\partial \hat{\mathbf{s}}_n} \cdots \mathbf{H}_n^T, \tag{8.14}$$

which is independent of the transmitted signal $\mathbf{x}$.

After receiving the N_{ue} gradients, the encoder aggregates all $\nabla_{\mathbf{x}} J_n$ in a federated learning scheme

$$\nabla_{\mathbf{x}} J = \sum_{n=1}^{N_{\text{ue}}} \nabla_{\mathbf{x}} J_n, \tag{8.15}$$

which yields the encoder gradient

$$\nabla_{\theta} J = \nabla_{\mathbf{x}} J \frac{\partial \mathbf{x}}{\partial \theta}. \tag{8.16}$$

Then, for the PT-RBF, UE_n transmits the vector

$$\boldsymbol{\psi}_{\text{fl},n}^{\{0\}} = \mathbf{H}_n^T \boldsymbol{\psi}_{\text{dec},n}^{\{0\}}, \tag{8.17}$$

and, at the receiver, the federated learning aggregation is

$$\boldsymbol{\psi}_{\text{enc}}^{\{L\}} = \sum_{n=1}^{N_{\text{ue}}} \boldsymbol{\psi}_{\text{fl},n}^{\{0\}}. \tag{8.18}$$

As in Section 8.4.2, this approach is valid for any complex-valued neural network by replacing gradients in (8.15) and (8.16).

This federated learning allows each UE to operate independently with its decoder and training process, fully decoupling the UEs. The encoder at the transmitter learns to encode signals that can be correctly decoded by each UE while mitigating inter-user interference. Consequently, data intended for different UEs can be multiplexed efficiently, enhancing the overall Mutual Information (MI).

Extending the single-user autoencoder framework to a multi-user scenario, we leverage the neural network's ability to learn complex mappings in a high-dimensional space. Each UE's decoder adapts to its specific channel conditions and interference environment, while the shared encoder learns to optimize the transmitted signals for all UEs collectively.

This method requires a feedback mechanism for UEs to return their local gradients to the transmitter. Although this introduces some overhead, it is feasible in systems where feedback channels are available and can be efficiently managed. Overall, the proposed multi-user autoencoder facilitates efficient data and user multiplexing in MIMO systems, offering a scalable solution for multi-user communications with CVNNs.

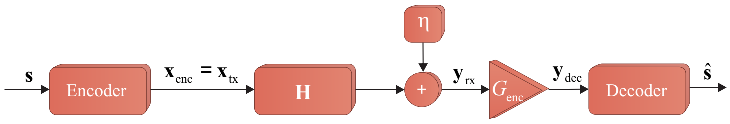

(a)

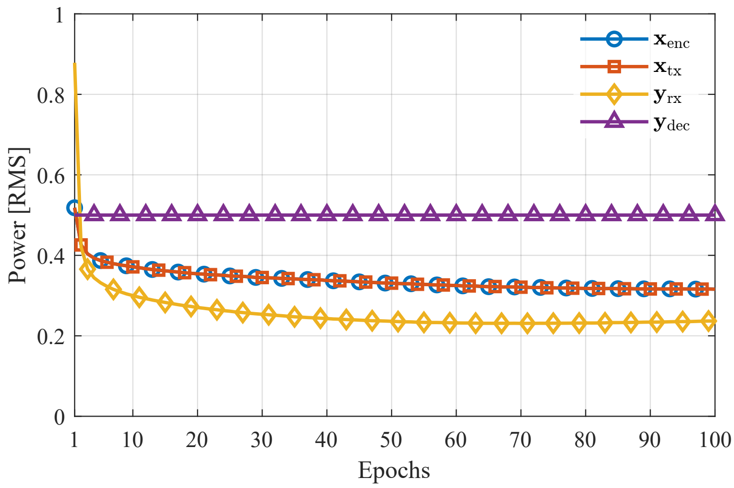

(b)

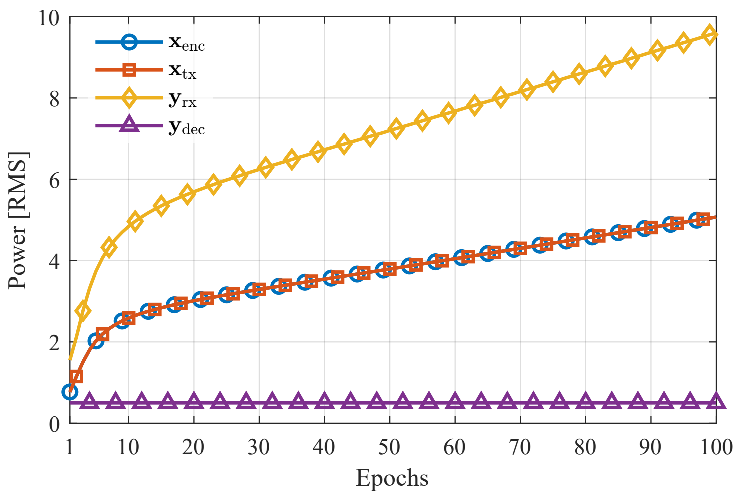

(c)

Figure 8.4.3 – (a) Block diagram of the direct transmission model. (b) Power analysis of the direct model in a 4x4 MIMO system with 16-QAM modulation under a noise-free condition (SNR = 100 dB). (c) Power analysis of the direct model under noisy conditions (SNR = 8 dB).

8.4.4 Transmission Power Analysis

The proposed approach is evaluated using four transmission models: direct, normalized, regularized, and a combination of regularization with normalization. Each model addresses specific challenges in maintaining stable transmission power and ensuring efficient signal recovery.

8.4.4.1 Direct Model

In the direct model, shown in Fig. 8.4.3a, the encoded signal is transmitted without additional processing. This baseline model helps to understand the transmission behavior and serves as a basis for enhancements.

To ensure compatibility with the neural network decoder, the received signal is normalized as $\mathbf{y}_{\text{dec}} = \mathbf{y}_{\text{rx}} G_{\text{dec}}$, with

$$G_{\text{dec}} = \frac{1}{P_{\mathbf{y}_{\text{rx}}} \sqrt{N_{\text{rx}}}}, \tag{8.19}$$

in which $P_{\mathbf{y}_{\text{rx}}}$ is the received root mean square (RMS) power.

In a noise-free environment, the system stabilizes after a brief transient phase, as shown in Fig. 8.4.3b. However, as shown in Fig. 8.4.3c, when noise is introduced, we observe that the encoder increases its output power in an attempt to compensate for the noise $\boldsymbol{\eta}$, leading to an unbounded growth in $\mathbf{x}_{\text{enc}}$. This uncontrolled power escalation is impractical for real-world applications with power constraints.

8.4.4.2 Power-Normalized Transmission

The power-normalized model introduces a normalization step before transmission to control the transmitted power. The encoded signal is scaled to have unit power $\mathbf{x}_{\text{tx}} = \mathbf{x}_{\text{enc}} G_{\text{enc}}$, in which

$$G_{\text{enc}} = \frac{1}{P_{\mathbf{x}_{\text{enc}}}}. \tag{8.20}$$

This modification, depicted in Fig. 8.4.4a, stabilizes the transmitted power. However, the encoder's output $\mathbf{x}_{\text{enc}}$ still grows indefinitely (Fig. 8.4.4b), which is expected since there is no direct restriction preventing the encoder from increasing its output values. This uncontrolled growth may cause overflow or saturation issues within the neural network.

8.4.4.3 Regularization

To prevent the indefinite growth of $\mathbf{x}_{\text{enc}}$, the regularized model applies L2 regularization to the encoder output layer, as shown in Fig. 8.4.5a. L2 regularization is a technique that adds a penalty term to the loss function, proportional to the squared magnitude of the neural network parameter. This penalty discourages the network from assigning large

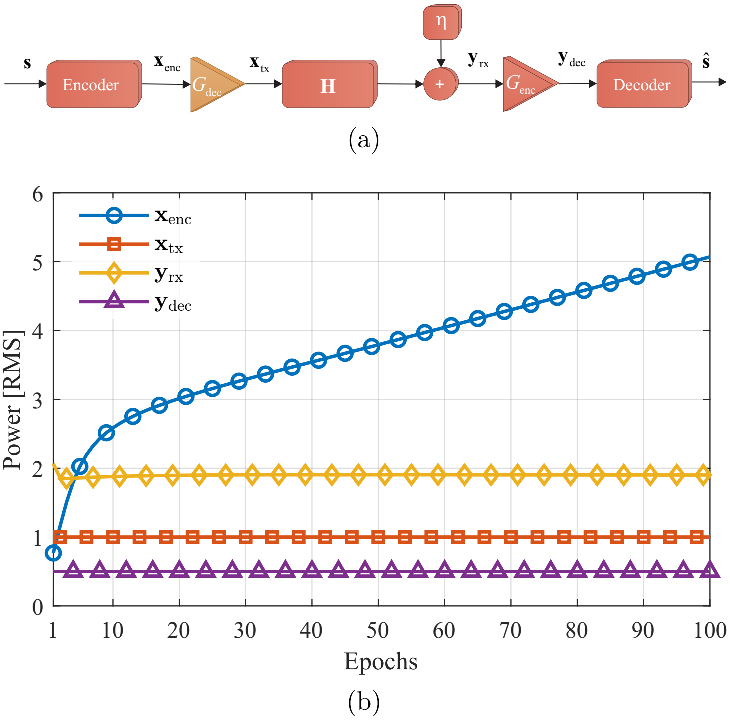

Figure 8.4.4 – (a) Block diagram of the power-normalized model. The gain G_{enc} normalizes the encoded signal before transmission. (b) Power analysis of the power-normalized model. The transmitted power is stabilized, but $\mathbf{x}_{\text{enc}}$ continues to rise indefinitely, potentially leading to overflow or saturation.

weights, effectively controlling the magnitude of the encoder's output, and potentially preventing overfitting.

The update rule for a generic parameter θ, with L2 regularization, is

$$\theta[k+1] = \theta[k] - \eta_\theta \left(\nabla_\theta J[k] + \mu[k]\theta[k] \right), \tag{8.21}$$

in which η_θ is the learning rate and $\mu[k]$ is the regularization factor.

The regularization factor $\mu[k]$ is dynamically adjusted using a parametric sigmoid function to ensure that regularization is applied effectively, as

$$\mu[k] = \frac{c}{1 + \exp(-a \cdot P_{\mathbf{x}_{\text{enc}}}[k] + b)}, \tag{8.22}$$

in which $P_{\mathbf{x}_{\text{enc}}}[k]$ is the RMS power of the encoder's output. In this function, a is the smoothing factor that determines the steepness of the sigmoid curve; a higher value of a results in a sharper transition, causing $\mu[k]$ to increase rapidly once $P_{\mathbf{x}_{\text{enc}}}[k]$ exceeds a certain threshold. The parameter b is the shift factor, controlling the point along the $P_{\mathbf{x}_{\text{enc}}}[k]$ axis where the sigmoid function transitions; adjusting b shifts the curve left or right, determining when regularization begins to increase. Finally, c is the scaling factor that sets the maximum value of $\mu[k]$; this parameter limits the regularization factor to prevent it from becoming excessively large.

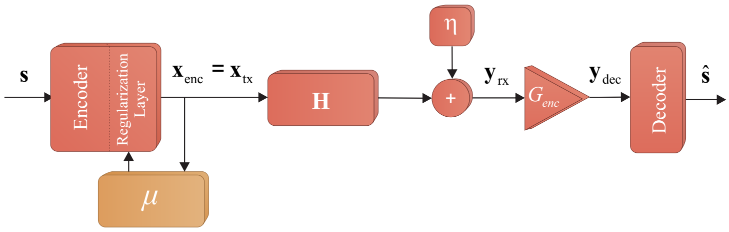

(a)

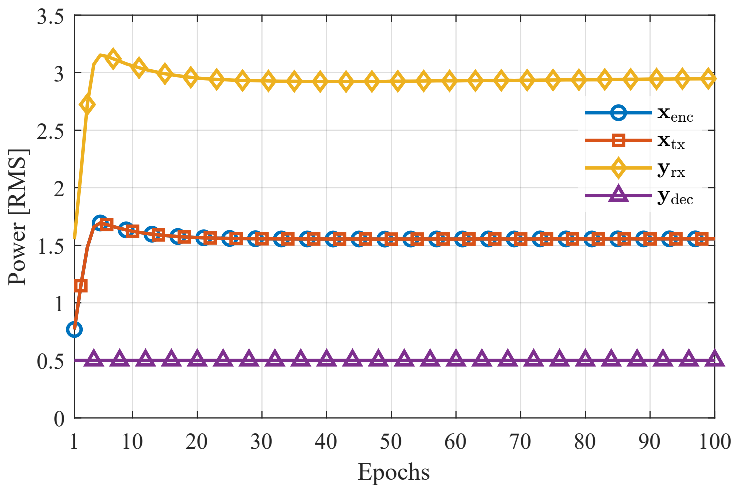

(b)

Figure 8.4.5 – (a) Block diagram of the regularized model. L2 regularization is applied to the encoder's output layer to control the output magnitude. (b) Power analysis of the regularized model. L2 regularization stabilizes $\mathbf{x}_{enc}$, but a small transient is observed at the beginning of transmission.

By tuning a, b, and c, the regularization factor $\mu[k]$ remains low when the encoder's output power is within acceptable limits and increases only when necessary to prevent excessive growth. As shown in Fig. 8.4.5b, regularization stabilizes $\mathbf{x}_{enc}$. However, a small transient in transmitted power remains at the start of transmission.

8.4.4.4 Regularization with Normalization

To eliminate the transient issue, the regularization with normalization model combines both techniques, as shown in Fig. 8.4.6a. The encoded signal is regularized and then normalized before transmission.

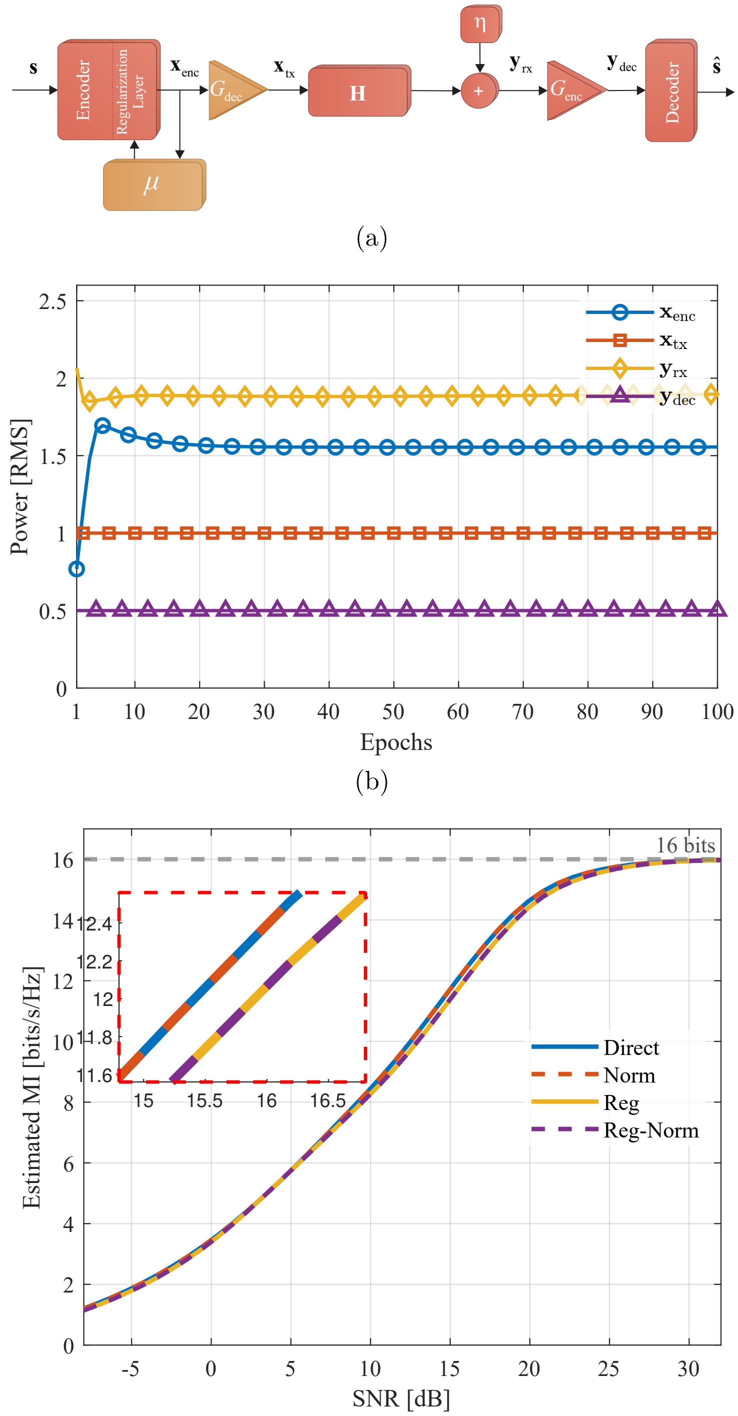

(a) (b) (c)

Figure 8.4.6 – (a) Block diagram of the regularization with normalization model. The signal is regularized and normalized before transmission and further normalized at the receiver. (b) Power analysis of the regularization with normalization model. Both regularization and normalization contribute to a fully stabilized transmitted signal. (c) MI performance of the transmission model depending on the power constraint. Regularized models show a slight drop in performance at lower SNRs, between 8 dB and 24 dB, but provide enhanced power control.

This approach ensures consistent and stable power levels throughout transmission, as evidenced in Fig. 8.4.6b. Both $\mathbf{x}_{\text{enc}}$ and $\mathbf{x}_{\text{tx}}$ remain stable, addressing the issues identified in previous models. Fig. 8.4.6c compares the estimated MI performance of all models in a

Table 8.5.1 – PT-RBF architectures and hyperparameters.

	Shallow PT-RBF		Deep PT-RBF				MU PT-RBF		Lightweight MU PT-RBF	
	Tx	Rx	Tx		Rx		Tx	Rx	Tx	Rx
Hyperparam.	$l = 1$	$l = 1$	$l = 1$	$l = 2$	$l = 1$	$l = 2$	$l = 1$	$l = 1$	$l = 1$	$l = 1$
Neurons	250	125	50	50	25	25	250	10	250	4
η_w	5×10^{-6}	5×10^{-3}	5×10^{-4}	5×10^{-6}	5×10^{-3}	5×10^{-3}	5×10^{-6}	5×10^{-3}	5×10^{-6}	5×10^{-3}
η_b	5×10^{-6}	5×10^{-3}	5×10^{-4}	5×10^{-6}	5×10^{-3}	5×10^{-3}	5×10^{-6}	5×10^{-3}	5×10^{-6}	5×10^{-3}
η_γ	3×10^{-4}	3×10^{-3}	3×10^{-4}	3×10^{-4}	3×10^{-3}	3×10^{-3}	3×10^{-4}	3×10^{-3}	3×10^{-4}	3×10^{-3}
η_σ	5×10^{-4}	5×10^{-3}	5×10^{-4}	5×10^{-4}	5×10^{-3}	5×10^{-3}	5×10^{-4}	5×10^{-3}	5×10^{-4}	5×10^{-3}

l denotes the PT-RBF layer.

4x4 MIMO system with 16-QAM modulation. Although all models perform similarly at lower and higher SNRs, the regularized models exhibit a slight performance degradation at SNRs between 8 dB and 24 dB. Despite this minor drawback, the regularized models offer significant advantages in power control and system robustness.

8.5 RESULTS

In this section, we present the performance analysis of the proposed E2E MIMO system using complex-valued neural networks (CVNNs) in comparison with conventional MIMO precoding techniques. We specifically compare the results of our approach with well-established linear precoding methods of zero-forcing (ZF) and minimum mean square error (MMSE) precoding. Additionally, the theoretical upper bound is presented using SVD combined with water-filling (i.e., maximum achievable capacity for a MIMO system). All systems are evaluated over a static, flat-fading Rayleigh channel with perfect CSI at the receiver. The detailed configuration of the proposed E2E MIMO system is described in Table 8.5.1. The training was performed using batch sizes of 100. Each epoch comprehends 50×10^3 multiplexed symbols. L2 regularization was optimized for $a = 3$, $b = 15$, and $c = 1$. The PT-RBF parameters are initialized as proposed in (SOARES; MAYER; ARANTES, 2024) and updated using AdaMax, the adaptive moment estimation with infinite norm.

For the sake of comparison, the estimated MI is obtained from ten consecutive Monte Carlo simulations for each system. The simulation scenarios include different modulation schemes (4-QAM, 16-QAM, and 64-QAM) with varying levels of complexity and signal quality, demonstrating the robustness and adaptability of the proposed system for higher-order modulations. Results were averaged over ten subsequent simulations.

8.5.1 MIMO Results

We compare the proposed model's performance across different modulation schemes, including 4-QAM, 16-QAM, and 64-QAM, with four spatially multiplexed streams transmitted over four antennas. These simulations assess the MI gains achieved using our model.

8.5.1.1 4-QAM Modulation

In the first scenario, we utilize $N_{\text{tx}} = N_{\text{rx}} = 4$, with four spatially multiplexed 4-QAM streams. The proposed E2E CVNN is employed in a shallow architecture (Table 8.5.1). Fig. 8.5.1 illustrates the estimated MI performance as a function of the signal-to-noise ratio (SNR). As observed, the proposed model significantly outperforms both ZF and MMSE precoding techniques. This result highlights the robustness of the proposed E2E CVNN learning approach, which can adapt to the channel conditions and achieve near-optimal performance, closely approaching the theoretical upper bound.

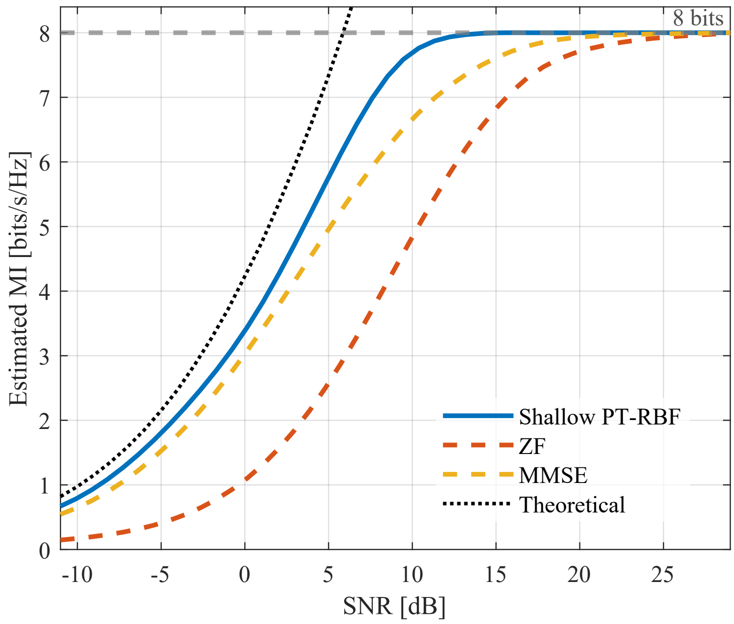

Figure 8.5.1 – Estimated MI analysis for the proposed system with 4-QAM modulation and $N_{\text{tx}} = N_{\text{rx}} = 4$. The solid blue line represents the proposed approach, the dashed yellow line is the MMSE, the dashed red line is the ZF, and the dotted black line is theoretical capacity.

8.5.1.2 Higher-Order Modulations

To further evaluate the model adaptability, the second scenario extends the modulation schemes to 16-QAM and 64-QAM. Fig. 8.5.2a presents the estimated MI analysis with 16-QAM modulation, while Fig. 8.5.2b shows the results with 64-QAM modulation. Despite the increased complexity of the modulation schemes, the proposed model demonstrates its ability to manage high-order modulation, continuing to outperform traditional ZF and MMSE precoding techniques. To handle this increase in the modulation order the model was optimized according to Table 8.5.1 with two layers both in the encoder and decoder. These results further solidify the robustness of our E2E approach across a variety of challenging scenarios.

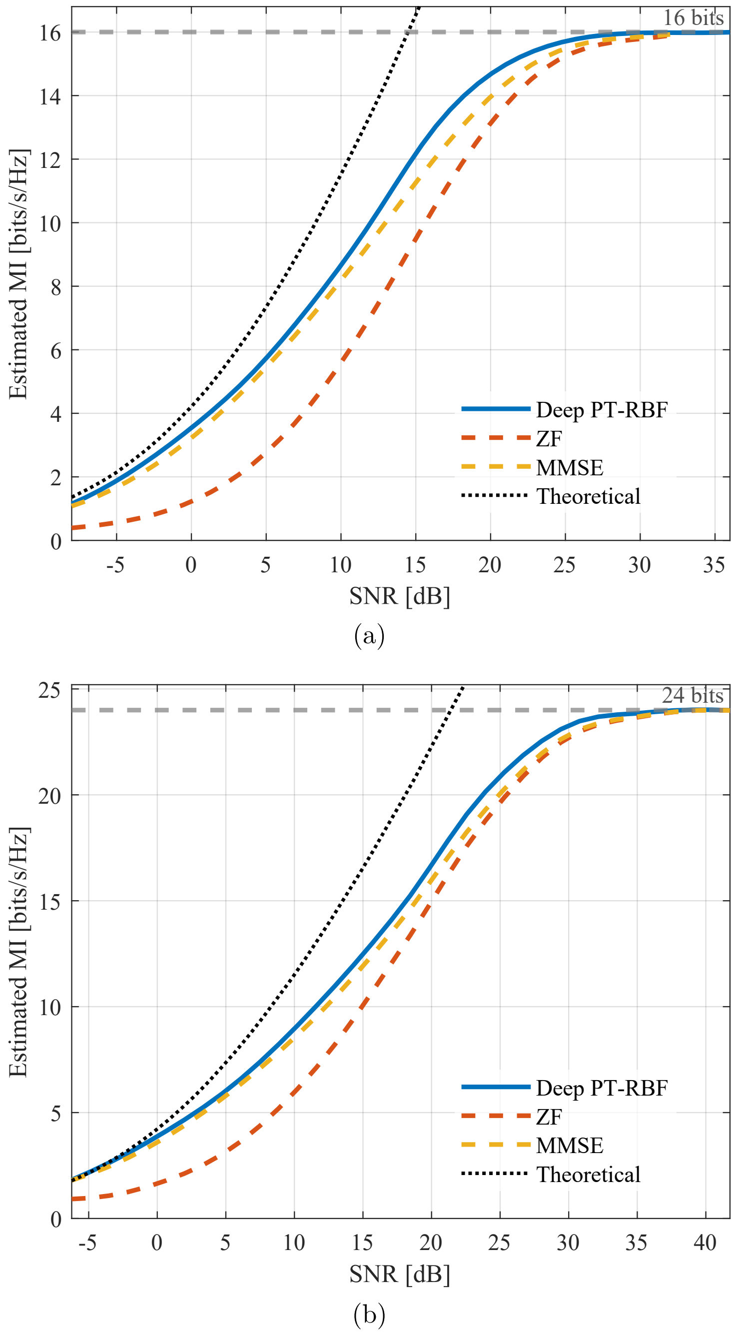

(a)

(b)

Figure 8.5.2 – Estimated MI analysis for $N_{\mathrm{tx}} = N_{\mathrm{rx}} = 4$: (a) 16QAM. (b) 64-QAM. The solid blue line represents the proposed approach, the dashed yellow line is the MMSE, the dashed red line is the ZF, and the dotted black line is theoretical capacity.

From this point forward, we will not compare the proposed system to ZF and MMSE precoding approaches, as the presented results have already established a reference for the effectiveness of our model. The following sections will focus on evaluating the performance of the proposed system in various challenging scenarios to further stress the model's capabilities.

8.5.1.3 Results in terms of MSE

Additionally, the performance of the model is evaluated in terms of the normalized mean squared error (NMSE) by comparing the estimated signal $\hat{\mathbf{s}}$ with the original reference signal $\mathbf{s}$ per epoch. Fig. 8.5.3 shows the results for 4×4 MIMO transmitting 4 streams in low SNR (Fig. 8.5.3a) and high SNR scenarios (Fig. 8.5.3b). Results demonstrate a smooth convergence and small standard deviation. Moreover, the maximum error is limited, indicating the convergence in both low and high SNR.

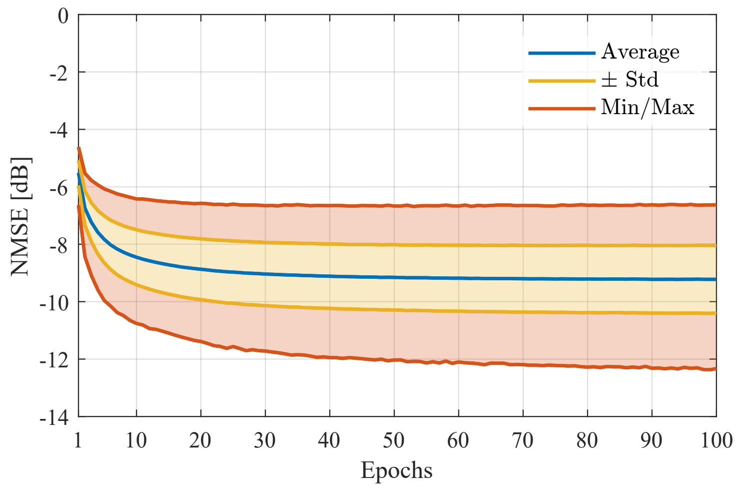

(a)

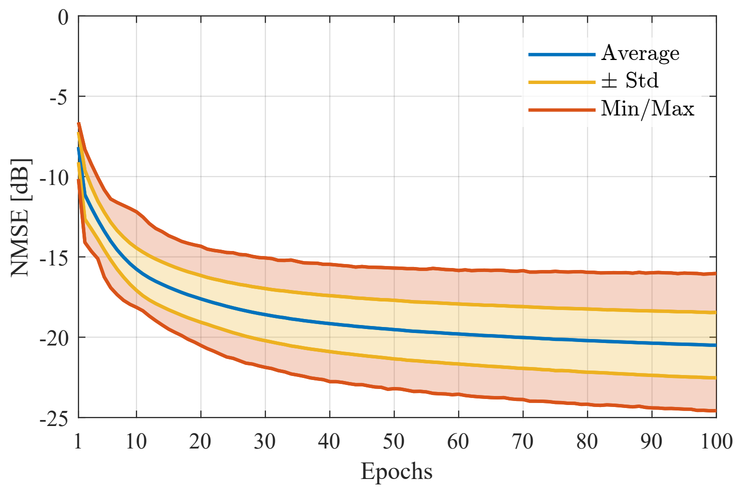

(b)

Figure 8.5.3 – NMSE convergence analysis of the proposed E2E learning with regularization and normalization for (a) SNR = 5 dB and (b) SNR = 13 dB.

8.5.1.4 Massive MIMO Schemes with 4-QAM Modulation

In this scenario, we extend the evaluation to massive MIMO configurations, exploring different numbers of antennas at both the transmitter and receiver, where $N_{\text{tx}} = N_{\text{rx}} = N_{\text{s}}$ is set to 4, 5, 10, and 20. The 4-QAM modulation scheme yields 8, 10, 20, and 40 bits/s/Hz of spectral efficiencies.

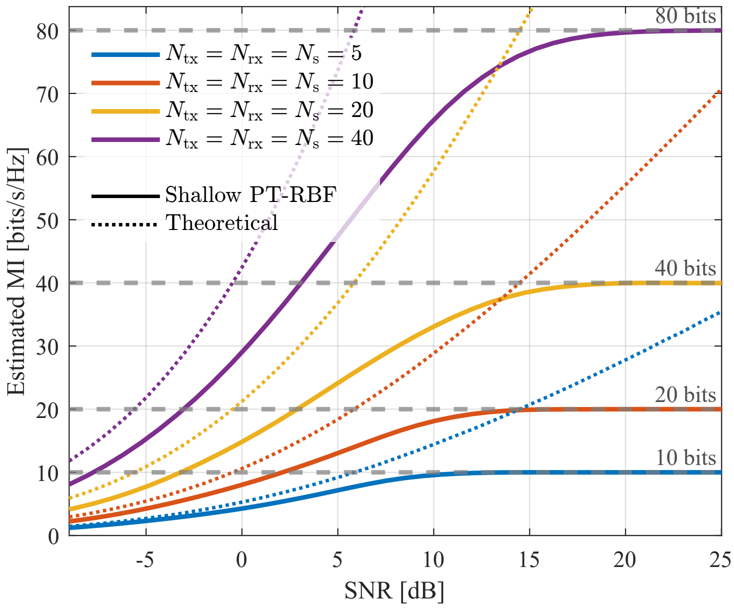

Figure 8.5.4 – Estimated MI analysis for MIMO configurations with $N_{tx} = N_{rx} = N_s$ and 4-QAM modulation, in which N_{tx}, N_{rx}, and N_s are set to 4, 5, 10, and 20. Solid lines represent the proposed approach and dotted lines the theoretical capacity.

Fig. 8.5.4 presents the performance of the proposed approach across these MIMO setups. For $N_{tx} = N_{rx} = N_s = 4$, the maximum MI is achieved with an SNR = 13 dB. In a more complex scenario, $N_{tx} = N_{rx} = N_s = 20$, the maximum MI is achieved for an SNR = 21 dB. Results demonstrate the model's capacity to handle a large number of antennas and streamings while maintaining robust performance. The proposed model shows remarkable adaptability and efficiency when scaling up to massive MIMO configurations, maintaining its superior performance even as the complexity of the system increases.

8.5.1.5 Streams Exceeding the Channel Rank

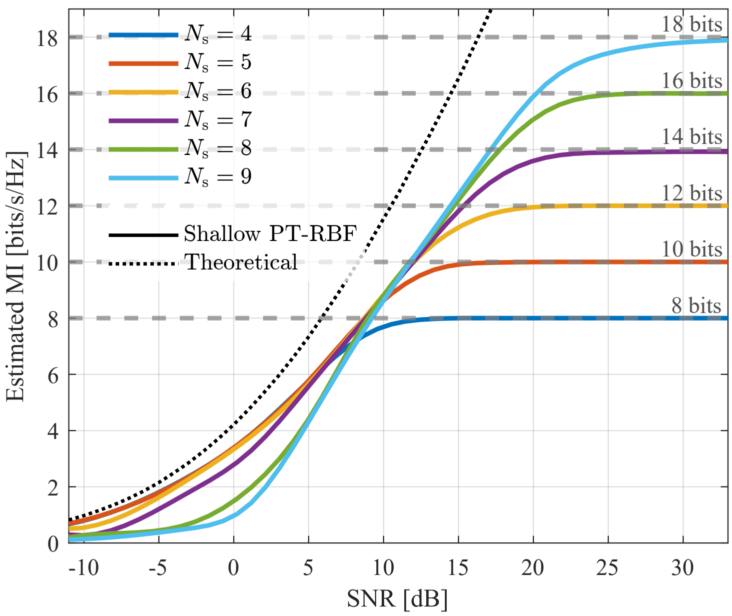

Figure 8.5.5 – Performance analysis with $N_T = N_R = 4$, 4-QAM modulation, and varying the number of streams N_s. Solid lines represent the proposed approach and the dotted line is the theoretical capacity. The ability of the proposed approach to exceed the traditional channel rank limit is shown, achieving maximum MI with 9 streams.

We explore the ability of the proposed approach to handle cases where the number of transmitted streams exceeds the channel rank. In a MIMO system, for a given number of transmitting antennas N_{tx} and receiving antennas N_{rx}, the maximum number of parallel streams that can be transmitted is determined by the rank of the channel matrix $\mathbf{H} \in \mathbb{C}^{N_{\text{rx}} \times N_{\text{tx}}}$, which is given by $\min(N_{\text{tx}}, N_{\text{rx}})$. This limitation applies to traditional methods such as SVD, MMSE, and ZF. In contrast, the proposed approach demonstrates the capability to multiplex more streams than the channel rank allows. This is illustrated in Fig. 8.5.5, in which the number of parallel streams varies from 4 to 9. Remarkably, the system achieves maximum MI for each stream, as evidenced by the 18 bits/s/Hz transmission when 9 streams are employed. However, to fully separate 8 and 9 streams, the training process required some optimization, increasing from 100 to 500 training epochs.

This ability to transmit more streams than the traditional limit offers a valuable degree of freedom when selecting the transmission rate. The system can increase MI by either increasing the modulation order or adding more parallel streams. This capability to parallelize streams also hints at the system's potential to efficiently multiplex multiple users.

8.5.2 MU-MIMO Results

The following results demonstrate the capability of the proposed federated learning approach to serve multiple users by multiplexing both users and data streams to enhance

MI.

8.5.2.1 Massive MU-MIMO Scheme with Several UEs

Fig. 8.5.6 presents five curves, each representing different configurations of user equipment (UE) and antennas: $N_{\text{ue}} = 2, 4, 6, 10$, and 20. Each UE is equipped with $N_{\text{rx}} = 2$ antennas and receives 2 data streams, which means that the total number of Rx antennas and data streams are matched to the number of transmit antennas, i.e., $N_{\text{tx}} = N_{\text{rx}} = \sum_n N_{\text{rx},n}$. The 4-QAM modulation is employed in all cases.

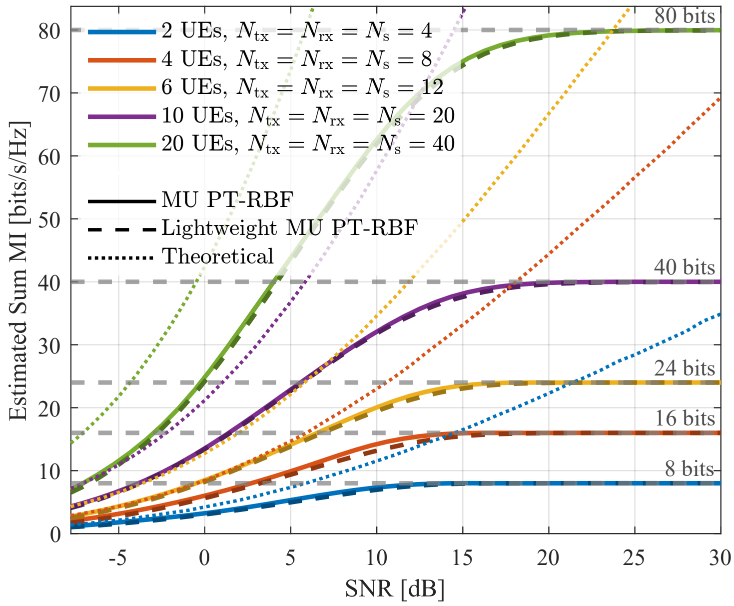

Figure 8.5.6 – 4-QAM MU-MIMO result analysis for $N_{\text{ue}} = 2, 4, 6, 10$, and 20, with $N_{\text{tx}} = N_{\text{rx}} = \sum_n N_{\text{rx},n}$. Solid lines represent the proposed approach and dotted lines the theoretical capacity.

For instance, with 2 UEs, there will be $2 \times 2 = 4$ Rx antennas and 4 data streams will be transmitted, resulting in 4 spatially multiplexed data streams. Similarly, in the setup with 20 UEs, the system will handle $20 \times 2 = 40$ Rx antennas and 40 data streams. Results show that the system can separate and achieve the maximum MI for each UE, 4 bits/s/Hz per UE, even in massive MU-MIMO setups, where up to 20 UEs are successfully multiplexed. It is important to highlight that, although the lightweight PT-RBF has a reduced number of neurons compared with the shallow PT-RBF (Table 8.5.1), the sum MI performance is almost the same, demonstrating that for input and output of lower dimension, less complexity is necessary at the decoder (i.e., at the UE).

8.5.2.2 Data Streams Exceeding the Channel Rank with 4-QAM

In addition to the previous scenarios, we further investigate the ability of the proposed approach to handle cases where the number of data streams exceeds the channel rank, i.e., $N_{\text{s}} > N_{\text{tx}}$. Fig. 8.5.7 presents the estimated sum MI results for a fixed number of transmitting antennas ($N_{tx} = 4$) and varying numbers of UEs ($N_{ue} = 2$, 3, and 4), each equipped with two receiving antennas. Each UE receives two data streams, resulting in a total number of streams $N_s = 2 \times N_{ue}$.

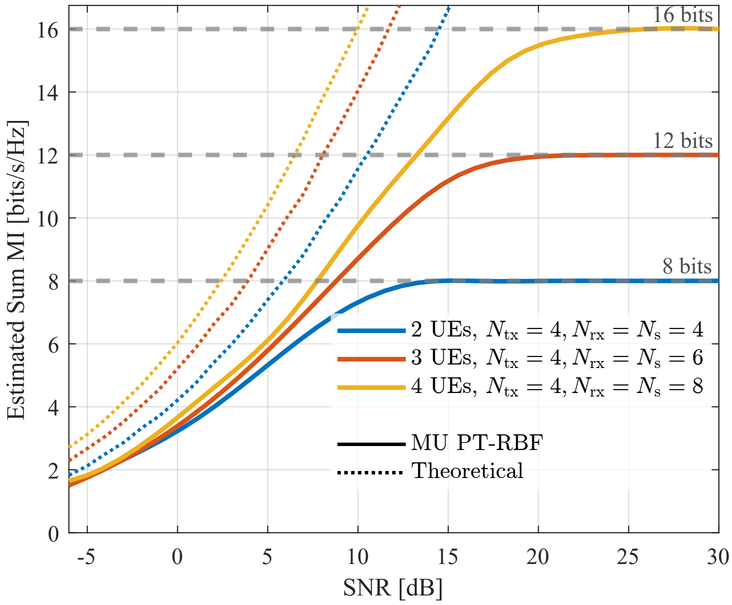

Figure 8.5.7 – 4-QAM MU-MIMO result analysis for $N_{ue} = 2$, 3, and 4, with $N_{tx} = 4$ and $N_{rx} = \sum_n N_{rx,n}$. Solid lines represent the proposed approach and dotted lines the theoretical capacity.

For the case of $N_{ue} = 2$, the total number of streams is equal to the number of transmitting antennas ($N_s = N_{tx} = 4$), and the proposed approach can achieve the maximum MI per UE. Remarkably, even when the total number of streams exceeds the number of transmitting antennas (e.g., $N_{ue} = 3$ and 4, resulting in $N_s = 6$ and 8, respectively), the proposed CVNN-based system still achieves near-optimal MI per UE. This observation aligns with the results presented in Section 8.5.1.5, where the system can handle more streams than the channel rank allows.

These results highlight the robustness and scalability of the proposed federated learning approach in multi-user scenarios. The ability to achieve maximum sum MI even when $N_s > N_{tx}$ showcases the system's capacity to efficiently multiplex data streams and users beyond the conventional channel rank limitations. This is particularly advantageous in practical deployments where the number of users and data streams may exceed the available transmitting antennas. By leveraging the learning capabilities of complex-valued neural networks, the system adapts to the increased demand, maintaining high spectral efficiency and effective resource utilization in massive MU-MIMO systems.

8.6 CONCLUSION

This paper presents a novel E2E learning architecture for massive MIMO communication systems using complex-valued neural networks (CVNNs). By processing signals directly in the complex domain, our approach preserves the inherent structure of wireless signals, eliminating the need to separate real and imaginary components. This leads to more efficient encoding and decoding processes and improved system performance. We integrated both encoding and decoding stages optimized for flat-fading Rayleigh channel conditions, focusing on improving Mutual Information (MI) and transmission efficiency. Through rigorous simulations, we demonstrated that the proposed CVNN-based architecture significantly outperforms traditional methods such as zero-forcing (ZF) and minimum mean square error (MMSE) precoding across various modulation schemes, including 4-QAM, 16-QAM, and 64-QAM. The results showed that our proposals closely approach the theoretical limits even in massive MIMO configurations.

A key contribution of our work is the extension to multi-user MIMO (MU-MIMO) scenarios. By incorporating federated learning, we designed a system capable of orthogonalizing data streams for multiple user equipment (UEs), effectively mitigating inter-user interference and enhancing spectral efficiency. Our simulations demonstrated that the proposed multi-user autoencoder can serve several UEs simultaneously while maintaining robust performance, highlighting its scalability and practicality for future wireless communication systems. The results have shown that it is possible to effectively transmit a number of data streams exceeding the rank of the channel matrix. Additionally, we introduced a regularization based power control mechanism to ensure constrained transmission power. This mechanism effectively stabilizes the transmitted signals, addressing common challenges in high-throughput MIMO systems, and contributing to the overall reliability of the communication process.

Future work will focus on extending the proposed architecture to more complex channel conditions, such as frequency-selective fading channels, and exploring its performance in practical deployment scenarios. Investigating the impact of imperfect channel state information (CSI) and developing robust training strategies to handle dynamic environments are also promising directions. Furthermore, integrating the proposed CVNN-based approach with emerging technologies such as massive MIMO in millimeter-wave (mmWave) and Terahertz (THz) bands could further enhance the capabilities of next-generation wireless networks.

REFERENCES

AIT AOUDIA, F.; HOYDIS, J. End-to-End Learning for OFDM: From Neural Receivers to Pilotless Communication. **IEEE Transactions on Wireless Communications**, v. 21, n. 2, p. 1049–1063, 2022. DOI: `10.1109/TWC.2021.3101364`. Cited on pages 157, 158.

ALBREEM, M. A. et al. Deep Learning for Massive MIMO Uplink Detectors. **IEEE Communications Surveys & Tutorials**, v. 24, n. 1, p. 741–766, 2022. DOI: 10.1109/COMST.2021.3135542. Cited on page 155.

AN, Y. et al. A Learning-Based End-to-End Wireless Communication System Utilizing a Deep Neural Network Channel Module. **IEEE Access**, v. 11, p. 17441–17453, 2023. DOI: 10.1109/ACCESS.2023.3245330. Cited on pages 157, 158.

AOUDIA, F. A.; HOYDIS, J. End-to-End Learning of Communications Systems Without a Channel Model. *In*: 2018 52nd Asilomar Conference on Signals, Systems, and Computers. [S.l.: s.n.], 2018. P. 298–303. DOI: 10.1109/ACSSC.2018.8645416. Cited on page 157.

AOUDIA, F. A.; HOYDIS, J. Model-Free Training of End-to-End Communication Systems. **IEEE Journal on Selected Areas in Communications**, v. 37, n. 11, p. 2503–2516, 2019. DOI: 10.1109/JSAC.2019.2933891. Cited on pages 156, 157.

BJÖRNSON, E. et al. Twenty-Five Years of Signal Processing Advances for Multiantenna Communications: From theory to mainstream technology. **IEEE Signal Processing Magazine**, v. 40, n. 4, p. 107–117, June 2023. ISSN 1558-0792. DOI: 10.1109/MSP.2023.3261505. Cited on pages 28, 155.

CRUZ, A. A.; MAYER, K. S.; ARANTES, D. S. RosenPy: An open source Python framework for complex-valued neural networks. **SoftwareX**, p. 1–18, 2024. Cited on page 155.

DÖRNER, S. et al. Deep Learning Based Communication Over the Air. **IEEE Journal of Selected Topics in Signal Processing**, v. 12, n. 1, p. 132–143, 2018. DOI: 10.1109/JSTSP.2017.2784180. Cited on pages 156, 157.

ENRICONI, M. P. et al. Phase transmittance RBF neural network beamforming for static and dynamic channels. **IEEE Antennas Wireless Propag. Lett.**, v. 19, n. 2, p. 243–247, Feb. 2020. Cited on pages 40, 83, 95–97, 155.

FELIX, A. et al. OFDM-Autoencoder for End-to-End Learning of Communications Systems. *In*: 2018 IEEE 19th International Workshop on Signal Processing Advances in Wireless Communications (SPAWC). [S.l.: s.n.], 2018. P. 1–5. DOI: 10.1109/SPAWC.2018.8445920. Cited on page 157.

FREIRE, P. J. et al. Complex-valued neural network design for mitigation of signal distortions in optical links. **Journal of Lightwave Technology**, v. 39, n. 6, p. 1696–1705, 2021. Cited on pages 109, 127, 155.

GUO, J. et al. Learning-based Integrated CSI Feedback and Localization in Massive MIMO. **IEEE Transactions on Wireless Communications**, p. 1–1, 2024. DOI: 10.1109/TWC.2024.3422399. Cited on pages 157, 158.

HE, H. et al. Model-Driven Deep Learning for MIMO Detection. **IEEE Transactions on Signal Processing**, v. 68, p. 1702–1715, 2020. DOI: 10.1109/TSP.2020.2976585. Cited on page 155.

HIROSE, A.; YOSHIDA, S. Generalization Characteristics of Complex-Valued Feedforward Neural Networks in Relation to Signal Coherence. **IEEE Transactions on Neural Networks and Learning Systems**, v. 23, n. 4, p. 541–551, 2012b. DOI: 10.1109/TNNLS.2012.2183613. Cited on pages 155, 161.

HORNIK, K.; STINCHCOMBE, M.; WHITE, H. Multilayer feedforward networks are universal approximators. **Neural Networks**, v. 2, n. 5, p. 359–366, 1989. ISSN 0893-6080. DOI: https://doi.org/10.1016/0893-6080(89)90020-8. Cited on page 159.

JI, J. et al. Deep Learning-based Multiuser Physical Layer Communication Without Known Channel. *In*: 2024 IEEE Wireless Communications and Networking Conference (WCNC). [S.l.: s.n.], 2024. P. 01–06. DOI: 10.1109/WCNC57260.2024.10571174. Cited on pages 157, 159.

LETIZIA, N. A.; TONELLO, A. M. Capacity-Driven Autoencoders for Communications. **IEEE Open Journal of the Communications Society**, v. 2, p. 1366–1378, 2021. DOI: 10.1109/OJCOMS.2021.3087815. Cited on pages 157, 158.

LI, P.; PEI, Y.; LI, J. A comprehensive survey on design and application of autoencoder in deep learning. **Applied Soft Computing**, v. 138, p. 110176, 2023. ISSN 1568-4946. DOI: https://doi.org/10.1016/j.asoc.2023.110176. Cited on page 156.

MAYER, K. S. et al. Blind Fuzzy Adaptation Step Control for a Concurrent Neural Network Equalizer. **Wireless Communications and Mobile Computing**, v. 2019, n. 1, p. 9082362, 2019c. DOI: https://doi.org/10.1155/2019/9082362. Cited on pages 40, 83, 95, 96, 109, 127, 161.

MAYER, K. S. **Complex-valued neural networks and applications in telecommunications**. 2022. Ph.D. Thesis – University of Campinas. Cited on pages 97, 102, 163.

MAYER, K. S. et al. Deep Phase-Transmittance RBF Neural Network for Beamforming With Multiple Users. **IEEE Wireless Communications Letters**, v. 11, n. 7, p. 1498–1502, 2022. DOI: 10.1109/LWC.2022.3177162. Cited on pages 30, 83, 95–97, 109, 127, 142, 145, 155, 156, 161–163.

O'SHEA, T.; HOYDIS, J. An Introduction to Deep Learning for the Physical Layer. **IEEE Transactions on Cognitive Communications and Networking**, v. 3, n. 4, p. 563–575, 2017. DOI: 10.1109/TCCN.2017.2758370. Cited on pages 156, 157.

QIN, Z. et al. Deep Learning in Physical Layer Communications. **IEEE Wireless Communications**, v. 26, n. 2, p. 93–99, 2019. DOI: 10.1109/MWC.2019.1800601. Cited on page 155.

RALEIGH, G. G.; CIOFFI, J. M. Spatio-temporal Coding for Wireless Communication. **IEEE Transactions on Communications**, v. 46, n. 3, p. 357–366, 1998. DOI: 10.1109/26.662641. Cited on page 161.

SAGDUYU, Y. E.; ULUKUS, S.; YENER, A. Task-Oriented Communications for NextG: End-to-end Deep Learning and AI Security Aspects. **IEEE Wireless Communications**, v. 30, n. 3, p. 52–60, 2023. DOI: 10.1109/MWC.006.2200494. Cited on pages 157, 158.

SINGH, A. et al. Autoencoder-Based End-to-End OTFS System Design With Hardware Impairments. **IEEE Wireless Communications Letters**, v. 13, n. 8, p. 2285–2289, 2024. DOI: 10.1109/LWC.2024.3412240. Cited on pages 157, 159.

SOARES, J. A.; MAYER, K. S.; ARANTES, D. S. On the Parameter Selection of Phase-transmittance Radial Basis Function Neural Networks for Communication Systems. *In*: IEEE International Conference on Machine Learning for Communication and Networking (ICMLCN). [S.l.: s.n.], 2024. P. 530–536. DOI: 10.1109/ICMLCN59089.2024.10624891. Cited on pages 131, 133, 142, 172.

SOARES, J. A.; MAYER, K. S.; ARANTES, D. S. Semi-Supervised ML-Based Joint Channel Estimation and Decoding for m-MIMO With Gaussian Inference Learning. **IEEE Wireless Communications Letters**, v. 12, n. 12, p. 2123–2127, 2023. DOI: 10.1109/LWC.2023.3309479. Cited on pages 30, 114, 133, 146, 155, 161, 162.

SOARES, J. A. et al. Complex-Valued Phase Transmittance RBF Neural Networks for Massive MIMO-OFDM Receivers. **Sensors**, v. 21, n. 24, 2021b. DOI: 10.3390/s21248200. Cited on page 155.

SONG, J. et al. Benchmarking and Interpreting End-to-End Learning of MIMO and Multi-User Communication. **IEEE Transactions on Wireless Communications**, v. 21, n. 9, p. 7287–7298, 2022. DOI: 10.1109/TWC.2022.3157467. Cited on pages 156–159.

WANG, B. et al. A Deep Learning-Based Intelligent Receiver for Improving the Reliability of the MIMO Wireless Communication System. **IEEE Transactions on Reliability**, v. 71, n. 2, p. 1104–1115, 2022. Cited on page 155.

WANG, C.-X. et al. On the Road to 6G: Visions, Requirements, Key Technologies, and Testbeds. **IEEE Communications Surveys & Tutorials**, v. 25, n. 2, p. 905–974, Apr. 2023. ISSN 1553-877X. DOI: 10.1109/COMST.2023.3249835. Cited on pages 28, 155.

WU, C. et al. Channel Prediction in High-Mobility Massive MIMO: From Spatio-Temporal Autoregression to Deep Learning. **IEEE Journal on Selected Areas in Communications**, v. 39, n. 7, p. 1915–1930, 2021. DOI: 10.1109/JSAC.2021.3078503. Cited on page 155.

WU, H. et al. Channel-Adaptive Wireless Image Transmission With OFDM. **IEEE Wireless Communications Letters**, v. 11, n. 11, p. 2400–2404, 2022b. DOI: 10.1109/LWC.2022.3204837. Cited on pages 157, 158.

XU, S. et al. Space–time domain equalization algorithm based on complex-valued neural network in a long-haul photonic-aided MIMO THz system. **Optics Letters**, Optica Publishing Group, v. 49, n. 5, p. 1253–1256, Mar. 2024. DOI: 10.1364/OL.512416. Cited on page 155.

YE, H.; LI, G. Y.; JUANG, B.-H. Deep Learning Based End-to-End Wireless Communication Systems Without Pilots. **IEEE Transactions on Cognitive Communications and Networking**, v. 7, n. 3, p. 702–714, 2021. DOI: 10.1109/TCCN.2021.3061464. Cited on pages 156–158.

YE, H.; LI, G. Y.; JUANG, B.-H. Power of deep learning for channel estimation and signal detection in OFDM systems. **IEEE Wireless Commun. Lett.**, v. 7, n. 1, p. 114–117, 2018. DOI: 10.1109/LWC.2017.2757490. Cited on pages 97, 147, 155.

YE, H. et al. Deep Learning-Based End-to-End Wireless Communication Systems With Conditional GANs as Unknown Channels. **IEEE Transactions on Wireless Communications**, v. 19, n. 5, p. 3133–3143, 2020. DOI: 10.1109/TWC.2020.2970707. Cited on pages 156–158.

YUAN, Q. et al. Deep Learning-Based Hybrid Precoding for Terahertz Massive MIMO Communication With Beam Squint. **IEEE Communications Letters**, v. 27, n. 1, p. 175–179, 2023. DOI: 10.1109/LCOMM.2022.3211514. Cited on page 155.

ZHANG, H.; ZHANG, L.; JIANG, Y. Overfitting and Underfitting Analysis for Deep Learning Based End-to-end Communication Systems. *In*: 11TH International Conference on Wireless Communications and Signal Processing (WCSP). [S.l.: s.n.], 2019. P. 1–6. DOI: 10.1109/WCSP.2019.8927876. Cited on pages 157, 158.

ZHANG, X.; VAEZI, M. Deep Autoencoder-Based Z-Interference Channels With Perfect and Imperfect CSI. **IEEE Transactions on Communications**, v. 72, n. 2, p. 861–873, 2024. DOI: 10.1109/TCOMM.2023.3328026. Cited on pages 157, 159.

Chapter 9

Conclusions

This chapter highlights the main contributions of this dissertation and suggests possible directions for future related work.

9.1 CONCLUDING REMARKS

In this dissertation, we proposed and analyzed a myriad of complex-valued neural networks and machine learning applications for telecommunications. The research presented has demonstrated significant advancements in the design and application of complex-valued neural networks (CVNNs) for various telecommunication tasks such as channel estimation, equalization, beamforming, and decoding. By leveraging the unique properties of CVNNs, we have shown improved performance in terms of accuracy, computational efficiency, and robustness, especially in challenging environments with high levels of noise and interference. The studies encompassed a range of scenarios including 5G wireless Rayleigh channels, dynamic MIMO-OFDM systems, and high Doppler frequencies, underscoring the versatility and effectiveness of our proposed methods.

Next, we summarize important aspects of our main contributions, challenges, and conclusions:

9.1.1 Main Contributions

Complex-Valued Neural Networks (CVNNs) for Telecommunications Developed and analyzed innovative CVNN architectures tailored for various telecommunication tasks including channel estimation, equalization, beamforming, and decoding. Introduced the phase-transmittance radial basis function (PT-RBF) neural network for massive MIMO-OFDM systems, demonstrating improved performance with lower computational complexity compared to traditional methods.

Parameter Initialization Techniques Proposed novel parameter initialization methods for PT-RBF and deep complex-valued radial basis function (C-RBF) neural networks. These techniques ensure successful convergence and enhance the robustness and efficiency of neural network deployments in complex digital communication environments.

Semi-supervised Learning Approaches Introduced semi-supervised learning techniques, specifically hard inference learning (HIL) and Gaussian inference learning (GIL), to enable CVNNs to learn from non-pilot-aided data, increasing their tracking ability and robustness in dynamic channels.

Parallel Processing in MIMO-OFDM Systems Developed a parallel decoding method utilizing distinct PT-RBF neural networks for each subcarrier in MIMO-OFDM systems. This approach significantly reduces decoding time and improves system adaptability by effectively managing nonlinear impairments and intersymbol interference.

End-to-End Learning in MIMO Systems Designed a novel end-to-end (E2E) learning architecture for massive MIMO systems using CVNNs. This approach fully utilizes the complex nature of communication signals, improving system capacity and transmission efficiency. A key contribution is the extension of this E2E framework to multi-user MIMO (MU-MIMO) scenarios with federated learning, enabling data stream orthogonalization for multiple users while ensuring stable transmission power with regularization.

9.1.2 Challenges

High Computational Complexity Addressed the challenge of high computational complexity in traditional decoding algorithms for MIMO systems by proposing efficient CVNN-based methods that maintain high performance with reduced computational requirements.

Dynamic and Noisy Environments Tackled the difficulties posed by dynamic and noisy environments in telecommunications by leveraging the intrinsic capabilities of CVNNs to process complex-valued data, ensuring robust performance under various conditions including high Doppler frequencies and nonlinear distortions.

Parameter Initialization Overcame the challenge of parameter initialization in multi-layered CVNN architectures by developing robust techniques that ensure successful convergence and optimal performance across different network configurations.

9.1.3 Conclusions

Enhanced Performance The proposed CVNN-based methods demonstrated significant improvements in bit error rate (BER), computational efficiency, and system capacity compared to traditional approaches, particularly in challenging telecommunication scenarios.

Scalability and Adaptability The scalability of the proposed neural network architectures makes them suitable for future telecommunication systems, including 5G, 6G, and beyond, with potential applications in ultra-massive MIMO setups and multi-user MIMO (MU-MIMO) systems.

Robustness and Reliability The robustness and reliability of the proposed methods were validated through extensive simulations conforming to technical standards, highlighting their effectiveness in real-world applications and paving the way for more adaptive and resilient communication systems.

9.2 FUTURE DIRECTIONS

According to the results obtained from the analysis of the proposed scenarios, several promising avenues for future research have been identified:

Scalability Exploring the scalability of the proposed CVNN architectures to ultra-massive MIMO setups with a higher number of antennas and subcarriers could provide deeper insights into their performance and feasibility in next-generation communication systems.

Optimization Further optimization of the training algorithms and parameter initialization procedures could enhance the efficiency and accuracy of the decoding process.

Broader Testing Testing the proposed approaches under a broader range of channel conditions and modulation schemes will help to validate their robustness and reliability in real-world applications, paving the way for more resilient and adaptive communication systems in the future.

Federated Learning Extensions Investigating the application of federated learning techniques in larger and more complex multi-user MIMO scenarios could provide new insights into how to manage interference and maximize system capacity across heterogeneous users.

REFERENCES

5G; NR; BASE STATION (BS) RADIO TRANSMISSION AND RECEPTION. Sophia Antipolis, France, Oct. 2022. (3GPP technical specification 38.104; version 17.7.0; release 17). Cited on pages 101, 114, 133, 146.

5G; NR; PHYSICAL CHANNELS AND MODULATION. Sophia Antipolis, France, Sept. 2022. (3GPP technical specification 38.211; version 17.3.0; release 17). Cited on pages 101, 114, 133, 146.

5G; STUDY ON CHANNEL MODEL FOR FREQUENCIES FROM 0.5 TO 100 GHZ. Sophia Antipolis, France, Apr. 2022. (3GPP technical report 38.901; version 17.0.0; release 17). Cited on pages 101, 114, 133, 146.

ABDI, H.; WILLIAMS, L. J. Principal component analysis. **WIREs Computational Statistics**, v. 2, n. 4, p. 433–459, July 2010. Cited on page 83.

AIT AOUDIA, F.; HOYDIS, J. End-to-End Learning for OFDM: From Neural Receivers to Pilotless Communication. **IEEE Transactions on Wireless Communications**, v. 21, n. 2, p. 1049–1063, 2022. DOI: `10.1109/TWC.2021.3101364`. Cited on pages 157, 158.

ALAMOUTI, S. M. A simple transmit diversity technique for wireless communications. **IEEE Journal on Selected Areas in Communications**, v. 16, n. 8, p. 1451–1458, 1998. DOI: `10.1109/49.730453`. Cited on pages 48, 49, 144.

ALAPURANEN, P.; SCHROEDER, J. Complex artificial neural network with applications to wireless communications. **Digit. Signal Process.**, v. 119, p. 1–6, 2021. Cited on page 95.

ALBREEM, M. A. et al. Deep Learning for Massive MIMO Uplink Detectors. **IEEE Communications Surveys & Tutorials**, v. 24, n. 1, p. 741–766, 2022. DOI: `10.1109/COMST.2021.3135542`. Cited on page 155.

ALI, M. S. et al. On improved DFT-based low-complexity channel estimation algorithms for LTE-based uplink NB-IoT systems. **Computer Communications**, v. 149, p. 214–224, Jan. 2020. Cited on page 83.

AN, Y. et al. A Learning-Based End-to-End Wireless Communication System Utilizing a Deep Neural Network Channel Module. **IEEE Access**, v. 11, p. 17441–17453, 2023. DOI: `10.1109/ACCESS.2023.3245330`. Cited on pages 157, 158.

AOUDIA, F. A.; HOYDIS, J. End-to-End Learning of Communications Systems Without a Channel Model. *In*: 2018 52nd Asilomar Conference on Signals, Systems, and Computers. [S.l.: s.n.], 2018. P. 298–303. DOI: `10.1109/ACSSC.2018.8645416`. Cited on page 157.

AOUDIA, F. A.; HOYDIS, J. Model-Free Training of End-to-End Communication Systems. **IEEE Journal on Selected Areas in Communications**, v. 37, n. 11, p. 2503–2516, 2019. DOI: 10.1109/JSAC.2019.2933891. Cited on pages 156, 157.

ASIF, R. M. et al. Energy efficiency augmentation in massive MIMO systems through linear precoding schemes and power consumption modeling. **Wireless Communications and Mobile Computing**, v. 2020, p. 1–13, 2020. DOI: 10.1155/2020/8839088. Cited on pages 39, 141.

BALEVI, E.; DOSHI, A.; ANDREWS, J. G. Massive MIMO channel estimation with an untrained deep neural network. **IEEE Trans. Wireless Commun.**, v. 19, n. 3, p. 2079–2090, Mar. 2020. Cited on pages 83, 95.

BARRACHINA, J. A. et al. Complex-valued vs. real-valued neural networks for classification perspectives: An example on non-circular data. *In*: 2021 IEEE International Conference on Acoustics, Speech and Signal Processing (ICASSP). [S.l.: s.n.], 2021. P. 2990–2994. Cited on pages 109, 127.

BIGUESH, M.; GERSHMAN, A. B. Training-based MIMO channel estimation: A study of estimator tradeoffs and optimal training signals. **IEEE Transactions on Signal Processing**, v. 54, n. 3, p. 884–893, 2006. ISSN 1053587X. DOI: 10.1109/TSP.2005.863008. Cited on pages 45, 64.

BJÖRNSON, E. et al. Twenty-Five Years of Signal Processing Advances for Multiantenna Communications: From theory to mainstream technology. **IEEE Signal Processing Magazine**, v. 40, n. 4, p. 107–117, June 2023. ISSN 1558-0792. DOI: 10.1109/MSP.2023.3261505. Cited on pages 28, 155.

CARDOSO, F. A. C. M. et al. Uma Versão Evolutiva do Algoritmo de Godard. *In*: XVIII Simpósio Brasileiro de Telecomunicações (SBrT2000). [S.l.: s.n.], 2000. DOI: 10.14209/sbrt.2000.5300275. Cited on page 30.

CARDOSO, F.; ARANTES, D. Genetic decoding of linear block codes. *In*: PROCEEDINGS of the 1999 Congress on Evolutionary Computation-CEC99 (Cat. No. 99TH8406). [S.l.: s.n.], July 1999. v. 3, 2302–2309 vol. 3. DOI: 10.1109/CEC.1999.785561. Cited on page 30.

CASTRO, C. et al. 100 Gbit/s terahertz-wireless real-time transmission using a broadband digital-coherent modem. *In*: PROC. 5G World Forum. Dresden: IEEE, Nov. 2019. P. 399–402. Cited on page 102.

CASTRO, M. C. F. d. et al. A Fuzzy Neural CBR Channel Rate Controller for MPEG2 Encoders. *In*: XVIII Simpósio Brasileiro de Telecomunicações (SBrT2000). [S.l.: s.n.], 2000. DOI: 10.14209/sbrt.2000.4120017. Cited on page 30.

CHA, B.; NOH, S.-K. Learning using LTE RSRP and NARNET in the same indoor area. *In*: PROC. Inter. Comput. Sci. Eng. Conf. Phuket: IEEE, Nov. 2019. P. 261–264. Cited on page 99.

CHEN, L. et al. Performance analysis and compensation of joint TX/RX I/Q imbalance in differential STBC-OFDM. **IEEE Trans. Veh. Technol.**, v. 66, n. 7, p. 6184–6200, 2017. Cited on page 95.

CHEN, S.; MCLAUGHLIN, S.; MULGREW, B. Complex-valued radial basic function network, part I: Network architecture and learning algorithms. **Signal Processing**, v. 35, n. 1, p. 19–31, 1994. Cited on page 127.

CHEN, S.; MULGREW, B.; GRANT, P. A clustering technique for digital communications channel equalization using radial basis function networks. **IEEE Transactions on Neural Networks**, v. 4, n. 4, p. 570–590, July 1993. ISSN 1941-0093. DOI: `10.1109/72.238312`. Cited on page 30.

CHEN, S. et al. Complex-valued radial basis function networks. *In*: 1993 Third International Conference on Artificial Neural Networks. [S.l.: s.n.], May 1993. P. 148–152. Cited on page 29.

CHEN, X.; JIANG, M. Enhanced adaptive polar-linear interpolation aided channel estimation. **IEEE Wireless Commun. Lett.**, v. 8, n. 3, p. 693–696, 2019. Cited on page 95.

CHO, Y. S. et al. **MIMO-OFDM Wireless Communications with MATLAB**. 1. ed. [S.l.]: Wiley, 2010. ISBN 9780470825617. Cited on page 47.

CHOPRA, S. R.; GUPTA, A. Error analysis of grouped multilevel space-time trellis coding with the combined application of massive MIMO and cognitive radio. **Wireless Personal Communications**, v. 117, n. 2, p. 461–482, 2021. DOI: `10.1007/s11277-020-07878-y`. Cited on page 42.

CHU, J.; GAO, M.; LIU, X., et al. Channel estimation based on complex-valued neural networks in IM/DD FBMC/OQAM transmission system. **Journal of Lightwave Technology**, v. 40, n. 4, p. 1055–1063, 2022. Cited on pages 109, 127.

CONDOLUCI, M. et al. Flexible Numerology in 5G NR: Interference Quantification and Proper Selection Depending on the Scenario. **Mobile Information Systems**, v. 2021, p. 1–9, 2021. DOI: `10.1155/2021/6651326`. Cited on page 39.

CRUZ, A. A.; MAYER, K. S.; ARANTES, D. S. RosenPy: An open source Python framework for complex-valued neural networks. **SoftwareX**, p. 1–18, 2024. Cited on page 155.

CRUZ, A. A.; MAYER, K. S.; ARANTES, D. S. RosenPy: An open source python framework for complex-valued neural networks. **SSRN**, p. 1–18, 2022. Available from: <`https://ssrn.com/abstract=4252610`>. Cited on pages 109, 127.

DE CASTRO, F.; DE CASTRO, M.; ARANTES, D. A supervised neural constant bit rate video controller for MPEG2 encoders. *In*: ITS'98 Proceedings. SBT/IEEE International Telecommunications Symposium (Cat. No.98EX202). [S.l.: s.n.], Aug. 1998. v. 2, 504–509 vol.2. DOI: `10.1109/ITS.1998.718445`. Cited on page 30.

DE CASTRO, M.; DE CASTRO, C.; ARANTES, D. RBF neural networks with centers assignment via Karhunen-Loeve transform. *In*: IJCNN'99. International Joint Conference on Neural Networks. Proceedings (Cat. No.99CH36339). [S.l.: s.n.], July 1999. v. 2, 1265–1270 vol.2. DOI: `10.1109/IJCNN.1999.831143`. Cited on page 30.

DE SOUSA, T. F. B.; ARANTES, D. S.; FERNANDES, M. A. C. Adaptive Beamforming Applied to OFDM Systems. **Sensors**, v. 18, n. 10, p. 1–15, Oct. 2018. DOI: `10.3390/s18103558`. Cited on page 40.

DE SOUSA, T. F. B.; FERNANDES, M. A. C. Butterfly Neural Equalizer Applied to Optical Communication Systems with Two-Dimensional Digital Modulation. **Optics Express**, v. 26, n. 23, p. 30837–30850, Nov. 2018. DOI: `10.1364/OE.26.030837`. Cited on page 40.

DE SOUSA, T. F. B.; FERNANDES, M. A. C. Butterfly Neural Filter Applied to Beamforming. **IEEE Access**, v. 7, p. 96455–96469, July 2019. DOI: `10.1109/ACCESS.2019.2929590`. Cited on page 40.

DIALLO, M.; RABINEAU, R.; CARIOU, L. Robust DCT based channel estimation for MIMO-OFDM system. *In*: 2009 IEEE Wireless Communications and Networking Conference. [S.l.: s.n.], Apr. 2009. P. 1–5. Cited on page 83.

DILLI, R. Performance analysis of multi user massive MIMO hybrid beamforming systems at millimeter wave frequency bands. **Wireless Networks**, v. 27, n. 3, p. 1925–1939, 2021. DOI: `10.1007/s11276-021-02546-w`. Cited on pages 39, 141.

DING, T.; HIROSE, A. Online regularization of complex-valued neural networks for structure optimization in wireless-communication channel prediction. **IEEE Access**, v. 8, p. 143706–143722, 2020. Cited on pages 109, 127.

DINIZ, P. S. R. **Adaptive filtering: Algorithms and practical implementation**. 4. ed. New York, US: Springer, 2013. P. 83–84. Cited on page 80.

DOLECEK, G. V. **Random signals and processes primer with MATLAB**. 1. ed. New York, US: Springer, 2013. P. 69–70. Cited on page 78.

DONG, Z.; HUANG, H. A training algorithm with selectable search direction for complex-valued feedforward neural networks. **Neural Netw.**, v. 137, p. 75–84, 2021. DOI: `10.1016/j.neunet.2021.01.014`. Cited on pages 40, 96, 97.

DÖRNER, S. et al. Deep Learning Based Communication Over the Air. **IEEE Journal of Selected Topics in Signal Processing**, v. 12, n. 1, p. 132–143, 2018. DOI: `10.1109/JSTSP.2017.2784180`. Cited on pages 156, 157.

DURGA, R. V.; MCLAUCHLIN, A. The proposed novel sphere decoder for MIMO detection. *In*: 2021 International Conference on Artificial Intelligence and Smart Systems (ICAIS). [S.l.: s.n.], 2021. P. 1240–1245. DOI: `10.1109/ICAIS50930.2021.9396022`. Cited on page 41.

ELBIR, A. M.; COLERI, S. Federated learning for channel estimation in conventional and RIS-assisted massive MIMO. **IEEE Trans. Wireless Commun.**, v. 21, n. 6, p. 4255–4268, 2022. Cited on page 95.

ELNAKEEB, A.; MITRA, U. Bilinear Channel Estimation for MIMO OFDM: Lower Bounds and Training Sequence Optimization. **IEEE Transactions on Signal Processing**, v. 69, p. 1317–1331, 2021. DOI: 10.1109/TSP.2021.3056591. Cited on page 40.

ENRICONI, M. P. et al. Phase transmittance RBF neural network beamforming for static and dynamic channels. **IEEE Antennas Wireless Propag. Lett.**, v. 19, n. 2, p. 243–247, Feb. 2020. Cited on pages 40, 83, 95–97, 155.

ETSI. 5G; NR; Physical channels and modulation (3GPP TS 38.211 version 17.2.0 Release 17). **3GPP**, 2022a. Cited on pages 57, 88.

ETSI. 5G; Study on channel model for frequencies from 0.5 to 100 GHz (3GPP TR 38.901 version 17.1.0 Release 17). **3GPP**, 2022b. Cited on pages 57, 58, 89.

FAZAL-E-ASIM et al. Kronecker product-based space-time block codes. **IEEE Wireless Commun. Lett.**, v. 11, n. 2, p. 386–390, 2022. Cited on page 95.

FELIX, A. et al. OFDM-Autoencoder for End-to-End Learning of Communications Systems. *In*: 2018 IEEE 19th International Workshop on Signal Processing Advances in Wireless Communications (SPAWC). [S.l.: s.n.], 2018. P. 1–5. DOI: 10.1109/SPAWC.2018.8445920. Cited on page 157.

FERRARI, R. et al. Unsupervised channel equalization using fuzzy prediction-error filters. *In*: 2003 IEEE XIII Workshop on Neural Networks for Signal Processing (IEEE Cat. No.03TH8718). [S.l.: s.n.], Sept. 2003. P. 869–878. DOI: 10.1109/NNSP.2003.1318086. Cited on page 30.

FERRARI, R. **Fuzzy filters based communication channels equalization**. 2005. Dissertação de Mestrado – Universidade Estadual de Campinas, Faculdade de Engenharia Elétrica e de Computação, Campinas, SP, Brazil. Orientador: João Marcos Travassos Romano. DOI: 10.47749/T/UNICAMP.2005.359287. Available from: <https://doi.org/10.47749/T/UNICAMP.2005.359287>. Cited on page 30.

FIGUEIREDO, F. A. P. de et al. Channel estimation for massive MIMO TDD systems assuming pilot contamination and flat fading. **Eurasip Journal on Wireless Communications and Networking**, v. 2018, 1 2018. Cited on page 84.

FREIRE, P. J. et al. Complex-valued neural network design for mitigation of signal distortions in optical links. **Journal of Lightwave Technology**, v. 39, n. 6, p. 1696–1705, 2021. Cited on pages 109, 127, 155.

GAO, J. et al. An attention-aided deep learning framework for massive MIMO channel estimation. **IEEE Trans. Wireless Commun.**, v. 21, n. 3, p. 1823–1835, 2022. Cited on page 95.

GHZAOUI, M. E. et al. Compensation of non-linear distortion effects in MIMO-OFDM systems using constant envelope OFDM for 5G applications. **Journal of Circuits, Systems and Computers**, v. 29, n. 16, p. 1–21, 2020. DOI: 10.1142/S0218126620502576. Cited on page 39.

GONG, Y.; LETAIEF, K. B. Performance evaluation and analysis of space-time coding in unequalized multipath fading links. **IEEE Transactions on Communications**, v. 48, n. 11, p. 1778–1782, 2000. DOI: 10.1109/26.886466. Cited on page 43.

GUERREIRO, J.; DINIS, R.; CAMPOS, L. On the Achievable Capacity of MIMO-OFDM Systems in the CathLab Environment. **Sensors**, v. 20, n. 3, p. 1–16, 2020. DOI: 10.3390/s20030938. Cited on pages 40, 141.

GUO, J. et al. Learning-based Integrated CSI Feedback and Localization in Massive MIMO. **IEEE Transactions on Wireless Communications**, p. 1–1, 2024. DOI: 10.1109/TWC.2024.3422399. Cited on pages 157, 158.

HAN, M. et al. Efficient Hybrid Beamforming Design in mmWave Massive MU-MIMO DF Relay Systems With the Mixed-Structure. **IEEE Access**, v. 9, p. 66141–66153, 2021. DOI: 10.1109/ACCESS.2021.3073847. Cited on page 40.

HASSAN, A. Y. A Frequency-Diversity System With Diversity Encoder and OFDM Modulation. **IEEE Access**, v. 9, p. 2805–2818, 2021. DOI: 10.1109/ACCESS.2020.3047688. Cited on page 39.

HE, B.; SU, H.; HUANG, J. Joint beamforming and power allocation between a multistatic MIMO radar network and multiple targets using game theoretic analysis. **Digital Signal Processing**, v. 115, p. 1–13, 2021. DOI: 10.1016/j.dsp.2021.103085. Cited on page 39.

HE, H. et al. Deep learning-based channel estimation for beamspace mmWave massive MIMO systems. **IEEE Wireless Commun. Lett.**, v. 7, n. 5, p. 852–855, 2018. Cited on page 95.

HE, H. et al. Model-Driven Deep Learning for MIMO Detection. **IEEE Transactions on Signal Processing**, v. 68, p. 1702–1715, 2020. DOI: 10.1109/TSP.2020.2976585. Cited on page 155.

HE, R.; SHEN, Z. System Design and Performance of Ship-borne Satellite High-speed Data Reliable Transportation Based on Coded STBC-OFDM. *In*: 2022 7th International Conference on Intelligent Computing and Signal Processing (ICSP). [S.l.: s.n.], 2022. P. 1302–1306. DOI: 10.1109/ICSP54964.2022.9778435. Cited on page 141.

HELD, L.; BOVÉ, D. S. **Applied statistical inference: Likelihood and bayes**. 1. ed. Berlin, Germany: Springer, 2014. P. 322. Cited on page 78.

HIROSE, A.; YOSHIDA, S. Generalization characteristics of complex-valued feedforward neural networks in relation to signal coherence. **IEEE Trans. Neural Netw. Learn. Syst.**, v. 23, n. 4, p. 541–551, 2012a. Cited on pages 95, 96, 109, 127.

HIROSE, A.; YOSHIDA, S. Generalization Characteristics of Complex-Valued Feedforward Neural Networks in Relation to Signal Coherence. **IEEE Transactions on Neural Networks and Learning Systems**, v. 23, n. 4, p. 541–551, 2012b. DOI: `10.1109/TNNLS.2012.2183613`. Cited on pages 155, 161.

HORNIK, K.; STINCHCOMBE, M.; WHITE, H. Multilayer feedforward networks are universal approximators. **Neural Networks**, v. 2, n. 5, p. 359–366, 1989. ISSN 0893-6080. DOI: `https://doi.org/10.1016/0893-6080(89)90020-8`. Cited on page 159.

HU, T. et al. Regularization matters: A nonparametric perspective on overparametrized neural network. *In*: PROCEEDINGS of The 24th International Conference on Artificial Intelligence and Statistics. [S.l.: s.n.], 2021. P. 829–837. Cited on pages 109, 127.

HU, Z.; ZHAO, H.; XUE, J. Error exponent for Nakagami-m fading massive MIMO channels. *In*: 2020 IEEE 6th International Conference on Computer and Communications (ICCC). [S.l.: s.n.], 2020. P. 59–63. DOI: `10.1109/ICCC51575.2020.9345091`. Cited on pages 45, 143.

HUMBIRD, K. D.; PETERSON, J. L.; MCCLARREN, R. G. Deep neural network initialization with decision trees. **IEEE Transactions on Neural Networks and Learning Systems**, v. 30, n. 5, p. 1286–1295, 2019. Cited on pages 109, 127.

HWANG, S. et al. Compressive Sensing-Based Radar Imaging and Subcarrier Allocation for Joint MIMO OFDM Radar and Communication System. **Sensors**, v. 21, n. 7, p. 1–16, 2021. DOI: `10.3390/s21072382`. Cited on page 39.

JAFARKHANI, H. A quasi-orthogonal space-time block code. **IEEE Transactions on Communications**, v. 49, n. 1, p. 1–4, 2001. DOI: `10.1109/26.898239`. Cited on pages 46–49, 54–56, 60, 65, 68, 141, 143, 144.

JAMALI, V. et al. Intelligent Surface-Aided Transmitter Architectures for Millimeter-Wave Ultra Massive MIMO Systems. **IEEE Open Journal of the Communications Society**, v. 2, p. 144–167, 2021. DOI: `10.1109/OJCOMS.2020.3048063`. Cited on page 39.

JANKIRAMAN, M. **Space-time Codes and MIMO Systems**. 1. ed. [S.l.]: Artech House, 2004. ISBN 9781580538664. Available from: <`https://books.google.com.br/books?id=HU-T7y16AGEC`>. Cited on pages 42, 43, 45, 47, 143.

JI, J. et al. Deep Learning-based Multiuser Physical Layer Communication Without Known Channel. *In*: 2024 IEEE Wireless Communications and Networking Conference (WCNC). [S.l.: s.n.], 2024. P. 01–06. DOI: `10.1109/WCNC57260.2024.10571174`. Cited on pages 157, 159.

JIA, Z.; CHENG, W.; ZHANG, H. A partial learning-based detection scheme for massive MIMO. **IEEE Wireless Commun. Lett.**, v. 8, n. 4, p. 1137–1140, 2019. Cited on pages 95, 96.

KAMIYAMA, T.; KOBAYASHI, H.; IWASHITA, K. Neural network nonlinear equalizer in long-distance coherent optical transmission systems. **IEEE Photonics Technology Letters**, v. 33, n. 9, p. 421–424, 2021. Cited on pages 109, 127.

KARA, F.; KAYA, H.; YANIKOMEROGLU, H. Power-time channel diversity (PTCD): A novel resource-efficient diversity technique for 6G and beyond. **IEEE Wireless Communications Letters**, p. 1–5, 2022. Cited on page 83.

KIM, T.; ADALI, T. Fully complex multi-layer perceptron network for nonlinear signal processing. **J. VLSI Signal Process. Syst. Signal Image Video Technol.**, v. 32, p. 29–43, 2002. Cited on pages 96, 97.

KO, K. et al. Joint power allocation and scheduling techniques for BER minimization in multiuser MIMO systems. **IEEE Access**, v. 9, p. 66675–66686, 2021. DOI: `10.1109/ACCESS.2021.3074980`. Cited on pages 39, 141.

KUMAR, S.; SINGH, A.; MAHAPATRA, R. DLNet: Deep learning-aided massive MIMO decoder. **AEU-Int. J. Electron. Commun.**, p. 154350, 2022. Cited on pages 95, 96.

LEE, C.; HASEGAWA, H.; GAO, S. Complex-valued neural networks: A comprehensive survey. **IEEE/CAA J. Autom. Sin.**, v. 9, n. 8, p. 1406–1426, 2022. Cited on page 95.

LETIZIA, N. A.; TONELLO, A. M. Capacity-Driven Autoencoders for Communications. **IEEE Open Journal of the Communications Society**, v. 2, p. 1366–1378, 2021. DOI: `10.1109/OJCOMS.2021.3087815`. Cited on pages 157, 158.

LI, F. et al. Construction of Golay complementary matrices and its applications to MIMO omnidirectional transmission. **IEEE Transactions on Signal Processing**, v. 69, p. 2100–2113, 2021. DOI: `10.1109/TSP.2021.3067467`. Cited on pages 39, 45, 143.

LI, H. et al. CVLNet: A complex-valued lightweight network for CSI feedback. **IEEE Wireless Communications Letters**, v. 11, n. 5, p. 1092–1096, 2022. Cited on pages 109, 127.

LI, P.; PEI, Y.; LI, J. A comprehensive survey on design and application of autoencoder in deep learning. **Applied Soft Computing**, v. 138, p. 110176, 2023. ISSN 1568-4946. DOI: `https://doi.org/10.1016/j.asoc.2023.110176`. Cited on page 156.

LI, Y. Optimum training sequences for OFDM systems with multiple transmit antennas. *In*: GLOBECOM '00 - IEEE. Global Telecommunications Conference. Conference Record (Cat. No.00CH37137). [S.l.: s.n.], 2000. v. 3, p. 1478–1482. DOI: `10.1109/GLOCOM.2000.891886`. Cited on page 45.

LOSS, D. et al. Phase Transmittance RBF Neural Networks. **Electronics Letters**, v. 43, n. 16, p. 882–884, Aug. 2007a. DOI: `10.1049/el:20070016`. Cited on pages 40, 41, 51, 59, 109, 111, 127.

LOSS, D. V. et al. Concurrent Blind Channel Equalization with Phase Transmittance RBF Neural Networks. **Journal of the Brazilian Computer Society**, v. 13, n. 1,

p. 18–25, 2007b. ISSN 1678-4804. DOI: 10.1007/BF03192398. Available from: <https://doi.org/10.1007/BF03192398>. Cited on page 30.

MAJUMDER, M. et al. Optimal Bit Allocation-Based Hybrid Precoder-Combiner Design Techniques for mmWave MIMO-OFDM Systems. **IEEE Access**, v. 9, p. 54109–54125, 2021. DOI: 10.1109/ACCESS.2021.3070921. Cited on pages 40, 141.

MANDIC, D. P.; GOH, V. S. L. **Complex Valued Nonlinear Adaptive Filters: Noncircularity, Widely Linear and Neural Models**. 1. ed. Chippenham, WT, UK: John Wiley & Sons, Inc., 2009. P. 73, 77. ISBN 978-0-470-06635-5. Cited on pages 80, 81.

MAREY, M.; DOBRE, O. A.; MOSTAFA, H. Cognitive Radios Equipped With Modulation and STBC Recognition Over Coded Transmissions. **IEEE Wireless Communications Letters**, v. 11, n. 7, p. 1513–1517, 2022. DOI: 10.1109/LWC.2022.3177638. Cited on page 141.

MAREY, M.; MOSTAFA, H. Turbo Modulation Identification Algorithm for OFDM Software-Defined Radios. **IEEE Communications Letters**, v. 25, n. 5, p. 1707–1711, 2021. DOI: 10.1109/LCOMM.2021.3054590. Cited on page 39.

MAREY, M. et al. STBC Recognition for OFDM Transmissions: Channel Decoder Aided Algorithm. **IEEE Communications Letters**, v. 26, n. 7, p. 1658–1662, 2022. DOI: 10.1109/LCOMM.2022.3170524. Cited on page 141.

MAYER, K. S.; SOARES, J. A.; ARANTES, D. S. Complex MIMO RBF Neural Networks for Transmitter Beamforming over Nonlinear Channels. **Sensors**, v. 20, n. 2, p. 1–15, Jan. 2020. DOI: 10.3390/s20020378. Cited on pages 31, 40, 41, 51, 54, 79, 83, 95, 96, 109, 127.

MAYER, K. S. et al. A new CPFSK demodulation approach for software defined radio. **Journal of Circuits, Systems and Computers**, v. 28, n. 14, p. 1–14, 2019a. DOI: 10.1142/S0218126619502438. Cited on pages 40, 141.

MAYER, K. S. et al. High data-rates and high-order DP-QAM optical links can be efficiently implemented with concurrent equalization. *In*: 22ND Photonics North (PN). [S.l.: s.n.], 2020a. P. 1. DOI: 10.1109/PN50013.2020.9167008. Cited on pages 40, 141.

MAYER, K. S. et al. Nonlinear Modified Concurrent Equalizer. **Journal of Communication and Information Systems**, v. 34, n. 1, p. 201–205, Sept. 2019b. DOI: 10.14209/jcis.2019.21. Cited on page 40.

MAYER, K. S. et al. Soft failure localization using machine learning with SDN-based network-wide telemetry. *In*: 46TH European Conference on Optical Communication (ECOC 2020). [S.l.: s.n.], 2020b. P. 1–4. DOI: 10.1109/ECOC48923.2020.9333313. Cited on page 40.

MAYER, K. S. et al. Blind Fuzzy Adaptation Step Control for a Concurrent Neural Network Equalizer. **Wireless Communications and Mobile Computing**, v. 2019, n. 1, p. 9082362, 2019c. DOI: https://doi.org/10.1155/2019/9082362. Cited on pages 40, 83, 95, 96, 109, 127, 161.

MAYER, K. S. et al. Machine-learning-based soft-failure localization with partial software-defined networking telemetry. **Journal of Optical Communications and Networking**, v. 13, n. 10, E122–E131, June 2021. Cited on page 40.

MAYER, K. S. **Complex-valued neural networks and applications in telecommunications**. 2022. Ph.D. Thesis – University of Campinas. Cited on pages 97, 102, 163.

MAYER, K. S. et al. Deep Phase-Transmittance RBF Neural Network for Beamforming With Multiple Users. **IEEE Wireless Communications Letters**, v. 11, n. 7, p. 1498–1502, 2022. DOI: `10.1109/LWC.2022.3177162`. Cited on pages 30, 83, 95–97, 109, 127, 142, 145, 155, 156, 161–163.

MEI, K. et al. A low complexity learning-based channel estimation for OFDM systems with online training. **IEEE Transactions on Communications**, v. 69, n. 10, p. 6722–6733, 2021. Cited on pages 57, 89.

MIRFARSHBAFAN, S. H. et al. Algorithm and VLSI design for 1-Bit data detection in massive MIMO-OFDM. **IEEE Open Journal of Circuits and Systems**, v. 1, p. 170–184, 2020. DOI: `10.1109/OJCAS.2020.3022514`. Cited on page 39.

MORSALI, A. et al. Design criteria for omnidirectional STBC in massive MIMO systems. **IEEE Wireless Commun. Lett.**, v. 8, n. 5, p. 143–1439, 2019. Cited on page 95.

NAIK, R. P. et al. Performance of Orthogonal and Non-Orthogonal Space Time Block Code Through the Underwater Wireless Optical Channels. *In*: 2023 IEEE International Conference on Advanced Networks and Telecommunications Systems (ANTS). [S.l.: s.n.], 2023. P. 373–378. DOI: `10.1109/ANTS59832.2023.10469512`. Cited on page 141.

NARKHEDE, M. V.; BARTAKKE, P. P.; SUTAONE, M. S. A review on weight initialization strategies for neural networks. **Artificial Intelligence Review**, v. 55, p. 291–322, 2022. Cited on pages 109, 127.

NASER, S. et al. Space-Time Block Coded Spatial Modulation for Indoor Visible Light Communications. **IEEE Photonics Journal**, v. 14, n. 1, p. 1–11, 2022. DOI: `10.1109/JPHOT.2021.3126873`. Cited on page 141.

NEUMANN, D.; WIESE, T.; UTSCHICK, W. Learning the MMSE channel estimator. **IEEE Transactions on Signal Processing**, v. 66, n. 11, p. 2905–2917, June 2018. Cited on pages 83, 90.

O'SHEA, T.; HOYDIS, J. An Introduction to Deep Learning for the Physical Layer. **IEEE Transactions on Cognitive Communications and Networking**, v. 3, n. 4, p. 563–575, 2017. DOI: `10.1109/TCCN.2017.2758370`. Cited on pages 156, 157.

OSMAN, A. M. et al. A Modified Method of Filtering for FBMC Based 5G Communications on Minimizing Doppler Shift. *In*: 2021 6th International Conference for Convergence in Technology (I2CT). [S.l.: s.n.], 2021. P. 1–4. DOI: `10.1109/I2CT51068.2021.9417931`. Cited on pages 40, 141.

PATRA, S.; MULGREW, B. Efficient architecture for Bayesian equalization using fuzzy filters. **IEEE Transactions on Circuits and Systems II: Analog and Digital Signal Processing**, v. 45, n. 7, p. 812–820, July 1998. ISSN 1558-125X. DOI: 10.1109/82.700928. Cited on page 30.

PINTO, R. P. et al. Demonstration of machine-intelligent soft-failure localization using SDN telemetry. *In*: OPTICAL Fiber Communications Conference and Exhibition (OFC 2021). [S.l.: s.n.], 2021. P. 1–3. Cited on page 40.

QIAN, Y.; XIAO, L.; JIANG, T. SM-STBC aided Orthogonal Time Frequency Space Modulation. *In*: 2022 IEEE Wireless Communications and Networking Conference (WCNC). [S.l.: s.n.], 2022. P. 2172–2177. DOI: 10.1109/WCNC51071.2022.9771767. Cited on page 141.

QIN, Z. et al. Deep Learning in Physical Layer Communications. **IEEE Wireless Communications**, v. 26, n. 2, p. 93–99, 2019. DOI: 10.1109/MWC.2019.1800601. Cited on page 155.

RALEIGH, G. G.; CIOFFI, J. M. Spatio-temporal Coding for Wireless Communication. **IEEE Transactions on Communications**, v. 46, n. 3, p. 357–366, 1998. DOI: 10.1109/26.662641. Cited on page 161.

SAAD, W.; BENNIS, M.; CHEN, M. A Vision of 6G Wireless Systems: Applications, Trends, Technologies, and Open Research Problems. **IEEE Network**, v. 34, n. 3, p. 134–142, 2020. Cited on page 40.

SACI, A. et al. One-Shot Blind Channel Estimation for OFDM Systems Over Frequency-Selective Fading Channels. **IEEE Transactions on Communications**, v. 65, n. 12, p. 5445–5458, 2017. DOI: 10.1109/TCOMM.2017.2740925. Cited on page 141.

SAGDUYU, Y. E.; ULUKUS, S.; YENER, A. Task-Oriented Communications for NextG: End-to-end Deep Learning and AI Security Aspects. **IEEE Wireless Communications**, v. 30, n. 3, p. 52–60, 2023. DOI: 10.1109/MWC.006.2200494. Cited on pages 157, 158.

SAMBRIDGE, M. et al. Trans-dimensional inverse problems, model comparison and the evidence. **Geophysical Journal International**, v. 167, n. 2, p. 528–542, Nov. 2006. DOI: 10.1111/j.1365-246X.2006.03155.x. Cited on page 78.

SANOOPKUMAR, P. S.; MUNEER, P.; SAMEER, S. M. A joint equalization and decoding technique for multiuser massive MIMO uplink system with transmitter and receiver RF impairments under doubly selective channels. **IEEE Syst. J.**, p. 1–11, 2022. Cited on page 96.

SCARDAPANE, S. et al. Complex-valued neural networks with nonparametric activation functions. **IEEE Trans. Emerg. Topics Comput. Intell.**, v. 4, n. 2, p. 140–150, 2020. Cited on pages 96, 97.

SCHMIDHUBER, J. Deep learning in neural networks: An overview. **Neural Netw.**, v. 61, p. 85–117, 2015. Cited on page 97.

SHANG, B. et al. Spatial spectrum sensing in uplink two-tier user-centric deployed HetNets. **IEEE Transactions on Wireless Communications**, v. 19, n. 12, p. 7957–7972, 2020. DOI: 10.1109/TWC.2020.3018408. Cited on pages 39, 141.

SHARIATI, N. et al. Low-complexity channel estimation in large-scale MIMO using polynomial expansion. *In*: 2013 IEEE 24th Annual International Symposium on Personal, Indoor, and Mobile Radio Communications (PIMRC). [S.l.: s.n.], Sept. 2013. P. 1157–1162. Cited on page 83.

SHIMIZU, D. Y. et al. A deep neural network model for link failure identification in multi-path ROADM based networks. *In*: 22ND Photonics North (PN). [S.l.: s.n.], 2020. P. 1. DOI: 10.1109/PN50013.2020.9166978. Cited on page 40.

SHR, K.-T.; CHEN, H.-D.; HUANG, Y.-H. A low-complexity Viterbi decoder for space-time trellis codes. **IEEE Transactions on Circuits and Systems I: Regular Papers**, v. 57, n. 4, p. 873–885, 2010. DOI: 10.1109/TCSI.2009.2027648. Cited on page 43.

SINDHU, P.; HAMEED, A. Efficient quasi-orthogonal space-time block codes for five and six transmit antennas. *In*: 2015 IEEE International Conference on Electronics, Computing and Communication Technologies (CONECCT). [S.l.: s.n.], 2015. P. 1–5. DOI: 10.1109/CONECCT.2015.7383923. Cited on pages 47, 144.

SINGH, A. et al. Autoencoder-Based End-to-End OTFS System Design With Hardware Impairments. **IEEE Wireless Communications Letters**, v. 13, n. 8, p. 2285–2289, 2024. DOI: 10.1109/LWC.2024.3412240. Cited on pages 157, 159.

SINGH, S. K.; KUMAR, A. Modified design of STBC Encoder for reducing Non-Linear distortions in OFDM Channel Estimation. *In*: 2022 Second International Conference on Advances in Electrical, Computing, Communication and Sustainable Technologies (ICAECT). [S.l.: s.n.], 2022. P. 1–5. DOI: 10.1109/ICAECT54875.2022.9807993. Cited on page 141.

SOARES, J. A. et al. Complex-valued phase transmittance RBF neural networks for massive MIMO-OFDM receivers. **Sensors**, v. 21, n. 24, p. 1–31, Dec. 2021a. ISSN 1424-8220. DOI: 10.3390/s21248200. Available from: <https://www.mdpi.com/1424-8220/21/24/8200>. Cited on pages 83, 95–99, 109, 127, 142–145, 148.

SOARES, J. A.; MAYER, K. S.; ARANTES, D. S. On the Parameter Selection of Phase-transmittance Radial Basis Function Neural Networks for Communication Systems. *In*: IEEE International Conference on Machine Learning for Communication and Networking (ICMLCN). [S.l.: s.n.], 2024. P. 530–536. DOI: 10.1109/ICMLCN59089.2024.10624891. Cited on pages 131, 133, 142, 172.

SOARES, J. A. **Complex phase-transmittance RBF neural network for massive MIMO-OFDM decoding**. Feb. 2021. MA thesis – Department of Communications, School of Electrical and Computer Engineering, University of Campinas. Available from: <http://acervus.unicamp.br/index.asp?codigo_sophia=1165045>. Cited on pages 39–52, 54, 56–60, 63, 68, 69.

SOARES, J. A.; MAYER, K. S.; ARANTES, D. S. Semi-Supervised ML-Based Joint Channel Estimation and Decoding for m-MIMO With Gaussian Inference Learning. **IEEE Wireless Communications Letters**, v. 12, n. 12, p. 2123–2127, 2023. DOI: 10.1109/LWC.2023.3309479. Cited on pages 30, 114, 133, 146, 155, 161, 162.

SOARES, J. A. et al. Complex-Valued Phase Transmittance RBF Neural Networks for Massive MIMO-OFDM Receivers. **Sensors**, v. 21, n. 24, 2021b. DOI: 10.3390/s21248200. Cited on page 155.

SOKAL, B. et al. Tensor-Based Receiver for Joint Channel, Data, and Phase-Noise Estimation in MIMO-OFDM Systems. **IEEE Journal of Selected Topics in Signal Processing**, v. 15, n. 3, p. 803–815, 2021. DOI: 10.1109/JSTSP.2021.3061917. Cited on pages 40, 141.

SONG, J. et al. Benchmarking and Interpreting End-to-End Learning of MIMO and Multi-User Communication. **IEEE Transactions on Wireless Communications**, v. 21, n. 9, p. 7287–7298, 2022. DOI: 10.1109/TWC.2022.3157467. Cited on pages 156–159.

SWAIN, R. R.; KHILAR, P. M.; DASH, T. Multifault diagnosis in WSN using a hybrid metaheuristic trained neural network. **Digital Communications and Networks**, v. 6, n. 1, p. 86–100, 2020. DOI: 10.1016/j.dcan.2018.02.001. Cited on page 40.

TAROKH, V.; JAFARKHANI, H.; CALDERBANK, A. R. Space-time block codes from orthogonal designs. **IEEE Transactions on Information Theory**, v. 45, n. 5, p. 1456–1467, 1999. DOI: 10.1109/18.771146. Cited on pages 45, 47, 54, 68, 69, 143.

TEMIZ, M.; ALSUSA, E.; BAIDAS, M. W. A dual-functional massive MIMO OFDM communication and radar transmitter architecture. **IEEE Transactions on Vehicular Technology**, v. 69, n. 12, p. 14974–14988, 2020. DOI: 10.1109/TVT.2020.3031686. Cited on page 39.

TENOUDJI, F. C. **Analog and digital signal analysis: From basics to applications**. 1. ed. Paris, France: Springer, 2016. P. 387, 469, 471. Cited on page 80.

TIRKKONEN, O.; BOARIU, A.; HOTTINEN, A. Minimal non-orthogonality rate 1 space-time block code for 3+ Tx antennas. *In*: 2000 IEEE Sixth International Symposium on Spread Spectrum Techniques and Applications. ISSTA 2000. Proceedings (Cat. No.00TH8536). [S.l.: s.n.], 2000. v. 2, p. 429–432. DOI: 10.1109/ISSSTA.2000.876470. Cited on pages 47, 143.

TOKA, M.; KUCUR, O. Performance of MRT/RAS MIMO-NOMA with residual hardware impairments. **IEEE Wireless Communications Letters**, v. 10, n. 5, p. 1071–1074, 2021. DOI: 10.1109/LWC.2021.3057432. Cited on page 42.

TURNBULL, D.; ELKAN, C. Fast recognition of musical genres using RBF networks. **IEEE Transactions on Knowledge and Data Engineering**, v. 17, n. 4, p. 580–584, 2005. Cited on pages 109, 127.

VERENZUELA, D. et al. Massive-MIMO iterative channel estimation and decoding (MICED) in the uplink. **IEEE Trans. Commun.**, v. 68, n. 2, p. 854–870, 2020. Cited on page 96.

VOIGTLAENDER, F. The universal approximation theorem for complex-valued neural networks. **Applied and Computational Harmonic Analysis**, v. 64, p. 33–61, 2023. ISSN 1063-5203. DOI: https://doi.org/10.1016/j.acha.2022.12.002. Available from: <https://www.sciencedirect.com/science/article/pii/S1063520322001014>. Cited on pages 29, 95.

WALLACE, M.; TSAPATSOULIS, N.; KOLLIAS, S. Intelligent initialization of resource allocating RBF networks. **Neural Networks**, v. 18, n. 2, p. 117–122, 2005. Cited on pages 109, 110, 127.

WANG, B. et al. A Deep Learning-Based Intelligent Receiver for Improving the Reliability of the MIMO Wireless Communication System. **IEEE Transactions on Reliability**, v. 71, n. 2, p. 1104–1115, 2022. Cited on page 155.

WANG, C.-X. et al. On the Road to 6G: Visions, Requirements, Key Technologies, and Testbeds. **IEEE Communications Surveys & Tutorials**, v. 25, n. 2, p. 905–974, Apr. 2023. ISSN 1553-877X. DOI: 10.1109/COMST.2023.3249835. Cited on pages 28, 155.

WEIFENG SU; XIANG-GEN XIA. Quasi-orthogonal space-time block codes with full diversity. *In*: GLOBAL Telecommunications Conference, 2002. GLOBECOM '02. IEEE. [S.l.: s.n.], 2002. v. 2, p. 1098–1102. DOI: 10.1109/GLOCOM.2002.1188366. Cited on pages 47, 143, 144.

WU, C. et al. Quasi-Orthogonal Space-Time Block Coded Spatial Modulation. **IEEE Transactions on Communications**, v. 70, n. 12, p. 7872–7885, 2022a. DOI: 10.1109/TCOMM.2022.3216805. Cited on page 141.

WU, C. et al. Channel Prediction in High-Mobility Massive MIMO: From Spatio-Temporal Autoregression to Deep Learning. **IEEE Journal on Selected Areas in Communications**, v. 39, n. 7, p. 1915–1930, 2021. DOI: 10.1109/JSAC.2021.3078503. Cited on page 155.

WU, H. et al. Channel-Adaptive Wireless Image Transmission With OFDM. **IEEE Wireless Communications Letters**, v. 11, n. 11, p. 2400–2404, 2022b. DOI: 10.1109/LWC.2022.3204837. Cited on pages 157, 158.

WU, S. et al. Message-passing receiver for joint channel estimation and decoding in 3D massive MIMO-OFDM systems. **IEEE Trans. Wireless Commun.**, v. 15, n. 12, p. 8122–8138, 2016. Cited on page 96.

XIAO, C.; YANG, S.; FENG, Z. Complex-valued depthwise separable convolutional neural network for automatic modulation classification. **IEEE Transactions on Instrumentation and Measurement**, v. 72, p. 1–10, 2023. Cited on pages 109, 127.

XIU, H. et al. A DFDD Based Detector for Space-Time Block Coded Differential Spatial Modulation Under Time-Selective Channels. **IEEE Communications Letters**, v. 26, n. 2, p. 359–363, 2022. DOI: 10.1109/LCOMM.2021.3132697. Cited on page 141.

XU, H.; PILLAY, N. Multiple Complex Symbol Golden Space-Time Labeling Diversity. **IEEE Access**, v. 9, p. 70233–70241, 2021. DOI: 10.1109/ACCESS.2021.3078827. Cited on page 43.

XU, J. et al. The performance analysis of complex-valued neural network in radio signal recognition. **IEEE Access**, v. 10, p. 48708–48718, 2022. Cited on pages 95, 109, 127.

XU, S. et al. Space–time domain equalization algorithm based on complex-valued neural network in a long-haul photonic-aided MIMO THz system. **Optics Letters**, Optica Publishing Group, v. 49, n. 5, p. 1253–1256, Mar. 2024. DOI: 10.1364/OL.512416. Cited on page 155.

YANG, X. et al. Automatic modulation mode recognition of communication signals based on complex-valued neural network. *In*: 2022 International Conference on Computing, Communication, Perception and Quantum Technology (CCPQT). [S.l.: s.n.], 2022. P. 32–37. Cited on pages 109, 127.

YANG, Y. et al. Graph neural network-based channel tracking for massive MIMO networks. **IEEE Commun. Lett.**, v. 24, n. 8, p. 1747–1751, 2020. Cited on pages 95, 96.

YAO, G.; CHEN, H.; HU, J. An improved expectation propagation based detection scheme for MIMO systems. **IEEE Transactions on Communications**, v. 69, n. 4, p. 2163–2175, 2021. DOI: 10.1109/TCOMM.2020.3048942. Cited on page 42.

YE, H.; LI, G. Y.; JUANG, B.-H. Deep Learning Based End-to-End Wireless Communication Systems Without Pilots. **IEEE Transactions on Cognitive Communications and Networking**, v. 7, n. 3, p. 702–714, 2021. DOI: 10.1109/TCCN.2021.3061464. Cited on pages 156–158.

YE, H.; LI, G. Y.; JUANG, B.-H. Power of deep learning for channel estimation and signal detection in OFDM systems. **IEEE Wireless Commun. Lett.**, v. 7, n. 1, p. 114–117, 2018. DOI: 10.1109/LWC.2017.2757490. Cited on pages 97, 147, 155.

YE, H. et al. Deep Learning-Based End-to-End Wireless Communication Systems With Conditional GANs as Unknown Channels. **IEEE Transactions on Wireless Communications**, v. 19, n. 5, p. 3133–3143, 2020. DOI: 10.1109/TWC.2020.2970707. Cited on pages 156–158.

YERRAPRAGADA, A. K.; KELLEY, B. On the Application of K-User MIMO for 6G Enhanced Mobile Broadband. **Sensors**, v. 20, n. 21, p. 1–16, 2020. DOI: 10.3390/s20216252. Cited on pages 40, 141.

YIN, X. et al. Modeling city-canyon pedestrian radio channels based on passive sounding in in-service networks. **IEEE Transactions on Vehicular Technology**, v. 65, n. 10, p. 7931–7943, Oct. 2016. Cited on page 83.

YOON, E. et al. LDPC Decoding With Low Complexity for OFDM Index Modulation. **IEEE Access**, v. 9, p. 68435–68444, 2021. DOI: 10.1109/ACCESS.2021.3077256. Cited on page 39.

YU, D. et al. Low complexity complex matrix inversion method for MIMO communication systems. *In*: 2015 International Conference on Wireless Communications & Signal Processing (WCSP). [S.l.: s.n.], Oct. 2015. P. 1–5. Cited on page 87.

YUAN, Q. et al. Deep Learning-Based Hybrid Precoding for Terahertz Massive MIMO Communication With Beam Squint. **IEEE Communications Letters**, v. 27, n. 1, p. 175–179, 2023. DOI: 10.1109/LCOMM.2022.3211514. Cited on page 155.

ZHANG, H. et al. An optical neural chip for implementing complex-valued neural network. **Nat. Commun.**, v. 12, n. 457, p. 1–11, 2021a. Cited on pages 42, 95.

ZHANG, H.; ZHANG, L.; JIANG, Y. Overfitting and Underfitting Analysis for Deep Learning Based End-to-end Communication Systems. *In*: 11TH International Conference on Wireless Communications and Signal Processing (WCSP). [S.l.: s.n.], 2019. P. 1–6. DOI: 10.1109/WCSP.2019.8927876. Cited on pages 157, 158.

ZHANG, S.-Q.; GAO, W.; ZHOU, Z.-H. Towards understanding theoretical advantages of complex-reaction networks. **Neural Netw.**, v. 151, p. 80–93, 2022. Cited on pages 83, 95, 109, 127.

ZHANG, X.; VAEZI, M. Deep Autoencoder-Based Z-Interference Channels With Perfect and Imperfect CSI. **IEEE Transactions on Communications**, v. 72, n. 2, p. 861–873, 2024. DOI: 10.1109/TCOMM.2023.3328026. Cited on pages 157, 159.

ZHANG, Y. et al. CV-3DCNN: Complex-valued deep learning for CSI prediction in FDD massive MIMO systems. **IEEE Wireless Communications Letters**, v. 10, n. 2, p. 266–270, 2021b. Cited on pages 109, 127.

ZHANG, Y.; ZAKHAROV, Y. V.; LI, J. Soft-decision-driven sparse channel estimation and turbo equalization for MIMO underwater acoustic communications. **IEEE Access**, v. 6, p. 4955–4973, 2018. Cited on page 99.

ZHAO, W.; HUANG, H. Adaptive orthogonal gradient descent algorithm for fully complex-valued neural networks. **Neurocomputing**, v. 546, p. 1–8, 2023. Cited on page 95.

ZHAO, X. et al. Analysis of a distributed MIMO channel capacity under a special scenario. **EURASIP Journal on Wireless Communications and Networking**, v. 2019, n. 189, p. 1–7, 2019. Cited on page 42.

ZHENG, X.; LAU, V. K. N. Online deep neural networks for mmWave Massive MIMO channel estimation with arbitrary array geometry. **IEEE Trans. Signal Process.**, v. 69, p. 2010–2025, 2021. Cited on page 95.

ZHONG, Y.; XIAO, Y.; NIU, H. Transmit Antenna Selection and Artificial Noise Design for Secure STBC-SM Transmission. *In*: 2022 IEEE 95th Vehicular Technology Conference:

(VTC2022-Spring). [S.l.: s.n.], 2022. P. 1–6. DOI: `10.1109/VTC2022-Spring54318.2022.9860380`. Cited on page 141.

ZOU, F. et al. A novel PAPR reduction scheme for OFDM systems based on neural networks. **Wireless Communications and Mobile Computing**, v. 2021, p. 1–8, 2021. DOI: `10.1155/2021/5574807`. Cited on pages 40, 141.

APPENDIX A – PERMISSION TO REPRODUCE COPYRIGHTED MATERIAL

RightsLink

Sign in/Register

IEEE Requesting permission to reuse content from an IEEE publication

Semi-Supervised ML-Based Joint Channel Estimation and Decoding for m-MIMO With Gaussian Inference Learning

Author: Jonathan Aguiar Soares

Publication: IEEE Wireless Communications Letters

Publisher: IEEE

Date: Dec 1, 2023

Thesis / Dissertation Reuse

The IEEE does not require individuals working on a thesis to obtain a formal reuse license, however, you may print out this statement to be used as a permission grant:

Requirements to be followed when using any portion (e.g., figure, graph, table, or textual material) of an IEEE copyrighted paper in a thesis:

1) In the case of textual material (e.g., using short quotes or referring to the work within these papers) users must give full credit to the original source (author, paper, publication) followed by the IEEE copyright line © 2011 IEEE.
2) In the case of illustrations or tabular material, we require that the copyright line © [Year of original publication] IEEE appear prominently with each reprinted figure and/or table.
3) If a substantial portion of the original paper is to be used, and if you are not the senior author, also obtain the senior author's approval.

Requirements to be followed when using an entire IEEE copyrighted paper in a thesis:

1) The following IEEE copyright/ credit notice should be placed prominently in the references: © [year of original publication] IEEE. Reprinted, with permission, from [author names, paper title, IEEE publication title, and month/year of publication]
2) Only the accepted version of an IEEE copyrighted paper can be used when posting the paper or your thesis on-line.
3) In placing the thesis on the author's university website, please display the following message in a prominent place on the website: In reference to IEEE copyrighted material which is used with permission in this thesis, the IEEE does not endorse any of [university/educational entity's name goes here]'s products or services. Internal or personal use of this material is permitted. If interested in reprinting/republishing IEEE copyrighted material for advertising or promotional purposes or for creating new collective works for resale or redistribution, please go to http://www.ieee.org/publications_standards/publications/rights/rights_link.html to learn how to obtain a License from RightsLink.

If applicable, University Microfilms and/or ProQuest Library, or the Archives of Canada may supply single copies of the dissertation.

BACK CLOSE WINDOW

RightsLink

Sign in/Register

IEEE Requesting permission to reuse content from an IEEE publication

On the Parameter Selection of Phase-transmittance Radial Basis Function Neural Networks for Communication Systems

Conference Proceedings: null
Author: Jonathan A. Soares
Publisher: IEEE
Date: May 5, 2024

Thesis / Dissertation Reuse

The IEEE does not require individuals working on a thesis to obtain a formal reuse license, however, you may print out this statement to be used as a permission grant:

Requirements to be followed when using any portion (e.g., figure, graph, table, or textual material) of an IEEE copyrighted paper in a thesis:

1) In the case of textual material (e.g., using short quotes or referring to the work within these papers) users must give full credit to the original source (author, paper, publication) followed by the IEEE copyright line © 2011 IEEE.
2) In the case of illustrations or tabular material, we require that the copyright line © [Year of original publication] IEEE appear prominently with each reprinted figure and/or table.
3) If a substantial portion of the original paper is to be used, and if you are not the senior author, also obtain the senior author's approval.

Requirements to be followed when using an entire IEEE copyrighted paper in a thesis:

1) The following IEEE copyright/ credit notice should be placed prominently in the references: © [year of original publication] IEEE. Reprinted, with permission, from [author names, paper title, IEEE publication title, and month/year of publication]
2) Only the accepted version of an IEEE copyrighted paper can be used when posting the paper or your thesis on-line.
3) In placing the thesis on the author's university website, please display the following message in a prominent place on the website: In reference to IEEE copyrighted material which is used with permission in this thesis, the IEEE does not endorse any of [university/educational entity's name goes here]'s products or services. Internal or personal use of this material is permitted. If interested in reprinting/republishing IEEE copyrighted material for advertising or promotional purposes or for creating new collective works for resale or redistribution, please go to http://www.ieee.org/publications_standards/publications/rights/rights_link.html to learn how to obtain a License from RightsLink.

If applicable, University Microfilms and/or ProQuest Library, or the Archives of Canada may supply single copies of the dissertation.

BACK CLOSE WINDOW

RightsLink

Sign in/Register

Deep Complex-valued Radial Basis Function Neural Networks and Parameter Selection

Requesting permission to reuse content from an IEEE publication

Conference Proceedings: null
Author: Jonathan A. Soares
Publisher: IEEE
Date: Jul 14, 2024

Thesis / Dissertation Reuse

The IEEE does not require individuals working on a thesis to obtain a formal reuse license, however, you may print out this statement to be used as a permission grant:

Requirements to be followed when using any portion (e.g., figure, graph, table, or textual material) of an IEEE copyrighted paper in a thesis:

1) In the case of textual material (e.g., using short quotes or referring to the work within these papers) users must give full credit to the original source (author, paper, publication) followed by the IEEE copyright line © 2011 IEEE.
2) In the case of illustrations or tabular material, we require that the copyright line © [Year of original publication] IEEE appear prominently with each reprinted figure and/or table.
3) If a substantial portion of the original paper is to be used, and if you are not the senior author, also obtain the senior author's approval.

Requirements to be followed when using an entire IEEE copyrighted paper in a thesis:

1) The following IEEE copyright/ credit notice should be placed prominently in the references: © [year of original publication] IEEE. Reprinted, with permission, from [author names, paper title, IEEE publication title, and month/year of publication]
2) Only the accepted version of an IEEE copyrighted paper can be used when posting the paper or your thesis on-line.
3) In placing the thesis on the author's university website, please display the following message in a prominent place on the website: In reference to IEEE copyrighted material which is used with permission in this thesis, the IEEE does not endorse any of [university/educational entity's name goes here]'s products or services. Internal or personal use of this material is permitted. If interested in reprinting/republishing IEEE copyrighted material for advertising or promotional purposes or for creating new collective works for resale or redistribution, please go to http://www.ieee.org/publications_standards/publications/rights/rights_link.html to learn how to obtain a License from RightsLink.

If applicable, University Microfilms and/or ProQuest Library, or the Archives of Canada may supply single copies of the dissertation.

BACK CLOSE WINDOW

CCC RightsLink

Sign in/Register

IEEE Requesting permission to reuse content from an IEEE publication

Neural Network-based Subcarrier-level Joint Channel Estimation and Decoding for MIMO-OFDM Receivers

Conference Proceedings: null

Author: Jonathan A. Soares

Publisher: IEEE

Date: Nov 6, 2024

Thesis / Dissertation Reuse

The IEEE does not require individuals working on a thesis to obtain a formal reuse license, however, you may print out this statement to be used as a permission grant:

Requirements to be followed when using any portion (e.g., figure, graph, table, or textual material) of an IEEE copyrighted paper in a thesis:

1) In the case of textual material (e.g., using short quotes or referring to the work within these papers) users must give full credit to the original source (author, paper, publication) followed by the IEEE copyright line © 2011 IEEE.
2) In the case of illustrations or tabular material, we require that the copyright line © [Year of original publication] IEEE appear prominently with each reprinted figure and/or table.
3) If a substantial portion of the original paper is to be used, and if you are not the senior author, also obtain the senior author's approval.

Requirements to be followed when using an entire IEEE copyrighted paper in a thesis:

1) The following IEEE copyright/ credit notice should be placed prominently in the references: © [year of original publication] IEEE. Reprinted, with permission, from [author names, paper title, IEEE publication title, and month/year of publication]
2) Only the accepted version of an IEEE copyrighted paper can be used when posting the paper or your thesis on-line.
3) In placing the thesis on the author's university website, please display the following message in a prominent place on the website: In reference to IEEE copyrighted material which is used with permission in this thesis, the IEEE does not endorse any of [university/educational entity's name goes here]'s products or services. Internal or personal use of this material is permitted. If interested in reprinting/republishing IEEE copyrighted material for advertising or promotional purposes or for creating new collective works for resale or redistribution, please go to http://www.ieee.org/publications_standards/publications/rights/rights_link.html to learn how to obtain a License from RightsLink.

If applicable, University Microfilms and/or ProQuest Library, or the Archives of Canada may supply single copies of the dissertation.

BACK   CLOSE WINDOW